

Understanding the long-term evolution of C-S-H phases present in cement backfills

Sumanjani Vinnakota

Submitted in accordance with the requirements for the degree of Doctor of
Philosophy

The University of Leeds
School of Civil Engineering

March 2019

The candidate confirms that the work submitted is her own and that appropriate credit has been given where reference has been made to the work of others.

This copy has been supplied on the understanding that it is copyright material and that no quotation from the thesis may be published without proper acknowledgement.

© 2019 The University of Leeds and Sumanjani Vinnakota

The right of Sumanjani Vinnakota to be identified as Author of this work has been asserted by her in accordance with the Copyright, Designs and Patents

Act 1988.

Acknowledgements

I am grateful to Radioactive Waste Management for funding this project, presenting me with a valuable opportunity to be a part of the collaboration. I would like to thank my supervisor Prof. Ian G. Richardson for his supervision, guidance and support throughout my PhD research.

I would also like to thank my co-supervisor Prof. Rik Brydson and members from Wood: Dr Steve Swanton, Dr James Schofield and from RWM: Dr Amy Shelton, Dr Steve Williams, involved with this project and who provided me with required feedback and support.

I would like to extend my thanks to all my colleagues: Julia, Joe, Hong, Ali, Sam, Toby and Ahmad for your company and all those valuable discussions. I would also like to thank all the civil engineering staff who gave me support particularly the technical staff: Karen, Lucy, Vicky, Les, Dave, Emma, Ryan, Sheena and Becky. Additional thanks to Zabeada, Nicole and Stuart for all the training and help in electron microscopy.

Thanks to my parents and my brother for being supportive throughout. Thanks to Elezabath for all those stress relief evenings and for making my stay in Leeds memorable. Finally, a special thanks to Avichal for putting up with me over the last few years and for all the incredible support and motivation.

Dedicated to my parents and my brother!!

Abstract

In the UK, cement grouts are used to encapsulate some intermediate level radioactive wastes (ILW) and as a potential backfill around waste packages in a Geological Disposal Facility (GDF). The main binding phase in these cementitious backfills is calcium silicate hydrate (C-S-H) which changes with time. Hence, to ensure the long-term performance of these backfills, it is essential to study how the main phases in the hardened cement evolve with time. This PhD project aims to characterize various backfill materials and then to synthesize and characterize the analogues of the main binding C-S-H present in the backfill material. This study also investigates the structural and morphological evolution of C-S-H phases due to leaching and hydrothermal ageing.

Single phase synthetic C-S-H phases without the use of C_3S or alkalis are synthesized via various methods with high Ca/Si ratios in the range 1.5 – 2.0 and analysed using techniques like NMR, TEM – EDX, STA and XRD to understand the morphology, chemical composition and silicate structure. The results obtained indicate that the C-S-H morphology of samples synthesized via silica – lime reactions with Ca/Si of ~ 2.0 is fibrous. The morphology of C-S-H in samples synthesized by constant lime concentration method depends on the lime concentration in the solution. As the lime concentration is increased, the morphology is found to change from foil-like to fibrous with Ca/Si ratios increasing from 1.5 – 1.8. On artificial ageing (leaching and hydrothermal ageing) of these high Ca/Si ratio C-S-H phases, the morphology, composition and silicate structure changed as a result of degradation of the C-S-H phase.

Contents

List of Figures	ix
List of Tables	xix
List of abbreviations	xxi
Chapter 1 Introduction.....	1
1.1 Background of the study.....	1
1.2 Outline of thesis.....	4
Chapter 2 Literature review	6
2.1 Portland cement	6
2.1.1 Tricalcium silicate.....	7
2.1.2 Dicalcium silicate.....	8
2.1.3 Tricalcium aluminate	10
2.1.4 Aluminoferrite	12
2.1.5 Hydration reactions and hydration products	12
2.1.6 Model structures of C-S-H.....	16
2.1.6.1 Tobermorite	16
2.1.6.2 Jennite	17
2.1.7 Models for C-S-H	19
2.1.7.1 Powers.....	19
2.1.7.2 Feldman and Sereda	19
2.1.7.3 Fuji and Kondo	21
2.1.7.4 Taylor.....	21
2.1.7.5 Richardson and Groves	23
2.1.7.6 Cong and Kirkpatrick	26
2.1.7.7 Chen et al	27
2.1.7.8 Pellenq.....	27
2.1.7.9 Richardson's model structures for C-(A)-S-H (I)	29
2.2 Methods to synthesize C-S-H phases	34
2.2.1 Cong and Kirkpatrick.....	34
2.2.2 Chen et al.....	35
2.2.3 Ishida et al.....	36
2.2.4 Nonat and Lecoq.....	37
2.2.5 Grudemo	38

2.2.6	Taylor	40
2.2.7	Rodriguez.....	41
2.2.8	Kumar et al.....	42
2.3	Use of cementitious materials in radioactive waste management ..	43
2.3.1	Introduction	43
2.3.2	Classification of radioactive wastes.....	44
2.3.3	Role of a backfill.....	45
2.3.4	Nirex Reference Vault Backfill.....	47
2.4	Process of Leaching.....	48
2.4.1	Effects of Leaching.....	51
2.5	Hydrothermal ageing	54
Chapter 3 Characterization Techniques.....		55
3.1	Simultaneous Thermal Analysis	55
3.1.1	Introduction	55
3.1.2	Sample preparation.....	58
3.2	X - Ray Diffraction (XRD)	58
3.2.1	Introduction	58
3.2.2	Sample preparation.....	60
3.3	Magic Angle Spinning Nuclear Magnetic Resonance (MAS NMR).....	61
3.3.1	Introduction	61
3.3.1.1	²⁹ Si MAS NMR.....	63
3.3.1.2	²⁷ Al MAS NMR.....	67
3.3.2	Sample preparation.....	68
3.3.3	Igor fitting method	69
3.4	Transmission Electron Microscopy (TEM)	69
3.4.1	Introduction	69
3.4.2	Sample preparation.....	71
Chapter 4 Experimental Methods		74
4.1	NRVB sample description.....	74
4.2	Synthesis of high Ca/Si ratio C-S-H phases by hydrothermal method 76	
4.2.1	Introduction	76
4.2.2	Experimental synthesis	79
4.3	Synthesis of high Ca/Si ratio C-S-H phases by constant lime concentration method.....	83

4.3.1	Introduction	83
4.3.2	Experimental Synthesis.....	86
4.4	Leaching and Hydrothermal ageing of synthetic C-S-H gels	93
Chapter 5	Results and discussion of NRVB samples (described in Table 4:2, Experimental Methods).....	96
5.1	TEM - EDX	96
5.2	²⁹ Si NMR	102
5.3	²⁷ Al NMR	105
5.4	STA	107
5.5	XRD.....	111
5.6	Structural chemical formula for C-A-S-H(I) in S4	113
Chapter 6	Results and discussion of static and ball mill hydration of β-C₂S	115
6.1	Characterization results of sample A and sample C (described in Table 4:4, Experimental Methods).....	115
6.1.1	TEM – EDX	115
6.1.2	²⁹ Si NMR	119
6.1.3	STA and XRD.....	120
6.2	Characterization results of static hydrated samples (SHC) (described in Table 4:5, Experimental Methods)	124
6.2.1	TEM – EDX	124
6.2.2	²⁹ Si NMR	126
6.2.3	STA and XRD.....	134
6.3	Characterization results of ball mill hydrated samples (BHC) (described in Table 4:5, Experimental Methods)	137
6.3.1	TEM - EDX.....	137
6.3.2	²⁹ Si NMR	141
6.3.3	STA and XRD.....	148
6.4	Comparison of MCL variation with Ca/Si ratios for static and ball mill hydrated C-S-H phases with reported data from literature	152
Chapter 7	Results and discussion of C-S-H phases synthesised by constant lime concentration method	156
7.1	Characterization Results of C-S-H phases (described in Table 4.8, Experimental Methods).....	156
7.1.1	TEM - EDX.....	156
7.1.2	²⁹ Si NMR	167
7.1.3	STA and XRD.....	180

Chapter 8 Results and discussion of artificial ageing on synthetic C-S-H samples	185
8.1 Characterization results of C-S-H samples (described in Table 4:9, Experimental Methods).....	185
8.1.1 TEM – EDX of static leached C-S-H samples	185
8.1.2 ²⁹ Si NMR of static leached C-S-H samples	189
8.1.3 STA of static leached C-S-H samples	197
8.1.4 TEM - EDX of dynamic leached samples	200
8.1.5 ²⁹ Si NMR of dynamic leached C-S-H samples	207
8.1.6 STA of dynamic leached C-S-H samples	215
8.1.7 TEM-EDX of hydrothermally aged C-S-H sample	218
8.1.8 ²⁹ Si NMR of Hydrothermally aged C-S-H sample.....	219
8.1.9 STA of hydrothermally aged C-S-H sample	222
8.1.10 Comparison of MCL variation with Ca/Si ratios for all the artificially aged C-S-H phases	224
Chapter 9 Conclusions and further work.....	226
References.....	232

List of Figures

Figure 1.1 Multi-barrier concept for disposal of ILW [2].	1
Figure 2.1 Schematic illustration of the phase transitions of dicalcium silicate [20].	9
Figure 2.2 Rate of heat evolution in hydration of Portland cement [12].	14
Figure 2.3 Microstructural development in a cement grain [11].	15
Figure 2.4 Structure of 1.4 nm tobermorite [30].	17
Figure 2.5 Structure of Jennite [30].	18
Figure 2.6 Powers model for C-S-H with needles representing the gel particles and C representing the capillary pore [34].	19
Figure 2.7 Feldman and Sereda model for the C-S-H gel nanostructure. Interlayer water is indicated by (X), physically adsorbed water is indicated by (O), A indicates tobermorite sheets [35].	20
Figure 2.8 The dreierketten structure showing paired (bottom row) and bridging (top row) tetrahedral. The site B shows a missing bridging tetrahedra [37].	21
Figure 2.9 Calculated Ca/Si ratio vs chain length for jennite and 1.4 nm tobermorite modified by omission of bridging tetrahedra [37].	22
Figure 2.10 Ca/Si ratio from TEM analyses of C-S-H in a hardened Cement paste hydrated for 2 years versus the reciprocal mean chain length [31].	25
Figure 2.11 Proposed defect-tobermorite structural model for C-S-H, showing dreierketten and central CaO layers (filled circles). The interlayer Ca^{2+} , OH^- groups, and H_2O molecules are omitted. The layer on top (a) represents a relatively perfect 1.4nm tobermorite layer with a small number of bridging tetrahedral removed and relatively long structural chains. The bottom layer (b) represents a distorted layer, with individual tetrahedral and entire chains maybe tilted, rotated or displaced along the b axis. Most bridging tetrahedral are missing, resulting in many dimers and entire segments of the silicate chains can be missing, reproduced from [40].	26
Figure 2.12 Molecular model of C-S-H. The blue and white spheres depict water molecules. The green and grey spheres depict interlayer and intra-layer calcium ions and the yellow and red bars depict silicon and oxygen in silicate tetrahedra [42].	28
Figure 2.13 Data from the literature showing layer spacing vs. Ca/Si ratio of C-S-H phases [45]. The middle solid line represents the model structures for C-(A)-S-H.	30
Figure 2.14 Data from the literature showing $\text{H}_2\text{O}/\text{Si}$ vs. Ca/Si ratios of C-S-H phases [45].	31

Figure 2.15 Ca/Si ratio of C-S-H phases synthesized by full hydration of C ₃ S at constant lime concentration.....	38
Figure 2.16 Schematic design of the apparatus [9].	39
Figure 2.17 Ca/Si ratios vs [CaO] plotted [4].	40
Figure 2.18 Ca/Si ratios versus [CaO] plotted for the C-S-H phases synthesized.	41
Figure 2.19 Schematic representation of the apparatus used for the synthesis of C-S-H phases [65].	42
Figure 2.20 Schematic representation of evolution of pH as a result of cement evolution [75].	51
Figure 3.1 STA data for a partially carbonated cement paste.	56
Figure 3.2 Schematic representation of Bragg's law [63].	59
Figure 3.3 Energy level diagram for nucleus with spin $I = \frac{1}{2}$ [105].	62
Figure 3.4 Schematic representation of Q ⁿ sites.	64
Figure 3.5 (A) Schematic representation of pentameric silicate chain, (B) pentameric chain with Al substituting for Si in the bridging site, (C) pentameric chain with Al substituting for Si in the non-bridging site [115].	66
Figure 3.6 Schematic representation of Transmission Electron Microscope.	70
Figure 4.1 Acid digestion vessel used for high temperature and high-pressure reactions.	81
Figure 4.2 Experimental setup showing vacuum pump and circulator.	84
Figure 4.3 Experimental setup showing the reactor.	85
Figure 4.4 Experimental setup showing the lid of the reactor.	85
Figure 4.5 Schematic representation of the reaction vessel.	90
Figure 4.6 Schematic representation of the experiment.	90
Figure 5.1 TEM micrographs showing different phases present in S1.	96
Figure 5.2 TEM micrographs showing different phases present in S2.	97
Figure 5.3 TEM micrographs showing different phases present in S3.	97
Figure 5.4 TEM micrographs showing different phases present in S4.	98
Figure 5.5 Atomic ratio plots for S1 (top) and S2 (bottom).	99
Figure 5.6 Atomic ratio plots for S3 (top) and S4 (bottom).	101
Figure 5.7 ²⁹ Si NMR spectra of S1 including experimental spectrum (middle, brown), residual (top, red x1) and the individual frequencies.	103

Figure 5.8 ²⁹ Si NMR spectra of S2 including experimental spectrum (middle, brown), residual (top, red x1) and the individual frequencies.....	103
Figure 5.9 ²⁹ Si NMR spectra of S3 including experimental spectrum (middle, brown), residual (top, red x1) and the individual frequencies.....	104
Figure 5.10 ²⁹ Si NMR spectra of S4 including experimental spectrum (middle, brown), residual (top, red x1) and the individual frequencies.....	105
Figure 5.11 ²⁷ Al NMR spectra of S1 and S2.....	106
Figure 5.12 ²⁷ Al NMR spectra of S3 and S4.....	106
Figure 5.13 STA trace of S1 showing DTA in grey and % TG in red....	108
Figure 5.14 STA trace of S2 showing DTA in grey and % TG in red....	109
Figure 5.15 STA trace of S3 showing DTA in grey and % TG in red....	109
Figure 5.16 STA trace of S4 showing DTA in grey and % TG in red....	110
Figure 5.17 XRD traces for S1 and S2.....	112
Figure 5.18 XRD traces for S3 and S4.....	112
Figure 6.1 TEM images of sample A showing scawtite on top, hillebrandite in middle and jaffeite on bottom.....	116
Figure 6.2 Histograms of Ca/Si ratios measured by TEM – EDX for all the phases in sample A.	117
Figure 6.3 TEM micrograph of β-C ₂ S phase and the corresponding SAED pattern in sample C.....	118
Figure 6.4 Histogram of Ca/Si ratios measured by TEM – EDX for β-C ₂ S phase in sample C.	118
Figure 6.5 ²⁹ Si NMR simulated spectrum for sample A including experimental spectrum (middle, brown), residual (top, red x1) and the individual frequencies.....	119
Figure 6.6 ²⁹ Si NMR spectrum for sample C including experimental spectrum (middle, brown), residual (top, red x1) and the individual frequencies.....	120
Figure 6.7 STA pattern of C-S-H – sample A, grey curve represents the DTA plot and the red curve represents the % weight loss.....	121
Figure 6.8 STA pattern of C-S-H – sample C, grey curve represents the DTA plot and the red curve represents the % weight loss.....	122
Figure 6.9 XRD pattern of sample A along with the reference patterns.	123
Figure 6.10 XRD pattern of sample C along with the reference patterns.	123

Figure 6.11 TEM micrographs of SHC – 1 along with the SAED pattern.	124
Figure 6.12 TEM micrographs of SHC – 2 along with the SAED pattern.	125
Figure 6.13 Histograms of Ca/Si ratios measured from TEM – EDX for samples SHC – 1 and SHC – 2.....	125
Figure 6.14 ²⁹ Si NMR spectra of SHC -1 including experimental spectrum (middle, brown), residual (top, red x1) and the individual frequencies.....	126
Figure 6.15 ²⁹ Si NMR spectra of SHC - 2 including experimental spectrum (middle, brown), residual (top, red x1) and the individual frequencies.	127
Figure 6.16 ²⁹ Si NMR spectra of SHC - 3 including experimental spectrum (middle, brown), residual (top, red x1) and the individual frequencies.....	127
Figure 6.17 ²⁹ Si NMR spectra of SHC - 4 including experimental spectrum (middle, brown), residual (top, red x1) and the individual frequencies.....	128
Figure 6.18 ²⁹ Si NMR spectra of SHC - 5 including experimental spectrum (middle, brown), residual (top, red x1) and the individual frequencies.....	128
Figure 6.19 ²⁹ Si NMR spectra of SHC - 6 including experimental spectrum (middle, brown), residual (top, red x1) and the individual frequencies.....	129
Figure 6.20 Ca/Si obtained by TEM-EDX analysis versus reciprocal mean chain length obtained by NMR analysis. The structural units for tobermorite and jennite with minimum (w=0), intermediate (w=1) and maximum (w=2) degree of protonation are plotted along with data points from current work. The vertical dashed lines represent the (3n - 1) structural units: dimer (2), pentamer (5) etc.....	132
Figure 6.21 STA patterns of SHC samples showing DTA in grey and % TG in red.....	136
Figure 6.22 XRD patterns of SHC samples along with the reference patterns.....	136
Figure 6.23 TEM micrograph of sample BHC – 1 along with the SAED pattern.....	138
Figure 6.24 TEM micrograph of sample BHC – 2 along with the SAED pattern.....	138
Figure 6.25 TEM micrograph of sample BHC – 3 along with the SAED pattern.....	139
Figure 6.26 TEM micrograph of sample BHC – 4 along with the SAED pattern.....	139

Figure 6.27 Histograms of Ca/Si ratios measured from TEM – EDX for samples BHC – 1, BHC – 2, BHC – 3, BHC – 4.....	140
Figure 6.28 ²⁹ Si NMR spectra for BHC - 1 showing the experimental spectrum (middle, brown), residual (top, red x1) and the individual frequencies.....	142
Figure 6.29 ²⁹ Si NMR spectra for BHC - 2 showing the experimental spectrum (middle, brown), residual (top, red x1) and the individual frequencies.....	142
Figure 6.30 ²⁹ Si NMR spectra for BHC - 3 showing the including experimental spectrum (middle, brown), residual (top, red x1) and the individual frequencies.....	143
Figure 6.31 ²⁹ Si NMR spectra for BHC - 4 showing the experimental spectrum (middle, brown), residual (top, red x1) and the individual frequencies.....	143
Figure 6.32 Ca/Si obtained by TEM-EDX analysis versus reciprocal mean chain length obtained by NMR analysis. The structural units for tobermorite and jennite with minimum (w=0), intermediate (w=1) and maximum (w=2) degree of protonation are plotted along with data points from current work. The vertical dotted lines represent the (3n - 1) structural units: dimer (2), pentamer (5) etc.....	146
Figure 6.33 STA traces of BHC samples (top left: BHC – 1, top right: BHC – 2, bottom left: BHC – 3, bottom right: BHC – 4) showing DTA in grey and % TG in red.....	149
Figure 6.34 ²⁹ Si NMR of C-S-H sample heated to 1000 °C.....	150
Figure 6.35 XRD patterns of BHC samples along with the reference patterns.....	151
Figure 6.36 Variation of MCL with mean Ca/Si ratios for all the C-S-H samples synthesized. Reported data from literature is also plotted along with various degrees of protonation from Richardson and Groves' model [31][40][41][45][63][163].....	153
Figure 6.37 Variations of % Q ⁰ , Q ¹ and Q ² for all the samples plotted against hydration times (top left: SHC samples hydrated at w/s = 0.5, top right: SHC samples hydrated at w/s = 1.0, bottom: BHC samples hydrated at w/s = 10).	154
Figure 6.38 Variation of MCL plotted against hydration time for static and ball mill hydrated samples.	155
Figure 7.1 TEM micrographs of AR – 1 (synthesized at 25 °C) showing foil-like C-S-H with Ca/Si = 1.51.	158
Figure 7.2 TEM micrographs of AR – 2 (synthesized at 20 °C) showing foil-like C-S-H with Ca/Si = 1.56.	158
Figure 7.3 TEM micrographs of AR – 3 (synthesized at 15 °C) showing mixture of foils and fibres with Ca/Si = 1.61.	159

Figure 7.4 TEM micrographs of AR – 4 (synthesized at 10 °C) showing mixture of foils and fibres with Ca/Si = 1.64.	159
Figure 7.5 TEM micrographs of AR – 5 (synthesized at 5 °C) showing fibrillar C-S-H with Ca/Si = 1.69.....	160
Figure 7.6 TEM micrographs of AR – 6 (synthesized at 1 °C) showing fibrillar C-S-H with Ca/Si = 1.74.....	160
Figure 7.7 TEM micrographs of AR – 7 (synthesized at 1 °C) showing spiky fibres with Ca/Si = 1.79.....	161
Figure 7.8 TEM micrographs of AR – 8 (synthesized at 1 °C) showing spiky fibres with Ca/Si = 1.81.....	161
Figure 7.9 Histograms of Ca/Si ratios measured using TEM – EDX.	163
Figure 7.10 Ca/Si ratios obtained from TEM – EDX plotted against reaction temperature (top) and initial lime concentration (bottom). The length of the vertical bars represents the minimum and maximum Ca/Si values and the dark circles represent the mean values.....	164
Figure 7.11 Mean Ca/Si ratios of the samples with the corresponding initial and final lime concentrations measured.	165
Figure 7.12 Ca/Si ratio vs [CaO] in solution for the present work. Other data reported by Taylor [4], Grudemo [9], Nonat and Lecoq [61], Rodriguez [63], Bourbon et al. [166], Kulik [167] and Haas and Nonat [163] are also plotted.	166
Figure 7.13 Ca/Si ratios vs [CaO] in solution depicting data from Taylor’s [4], Grudemo’s [9] and current work (blue). The plot on the right side is the enlarged version of the data points from current work.	167
Figure 7.14 ²⁹ Si NMR spectra for AR – 1 including experimental spectrum (middle, brown), residual (top, red x1) and the individual frequencies.....	168
Figure 7.15 ²⁹ Si NMR spectra for AR – 2 including experimental spectrum (middle, brown), residual (top, red x1) and the individual frequencies.....	168
Figure 7.16 ²⁹ Si NMR spectra for AR – 3 including experimental spectrum (middle, brown), residual (top, red x1) and the individual frequencies.....	169
Figure 7.17 ²⁹ Si NMR spectra for AR – 4 including experimental spectrum (middle, brown), residual (top, red x1) and the individual frequencies.....	169
Figure 7.18 ²⁹ Si NMR spectra for AR – 5 including experimental spectrum (middle, brown), residual (top, red x1) and the individual frequencies.....	170
Figure 7.19 ²⁹ Si NMR spectra for AR – 6 including experimental spectrum (middle, brown), residual (top, red x1) and the individual frequencies.....	170

Figure 7.20 ²⁹ Si NMR spectra for AR – 7 including experimental spectrum (middle, brown), residual (top, red x1) and the individual frequencies.....	171
Figure 7.21 ²⁹ Si NMR spectra for AR – 8 including experimental spectrum (middle, brown), residual (top, red x1) and the individual frequencies.....	171
Figure 7.22 Mean silicate chain lengths calculated from ²⁹ Si NMR data plotted against mean Ca/Si ratios calculated from TEM - EDX....	174
Figure 7.23 Ca/Si obtained by TEM-EDX analysis versus reciprocal mean chain length obtained by NMR analysis. The structural units for tobermorite and jennite with minimum (w=0), intermediate (w=1) and maximum (w=2) degree of protonation are plotted along with data points from current work. The vertical dashed lines represent the (3n - 1) structural units: dimer (2), pentamer (5) etc.....	175
Figure 7.24 MCL versus Ca/Si ratios for all the C-S-H samples synthesized. Reported data from literature is also plotted along with various degrees of protonation from Richardson and Grove's model [31][41][45][63][163]	179
Figure 7.25 STA traces of all C-S-H samples synthesized showing DTA in grey and % TG in red.....	182
Figure 7.26 DSC (grey) and % TG (red) curves along with water and CO ₂ traces of the C-S-H phase synthesized at 5 °C.....	183
Figure 7.27 ²⁹ Si MAS NMR spectra of C-S-H phase (synthesized at 5 °C) heated to 1000 °C.....	183
Figure 7.28 XRD patterns of the C-S-H samples with the reference patterns for CH and CC.....	184
Figure 8.1 TEM micrographs of static leached samples (top left: SL – 1, top right: SL – 2, middle left: SL – 7, middle right: SL – 8, bottom: SL – 9) showing foil-like morphology.....	185
Figure 8.2 Histograms of Ca/Si ratios measured using TEM – EDX. ...	187
Figure 8.3 Mean Ca/Si ratios plotted against degree of leaching for all the static leached samples.....	188
Figure 8.4 ²⁹ Si NMR spectra of SL - 1 including experimental spectrum (middle, brown), residual (top, red x1) and the individual frequencies.....	190
Figure 8.5 ²⁹ Si NMR spectra of SL - 2 including experimental spectrum (middle, brown), residual (top, red x1) and the individual frequencies.....	191
Figure 8.6 ²⁹ Si NMR spectra of SL - 7 including experimental spectrum (middle, brown), residual (top, red x1) and the individual frequencies.....	191

Figure 8.7 ²⁹ Si NMR spectra of SL - 8 including experimental spectrum (middle, brown), residual (top, red x1) and the individual frequencies.....	192
Figure 8.8 ²⁹ Si NMR spectra of SL - 9 including experimental spectrum (middle, brown), residual (top, red x1) and the individual frequencies.....	192
Figure 8.9 Ca/Si obtained by TEM-EDX analysis versus reciprocal mean chain length obtained by NMR analysis. The structural units for tobermorite and jennite with minimum (w=0), intermediate (w=1) and maximum (w=2) degree of protonation are plotted along with data points from current work. The vertical dashed lines represent the (3n - 1) structural units: dimer (2), pentamer (5) etc.....	194
Figure 8.10 STA patterns of SL samples showing DSC in grey and % TG in red (top left: SL - 1, top right: SL - 2, middle left: SL - 7, middle right: SL - 8, bottom: SL - 9).....	198
Figure 8.11 Water and CO ₂ traces of all the static leached samples...	199
Figure 8.12 DSC curves showing the transformation temperature of C-S-H to β-wollastonite in all the static leached samples.	199
Figure 8.13 TEM micrographs of DL - 1 showing foil-like morphology.	201
Figure 8.14 TEM micrographs of DL - 2 showing foil-like morphology.	202
Figure 8.15 TEM micrographs of DL - 3 showing foil-like morphology.	202
Figure 8.16 TEM micrographs of DL - 4 showing foil-like morphology.	203
Figure 8.17 TEM micrographs of DL - 5 showing foil-like morphology.	203
Figure 8.18 TEM micrographs of DL - 6 showing foil-like morphology.	204
Figure 8.19 TEM micrographs of DL - 7 showing foil-like morphology.	204
Figure 8.20 TEM micrographs of DL - 8 showing foil-like morphology.	205
Figure 8.21 Histograms of Ca/Si ratios measured using TEM – EDX. .	206
Figure 8.22 Mean Ca/Si ratios versus degree of leaching plotted for all the dynamic leached samples.	206
Figure 8.23 ²⁹ Si NMR spectra for DL – 3 showing the experimental spectrum (middle, brown), residual (top, red x1) and the individual frequencies.....	209

Figure 8.24 ²⁹ Si NMR spectra for DL – 4 showing the experimental spectrum (middle, brown), residual (top, red x1) and the individual frequencies.....	209
Figure 8.25 ²⁹ Si NMR spectra for DL – 5 showing the experimental spectrum (middle, brown), residual (top, red x1) and the individual frequencies.....	210
Figure 8.26 ²⁹ Si NMR spectra for DL – 6 showing the experimental spectrum (middle, brown), residual (top, red x1) and the individual frequencies.....	210
Figure 8.27 ²⁹ Si NMR spectra for DL – 7 showing the experimental spectrum (middle, brown), residual (top, red x1) and the individual frequencies.....	211
Figure 8.28 ²⁹ Si NMR spectra for DL – 8 showing the experimental spectrum (middle, brown), residual (top, red x1) and the individual frequencies.....	211
Figure 8.29 Mean silicate chain lengths calculated from ²⁹ Si NMR data plotted against Ca/Si ratios measured from TEM - EDX.....	212
Figure 8.30 Mean Ca/Si obtained by TEM-EDX analysis versus reciprocal mean chain length obtained by NMR analysis. The structural units for tobermorite and jennite with minimum (w=0), intermediate (w=1) and maximum (w=2) degree of protonation are plotted along with data points from current work. The vertical dotted lines represent the (3n - 1) structural units: dimer (2), pentamer (5) etc.....	213
Figure 8.31 STA patterns of DL samples showing DSC in grey and % TG in red (top left: DL – 3, top right: DL – 4, middle left: DL – 5, middle right: DL – 6, bottom left: DL – 7, bottom right: DL – 8).	216
Figure 8.32 Water and CO ₂ traces of all the dynamic leached samples.	217
Figure 8.33 DSC curves showing the transformation temperature of C-S-H to β-wollastonite in all the dynamic leached samples.	217
Figure 8.34 TEM micrographs of hydrothermally aged C-S-H sample showing foil-like morphology with Ca/Si = 1.54. The SAED pattern is also shown.	218
Figure 8.35 Histogram of Ca/Si ratios measured using TEM – EDX. ...	219
Figure 8.36 ²⁹ Si NMR spectra for hydrothermally aged C-S-H sample showing the experimental spectrum (middle, brown), residual (top, red x1) and the individual frequencies.....	220
Figure 8.37 Mean Ca/Si obtained by TEM-EDX analysis versus reciprocal mean chain length obtained by NMR analysis. The structural units for tobermorite and jennite with minimum (w=0), intermediate (w=1) and maximum (w=2) degree of protonation are plotted along with data points from current work. The vertical dotted lines represent the (3n - 1) structural units: dimer (2), pentamer (5) etc.....	221

Figure 8.38 STA pattern of hydrothermally aged C-S-H sample showing DSC in grey and % TG in red. Water and CO₂ traces are also shown.223

Figure 8.39 MCL versus Ca/Si ratios for all the C-S-H samples synthesized. Reported data from literature is also plotted along with various degrees of protonation from Richardson and Grove's model [31][41][45][63][163].224

List of Tables

Table 2:1 Essential requirements of a vault backfill [67].	46
Table 2:2 Desirable characteristics of a vault backfill [67].	47
Table 3:1 Characteristic NMR shifts of silicate species in cement samples.	65
Table 4:1 Current NRVB formulation.	74
Table 4:2 Description of the NRVB samples analysed.	75
Table 4:3 Typical sequence of hydration of C_3S [102].	78
Table 4:4 Reactants and reaction conditions for synthesis of $\beta - C_2S$ from hillebrandite.	81
Table 4:5 Reactants and experimental conditions for static and ball mill hydration.	83
Table 4:6 Temperatures and the corresponding conductivity and concentration values measured for initial calibrations.	89
Table 4:7 Showing the reaction temperatures and the corresponding conductivities and lime concentrations measured.	91
Table 4:8 Experimental details and reaction conditions of the C-S-H phases synthesized.	92
Table 4:9 showing the experimental and sample details of static and dynamic leaching experiments.	94
Table 5:1 Ca/Si ratios of C-A-S-H phase obtained by TEM – EDX.	101
Table 5:2 Results of deconvolution of ^{29}Si NMR showing % silicate species and MCL.	107
Table 5:3 % CH and % CC in the NRVB samples.	110
Table 6:1 TEM - EDX results showing mean Ca/Si ratios for different phases present in sample A.	115
Table 6:2 Ca/Si ratios of C-S-H phases obtained from TEM – EDX analysis for samples SHC – 1 and SHC – 2.	125
Table 6:3 Results of deconvolution of the ^{29}Si NMR spectra: % silicate species and MCL.	130
Table 6:4 Calculated values required for the formulation using T/J viewpoint.	133
Table 6:5 Calculated values required for the formulation using T/CH viewpoint.	134
Table 6:6 % CH_{res} in all the SHC samples calculated using tangent method.	135
Table 6:7 Ca/Si ratios of C-S-H phases obtained by TEM – EDX for ball mill hydrated samples.	140

Table 6:8 Results of deconvolution of the ²⁹ Si NMR spectra showing % of silicate species and MCL. Ca/Si ratios measured by TEM – EDX are also included.....	144
Table 6:9 Calculated values required for the formulation using T/J viewpoint.	146
Table 6:10 Calculated values required for the formulation using T/CH viewpoint.	147
Table 6:11 % CH _{res} and % CC _{res} in all the BHC samples calculated using tangent method.....	149
Table 7:1 Atomic ratios of C-S-H phases obtained by TEM – EDX.	162
Table 7:2 Chemical shifts of Q ¹ and Q ² peaks used for deconvolutions of the spectra.....	172
Table 7:3 Results of deconvolution of the ²⁹ Si NMR spectra: % silicate species and MCL.....	173
Table 7:4 Calculated values required for the formulation using T/J viewpoint.	176
Table 7:5 Calculated values required for the formulation using T/CH viewpoint.	178
Table 7:6 The residual % CH and % CC of the C-S-H phases calculated from STA data.	181
Table 8:1 Mean Ca/Si ratios of C-S-H phases obtained by TEM – EDX.	186
Table 8:2 Results of deconvolution of the ²⁹ Si NMR spectra: % silicate species and MCL.....	193
Table 8:3 Calculated values required for the formulation using T/J viewpoint.	195
Table 8:4 Calculated values required for the formulation using T/CH viewpoint.	196
Table 8:5 Variation in transformation temperature of C-S-H to β-wollastonite with mean Ca/Si ratios.....	200
Table 8:6 Mean Ca/Si ratios of C-S-H phases obtained from TEM – EDX analysis for all the dynamic leached samples.....	207
Table 8:7 Results of deconvolution of the ²⁹ Si NMR spectra showing % of silicate species and MCL. Mean Ca/Si ratios measured by TEM – EDX are also included.....	212
Table 8:8 Calculated values required for the formulation using T/J viewpoint.	214
Table 8:9 Variation in transformation temperature of C-S-H to β-wollastonite with mean Ca/Si ratios.....	218

List of abbreviations

AFm: Monosulfoaluminate

AFt: Trisulfoaluminate (Ettringite)

Al[IV]: Tetrahedrally coordinated aluminium

Al[V]: Pentahedral coordinated aluminium

Al[VI]: Octahedrally coordinated aluminium

BFS: Blast furnace slag

BSE: Backscattered electron

C₃A: Tricalcium aluminate

C₄AF: Calcium aluminate ferrite

C₃S: Tricalcium silicate

C₂S: Dicalcium silicate

C-A-S-H: Calcium aluminium silicate hydrate

C \bar{C} : Calcium carbonate or calcite

CH: Calcium hydroxide or portlandite

C-S-H: Calcium silicate hydrate

DSC: Differential scanning calorimetry

DTA: Differential thermal analysis

EDX: Energy dispersive X – ray analysis

GDF: Geological disposal facility

GGBS: Ground granulated blast furnace slag

HG: Hydrogarnet

HLW: High level waste

Ht: Hydrotalcite

ILW: Intermediate level waste

IP C-S-H: Inner product C-S-H

LLW: Low level waste

MAS NMR – Magic angle spinning solid state nuclear magnetic resonance

Mc: Monocarboaluminate

MCL: Mean chain length

NRVB: Nirex reference vault backfill

OPC: Ordinary Portland cement

OP C-S-H: Outer product C-S-H

PFA: Pulverised fuel ash

PTFE: Polytetrafluoroethylene

SAED: Selected area electron diffraction

SEM: Scanning electron microscopy

STA: Simultaneous thermal analysis

TEM: Transmission electron microscopy

TGA: Thermogravimetry analysis

w/s: water to solid ratio

XRD: X – ray diffraction

Cement chemistry analogy

A: Al_2O_3

C: CaO

\bar{C} : CO_2

F: Fe_2O_3

H: H_2O

S: SiO_2

Chapter 1 Introduction

1.1 Background of the study

The radioactive wastes emerging from the nuclear power industry need to be disposed of carefully to prevent adverse effects to the environment. One potential option for disposal of Intermediate level wastes (ILW) is based around a multi-barrier concept (Figure 1.1) involving encapsulation of wastes within a cement grout in steel containers prior to disposal in a geological disposal facility (GDF) [1] located deep underground.

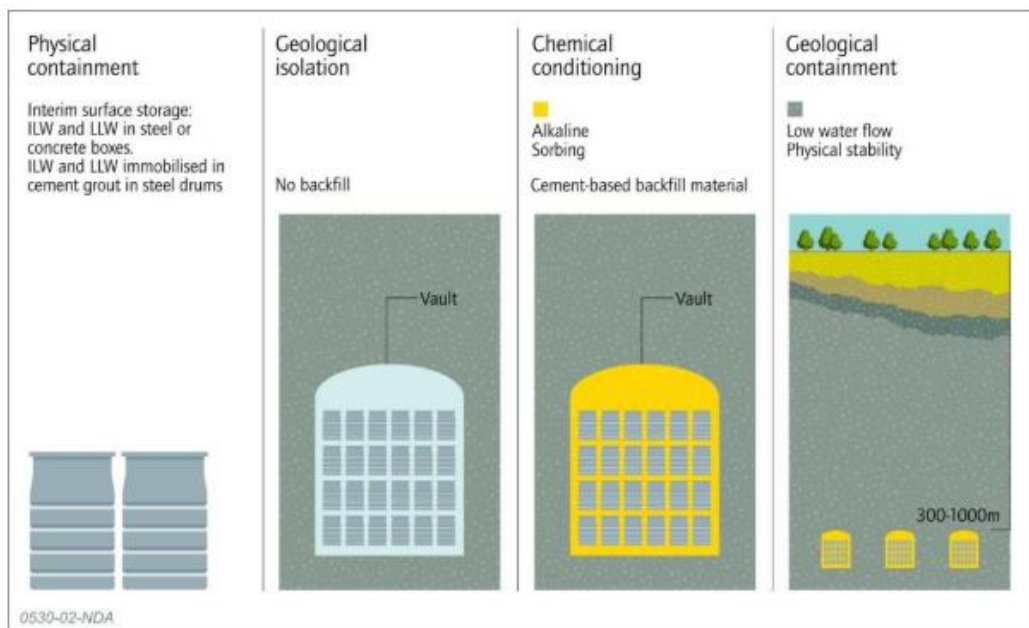


Figure 1.1 Multi-barrier concept for disposal of ILW [2].

The gaps or voids between the walls of GDF vaults and walls of the containers are filled with cementitious materials called backfill which provides a physical and chemical barrier to radionuclide release. The Nirex Reference Vault Backfill (NRVB) is a cementitious material that has been designed to backfill the vaults in

a repository for ILW in a high strength rock geological environment. It complements the encapsulation grout used to immobilise most of the radioactive wastes by fulfilling one of the most important safety functions of a backfill material – solubility limitation created by high pH conditions.

Generally, cementitious grouts containing ordinary Portland cement (OPC) blended with large amounts of ground granulated blast furnace slag (GGBS) and pulverised fuel ash (PFA) are used to encapsulate the ILW. The main binding calcium silicate hydrate (C-S-H) phase in these grouts has a mean Ca/Si ratio < 1.4, high level substitution of Al^{3+} for Si^{4+} ions, long aluminosilicate anions and foil-like morphology [3]. It is the C-S-H that is primarily responsible for several safety functions of a backfill such as pH, sorption capacity, strength and permeability. The C-S-H in a backfill like NRVB has a much higher Ca/Si ratio (1.7 – 2.2), shorter silicate anions and fibrillar morphology. However, the long-term ageing of the backfill material (NRVB) may affect its main chemical and physical properties and all the features may change with time and have an impact on the long - term performance of the backfill. To understand the potential effects of ageing on the microstructure and composition of a cementitious backfill, it is necessary to understand the nature of the main hydrate phase (C-S-H) in cement and then develop an understanding of its ageing. Synthetic C-S-H phases can be considered as model systems for understanding the nature of C-S-H phases in real cements, which is generally a mixture of other phases, thus making its characterization difficult.

This work is sponsored by Radioactive Waste Management (RWM) and carried out at University of Leeds with a primary objective to investigate the nature of high Ca/Si ratio synthetic C-S-H phases analogous to the C-S-H phases present

in backfills and the effect of ageing on the composition and microstructure of these phases. Several characterization techniques including TEM – EDX, ^{29}Si NMR spectroscopy, ^{27}Al NMR spectroscopy, XRD, STA are administered to study the morphology of the microstructure of C-S-H and other features.

It is found that preparation of synthetic C-S-H with a Ca/Si ratio > 1.4 is difficult unless anhydrous tricalcium silicate (C_3S) or dicalcium silicate (C_2S) is used as a starting material and portlandite (CH) precipitation can be prevented by using high water to solid ratios. Taylor [4] and Brunauer and Greenberg [5] were the first to synthesize highly ordered C-S-H phases with Ca/Si ratio > 1.4 by prolonged reaction of C_3S and $\beta\text{-C}_2\text{S}$ in aqueous suspensions. Since then there have been several attempts made to synthesize high Ca/Si ratio C-S-H phases using various methods. Three methods for synthesizing high Ca/Si ratio C-S-H phases that seem to have been successful are proposed in this work. These high Ca/Si ratio C-S-H phases can be analogous and thus can be considered as model systems for comparison with the C-S-H phases present in NRVB.

Task 1: Characterization and analysis of NRVB samples.

Four NRVB samples (fresh and aged) were provided by Wood and several characterization techniques were implemented to study the morphology, composition and silicate anion structure of C-S-H phases present in these NRVB samples. The aim of this task is to study the nature of the C-S-H phases in freshly cured NRVB and in samples that have been leached and hydrothermally aged.

Task 2A: Synthesize and characterize C-S-H phases with Ca/Si ≈ 2 .

The method implemented to synthesize high Ca/Si ratio C-S-H phases was the static hydration and ball mill hydration of highly reactive β – C₂S synthesized by heating hillebrandite [6][7][8] as reported by Ishida et al.

Task 2B: Synthesize and characterize C-S-H phases with Ca/Si > 1.6.

Method: Constant lime concentration method using CH and TEOS [9]. Grudemo synthesized C-S-H phases with Ca/Si ratio 1.5 – 1.6, free of intermixture with other phases.

An attempt is made in this project to reproduce Grudemo's method to synthesize crystalline C-S-H phases with Ca/Si ratio > 1.6 [9].

Task 3: Leaching of C-S-H samples.

The objective of this task is to investigate and understand the effects of leaching on the composition and microstructure of C-S-H phases. This task also aims to compare the leaching effects on synthetic C-S-H phases with those present in NRVB samples.

Task 4: Hydrothermal ageing of C-S-H samples.

The objective of this task is to accelerate the ageing by hydrothermal treatment of a high Ca/Si ratio C-S-H gel and to investigate the evolution of the C-S-H phase. The temperature rise in GDF post closure makes it important to understand the effect of temperature on the microstructure and composition of C-S-H phases.

1.2 Outline of thesis

Chapter 2 presents a fundamental literature review covering the composition of Portland cement, hydration mechanism and hydration products. Various

proposed structural models for C-S-H and its natural analogues are discussed. Different methods to synthesize C-S-H gels reported in the literature are also discussed and compared.

Chapter 3 provides description of various characterization techniques used for the analysis of C-S-H phases in this work. A detailed description of each technique along with the details of sample preparation for the analysis are discussed.

Chapter 4 includes a description of materials studied in this work followed by a discussion on experimental methods implemented to synthesize the C-S-H phases in this work.

Chapter 5 includes the related results and discussion of the characterization of NRVB samples. A detailed description of bulk analysis results and electron microscopy results is provided.

Chapter 6 includes the results and discussion of hydrothermally synthesized C-S-H phases. The bulk analysis results and electron microscopy results are discussed in detail.

Chapter 7 includes the results and discussion of the C-S-H phases synthesized via constant lime concentration method. The details of bulk analysis results and electron microscopy results are discussed.

Chapter 8 provides details of the artificially aged C-S-H phases. Results from bulk analysis and electron microscopy are discussed in detail.

Chapter 9 provides a summary of the conclusions from chapter 5 – 8 and discusses further work and potential considerations.

Chapter 2 Literature review

2.1 Portland cement

A cement is a material that hardens from a plastic state by binding together the solid aggregates. It is hydraulic in nature meaning it will set and harden in wet conditions or under water [10]. The chemical and physical properties of cement paste vary with morphology, Ca/Si ratio and water content.

Portland cement is produced by heating a mixture of limestone and clay or shale to a temperature of about 1400 °C. About 1100-1400 Kcal/g of energy is consumed for the formation of cement clinker. The calcareous ingredients such as limestone or chalk act as a source of calcium oxide (CaO) and shale or clay act as a source of silica (SiO₂), aluminium oxide (Al₂O₃) and iron oxide (Fe₂O₃). These raw materials also act as a source for small amounts of compounds like magnesia (MgO), alkalis, phosphates, zinc oxide (ZnO) and sulfides.

Upon heating to 1400°C, following reactions occur [11]:

- At 100 °C, free water is removed by evaporation. This is known as the drying zone.
- At 750 °C, bound water from the clay is expelled and this zone is known as the pre-heating zone.
- At 750 °C – 1000 °C, dissociation of calcium carbonate takes place and hence this zone is termed the calcining zone.
- At 1000 °C – 1400 °C, fusion occurs, and the materials combine to form C₃S, C₂S and hardened cement clinker.

Upon cooling, crystallisation occurs and calcium aluminate and calcium aluminoferrite are formed. The resultant mixture is cooled and 5 % gypsum (calcium sulfate dihydrate) is added which is then ground to form cement.

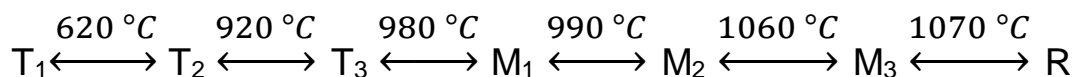
The four major phases present in the hydraulic Portland cement are:

- Alite (C_3S)
- Belite (C_2S)
- Tricalciumaluminate (C_3A)
- Tetracalciumaluminoferrite phase (C_4AF)

Apart from these major phases, a few minor phases are also present such as sulfates and oxides.

2.1.1 Tricalcium silicate

Tricalcium Silicate (C_3S) or Ca_3SiO_5 is an orthosilicate that exhibits three triclinic (T), three monoclinic (M) and one rhombohedral (R) forms [12]. Their existence has been established by XRD and DTA.



Where T = triclinic, M = monoclinic and R = rhombohedral.

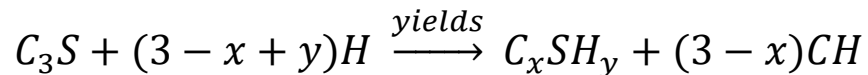
All these phases are equally hydraulic meaning they develop similar strength when stored under water.

C_3S is stable within the temperature range $1250\text{ }^\circ\text{C} - 1800\text{ }^\circ\text{C}$. These high temperature forms can be stabilised to ambient temperature by adding impurities such as Mg^{2+} , Al^{3+} , Fe^{3+} with smaller amounts of K^+ , Na^+ , SO_3 [12]. This impure form of C_3S with the presence of foreign ions is known as alite. In 1974, Regourd

and Guinier using powder XRD established that the two forms present in commercial clinkers are rhombohedral and triclinic [13]. However, in 1978 Maki with the help of microscopy determined that the two forms present in commercial clinkers are both monoclinic (M_1 and M_3) [14].

Alite is the most important constituent of Portland cement and it constitutes over 50 % - 80 % of the clinker.

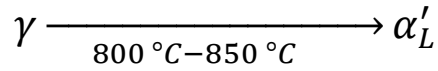
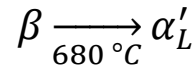
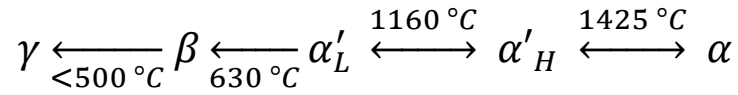
On addition of water to C_3S , the ions ($H_2SiO_4^{2-}$, OH^- , Ca^{2+}) are dissolved from the grain surface and the hydration of alite results in CH and an amorphous C-S-H [12].



This is the first reaction that takes place rapidly in the hydration process and gives the maximum strength at ages up to 28 days. The CH phase has hexagonal crystals and is known to exist as finely dispersed microcrystals in Portland cement pastes with low Ca/Si ratio [15] and in C_3S pastes it exists as large imperfect crystals [16]. The shape and size of the CH depends on the space available for its growth. In cements its growth is usually impeded by the surrounding solid. The thinned sections of C_3S paste when examined under TEM showed Ca/Si ratio of C-S-H has a mean value of 1.7 to 1.8 but it varies from 1.2 to 2.1 over the nanometre scale [17].

2.1.2 Dicalcium silicate

Dicalcium Silicate (C_2S) or Ca_2SiO_4 is an orthosilicate, which undergoes following phase transitions:



It is known to exist in many forms depending on the direction of temperature [18]. Figure 2.1 shows the schematic illustration of the phase transitions. There are four main structures γ , β , α and α' where α' has two different forms, α'_L and α'_H . These different phases are not equally hydraulic with γ being less hydraulic than β [19]. This can be understood by the arrangement of Ca^{2+} and SiO_4^{4-} ions.

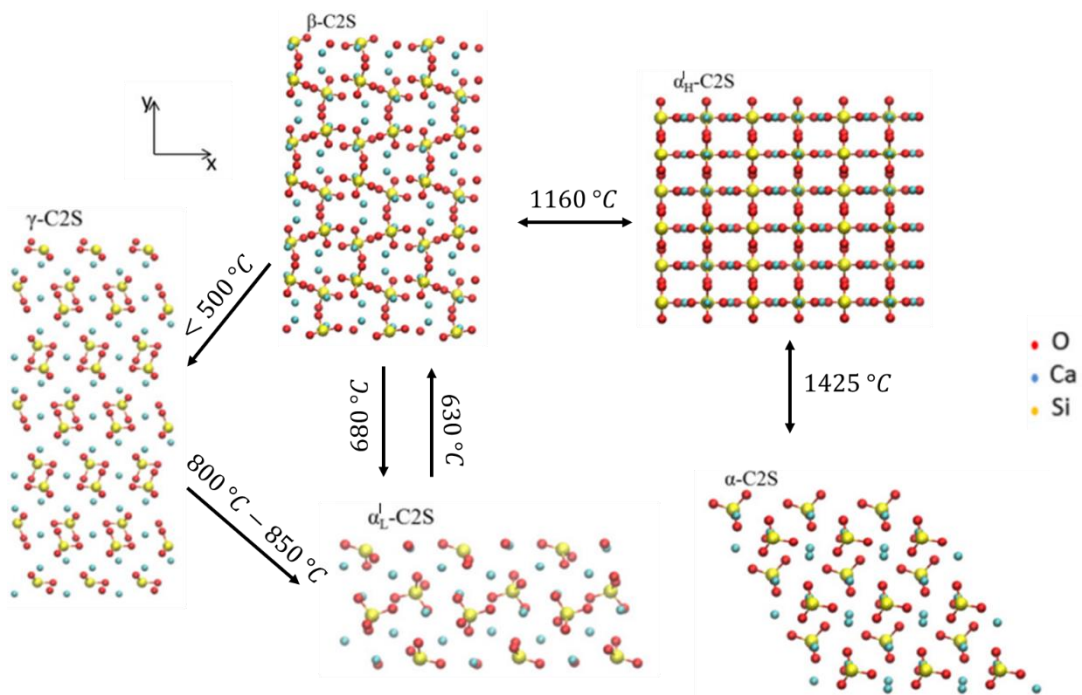


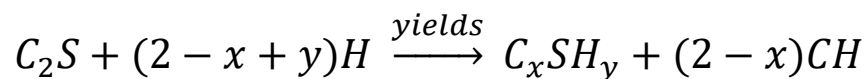
Figure 2.1 Schematic illustration of the phase transitions of dicalcium silicate [20].

The high temperature forms of C₂S are stabilised in the same way as C₃S, which is done by substitution of ions. This stabilised and impure form of C₂S is found in

commercial clinker and is known as belite. The ions that are most commonly found in belite are Al^{3+} , Fe^{3+} , Mg^{2+} , K^+ , SO_4^{2-} , PO_4^{3-} . According to Yamaguchi and Tagaki, β is the form present in commercial clinker [21]. However, some research also suggests that the forms present in commercial clinker are both α and α' [21]. The absence of Y form in commercial clinkers is due to its slow reaction rate and non-hydraulic nature [22]. Comparing the rates of hydration of different polymorphs, the $Y\text{-C}_2\text{S}$ polymorph of the dicalcium silicate has shown much lower rate of hydration than the rest of the polymorphs. This is one of the reasons for the rare occurrence of $Y\text{-C}_2\text{S}$ in the commercial cement clinkers. The reason for the slow reaction is the arrangement of oxygen atoms. In $Y\text{-C}_2\text{S}$ the oxygen atoms are arranged in a regular octahedral manner around Ca^{2+} ions whereas in the rest of the polymorphs oxygen atoms are arranged irregularly [12][23]. However, the rate of hydration does not affect the composition of C-S-H.

Belite constitutes around 15 % - 30 % of the cement clinker.

The reaction of C_2S with water results in the same hydration products as for C_3S , but the rate of hydration is much slower.



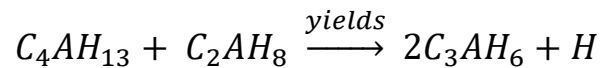
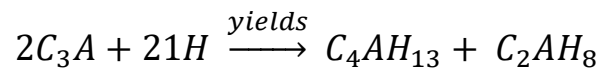
The amount of CH produced in the above reaction is one fifth of the CH produced in the hydration of C_3S .

2.1.3 Tricalcium aluminate

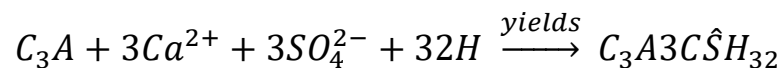
Tricalcium aluminate (C_3A) unlike alite and belite does not exhibit polymorphism. It does not undergo any phase transitions and is cubic in its pure form. Jeffery in the 1975 explained the cubic structure made up from Ca^{2+} ions and AlO_4

tetrahedra [24]. In 1976, Regourd and Guinier showed that the alkalis in the solid solution of the cement clinker altered the symmetry of the structure of C_3A [18]. The Na^+ ions being most common in the solid solution replace Ca^{2+} ions and fill the vacant sites in the centre of the AlO_4 tetrahedra and these resulted in the structural change from cubic to orthorhombic and monoclinic with increase in the percentage of Na_2O [25].

The reaction of C_3A with water along with added gypsum is strong during the first few hours of hydration. Gypsum ($C\hat{S}H_2$) allows a timely reaction. The absence of gypsum results in a rapid initial reaction which then leads to a flash set. C_3A on reaction with water and added gypsum results in unstable phases and the eventually converts to ettringite ($C_6A\hat{S}_3H_{32}$) which builds up as a layer on the C_3A particles and prevents rapid hydration.

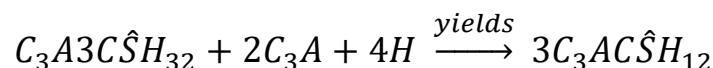


In the presence of gypsum:



Ettringite which is calcium aluminate trisulfate exists as long hexagonal needles.

It is converted into calcium aluminate monosulphate ($C_4A\hat{S}H_{12}$) when sulfate ion supply becomes insufficient.

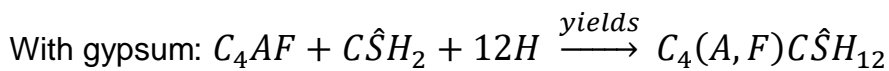
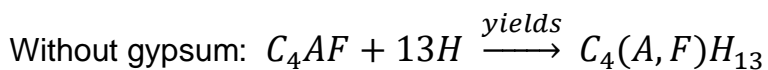


Monosulphate exists as poorly crystalline hexagonal shaped crystals. However, in the presence of carbonate ions monocarboaluminate instead of monosulphate

is formed. Pure aluminate has a cubic crystal modification. However, the crystal structure is altered from cubic to the monoclinic and orthorhombic [26][27]. In commercially available cements only cubic and orthorhombic forms are found [18]. The alkali content in the pore water alters the hydration rate of aluminate. The higher is the alkali content larger is the amount of dissolution of aluminate and ettringite production.

2.1.4 Aluminoferrite

Bussem in the year 1939 determined the formula for aluminoferrite as C_4AF . It is made up of C_2F and C_2A . C_2F exhibits a layered structure which is built from FeO_6 octahedra and FeO_4 tetrahedra and Ca^{2+} ions are packed between them. The Fe^{3+} ions in the tetrahedral sites are replaced by Al^{3+} ions first. However, research shows high levels of Al^{3+} ion substitution in the octahedral sites [28][29]. Aluminoferrite reacts slightly with water but reactivity can increase with an increase in the Al/Fe ratio. However minimum hydraulicity is maintained. The hydration of C_4AF is slower compared to C_3A .



2.1.5 Hydration reactions and hydration products

The reaction of cement with water is a complex exothermic reaction that produces hydration products at different rates having different composition and crystallinity. Hydration reactions being exothermic evolve a large amount of heat (about 1453 cal/g) [30] and monitoring and measuring the rate of heat evolution has shown

that there are three main peaks in the cement hydration process associated with the microstructural development.

The various products formed on hydration of cement are CH, AFt, AFm and C-S-H. The C-S-H is the most important and abundant product of cement hydration where the hyphens indicate the variable composition of the phase. It exists as an amorphous or poorly crystalline material with mean Ca/Si ratio varying from 1.7 to 1.8. There are various parameters like cement composition, water to cement ratio, temperature for hydration which affects the chemical composition of C-S-H and the morphology and microstructure.

The hydration of cement results in changes of cement paste to a hard solid. The various stages of hydration are evaluated by studying the kinetics of hydration in relation to the rate of heat evolution. When the cement is mixed with water, the ionic species dissolve and a very high amount of heat is evolved [11]. The main stages in cement hydration that corresponds to the microstructural development are shown in Figure 2.3 and the rate of heat evolution is shown in Figure 2.2.

From 0 – 3 hours (Peak I): This is the induction or dormant period where a very large amount of heat is evolved due to the dissolution of C_3A , $CaSO_4$ and C_3S phases. However, heat evolution decreases drastically after 3 hours.

From 3 – 24 hours (Peak II): This is the main hydration peak where the hydration starts accelerating and cement starts setting. The period before the top of peak II is known as the acceleration period and the remaining part is known as deceleration period.

From 24 hours: This period is known as long term hydration and there is a peak III which is less intense than the other peaks due to the formation of AFm.

In the early age hydration, the primary reaction contributes to the initial heat evolution and the reaction being rapid also increases the temperature. This is represented as peak I in Figure 2.2 and corresponds to Figure 2.3 b. At this stage, aluminate and ferrite reacts with calcium sulfate in solution and results in the formation of an amorphous alumina/silica rich gel on the surface. CaSO_4 prevents the rapid reaction of aluminate phase with water thus avoiding 'flash set'. C_3A reacts with CaSO_4 and water to form AFt which builds up as a layer on the C_3A particles thus preventing rapid hydration. After 10 minutes of hydration, AFt (sulfoaluminate phase) rods nucleate at the edge of the gel and in solution. These are mostly found near the aluminate phase. The amount of AFt formed in the initial hours directly depends on the w/s ratio. There will be increased calcium and sulfate ions as the amount of water increases [11].

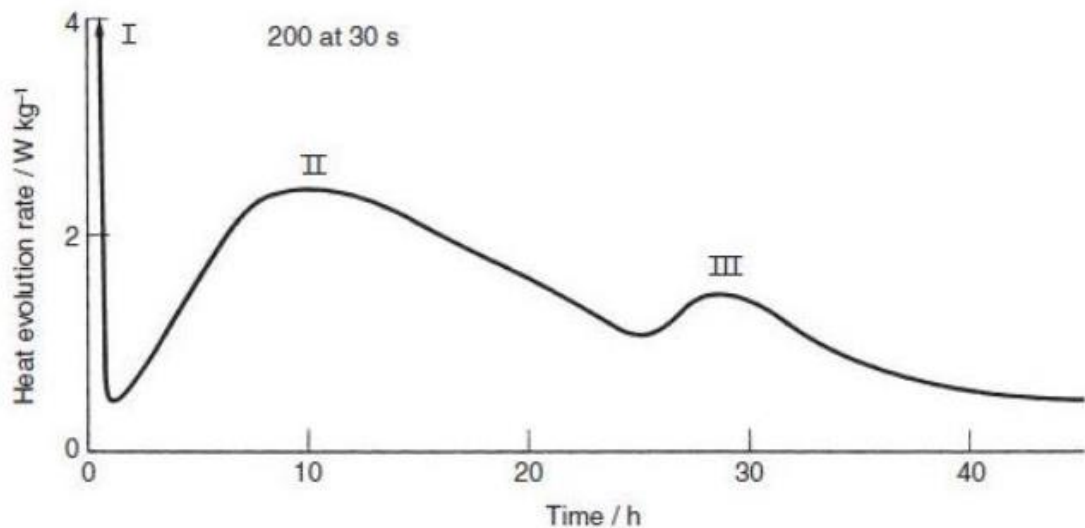


Figure 2.2 Rate of heat evolution in hydration of Portland cement [12].

It is only during the second period of hydration that the growth of C-S-H and CH can be seen, and the strength increases. This is when the rate of heat evolution

is maximum and is represented by peak II in Figure 2.2. The heat evolution is a result of hydration of alite which results in the formation of C-S-H. The C-S-H formed is called OP C-S-H (outer product) which grows on AFt rods in the spaces originally filled with water. This C-S-H growth is the main reason for setting and bonding of the paste. Figure 2.3 c represents this growth.

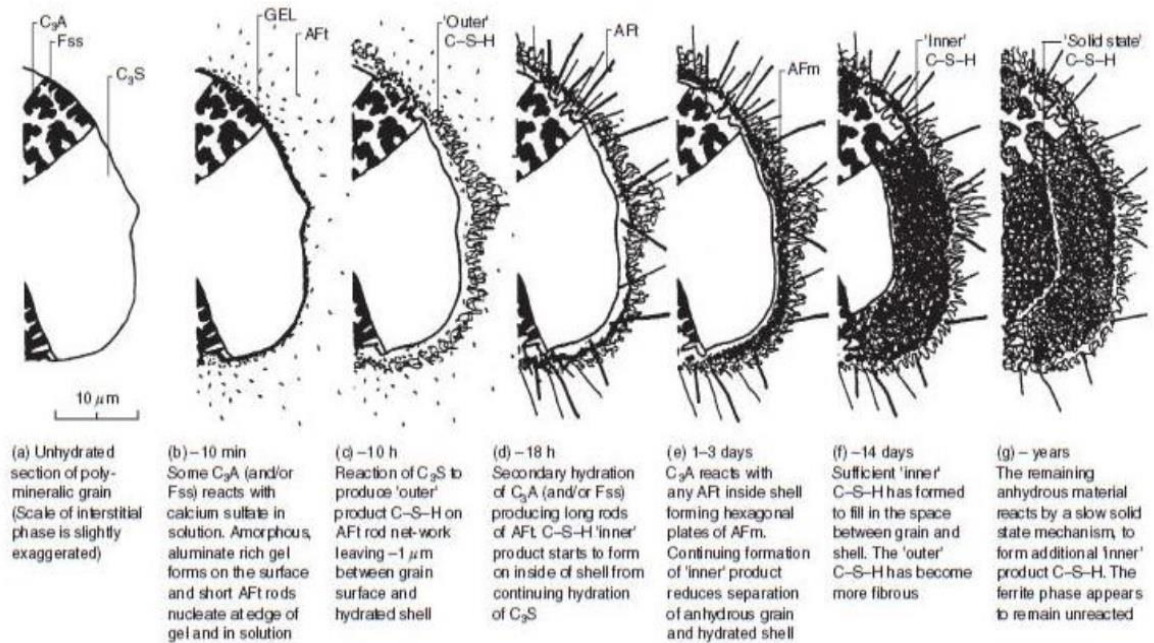


Figure 2.3 Microstructural development in a cement grain [11].

After approximately 16 hours of hydration, AFt grows in long rods (Figure 2.3 d) as a result of secondary hydration of aluminate phase with the formation of monosulfates (AFm). After this stage, C-S-H starts growing on the inside of the shell as IP C-S-H (Inner product). The late hydration only starts at 1 – 3 days and hexagonal AFm plates can be seen forming inside the shell (Figure 2.3 e) as a result of the reaction of C_3A and AFt. This prolonged formation of inner product gradually fills the space between the anhydrous grain and the shell (Figure 2.3 f). The outer product is gradually filled with C-S-H and CH (Figure 2.3 g). However,

the ferrite phase remains unreacted throughout [11]. As the hydration proceeds belite starts to react and large plates of AFm keeps forming at the expense of AFt.

2.1.6 Model structures of C-S-H

In 1919, Le Chatelier first proposed that the principal binding phase of cement is C-S-H and since then several investigations on C-S-H structure have been made by many researchers [31]. C-S-H being poorly crystalline and having variable composition makes it difficult to determine its structure. The XRD patterns of the C-S-H present in cement when compared with the patterns of natural minerals tobermorite and jennite has shown that there are a few common structural features.

2.1.6.1 Tobermorite

The structure of tobermorite is illustrated in Figure 2.4. There are two types of tobermorite, both being crystalline layered structures. These are 1.4 nm tobermorite $(Ca_5Si_6O_{16}(OH)_2 \cdot 8H_2O)$ and 1.1 nm tobermorite $(Ca_5Si_6O_{16}(OH)_2 \cdot 5H_2O)$. The 1.4 nm tobermorite when heated to 55 °C results in the formation of 1.1 nm tobermorite as the lattice shrinks due to the loss of interlayer water and when heated to 300 °C results in the formation of 0.9 nm tobermorite $(Ca_5Si_6O_{16}(OH)_2)$. The prefix describes the interlayer distance. It is clearly seen that the presence of water molecules has a direct relation to the interlayer distance. It has a Ca/Si ratio of 0.83. Bonaccorsi et al [32] backed this description by a detailed determination of its crystal structure. The structure of tobermorite consists of a central layer of CaO sheets with silicate dreierketten (silicate tetrahedra repeat in the set of three tetrahedra) chains attached on both

the sides. The water molecules and Ca^{2+} ions are present in the space between the different layers which balances the negative charge. The main layers consist of two types of calcium polyhedra, one bonded to four oxygen atoms and an OH group and the other bonded to four oxygen atoms and a water molecule. There are two types of silicate tetrahedra: paired tetrahedra and bridging tetrahedra. The paired tetrahedra are bonded to four oxygens of which it shares two oxygen atoms with the central layer. The bridging tetrahedra are bonded to three oxygens and one OH group.

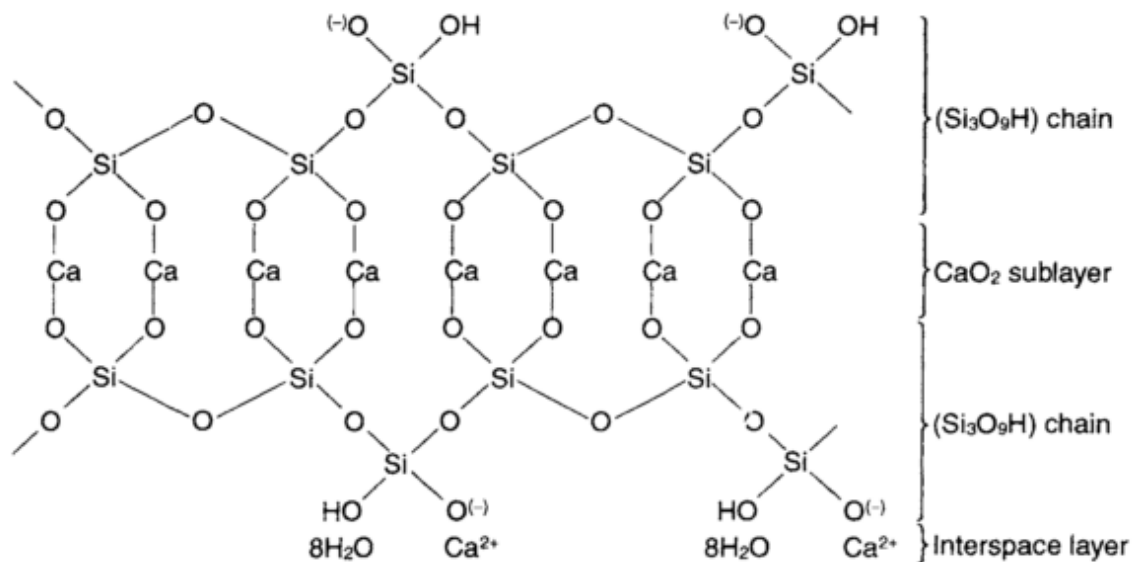


Figure 2.4 Structure of 1.4 nm tobermorite [30].

2.1.6.2 Jennite

The structure of jennite is illustrated in Figure 2.5. Jennite occurs as a natural mineral having a general formula $\text{Ca}_9(\text{Si}_6\text{O}_{18})(\text{OH})_6 \cdot 8\text{H}_2\text{O}$. Like tobermorite, it has a layered structure and can also undergo lattice shrinkage when heated to 70 °C – 90 °C resulting in the formation of metajennite due to the loss of water. It has a Ca/Si ratio of 1.5, higher than that of tobermorite. The structure of jennite

consists of a central CaO sheet with silicate dreierketten units attached on both the sides. The interlayer comprises of Ca atoms and water molecules. Cong and Kirkpatrick showed that jennite has single dreierketten with silicon atoms containing OH groups [33]. The major differences between the structures of 1.4 nm tobermorite and jennite are: -

- Every second dreierketten is replaced by OH ions and there are only half as many silicate chains as there are calcium atoms in the structure [31]. Jennite has both Ca-OH and Ca-O bonds in the main calcium layer whereas tobermorite contains only Ca-O bonds. This results in a Ca/Si ratio of 1.5.
- The CaO layers in jennite are more corrugated than that of 1.4 nm tobermorite.

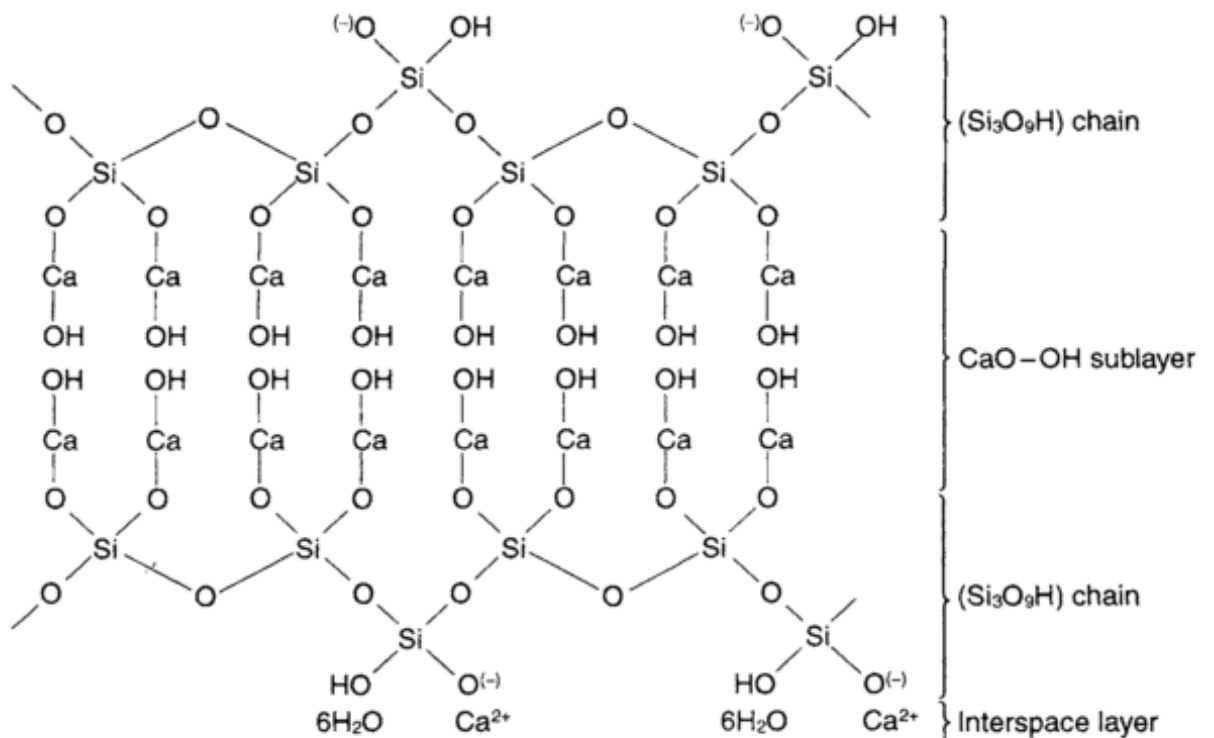


Figure 2.5 Structure of Jennite [30].

2.1.7 Models for C-S-H

2.1.7.1 Powers

In the year 1958, Powers termed C-S-H gel as 'cement gel' composed of gel particles and gel pores. This cement gel consists mostly of fibrous particles with straight edges forming a cross linked network. The fresh cement paste consists of this cement gel along with CH crystals and residues of originally water filled spaces. However, in the hardened cement paste these residues form interconnected channels or cavities interconnected by gel pores called capillary pores or capillary cavities [34]. Figure 2.6 illustrates the Powers model of C-S-H.

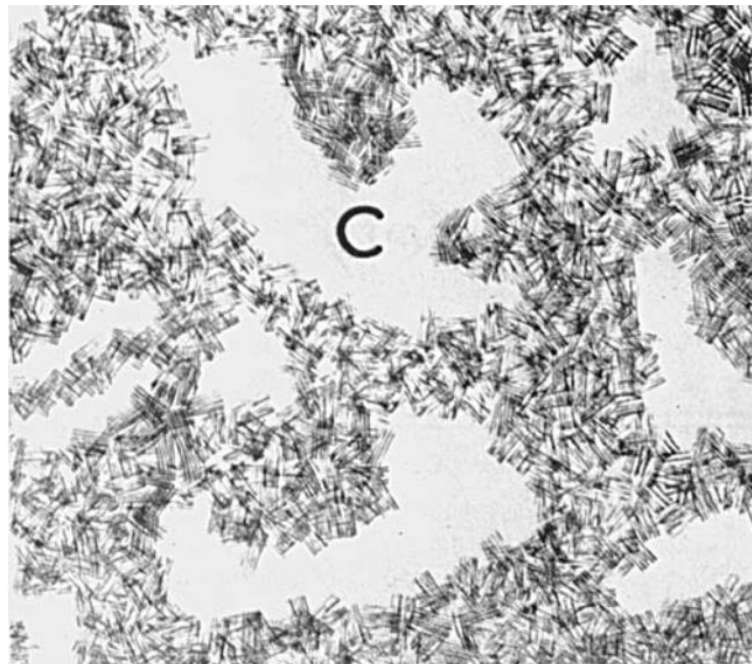


Figure 2.6 Powers model for C-S-H with needles representing the gel particles and C representing the capillary pore [34].

2.1.7.2 Feldman and Sereda

Feldman and Sereda [35] proposed a model for C-S-H based on the deformation behaviour, weight and Young modulus of cement paste with relative humidity

(RH) upon sorption and desorption. They noticed that Young's modulus remained constant upon sorption upto 50 % RH and then increased drastically until 100 % RH. However, upon desorption the Young's modulus remained constant till a very low value of RH and then decreased significantly. The weight changes showed a similar trend but the deformation behaviour upon sorption showed an increase at a constant rate from 0 % RH to 100 % RH. They proposed a layer structure of tobermorite layers with interlayer water between the layers (Figure 2.7). Upon sorption, water molecules enter from the edges by expanding them and the Young's modulus remains constant until the middle part is filled. Upon desorption, water molecules are lost from the edges and Young modulus remains constant until water from the middle part is lost.

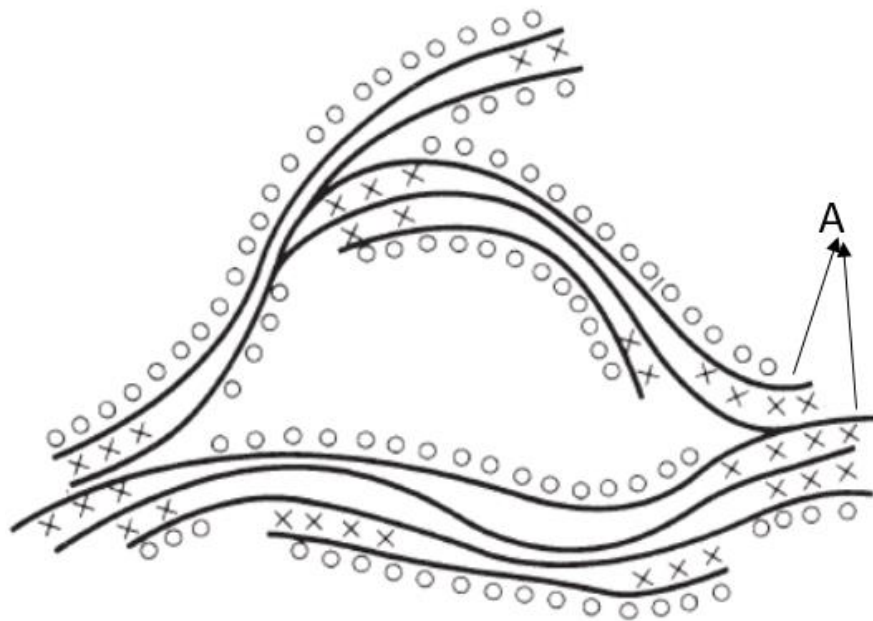


Figure 2.7 Feldman and Sereda model for the C-S-H gel nanostructure. Interlayer water is indicated by (X), physically adsorbed water is indicated by (O), A indicates tobermorite sheets [35].

2.1.7.3 Fuji and Kondo

According to Fuji and Kondo [36], C-S-H is a solid solution of 1.4 nm tobermorite and CH. They also claimed that the overall composition of C-S-H is between 1.4 nm and CH. The authors discussed the chemical composition and change in Gibb's free energy for the reaction of C-S-H and CH but properties like the range of Ca/Si ratio remained unaccounted.

2.1.7.4 Taylor

Taylor's model [37] for C-S-H is based on T/J structure, where majority of the disordered layers are related to structurally imperfect jennite and the minor proportions related to 1.4 nm tobermorite altered by the omission of bridging tetrahedra. The minimum and maximum values for Ca/Si in this model are 0.83 and 2.25 respectively.

Taylor reports the presence of "dreierketten" silicate chains with two of three tetrahedra sharing O atoms with the central Ca-O layer while the third that does not share being a bridging tetrahedra (Figure 2.8).

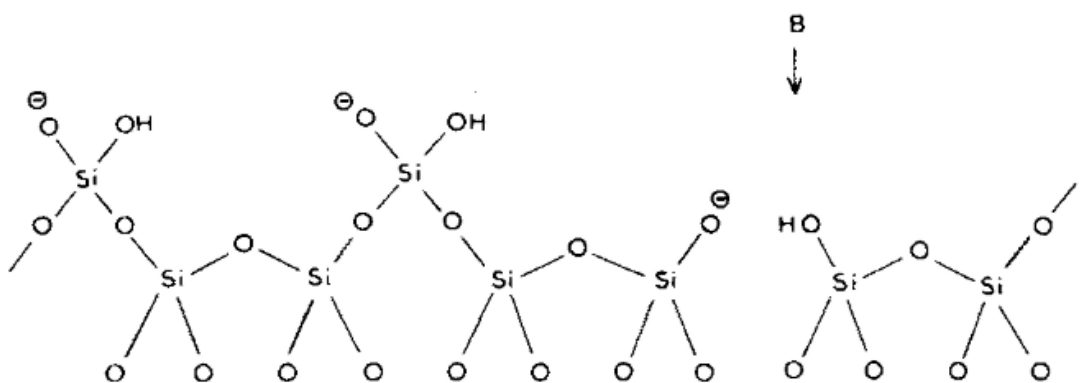


Figure 2.8 The dreierketten structure showing paired (bottom row) and bridging (top row) tetrahedral. The site B shows a missing bridging tetrahedra [37].

If all the bridging tetrahedra are missing from the structure, the theoretically infinite chain lengths of both tobermorite and jennite break, forming dimers, pentamers etc. and follow the $(3n-1)$ tetrahedra rule. This omission agrees with the experimental data that shows the difference in Ca/Si ratio of C-S-H when compared to that of tobermorite and jennite. The presence of enough H^+ ions as a result of the omission of the bridging tetrahedra means that the amount of interlayer Ca remains the same leaving the net charge unchanged. Based on these assumptions Taylor calculated the chain lengths of pure dimeric structures with a Ca/Si ratio of 1.25 in tobermorite and 2.25 in jennite.

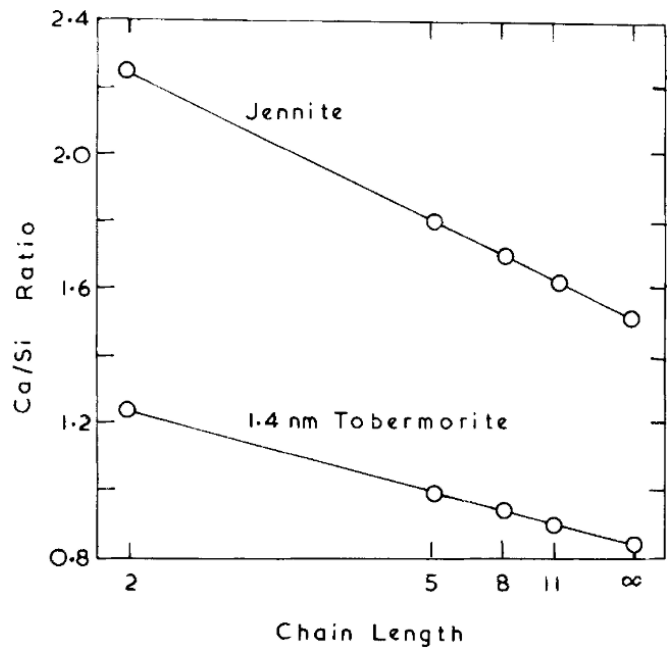


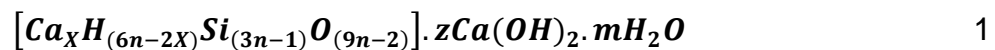
Figure 2.9 Calculated Ca/Si ratio vs chain length for jennite and 1.4 nm tobermorite modified by omission of bridging tetrahedra [37].

Taylor suggested that tobermorite is the first to nucleate resulting in C-S-H gel with lower Ca/Si at the start followed by the formation of both tobermorite and jennite dimers with increase in Ca/Si ratio to 1.25 – 2.25. With time, jennite pentamers form with a Ca/Si ratio of 1.8 consistent with that of C-S-H gel (Figure

2.9). Taylor in 1993 [38] mentioned about Al³⁺ ions replacing Si⁴⁺ ions in the bridging tetrahedra which was only predicted in the earlier work [37]. The Al³⁺ substitution for Si⁴⁺ increases as the Ca/Si ratio decreases.

2.1.7.5 Richardson and Groves

Richardson and Groves based their 'general' model on TEM investigations along with EDX and NMR. According to this model C-S-H is a highly disordered dreierketten layered structure with varying amounts of CH and silicate chains with finite length given by (3n-1) [39]. The proposed model describes C-S-H in two different viewpoints: T/CH (tobermorite/calcium hydroxide) (equation 1) and T/J (tobermorite/jennite) (equation 2) [39]. The main difference between these two viewpoints is based on the position of Ca²⁺ ions that are neither present in main layers nor take part in charge balancing. In T/CH viewpoint, Ca²⁺ ions are present within CH layers, between silicate layers of tobermorite like structure. In T/J viewpoint, Ca²⁺ ions form a part of the main jennite like layers. Also, Al or other cations can substitute for Si in the bridging tetrahedra and the charge can be balanced by incorporation of interlayer alkali or Ca²⁺ ions [29]. This model is useful to decide the combination of structural units in the C-S-H phase and thus determine its composition and structure. The general formula for T/CH viewpoint is given by:



Where,

X: (6n-w)/2; Ca²⁺ ions required to charge balance the silicate chain

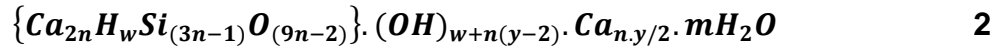
z: (w+n(y-2))/2

n: 1, 2, 3..... (number of units)

m: number of water molecules bound

(3n-1): silicate mean chain length

The general formula for T/J viewpoint is given by:



Where,

n: 1, 2, 3..... (number of units)

w: number of silanol groups

w/n: degree of protonation

(3n-1): silicate mean chain length

The above equation represents the tobermorite involving an amount of hydroxyl water hence allowing a flexible degree of protonation. The minimum and maximum values for Ca/Si ratios are 0.67 and 2.5, thus making this model more flexible than Taylor's model. Richardson and Grove's used this model to determine the Si/Ca and Al/Ca ratios for the possible T/CH and T/J units with variable protonation levels and aluminium substitution into vacant bridging sites. This model is very flexible, and the values of the indexes can be obtained experimentally. The silicate MCL: (3n-1) is obtained from ²⁹Si NMR analysis and the Ca/Si ratio is measured from TEM – EDX analysis. By knowing the value of n, y: [(Ca/Si)(6n-2)-4n]/n is determined. The degree of protonation (w) has range of values limited to maintain the layer structure and neutrality.

$$0 \leq y \leq 2: n(2-y) \leq w \leq 2n$$

$$2 \leq y \leq 4: 0 \leq w \leq 2n$$

$$4 \leq y \leq 6: 0 \leq w \leq n(6-y)$$

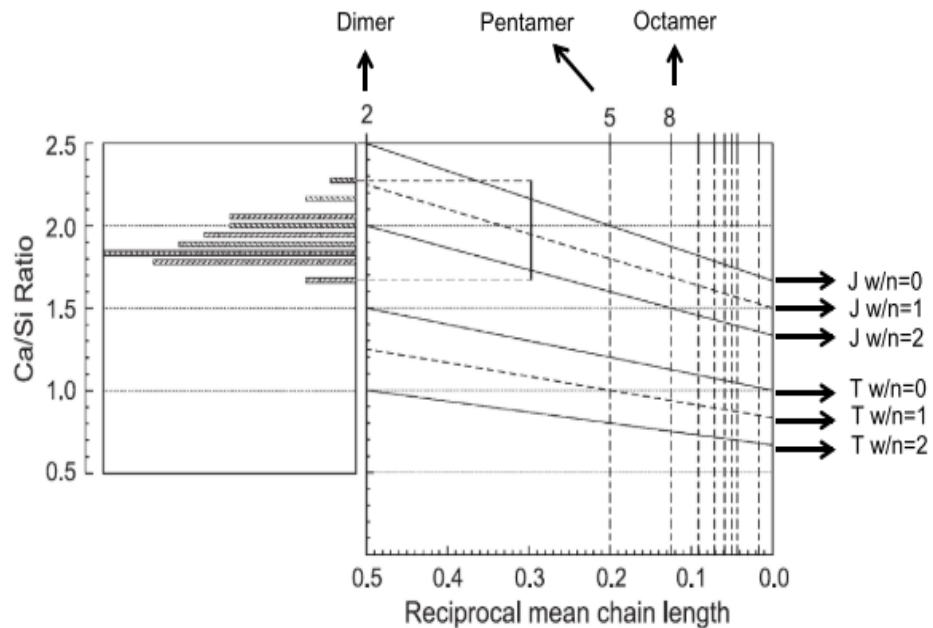


Figure 2.10 Ca/Si ratio from TEM analyses of C-S-H in a hardened Cement paste hydrated for 2 years versus the reciprocal mean chain length [31].

Figure 2.10 depicts the plot for C-S-H based on jennite dimers and pentamers describing the applicability of this model. Relation between Ca/Si ratios and reciprocal mean chain lengths for tobermorite (T) and jennite (J) units having various levels of protonation (shown on right) in Richardson and Groves' model is also shown [31]. This plot gives useful information about the combination of structural units and the experimental data points when placed over this plot gives structural information of the C-S-H phases. The flexibility of this model to provide chemical structural formulae over a broad range of Ca/Si ratios is the reason it is chosen in this work to derive structural formulae for the synthetic C-S-H phases. The main purpose is to discuss the applicability of both T/J and T/CH viewpoints for the C-S-H phases synthesized in this work.

2.1.7.6 Cong and Kirkpatrick

Cong and Kirkpatrick [40] proposed a model for C-S-H made up of disordered 1.4 nm tobermorite containing some significant defects.

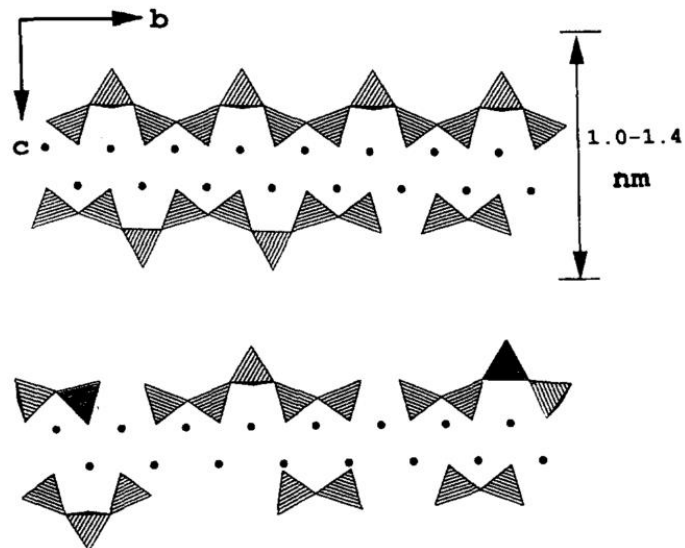


Figure 2.11 Proposed defect-tobermorite structural model for C-S-H, showing dreierketten and central CaO layers (filled circles). The interlayer Ca^{2+} , OH^- groups, and H_2O molecules are omitted. The layer on top (a) represents a relatively perfect 1.4nm tobermorite layer with a small number of bridging tetrahedral removed and relatively long structural chains. The bottom layer (b) represents a distorted layer, with individual tetrahedral and entire chains maybe tilted, rotated or displaced along the b axis. Most bridging tetrahedral are missing, resulting in many dimers and entire segments of the silicate chains can be missing, reproduced from [40].

They discussed the difficulty to produce C-S-H (II) phase and proposed different structures displayed in Figure 2.11 where one shows perfect tobermorite distorted by some missing bridging tetrahedra and the other one shows a highly

disordered structure that contains mostly dimers due to the removal of many bridging tetrahedra. Cong and Kirkpatrick further discussed the model with an imperfect tobermorite structure with the help of ^{29}Si MAS NMR and ^{17}O NMR [33]. They concluded that the tobermorite has a Ca/Si ratio of 0.9 containing only Q^2 sites and if this tobermorite loses a bridging tetrahedra, the Ca/Si ratio will increase. However, in the year 1999 they suggested that the incorporation of CH in the interlayer results in the increase of Ca/Si ratio, but they could not provide any direct evidence. They stated that the increase in intensity of Q^1 and Ca/Si ratio can be explained by the depolymerisation of silicate chains that does not occur by introducing CH into the interlayers.

2.1.7.7 Chen et al

Chen et al [41] reported the relationship between aqueous solubility and chemical structure of C-S-H phases synthesized by various methods using ^{29}Si MAS NMR spectroscopy and charge balance equations. They concluded that the differences in solubility arise from systematic variation in Ca/Si ratio, silicate structure and Ca-OH content. Based on these observations they concluded the solubility curves as a representation of metastable phases with structures ranging from tobermorite like to jennite like.

2.1.7.8 Pellenq

Pellenq proposed a molecular model to describe the structure of C-S-H from its Ca/Si ratio and density and disregarded the previous layer models based on structurally imperfect tobermorite and jennite. It is based on the distortion a monoclinic periodic computational cell of tobermorite having an interlayer spacing of 1.1 nm and a Ca/Si ratio of 1. Interlayer calcium ions are added to maintain

electro neutrality and SiO_2 groups are removed guided by NMR results, thus obtaining a modified C-S-H structure with a Ca/Si ratio of 1.65. The dry cell is then allowed to relax which caused a shift in the interlayer distance to 1.13 nm. Grand Canonical Monte Carlo simulations of water adsorption are then performed which resulted in an increase in the density to 2.56 gm/cm^3 , close to the experimental value obtained by neutron scattering [43]. Water adsorption resulted in an increase in the density and the density is controlled by a slight modification in the interlayer spacing. The final composition of the computational model of the hydrated C-S-H is reported to be $(\text{CaO})_{1.65}(\text{SiO}_2)(\text{H}_2\text{O})_{1.75}$ in close agreement with the neutron scattering experiments $(\text{CaO})_{1.7}(\text{SiO}_2)(\text{H}_2\text{O})_{1.8}$ [43]. Figure 2.12 illustrates the molecular model of C-S-H .

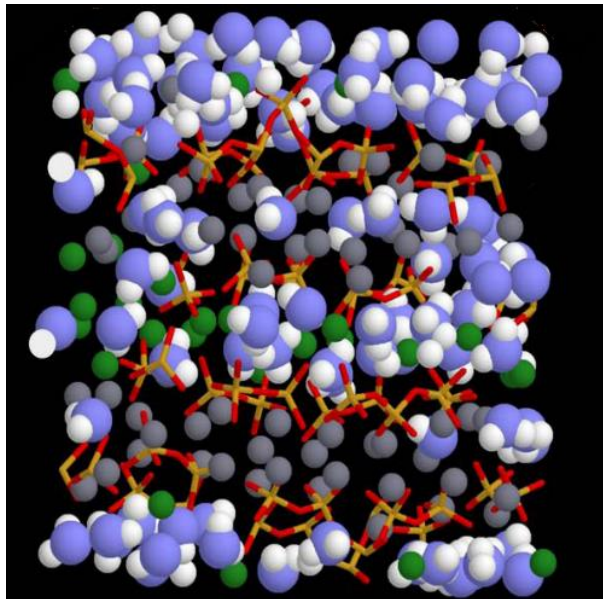


Figure 2.12 Molecular model of C-S-H. The blue and white spheres depict water molecules. The green and grey spheres depict interlayer and intralayer calcium ions and the yellow and red bars depict silicon and oxygen in silicate tetrahedra [42].

EXAFS, XRD, infrared and nanoindentation data has been generated from the final cell. Although the simulated data and the experimental data of C-S-H agree [39], this model is criticized due to unrealistic structure. Richardson [44] stated that Ca-O distances derived by this model differ from the known distances for crystalline C-S-H phases. He also stated that the generation of five, four and threefold coordination of calcium atoms is unrealistic as calcium atoms in most of the calcium silicates have a six or sevenfold coordination.

2.1.7.9 Richardson's model structures for C-(A)-S-H (I)

A model for C-A-S-H (I) based on clinotobermorite is derived by Richardson [45]. Orthotobermorite has always been used as a model for C-S-H phase. However, it is not possible to construct a model for a dimer which is crystal chemically stable based on orthotobermorite. Richardson developed crystal chemically plausible models based on clinotobermorite instead of orthotobermorite. Both orthotobermorites and clinotobermorites belong to the family of 11 Å tobermorites. While orthotobermorites have orthorhombic subcells (three unequal axes at right angles), the clinotobermorites presents monoclinic subcells (three unequal axes with two perpendicular and one skewed).

C-S-H (I) with Ca/Si ratios in the range 0.6 and 1.4 can be synthesized by using solutions of an alkali silicate and calcium nitrate or by using silica with CH or C₃S or β-C₂S. C-S-H phases with Ca/Si ratio < 1.4 has a structure derived from single chain tobermorites with vacant tetrahedral bridging sites. There are no interlayer calcium ions for the chains with infinite length and for each vacant bridging site one Ca²⁺ ion is added to the interlayer. For Ca/Si ratio > 1.4, the C-S-H structure is intermixed with Ca rich phase. The structure represented Ca-O octahedra similar to the ones present in CH and this justified the intergrowth of CH with the

dimeric structures explaining the T/CH view point [39]. Model structures presented in this work showed Ca-O distances and coordination numbers that are in agreement with the experimental data in the literature [4][9][46][47] such as basal spacing decreased with increase in Ca/Si ratio, H₂O/Si ratio increased with increase in Ca/Si ratio, basal spacing depended on the water content, formation of dimeric silicate anions with decreasing Ca/Si ratio, decreased site occupancy factor for bridging tetrahedra with increase in Ca/Si ratio. Figure 2.13 shows the experimental data of the basal spacing vs. Ca/Si ratios.

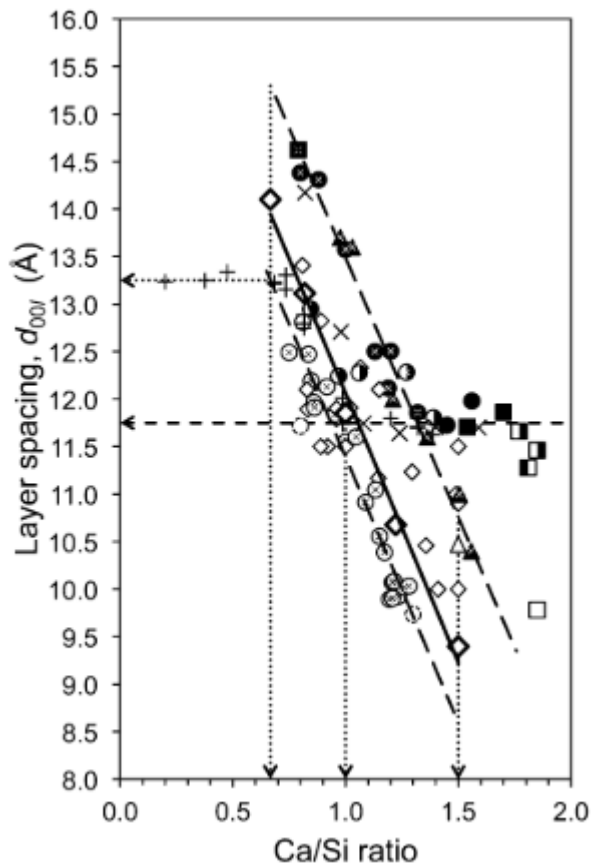


Figure 2.13 Data from the literature showing layer spacing vs. Ca/Si ratio of C-S-H phases [45]. The middle solid line represents the model structures for C-(A)-S-H.

While the bold diamonds on the middle line in Figure 2.13 represent model structures developed for an undecamer, pentamer, trimer and a dimer, the other two dotted lines represent the data taken from literature [9][40][48][49][50][51][52][53][54]. The difference in basal spacing between the two dotted lines in Figure 2.13 is because of the loss of water molecule from the interlayer region and this is supported by the observations on how drying methods effect the H_2O/Si ratio. Figure 2.14 shows the experimental data of H_2O/Si plotted against Ca/Si ratios. The dark circles represent phases that are lightly dried, and the white circles represent phases that are harshly dried.

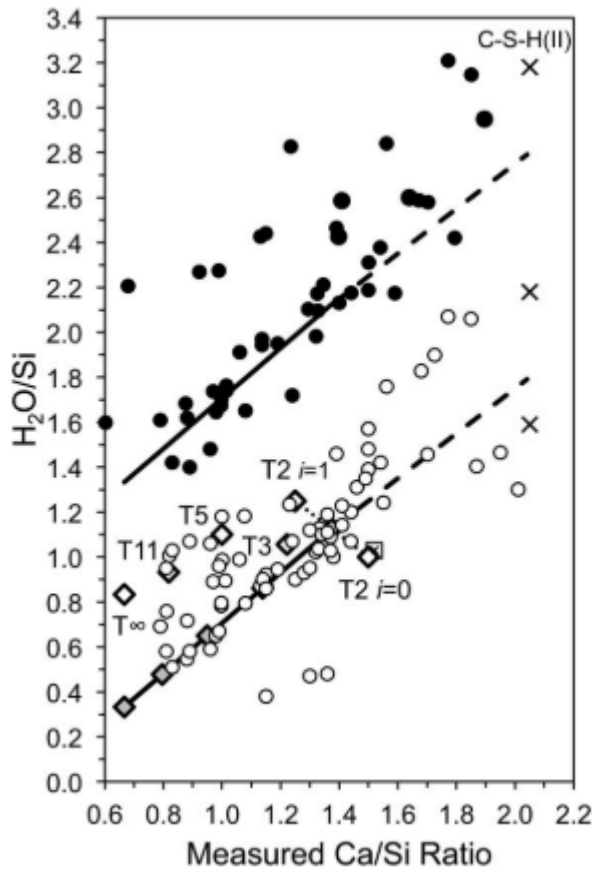
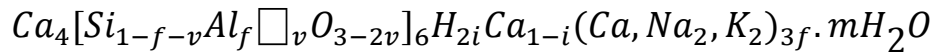


Figure 2.14 Data from the literature showing H_2O/Si vs. Ca/Si ratios of C-S-H phases [45].

The variation in data points in Figure 2.13 could be due to systematic errors in determining the Ca/Si ratios or experimental errors. While data points outside the lower dotted line for Ca/Si < 0.6 are due to intermixture of C-S-H and unreacted silica, data points outside the upper dotted line for Ca/Si ratio > 1.25 and basal spacing 11.75 are due to intermixture of C-S-H and CH. The data points between the two dotted lines are due to intermixture of C-S-H and CH or due to intermediate level of drying.

Generalised structural chemical formula for single chain tobermorites or C-A-S-H (I) [45]:



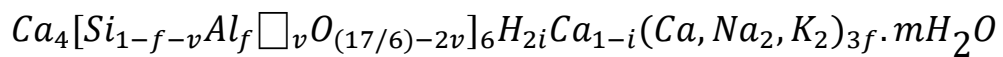
The Ca/Si ratio of Al free C-S-H (I) is:

$$\frac{Ca}{Si} = \frac{6-i}{6(1-v)}$$

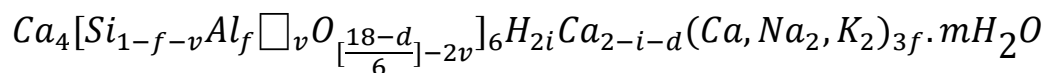
Also, the maximum Ca/Si ratio is obtained when the net charge is balanced by Ca²⁺ ions (i = 0).

$$(Ca/Si)_{max} = \frac{1}{(1-v)}$$

The formula for double chain tobermorites or the cross-linked C-A-S-H (I) phases:



Both the above formulae can be combined to represent a mixture of single and double chain phases:



The contents in the square bracket represent the aluminosilicate part.

□ : Vacant tetrahedral site

v : Fraction of tetrahedral sites that are vacant

f : Fraction that are occupied by Al

d : represents the fraction of double chain structure *i.e.* $0 \leq d \leq 1$

Where, $d = 0$ describes that the structure is entirely single chain

$d = 1$ describes that the structure is entirely double chain

i : reflects the extent to which the net charge is balanced by protons or Ca^{2+} ions.

The contents of the round brackets are additional interlayer ions, either monovalent alkali or Ca^{2+} cations that are needed to charge balance the Al^{3+} substitution for Si^{4+} . There are 4 main layer Ca atoms for every 6 tetrahedral sites.

Values for the variables in formulae can be determined from ^{29}Si NMR and TEM – EDX experiments.

$$v = \frac{1/2Q^1}{3/2Q^1 + Q^2 + 3/2Q^2(1Al) + Q^3 + Q^3(1Al)}$$

$$f = \frac{1/2Q^2(1Al)}{3/2Q^1 + Q^2 + 3/2Q^2(1Al) + Q^3 + Q^3(1Al)}$$

$$Al/Si = \frac{f}{1-f-v}$$

$$MCL = \frac{1-v}{v}$$

2.2 Methods to synthesize C-S-H phases

There are several methods reported in the literature for the synthesis of calcium silicate hydrates. Several attempts have been made to synthesize C-S-H phases with high Ca/Si ratio [52][55][56][57][58] but the maximum Ca/Si ratio achieved through various methods is ≈ 1.5 .

2.2.1 Cong and Kirkpatrick

C-S-H is synthesized by dissolution of SiO_2 gel in 5 ml of 1 M KOH solution mixed with 10 ml of 1 M CaCl_2 solution [59]. The Ca/Si ratio is controlled by varying the concentration of SiO_2 gel. The reaction temperature is maintained at room temperature and the reaction time is 15 minutes. The entire process is carried out under N_2 atmosphere to prevent carbonation. The samples obtained are filtered and dried under vacuum at room temperature. C-S-H gels with Ca/Si ratios 0.75 – 1.5 are obtained. However, some of the C-S-H samples synthesized, showed the presence of CH phase.

In the later study, Cong and Kirkpatrick [40] studied the single-phase calcium silicate hydrate (C-S-H) using ^{29}Si NMR, powder X-ray diffraction (XRD), and chemical analysis of the solution and solid. Three different methods were used to synthesize C-S-H phases with Ca/Si in the range 0.4 – 1.85.

- Hydration of highly reactive $\beta\text{-C}_2\text{S}$.
- Reaction of CaO and fumed silica.
- Reaction of fumed silica with highly reactive $\beta\text{-C}_2\text{S}$.

However, the Ca/Si ratio of a single-phase C-S-H without any intermixture with CH phase measured are in the range 0.6 -1.54.

2.2.2 Chen et al

Chen et al [41] synthesized C-S-H phases using a double decomposition method where solutions of $\text{Na}_2\text{SiO}_3 \cdot 5\text{H}_2\text{O}$ and $\text{Ca}(\text{NO}_3)_2 \cdot 4\text{H}_2\text{O}$ are mixed. This mixture is stirred for 1 hour in a tightly sealed plastic container filled with N_2 . The C-S-H precipitate obtained is washed with a 20 mM CH solution. Equilibration of C-S-H samples is carried out in three different ways.

- Equilibrated in H_2O or CH solution obtaining C-S-H phases with Ca/Si ratios from 0.92 – 1.48.
- Leached in NH_4NO_3 solution and then equilibrated in CH solution obtaining C-S-H phases with Ca/Si ratios from 1.26 – 1.45.
- Leached in H_2O and equilibrated in CH solution obtaining C-S-H phases with Ca/Si ratios from 1.26 – 1.35.

To obtain C-S-H phases with high Ca/Si ratios, C_3S is usually used. Chen et al also synthesized C-S-H phases by leaching a C_3S paste in NH_4NO_3 solution and then equilibrating in water. This technique results in decalcification of cement pastes without significant loss of Si and also the use of strongly concentrated solution accelerates the leaching thereby reducing the experiment times [60]. The Ca/Si ratios obtained are in the range of 0.62 – 1.4. C_3S is hydrated with deionized water at $w/s = 0.5$ for 3 days and then stored in a saturated CH solution for 8 months. Decalcification is done by immersing discs of samples in a solution of NH_4NO_3 after which the samples are removed and immersed in deionized water to remove NH_4NO_3 . They also synthesized C-S-H phases with high Ca/Si ratio by equilibrating the samples that are decalcified in NH_4NO_3 solution till the Ca/Si ratio is 1.09 and then recalcified them in a CH solution. The range of Ca/Si ratios obtained is 1.08 – 1.87. This method may however be not suitable to study

the morphology of C-S-H as leaching with NH_4NO_3 is a harsh method which affects the morphology.

2.2.3 Ishida et al

Ishida et al [6][7][8] reported the synthesis of high Ca/Si ratio C-S-H phases without the use of stabilizers using $\beta\text{-C}_2\text{S}$ obtained from hillebrandite by hydrothermal treatment. They could synthesize highly reactive $\beta\text{-C}_2\text{S}$ having a specific area of $7 \text{ m}^2/\text{g}$. Hillebrandite is synthesized as a starting material for obtaining $\beta\text{-C}_2\text{S}$. CaO and SiO_2 are taken in a molar ratio of 2:1 and w/s is 20:1. This mixture is heated at $250 \text{ }^\circ\text{C}$ for 5 hours. The product obtained is heated at $500 \text{ }^\circ\text{C}$ for 1 hour to obtain highly reactive $\beta\text{-C}_2\text{S}$. Two different hydration methods to synthesize C-S-H phases are studied.

- Static hydration [6]

$\beta\text{-C}_2\text{S}$ obtained is mixed with water at w/s ratio of 0.5 and 1.0 and the fully hydrated C-S-H phases are obtained in 28 days and 14 days respectively. The process of static hydration is carried out in a Teflon bottle and cured at $25 \text{ }^\circ\text{C}$. The samples obtained are filtered and vacuum dried at room temperature. The Ca/Si ratio of the C-S-H sample obtained is 1.81 with only evidence of traces of intermixing with CH phase. The silicate anion structure of the C-S-H phases synthesized showed the presence of Q^1 and Q^2 tetrahedra consisting of dimers and longer single-chains.

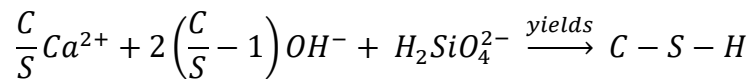
- Ball mill hydration [8]

$\beta\text{-C}_2\text{S}$ is mixed with water at w/s ratio of 10. Ball mill hydration is faster than static hydration. The process of ball mill hydration is carried out in a Teflon drum containing Zirconia beads and rotated at 110 rpm. Hydration of $\beta\text{-C}_2\text{S}$ for specific

periods is studied and the samples obtained are filtered and vacuum dried at room temperature. The hydration is completed in 2 days and C-S-H phase with Ca/Si ratio 1.81 and CH is obtained. Later, these two products react and form a single phase with Ca/Si ratio of 1.98. The silicate anion structure of the C-S-H phases synthesized showed the presence of Q¹ and Q² tetrahedra consisting of dimers and longer single-chains.

2.2.4 Nonat and Lecoq

Nonat and Lecoq [61] developed a method to synthesize C-S-H phases where C₃S is hydrated at constant lime concentration. The concentration is monitored by measuring the conductivity and controlled by addition of deionized water and removal of an equal volume of solution by which the overall volume is maintained. The dissolution of tricalcium silicate in water results in Ca²⁺, OH⁻ and H₂SiO₄²⁻ ions and the solution gradually is supersaturated with respect to C-S-H which precipitates [62].



Since all the Ca²⁺ ions produced by dissolution are not consumed by C-S-H precipitation, CH is precipitated.

To maintain the lime concentration constant, (3-Ca/Si) moles of CH are removed by withdrawing a volume of (3-Ca/Si)C₀ (C₀ is lime concentration that is to be kept constant) and replacing it with same volume of water. The concentration is monitored by measuring the conductivity throughout. The samples at the end of the reaction are filtered, washed with acetone and ether and then dried under vacuum.

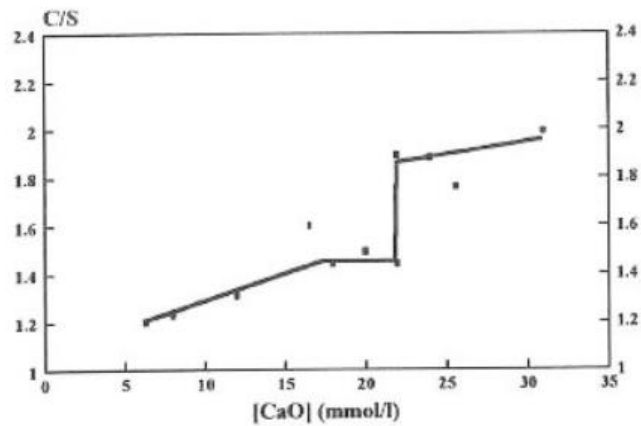


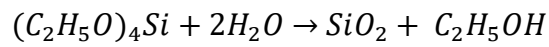
Figure 2.15 Ca/Si ratio of C-S-H phases synthesized by full hydration of C_3S at constant lime concentration.

C-S-H phases with Ca/Si ratios from 1.2 to 2.0 were synthesized by varying the lime concentration from 6 mmol/L – 30 mmol/L. Garrault and Nonat [62] showed that the C-S-H growth has a heterogeneous nucleation when C_3S hydration is performed above 8 mmol/L. The Ca/Si ratios vs [CaO] are plotted and illustrated in Figure 2.15. The Ca/Si ratio increased when the [CaO] increased from 6 mmol/L to 22 mmol/L. However, there is an abrupt change in the Ca/Si ratio at [CaO] of 22 mmol/L coinciding with the lime saturation with respect to CH.

2.2.5 Grudemo

Grudemo [9] successfully synthesized semi crystalline C-S-H phase with a Ca/Si ratio ≈ 1.6 using ethyl orthosilicate and lime solution maintained at constant concentration. He also studied the C-S-H morphology by TEM and outlined the transition from foils to fibrils with increasing Ca/Si ratio. To study the effect of Ca^{2+} concentration in solution on the morphology and composition of C-S-H, an apparatus (Figure 2.16) is designed having a closed stainless-steel vessel filled with lime solution of known concentration. There is also an outer vessel through which thermostat-controlled water is circulated. Ethyl orthosilicate diluted with

ethyl alcohol is added to the lime solution using a burette. The ethyl orthosilicate forms silica groups which react with the lime and C-S-H is precipitated.



The decrease in the lime concentration resulting from the precipitation of C-S-H was compensated by removal of water by means of a vacuum pump. The concentration of the solution throughout the experiment is monitored by measuring the conductivity which is proportional to the lime concentration. By regulating the rate of addition of ethyl orthosilicate and adding lime solution at the end, lime concentration is maintained constant. The precipitate at the end of the reaction is collected by suction and stored in polyethylene bottles.

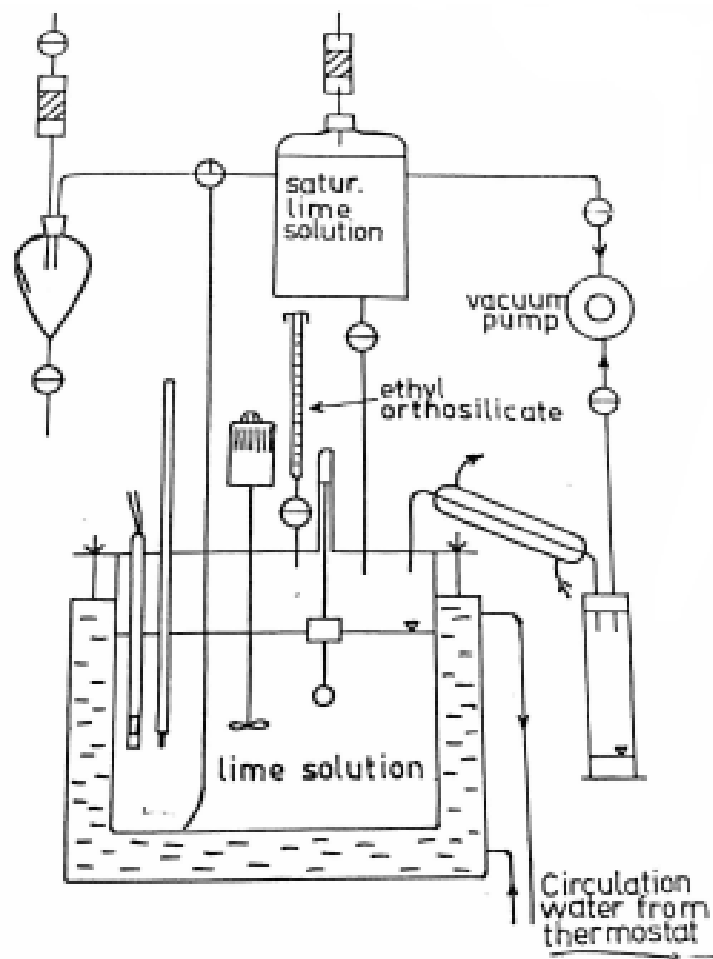


Figure 2.16 Schematic design of the apparatus [9].

Several experiments are conducted with lime concentrations ranging from 2 mmol/L to 24 mmol/L and the Ca/Si ratios of the C-S-H phases synthesized are in the range of 0.678 to 1.558.

2.2.6 Taylor

Taylor [4] synthesized C-S-H phases by decomposition of anhydrous tricalcium silicate, reaction of calcium hydroxide solution and silica gel and double decomposition of calcium nitrate with sodium silicate. The Ca/Si ratios vs [CaO] is plotted for the samples synthesized (Figure 2.17). However, it is seen that the C-S-H phases having Ca/Si > 1.5 are a mixture of low Ca/Si ratio C-S-H phase and CH. The phase equilibrium data (Figure 2.17) thus indicated the maximum Ca/Si ratio to be 1.5.

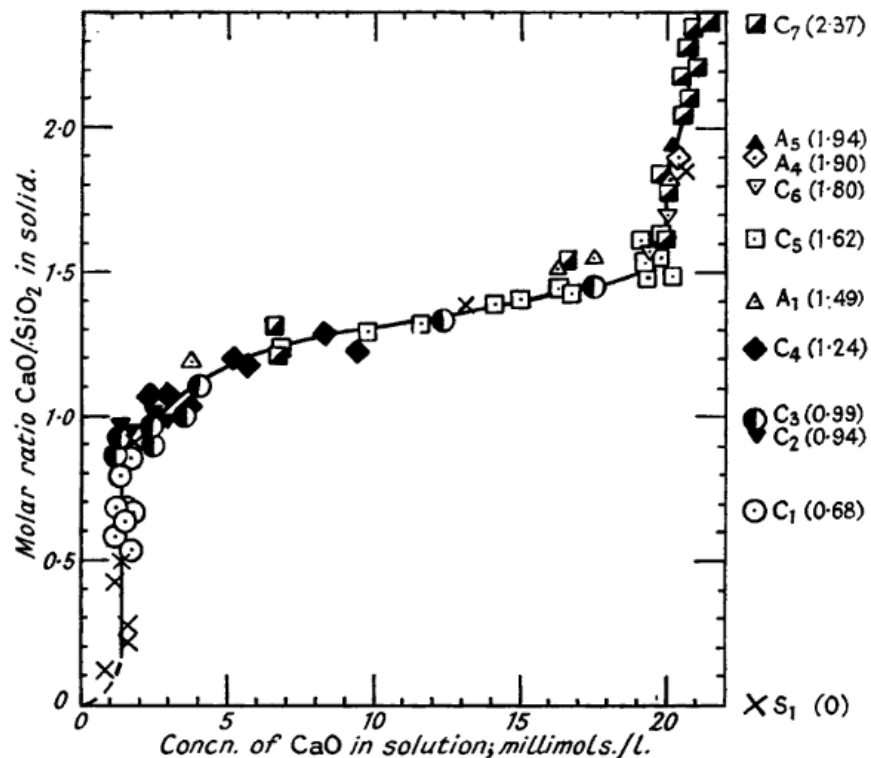


Figure 2.17 Ca/Si ratios vs [CaO] plotted [4].

2.2.7 Rodriguez

Rodriguez studied the relationship between the morphology of C-S-H, silicate anion structure and chemical composition [63]. The aim of this work is to determine if the morphological change is kinetically driven. The work concluded that morphological changes in C-S-H are due to lime concentrations rather than kinetics of hydration. The relation between the structure of C-S-H and morphology was also studied. Several samples were synthesized via silica lime reactions and hydration of C_3S at constant lime concentration (with/without accelerators). C-S-H phases synthesized by silica lime reactions showed foil-like morphology with a target Ca/Si ratio of 0.75 – 1.5. The morphology remained foil-like irrespective of the Ca/Si ratio. C-S-H phases were also synthesized with Ca/Si ratio in the range of 1.30 – 1.65 via hydration of C_3S at constant lime concentration method (kinetic C-S-H series, Ultrasound C-S-H series and Xseed C-S-H series).

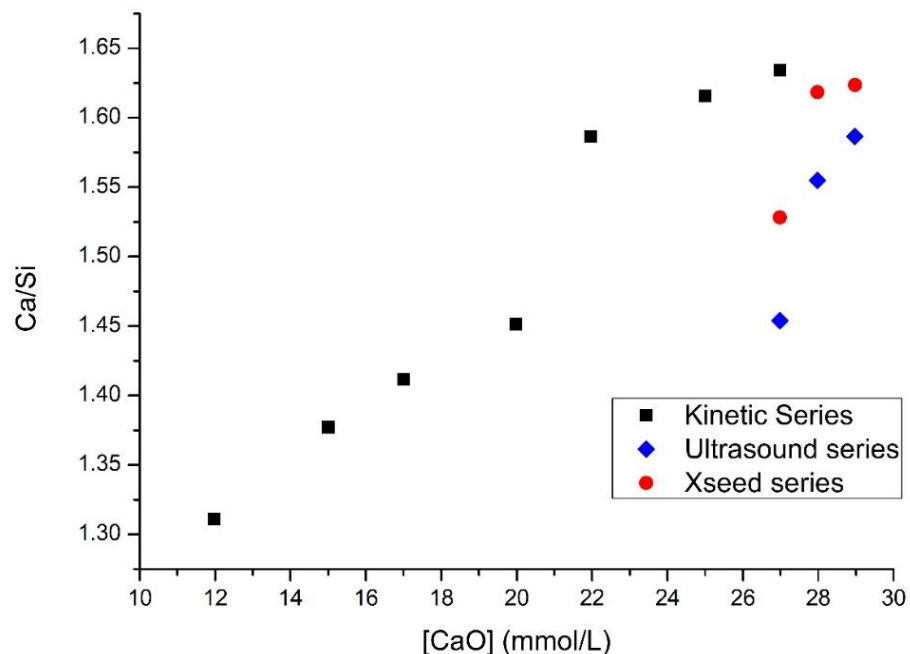


Figure 2.18 Ca/Si ratios versus [CaO] plotted for the C-S-H phases synthesized.

Figure 2.18 shows Ca/Si ratios plotted against lime concentrations for C-S-H samples synthesized using various accelerators. The experiments were conducted at lime concentrations between 12 mmol/L to 27 mmol/L. The morphology of C-S-H was determined to be dependent on lime concentration. Foil-like morphology with $\text{Ca/S} < 1.58$ was seen at lime concentrations < 22 mmol/L while a mixture of foils with $\text{Ca/Si} = 1.58$ can be seen at 22 mmol/L. However, fibrous morphology with $\text{Ca/Si} > 1.58$ was seen at lime concentrations > 22 mmol/L.

2.2.8 Kumar et al.

Kumar et al. [64][65] reported the synthesis of C-S-H phases with Ca/Si ratios in the range 1.0 – 2.0 without any CH phase intermixture. Figure 2.19 shows the synthetic apparatus used for the synthesis of high Ca/Si ratio C-S-H phases.

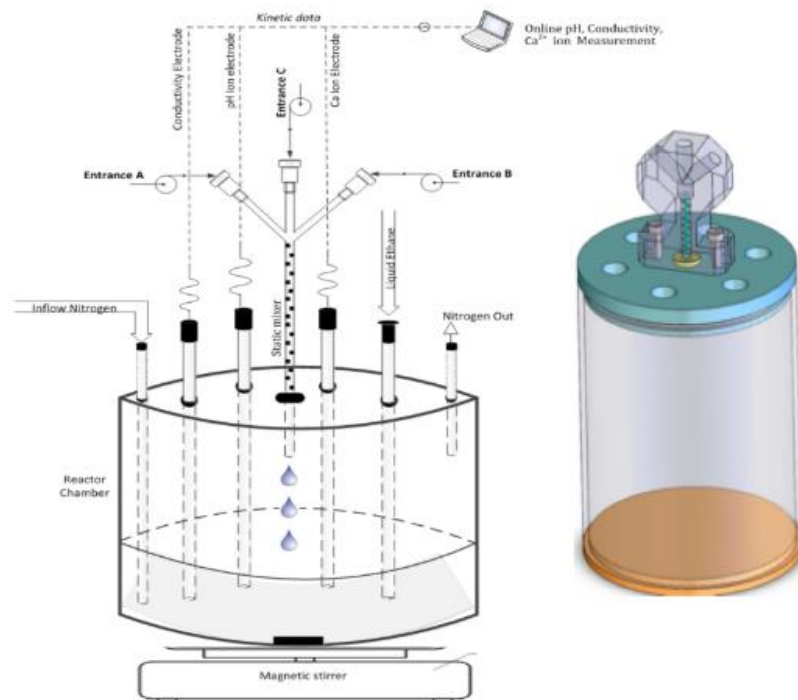


Figure 2.19 Schematic representation of the apparatus used for the synthesis of C-S-H phases [65].

Gibb's energy minimization software (GEMS) is used to calculate the pH required to obtain high Ca/Si ratio C-S-H phases. 0.1 M sodium silicate and 0.2 M calcium nitrate solutions are used as reactants and pH of the solution is continuously monitored. To achieve the pH values obtained by GEMS, concentrated sodium hydroxide is added during synthesis. The sample is collected allowing 24 hours for precipitation. The amount of OH⁻ added to the system resulted in an increase in Ca/Si ratios in the C-S-H phases. The ²⁹Si NMR characterization on the C-S-H phases showed the presence of Q¹ and Q² silicate tetrahedra. The morphology is foil-like (nanofolts) for C-S-H phases with Ca/Si ≥ 1.25 and nanoglobules are seen for the C-S-H phases with Ca/Si < 1.25.

2.3 Use of cementitious materials in radioactive waste management

2.3.1 Introduction

The nuclear industries produce wastes in the form of solids, liquids and gases which are contaminated through contact with radioactive substances. These radioactive wastes emerging from the nuclear power industries need to be disposed of carefully to prevent adverse effects on the environment in the long run. Hence, the disposal of these radioactive wastes has been the subject of a great deal of research that is going on for the past two and half decades. The objectives of radioactive waste management as described by Wilson [1] are:

- Concentration of the radioactive material in a small volume that will be isolated indefinitely from human contact.

- Where streams such as the water from fuel storage ponds are too bulky for anything but release into the environment, to remove from them all radioactivity or harmful material that poses a significant risk.

According to Sharp et al [66] the following advantages make cementitious materials highly suitable for encapsulation.

- Cheap and readily available.
- Durable and provides shielding for radiation.
- Have very low liquid and gas permeability in its hardened form.
- Used as a fluid grout and acts as a barrier for ion diffusion.
- Absence of organic additives thus avoiding the formation of metal organic complexes which can increase the solubility of some radionuclides.
- Maintains a high pH that will decrease the solubility of many radionuclides.
- Easy to process.

2.3.2 Classification of radioactive wastes

Almost all the industries produce wastes, some of which can be highly dangerous and can pollute environment. Radioactive wastes arising from various industries vary significantly in their properties like half-life, volume, nature and activity level. Hence disposal and storage must be tailored to the type of waste concerned to prevent the risk caused to the environment. In the UK, these radioactive wastes arising from several industries and nuclear power plants are grouped into three different categories based on the measure of radioactivity they contain.

Low level wastes (LLW) – Wastes with radioactivity less than 4 GBq/tonne alpha activity or 12 GBq/tonne beta/gamma activity. These wastes do not require any radiation shielding.

Intermediate level wastes (ILW) – Wastes with radioactivity more than the boundary limits of LLW. However, they have a lower activity and heat emission than HLW.

High level wastes (HLW) – Wastes from the reprocessing of irradiated fuel which emit heat and will be vitrified. They contain over 95 % of radioactivity in wastes from the generation of electricity by nuclear power.

LLW comprises paper, rags, clothing, filters etc. which are generally disposed by means of landfill disposal. Since LLW contains only 1% of radioactivity it does not require any shielding during handling and disposal. It is often burnt and reduced to ashes before disposal.

ILW comprises of materials such as resins, chemicals and contaminated materials from reactor decommissioning which are generally disposed by means of near surface disposal or deep geological disposal.

HLW is a by-product of reprocessing operations on nuclear fuel. It requires shielding and cooling as it is highly radioactive. It is generally disposed by means of deep underground disposal. HLW releases high amount of heat than ILW and LLW releases virtually no amount of heat during storage [66].

2.3.3 Role of a backfill

Geological Disposal is based on the combination of engineered and natural barriers working together over time to provide safety such that no harmful quantities of radioactivity ever reach the surface environment. The geological barrier provides a stable host rock environment, whilst the engineered barriers (e.g. waste packages and backfill) provide physical and chemical barriers designed to retain radionuclides. In the illustrative concepts for ILW, the

radioactive waste is immobilised in a cement grout and is sealed inside a corrosion resistant steel container which is then isolated from environment and is located deep underground in a rock structure.

Once the vaults are filled with the waste packages, the voids and spaces between and around the containers and vaults are backfilled with cementitious materials.

Historically, NRVB was designed for this purpose and therefore the desirable characteristics listed below in Table 2:1 and Table 2:2 were defined [67].

Essential Requirements of a Vault Backfill
<ul style="list-style-type: none">• Long term pore water should have pH 10.5 thus providing chemical barrier to radionuclides in the repository near field.• To provide adequate support for the placement of wastes and backfills, cube strengths of not less than 1.5 mpa at 7 days and not less than 4.0 mpa at 28 days if required.• Cube strength limit of 10 mpa at any age up to 50 years to assist grout removal should there be a future need to retrieve backfilled waste.• Workability must be suitable for flow without vibration into a horizontal space 5 m x 3 m x 75 mm high, which may be typical under package space.• The mix must be suitable for pumping along a horizontal pipeline at most 250 m in length.• Bleeding/settlement must not exceed 2 % to reduce the possibility of under package void formation and surfaces of weakness in the backfill.

Table 2:1 Essential requirements of a vault backfill [67].

Desirable Requirements of a Vault Backfill

- Act as a chemical barrier and provide high pH and high sorption capacity.
- Sufficient permeability for gas transport.
- Low heat of hydration.
- Use of cement additives should be avoided which might compromise the cement performance as a chemical barrier of the engineering properties.
- Mineral composition should be sufficiently durable to provide long - term chemical conditioning of repository pore water.
- Possess well understood mineral characteristics which can be predicted during the repository evolution.
- Use materials which can be reasonably assured in terms of quality and quantity during repository operational period.
- Suitable for placement by remote methods in waste vaults.
- Self-levelling and compacting and able to provide a firm level base for placement of further packages.
- Suitable for easy excavation to allow retrieval of waste packages if that is required.

Table 2:2 Desirable characteristics of a vault backfill [67].

2.3.4 Nirex Reference Vault Backfill

NRVB is a specially formulated cementitious backfill that has a C-S-H phase of Ca/Si ratio 1.7 – 2.2, shorter silicate anions and fibrillar morphology.

The safety functions of a NRVB backfill material:

- High pH

The cement backfill should have a pH > 10.5 in order to limit the solubility of some radionuclides. The long – term pH buffering capacity can be achieved through the slow dissolution of Ca rich phases. The high pH conditions provided by these cement backfills will result in an increase in OH⁻ ions and most of the radionuclides present are precipitated in the form of oxides and hydroxides. These hydroxides and oxides of radionuclides are generally insoluble in water, which prevents the transportation of radionuclides when groundwater flows through the vault. Also, high pH helps in minimising the corrosion of steel waste containers.

- High sorption capacity

The cement backfill should have a high surface area to which some radionuclides can attach strongly. This sorption causes the concentration of radionuclides to be reduced in the solution and retards their release into environment.

- High gas permeability

The degradation of some radioactive wastes can lead to the production of gases. To avoid the disruption of the engineered barriers, the backfill should allow free movement of gas from the waste container out in the rock.

2.4 Process of Leaching

Dissolution and alteration of the cementitious materials occur on long-term contact with water. Le Chatelier in 1800's first showed that the Ca/Si ratio of C-S-H varies, it decreases as C-S-H is leached in water and it increases as C-S-H is exposed to CH solution (depending on the starting composition).

Leaching is a dissolution reaction controlled by solubility and diffusion in cementitious materials that occurs on exposure to demineralized water or poorly mineralised water. It is the process of extracting minerals from solids by dissolving them in liquids. Apart from the main solid hydrates that include C-S-H, CH, AFm and AFt, hardened cement also contains pore spaces filled with highly basic interstitial solution ($\text{pH} \approx 13$) charged with different ions (Ca^{2+} , Na^+ , K^+ , OH^-) [68]. When cement comes in contact with the demineralised water ($\text{pH} \approx 7$), a concentration gradient is created in the interstitial pore solution between the surface and core of the material. This leads to the diffusion of ions from highly concentrated interstitial pore solution. To maintain the equilibrium between the interstitial pore solution and the solid phase, dissolution and precipitation of solid hydrates occurs. As leaching period increases the dissolution also increases initially (in long-term equilibrium is achieved in a static system). This results in a decrease of the pH of the interstitial pore solution and leads to the degradation of cement in the long term [69] and this decrease in pH of the pore solution may affect the migration behaviour of radionuclides in the context of a GDF [66]. The C-S-H is the main binding phase in the cementitious systems, thus making it important for the researchers to study its solubility, pH buffering capacity and leaching behaviour [70][71]. Ultimately, the residue at the end mainly consists of hydrous forms of silica, alumina and iron oxide as all the calcium oxide will have been leached out [72]. The rate of leaching is usually very low, and the degradation of cementitious materials rarely have an impact on the common structures. However, the impact of leaching is of significant importance for the cementitious materials used for radioactive waste disposal, as long term stability must be ensured for thousands of years [73].

Leaching by water involves two phenomena:

- The ionic species like Ca^{2+} and OH^- diffuse in the pores of cementitious matrix due to the concentration gradients between highly alkaline and basic interstitial solution and the external aggressive solution.
- The cementitious phases rich in Ca dissolve by hydrolysis to supply Ca ions to maintain equilibrium.

The first phase to dissolve is CH followed by AFm, C-S-H, AFt and $\text{C}\bar{\text{C}}$ [68]. Hydrotalcite, being poorly soluble at neutral pH, precipitates at the surface. The rate of leaching depends on several factors like the rate of percolation of water, temperature and concentration of solutes in water. Hydrogarnet (HG) is seen to be chemically inert during leaching [74]. C-S-H phase together with CH and alkalis contribute to high pH and calcium solubility in cement pastes. Figure 2.20 shows a schematic representation of degradation of cement and the corresponding pH values as a function of time. The initial pH is > 13 because of the dissolution of sodium hydroxide and potassium hydroxide thus resulting in highly alkaline conditions when exposed to ground water. However, this is only a short-term stage and pH decreases to 12.5 when these hydroxides are removed. This $\text{pH} \approx 12.5$ is then controlled by the dissolution of CH and C-S-H phases.

There are two common leaching methods used by researchers to study the impact on cementitious materials.

- Leaching with ammonium nitrate solution [35][36]

This is an accelerated technique which might reduce the leaching time and thus does not correspond to the natural leaching.

- Leaching with demineralised water [37]

This technique takes a long time due to slow kinetics of leaching degradation but is largely employed as it is more like the natural leaching. It is observed that the water leaching induces dissolution of phases like CH, C-S-H, AFm, AFt and the microstructure of C-S-H phases changes from fine fibrillar to foil-like and the aluminosilicate structure changes from single chain to double chain with cross linked interlayers. When cement is exposed to groundwater, CH is the first phase to leach out, thus increasing the porosity of the cement paste [76].

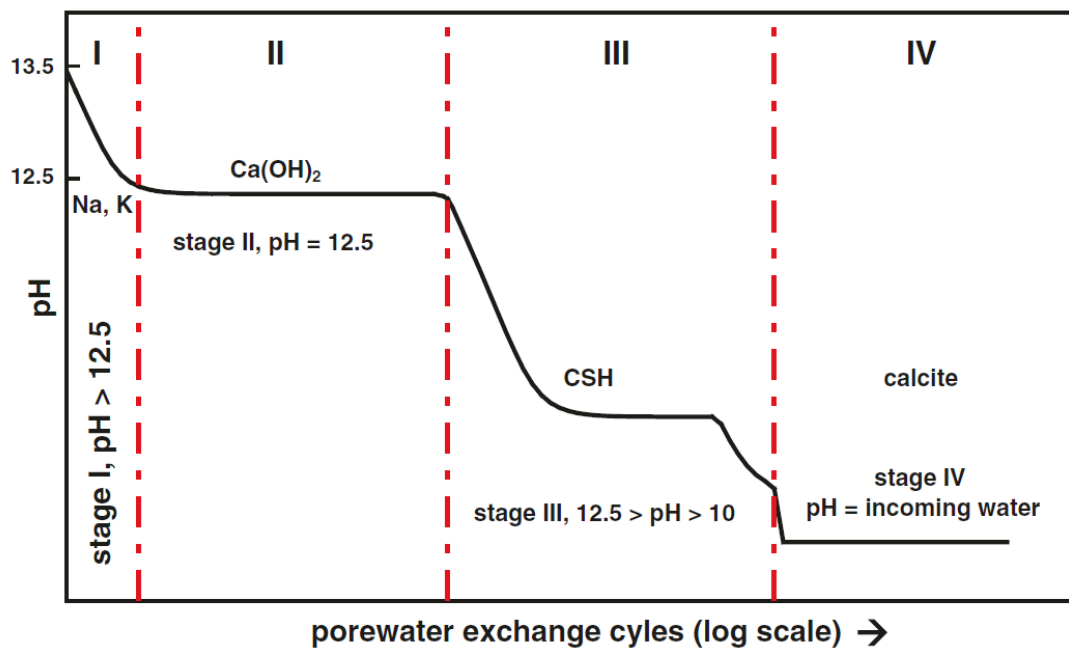


Figure 2.20 Schematic representation of evolution of pH as a result of cement evolution [75].

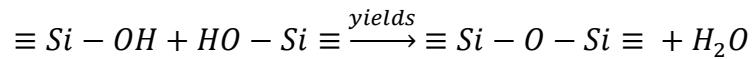
2.4.1 Effects of Leaching

Leaching affects the mechanical properties and pore structure of cementitious materials when groundwater percolates through geological vaults [69]. It has been found that cementitious materials evolve as Ca leaches on exposure to some harsh environments and this degradation can cause damage like cracking,

fracture etc. Removal of CH crystals results in macro porosity which affects the mechanical strength and decalcification of C-S-H results in a microporous gel with an increase in porosity. These changes result in a gradient of Ca/Si in the leaching zone. As the leaching progresses, both density and mechanical strength decreases. Carde et al. related the loss of mechanical strength to increase in the porosity which resulted from the removal of CH [80]. However, the effect on porosity and the mechanical strength is not discussed in this work. According to Francois et al. immersion time and mass loss have a linear relationship meaning as the leaching time increases, amount of mass loss also increases [77].

Leaching of C-S-H on exposure to ground water results in increase in porosity, permeability and decrease in strength. This evolution changes the microstructure of C-S-H and these changes play an important role in the study of cement-based repositories for radioactive wastes. Researchers have developed several solubility models [81][82][83][84][85] and also studied the effects of leaching on mechanical properties [77][86][87] and on permeability. Faucon *et. al* [88][89] by ^{57}Fe Mössbauer and ^{27}Al NMR spectroscopy studied that the structure of leached C-S-H in OPC pastes showed considerable substitutions of Fe^{3+} and Al^{3+} for Ca^{2+} and these substitutions reduce the rate of dissolution of the paste, thus stabilizing the structure. Also, silicate polymerization in C-S-H due to leaching results in macroscopic shrinkage in cement pastes [90]. Faucon et al [74] observed that the leaching of cement paste with demineralised water results in the successive dissolution of CH, AFm and then AFt. However, hydrotalcites dissolve very slowly at neutral pH values, thus explaining the precipitation of magnesium containing phases. He also observed that AFt is more resistant to leaching compared to AFm. This is in agreement with the observation that AFm dissolves at $\text{pH} \approx 11.6$

whereas Aft dissolves at pH \approx 10.7. Haga [75] found that leaching resulted in formation of Q³ species and the MCL of the C-S-H gel increased as the dissolution progressed. Leaching causes decalcification of C-S-H and an increase in silicate polymerization which Chen [90] referred to as polymerization shrinkage. He studied these leaching effects on samples with Ca/Si < 1.2 and suggested that the increase in polymerization is due to the leaching of interlayer Ca²⁺. Si-OH groups maintain the charge neutrality and thus condense with Si-OH groups of other tetrahedra forming longer chains.



This formation of siloxane bond causes the shrinkage of the cement gel.

Decalcification of cement pastes results in cracking and propagation of a fluid through the porous network. The surface leaches more than the core and thus surface shrinks more than the core. Hence, the shrinking surface stretches to accommodate the non-shrinking core and this leads to cracking at the surface. Similar affects are seen on carbonation and sulfate attack on cement pastes [47][48][90][91][92]. CO₂ dissolves in the pore solution of cement pastes, the CO₃²⁻ ions produced react with Ca²⁺ and form CaCO₃.

Harris et al. [82] observed that the dissolution of C-S-H gels during the initial stages show incongruency followed by an approach to congruency. The general method used for accelerated leaching experiments [93] is reducing the particle size to increase the surface area available for leaching and to stir the solution to decrease the time to achieve equilibrium. However, this method can overestimate the leaching rate.

2.5 Hydrothermal ageing

Ambient temperature at GDF depths of 500 m – 1000 m vary, and the average geothermal gradient is 26 °C per km in UK [94]. Following backfill, the temperature will rise significantly (to around 80 °C) in short-term due to the hydration of the cement backfill. The temperature drops as the heat generated from radioactive decay reduces with time. Temperature will have an influence on hydration and affect the long term performance of the cementitious materials [95]. Thus, it is important to understand the effects of temperature on the main binding C-S-H phase. The storage of cement at temperatures greater than 70 °C for long periods results in dissociation of AFm type phases and leads to incorporation of Al^{3+} , Fe^{3+} , SO_4^{2-} ions into C-S-H phases or the pore solution. Also, at elevated temperatures the amorphous C-S-H phase becomes more crystalline. The most striking feature of the hydrothermally aged cements is the growth of hexagonal CH crystals resulting from the decreased solubility of CH at higher temperatures [96]. This results in reduction of pH, which may have a long-term effect on the safety functions of a backfill.

Chapter 3 Characterization Techniques

3.1 Simultaneous Thermal Analysis

3.1.1 Introduction

STA is a combination of two different techniques: Thermogravimetric analysis (TG) and Differential thermal analysis (DTA) or Differential scanning calorimetry (DSC).

TG measures the change in weight of the sample as a function of temperature. The weight change is the result of release of gases on heating. DTA involves the heating of a reference sample and the sample of interest simultaneously under identical conditions while measuring the difference in temperature between the sample and the reference [97]. DSC measures the difference in the amount of heat required to increase the temperature of a sample and reference, measured as a function of temperature. Both the sample and reference are maintained at nearly the same temperature throughout the experiment. STA is used to determine the presence of different phases and to detect the phase transitions that occur. It helps in quantitatively identifying the phases present in the sample.

The heating of a cementitious material results in physical or chemical changes like mass loss or crystallinity transition. DTA/DSC shows these changes as a function of temperature with an exothermal change being a peak and an endothermal change being a trough [98]. This process of heating results in dehydration of hydrate phases and decarbonation of carbonate phases. The weight change for different systems occurs within a range of temperatures rather

than at one single point. The temperatures at which mass loss mainly occurs when a cementitious sample is heated to 1000 °C are:

- 100 °C – 300 °C - endothermic peaks representing the decomposition of gypsum, ettringite, C-S-H and carboaluminate hydrates.
- 400 °C – 550 °C - an endothermic peak representing the dehydration of CH.
- 600 °C – 850 °C - an endothermic peak representing the decarbonation of CC .

However, the decomposition of these phases is not strictly restricted to these temperature ranges. According to Thiery et al the carbonate phases and their crystal size have an effect on the decomposition temperature [99].

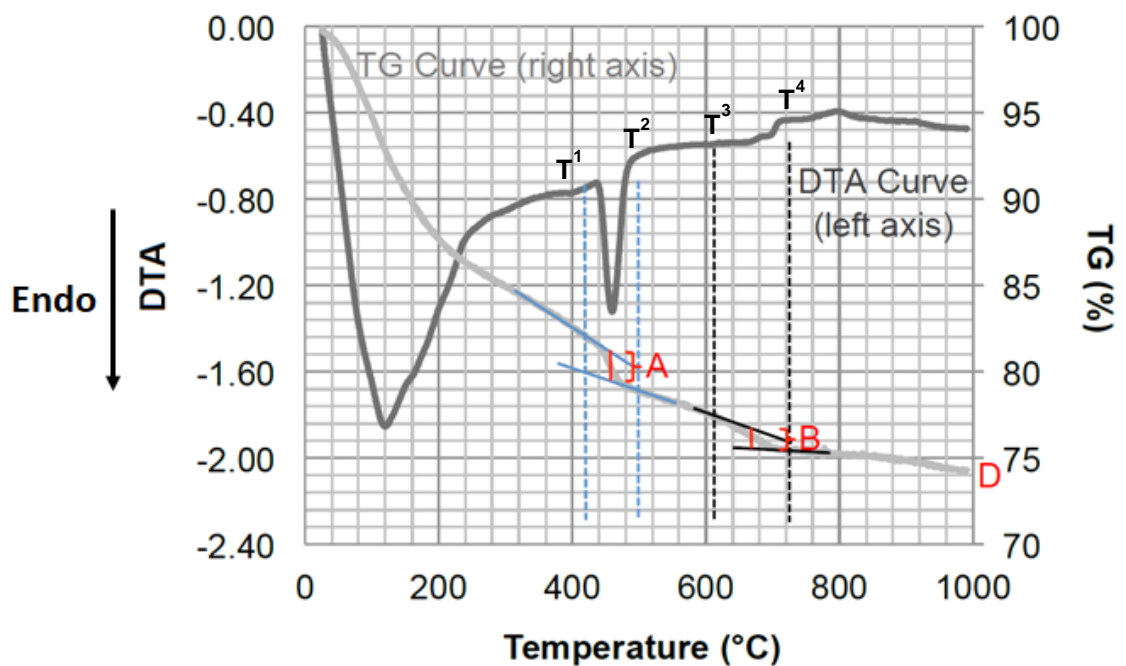


Figure 3.1 STA data for a partially carbonated cement paste.

Figure 3.1 shows TG curve (light grey) and DTA curve (dark grey) of a sample heated to 1000 °C. It also shows the temperature ranges in which mass loss

occurs due to dehydration and decarbonation of hydrate and carbonate phases respectively. The percentage of CH and $\bar{C}\bar{C}$ can be calculated from the TG curve using the tangent method [100]. Inflexion points T¹, T², T³ and T⁴ are identified as a mass loss and tangents are drawn. A vertical line is drawn passing through the middle point of the inflexion points and joining the tangents. The length of this vertical line is measured as % weight loss.

A - Weight loss due to dehydration of CH.

B - Weight loss due to decarbonation of $\bar{C}\bar{C}$.

Both A and B are calculated using the TG curve and tangent method.



Mol wt. 74 g/mol 56 g/mol 18 g/mol



Mol wt. 100 g/mol 56 g/mol 44 g/mol

From equation 1, 1 mole of CH (74 g/mol) decomposes to give 1 mole of H₂O (18 g/mol).

$$\% \text{ CH} = (74/18)*A$$

From equation 2, 1 mole of CC (100 g/mol) decomposes to give 1 mole of CO₂ (44 g/mol).

$$\% \bar{C}\bar{C} = (100/44)*B$$

The ignited mass (ig) is the mass of the solid material in the original mix (unless that solid material contained something that would lose mass upon heating, such

as calcium carbonate). The % CH and % $C\bar{C}$ referred to the ig are determined using the formula are:

$$\% \text{ CH (ig)} = [(74/18)*A/D]*100$$

$$\% C\bar{C} \text{ (ig)} = [(100/44)*B/D]*100$$

D - % residual mass at the end of 1000 °C.

3.1.2 Sample preparation

The instrument used for performing DTA is a Stanton Redcroft STA – 1500 series. The instrument used to perform DSC is a NETZSCH STA449 F5 series and gas analysis is performed on a AEOLOS QMS 403 D series. Samples are dried and ground to fine powder in mortar and pestle. Approximately 15 mg – 18 mg of the sample is packed into a platinum crucible and is heated from 20 °C to 1000 °C at a constant rate of 20 °C/min under continuous flow of nitrogen.

3.2 X - Ray Diffraction (XRD)

3.2.1 Introduction

Wilhelm Conrad Roöntgen over a century ago discovered the phenomenon of X-radiation, which eventually showed that the X-rays having wavelengths in angstrom (Å) range can penetrate solids and this resulted in the development of many techniques, one of which is XRD analysis [101]. It is used to analyse the phases present in the sample of interest. Each crystalline phase produces a unique diffraction pattern, thus providing data needed to identify the phases present [102].

XRD is an elastic interaction of an X-ray photon with an atom in various ways, being scattered, diffracted, reflected or absorbed. For constructive interference, the X-rays reflected at different planes should all be 'in phase'. This interaction is represented by Bragg's law: -

$$n\lambda = 2d\sin\theta$$

Where n is an integer (order of reflection), λ is the X-ray wavelength, d is the inter - planar spacing and θ is the angle of incidence representing the angle between the incident beam and the normal to the reflecting lattice plane.

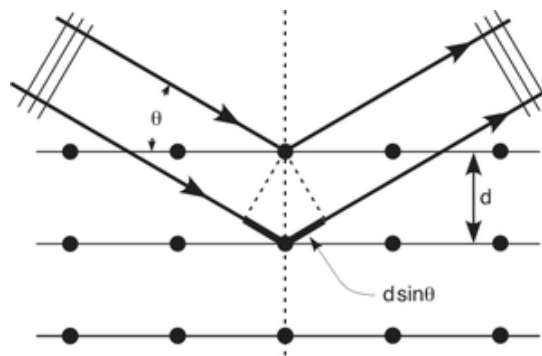


Figure 3.2 Schematic representation of Bragg's law [63].

Figure 3.2 illustrates the schematic representation of Bragg's law. When a metal is bombarded with electrons, X-rays are emitted due to the excess energy within the atom. When these emitted X-rays interact with the crystalline structure of the sample, there is a collision of X-rays with the electrons in the crystalline plane. This results in the diffracted X-ray beams [101]. These diffracted beams are detected and recorded in a diffraction pattern. Each crystalline structure will have characteristic peaks corresponding to a typical diffraction pattern and each of these peaks represent a group of planes in the crystal structure.

Intensity is measured as a function of θ and d is then calculated using θ . By comparing the experimental data obtained with standard patterns available for various compounds in databases – ICSD (Inorganic Crystal Structure Database), ICDD (International Centre for Diffraction Data) and COD (Crystallography Open Database) the phases present in the sample can be identified.

The well-defined crystals have sharper peaks whereas the amorphous phases show broad and non-uniform peaks [103].

3.2.2 Sample preparation

The XRD used for the analysis of the samples is D2 Phaser Bruker operated with Cu K α radiation at 10 mA and 30 kV with X-ray wavelength of 1.5418 Å. Samples are crushed and ground into a fine powder in a mortar and pestle. This is important to achieve good signal to noise ratio and minimise preferred orientation affects. Preferred orientation is seen when there is the presence of a large amount of needle or plate like crystals in the sample being analysed. This arises because crystals packed onto the sample holder tend to orient the same way, resulting in peaks with unusually high intensities. The finely ground powders are then packed to a flat surface onto a sample holder. If the powder is not packed evenly or if the sample holder is filled too high or too low with the sample, there is always an error which results in shift of peak positions thus making the interpretation difficult.

The sample holder is rotated at 15° rot/min with the minimum and maximum values for 2θ set at 3° and 70°. The minimum step size is 0.01 and the maximum time per step is 9 sec. The total time for one run with the above-mentioned parameters is \approx 15 hours. The sample holder is rotated to improve the

measurement statistics and obtain better results. The divergence slit and air scatter slit both are 1 mm. The soller slit used is 2.5 ° and the absorber used is 0.5 % Ni.

The C-S-H phase in cement paste is poorly crystalline causing indexing problems by producing broad peaks, generally termed as 'amorphous humps'. This hump can overlap with other peaks and influence the positions and relative intensities of crystalline phases. Also, the crystal size effect shows an influence on the XRD analysis. For the crystals having crystal size < 100 nm the peaks generally appear broad on the pattern hence obscuring other phases as the X-ray cannot undergo complete destructive interference in scattering [101]. All the reference patterns are taken from Inorganic Crystal Structural Database (ICSD) to identify the phases present in the samples.

3.3 Magic Angle Spinning Nuclear Magnetic Resonance (MAS NMR)

3.3.1 Introduction

Solid state nuclear magnetic resonance (NMR) characterization used to study cement pastes and cement-based materials provides an understanding of the silicate anion structure and the incorporation of aluminium in the C-S-H phase. Three different experiments in NMR are considered to characterize cement samples: ²⁹Si Direct Pulse (DP) NMR provides information on the coordination of silicate tetrahedra in local environments, ²⁷Al NMR provides information about the incorporation and coordination of aluminium present in the sample and ²⁹Si Cross Polarization (CP) provides data on the hydrates [104].

It was in the year 1948 that the NMR technique was first applied to the cement phases characterization. The basic principle of NMR is based on the fact that different nuclei have different characteristic spin (I), some with integral spins ($I = 1, 2, 3, \dots$), some with fractional spins ($I = 1/2, 3/2, 5/2, \dots$) and some with no spin ($I = 0$). When a strong magnetic field, such as that used in NMR, is applied on these nuclei, different energy levels are produced depending on the nuclear spin. When a strong magnetic field is applied on a nucleus with a non-zero spin, there is an energy transfer resulting in an energy difference between the energy states called as Zeeman splitting [105][106]. This is illustrated in the Figure 3.3.

In any nucleus, the total number of spin energy levels is given by $2I + 1$ each ranging from $I, I-1, I-2, \dots, -I$.

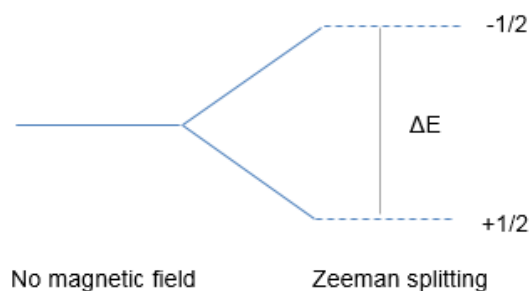


Figure 3.3 Energy level diagram for nucleus with spin $I = 1/2$ [105].

The nucleus is then perturbed by a pulse of radio frequency radiation which generates electronic transitions between the different energy levels. The nucleus removes this perturbation by absorbing or emitting a photon and this frequency is measured as a chemical shift (δ) [104][107]. Chemical shift and magnetic field strength are proportional to each other and hence δ is measured in parts per million (ppm).

Solid state NMR is affected by line broadening which results from the interaction of the spin nuclei (dipolar broadening, spin – spin couplings, quadrupole interaction, chemical shielding anisotropy). In solution NMR these interactions are of no concern due to molecular tumbling. This phenomenon can be replicated in solid state NMR by magic angle spinning (MAS) which significantly reduces these interactions. The sample is rotated around a fixed axis that is inclined by 54.7° relative to the magnetic field replicating molecular tumbling that is seen in solutions. Hence in solid state NMR the magic angle is set to 54.7° [105][106].

3.3.1.1 ^{29}Si MAS NMR

^{29}Si is the only silicon isotope with a magnetic moment and spin (I) = $\frac{1}{2}$, hence long experiment times are needed to obtain high quality spectra. Also due to long relaxation times of ^{29}Si nuclei, long recycle delay is needed. The natural abundance of ^{29}Si is less than 5 %. The spinning sidebands occur in ^{29}Si NMR when rotation frequency of the sample is less than the chemical shift anisotropy of that nuclei. They will always be spaced at the rotor frequency away from the isotropic signal. In the year 1982 Lippmaa *et al* used ^{29}Si NMR to obtain quantitative information regarding the environments of silicon tetrahedra [108]. The different tetrahedral environments are designated as Q^n , where Q represents silicate tetrahedron while n denotes the connectivity of the silicate tetrahedron via oxygen and hence the value of n is limited to the valency of oxygen i.e $0 \leq n \leq 4$ [109]. Table 3:1 shows the characteristic NMR chemical shifts of silicate species in cementitious materials. Q^0 denotes isolated tetrahedra in the range of - 66 ppm to - 74 ppm. Q^1 denotes end chain groups having chemical shift in the range of - 75 ppm to - 82 ppm. Q^2 denotes middle chain groups where both adjacent tetrahedra are occupied by silicon and have a chemical shift in the range of - 85

ppm to - 89 ppm. Q^3 denotes the branching sites with chemical shift in the range - 95 ppm to - 100 ppm and Q^4 denotes cross linking sites in a three-dimensional framework with chemical shift in the range - 103 ppm to - 115 ppm. $Q^n(mAl)$ denotes middle chain groups where adjacent tetrahedra are substituted by aluminium ions [110]. The silicate tetrahedra are connected via n bridging oxygens to m Al where m is the number of substituted aluminium ions. $Q^2(1Al)$ represents middle chain groups and has a chemical shift around - 82 ppm. There is also a peak between - 70 ppm and - 75 ppm indicating the presence of $Q^0(H)$ groups denoting a hydrated monomer.

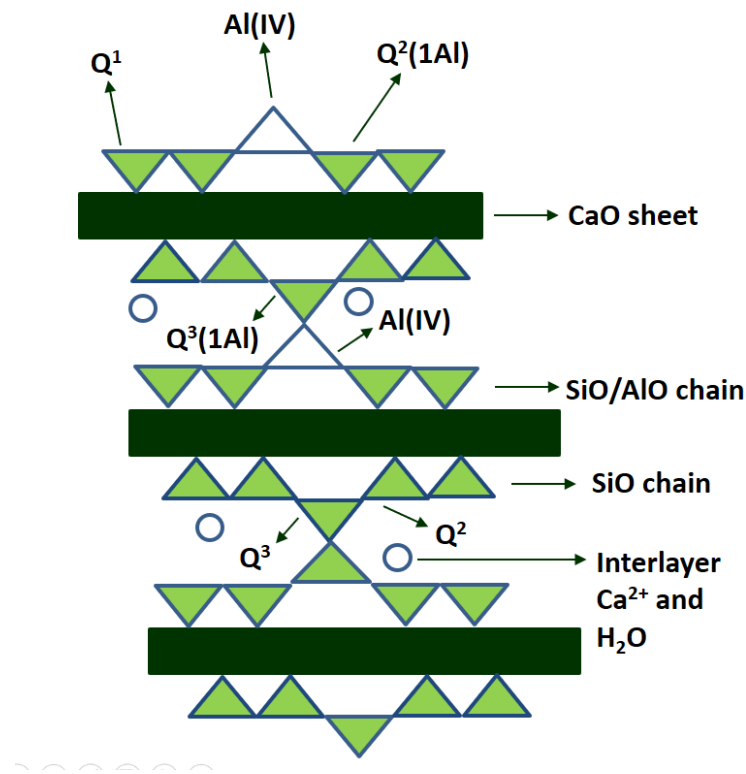


Figure 3.4 Schematic representation of Q^n sites.

Figure 3.4 shows the schematic representation of Q^n tetrahedra. The chemical shift indicates the local environment of silicon atoms and is determined by number of silicon and aluminium atoms surrounding the SiO_4 tetrahedra. Richardson et

al in 1994 were the first to perform a direct experimental comparison between TEM and NMR data [111]. They found a good agreement between the Al/Si ratios from both the characterizations. Hirljac et al in their work determined that there will be an increase in the mean chain length (MCL) with age due to an increase in the polymerisation [112]. Young [113] also showed that an increase in the temperature increases polymerisation.

Type of Silicate	Site	Tetrahedral Structure	Chemical shift (ppm)
Monomers	Q ⁰	O- O-SiO- O-	-66 to -74
Dimers (end chain groups)	Q ¹	O- O-SiOSi O-	-75 to -82
Middle chain groups	Q ²	O- SiOSiOSi O-	-85 to -89
	Q ² (1Al)	O- SiOSiOAl O-	-82
Chain branching sites	Q ³	Si O SiOSiOSi O-	-95 to -100
Three-dimensional network	Q ⁴	Si O SiOSiOSi O Si	-103 to -115

Table 3:1 Characteristic NMR shifts of silicate species in cement samples.

Research using ²⁹Si NMR on cement samples showed the presence of Q²(1Al), indicating aluminium incorporation in silicate chains but showed no evidence of Q¹(1Al) suggesting that aluminium substitutes for silicon only on the bridging tetrahedral sites [39][114]. Richardson et al also showed that the Al substitutes for Si in bridging sites only [115].

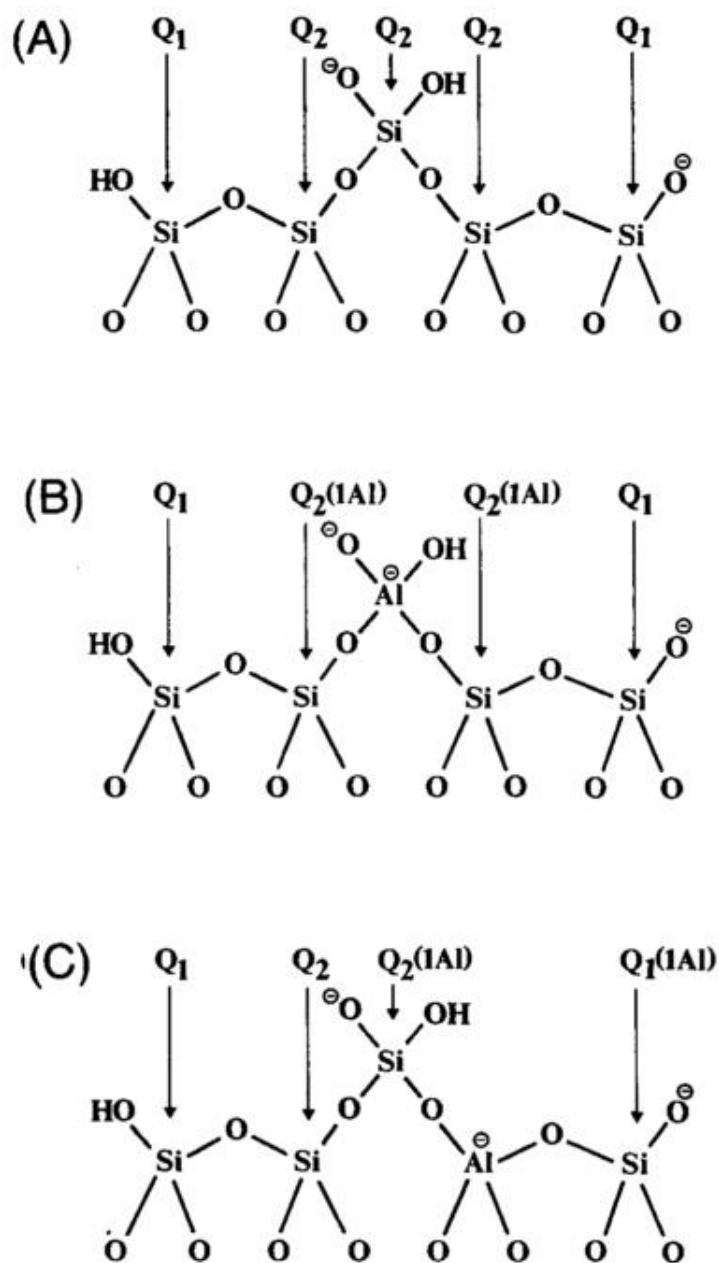


Figure 3.5 (A) Schematic representation of pentameric silicate chain, (B) pentameric chain with Al substituting for Si in the bridging site, (C) pentameric chain with Al substituting for Si in the non-bridging site [115].

The Al substitution for Si in bridging sites (Figure 3.5 (B)) would result in Q¹ and Q²(1Al) groups but Al substitution for Si in non-bridging sites (Figure 3.5 (C)) would show the presence of Q¹(1Al) groups. Further analysis of CP spectra

showed no trace of Q¹(1Al) and hence it is concluded that Al substitutes for Si only in bridging sites.

3.3.1.2 ²⁷Al MAS NMR

²⁷Al MAS NMR is a very important and useful technique in analysing cement samples as Al³⁺ is a very common guest ion that is incorporated into the C-S-H structure. The direct evidence for Al³⁺ ion substitution for Si⁴⁺ in cementitious systems is shown by Skibsted and Jakobsen [116]. ²⁷Al has a spin of $I = 5/2$ and a natural abundance of 99.99 % and hence requires far less experiment time than that of silicon. Also, nuclei having spin greater than $\frac{1}{2}$ exhibits a non-spherical electric charge distribution causing a quadrupole moment. This results in broadening of spectral lines making it difficult to make distinctions in the local environments [104]. However, ²⁷Al NMR can be used to differentiate between the tetrahedral (Al^[IV]) and octahedral (Al^[VI]) coordinations [116]. ²⁷Al MAS NMR also has disadvantages in the interpretation of the spectra as it is affected by the quadrupolar interaction resulting in side bands, thus leading to a field dependent shift in the position of resonance and peak broadening [117]. In order to avoid the side bands interfering with the spectrum, the spinning speed can be increased which pushes the side bands away from the centre band. However, this can result in a lower resolution of the spectrum making it difficult to define the peaks. Some research suggests that they could also result from the presence of ferromagnetic iron oxide (Fe₂O₃) [118] and the spinning side bands increase linearly with an increase in Fe₂O₃ content [118]. ²⁷Al isotropic chemical shifts for tetrahedral coordination of Al have a range of 100 – 50 ppm while for octahedral coordination of Al the range is 20 – 10 ppm [113]. The peaks at 9 ppm and 13 ppm are

indicative of Al incorporated into the AFm and AFt phases respectively, whereas a broad peak at 65 ppm corresponds to Al incorporated in C-S-H [119][120].

3.3.2 Sample preparation

The samples are ground in a pestle and mortar producing a very fine powder. These powders are packed in the rotors and analysed immediately.

^{29}Si and ^{27}Al NMR spectra for NRVB samples (S1, S2, S3 – described in the Experimental Methods) are collected using a Varian VNMRS 400 MHz spectrometer (magnetic field 9.4 T; operating frequencies of 79.438 MHz for ^{29}Si and 104.199 MHz for ^{27}Al). For ^{29}Si , the spectra are acquired over 13000-16000 scans using a spin rate of 6 kHz, a pulse recycle delay of 1s, a pulse duration of 4.5 μs and an acquisition time of 30-50 ms. For ^{27}Al , the spectra are acquired over 4000-7000 scans using a spin rate of 14kHz, a pulse recycle delay of 0.2s, a pulse duration of 1 μs and an acquisition time of 10 ms.

^{29}Si NMR spectra (for all synthetic C-S-H samples and S4 – described in Experimental methods) and ^{27}Al NMR spectra (for S4 – described in experimental Methods) are collected using a Bruker Avance III HD with a 9.4 T WB magnet with operating frequencies of 74.48 MHz for ^{29}Si and 104.26 MHz for ^{27}Al . For ^{29}Si , the spectra are acquired over 2000–16000 scans using a spin rate of 6 kHz, a pulse recycle delay of 10 s-30 s, pulse duration of 5.5 μs and an acquisition time of 0.04 s-0.09 s. For ^{27}Al , the spectra are acquired over 16000 scans using a spin rate of 12 kHz, a pulse recycle delay of 5 s, pulse duration of 0.231 μs and an acquisition time of 0.0099 s. A 7 mm zirconia rotor with KEL – F caps is used for collection of ^{29}Si data whereas a 2.5 mm Zirconia rotor with Vespal caps is

used for collection of ^{27}Al data. The magic angle of 54.7° in both the cases is set using KBr reference.

3.3.3 Igor fitting method

Deconvolution of ^{29}Si NMR spectra is performed using a user made procedure for Igor Pro developed by Love and Brough [121]. The baseline is fitted using a cubic multinomial function and the individual peaks are fitted with a Voigt line shape. Parameters like Intensity, peak shift, peak shape and peak width are released sequentially until the residual plot between the experimental and simulated spectra is at a minimum. Integrated areas of each of the fitted peaks are then used to calculate mean aluminosilicate chain length (MCL) and Al/Si ratio as shown in the equations below.

$$MCL = \frac{2}{\frac{Q^1}{Q^1 + Q^2 + 3/2Q^2(1Al)}}$$
$$\frac{Al}{Si} = \frac{1/2Q^2(1Al)}{Q^1 + Q^2 + Q^2(1Al)}$$

3.4 Transmission Electron Microscopy (TEM)

3.4.1 Introduction

TEM provides information on morphology, microstructure and chemical composition (via EDX analysis) [16][17][31][111][122][123][124] and thus helps in determining the structure of C-S-H [31]. It allows to study the details of the phases that cannot be captured by SEM such as morphology and chemical composition of the phases without any intermixing issues. However, TEM having a high voltage electron beam emitting from a cathode and accelerated by a voltage between cathode and anode may easily damage the phases during both

imaging and EDX analysis. The advantage of TEM over SEM is a smaller interaction volume due to the depth of the sample making EDX analysis more accurate. Radczewski et al. in 1939 published the earliest work on electron microscopy [125] and Grudemo published the most significant work on electron microscopy of dispersed specimens [9][126][127].

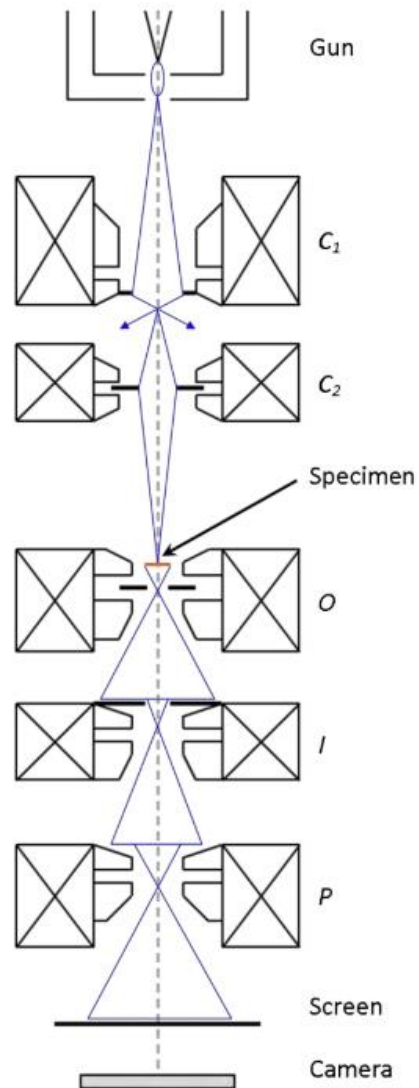


**Figure 3.6 Schematic representation of Transmission Electron
Microscope.**

The schematic layout of TEM is shown in Figure 3.6. The basic principle of TEM is based on the transmission of an electron beam through a sample. The electron beam is generated by a thermionic gun or field emission gun at the top of the column that is kept under vacuum. The resultant beam is focussed by one or more condenser lenses (C_1 and C_2) onto the sample that is in the holder inserted via an airlock. The objective lens (O) is below the sample above an intermediate lens (I) and the projector lens (P) forms the final image onto the fluorescent screen. SAED (Selected Area Electron Diffraction) is a technique that helps in identification and characterization of crystalline phases. Richardson in his chapter [102] provided a review of TEM analysis and discussed its application on several cement systems. This review discusses and highlights several studies in the literature.

3.4.2 Sample preparation

Samples are sliced into thin sections of 1 mm width using a Bucheler Isomet low speed cut off saw with a diamond edged wavering blade. These slices are hydration stopped using isopropanol and diethyl ether by solvent exchange method and then are stored in a desiccator to avoid carbonation and contamination. Solvent exchange method is used to stop the ongoing hydration reactions in cementitious materials by removal of the free water from the material. Organic solvents like isopropanol or ethanol or methanol are usually used, and diethyl ether is used at the end to remove isopropanol or ethanol or methanol. Hydration stopping for all the samples is done in isopropanol (about 15 ml) by soaking the 1 mm discs for 2 hours after which secondary replacement is done with diethyl ether followed by heating at 40 °C [106]. Once dried, the slices are attached to a clean glass slide with cyanoacrylate glue and thinned by hand using

different grades of SiC papers (600 μm , 800 μm , 1200 μm and 2400 μm) until the slices are thin enough to be 30 μm (measured using Vernier callipers) in width. Slices are then carefully removed from the glass slide by immersing the glass slide in a petri dish containing acetone until the glue is dissolved and then are glued between two 3 mm diameter copper TEM grids using epoxy. The copper grids have a 1 x 2 mm hole in the centre and the sample can be viewed through this hole. After this, samples are ion beam milled using Gatan Precision Ion Polishing System (PIPS). Milling is performed under vacuum until a hole is made in the centre of the sample. The PIPS is set at 3 KeV and the guns are set at a milling angle of 6 °. The glancing incidence of the guns to the specimen vastly reduces the input energy to the sample thus preventing damage due to thermal affects and the advantage of this technique is that a much larger electron transparent area is produced.

The synthetic C-S-H samples are ground to fine powders inside the glovebox and a small amount of this fine powder is added to a vial containing about 10 ml ethanol. The vial with the solution is sonicated for ~ 5 mins in an ultrasonic bath. A drop of the middle of the solution is then deposited over a 200-mesh copper grid with a carbon film.

All the samples are coated with carbon before viewing under TEM. Coating is performed using Agar Turbo Carbon Coater to prevent charging affects under microscope. The sample is then stored in a vacuum desiccator until further examination to avoid contamination.

The cement samples are examined using a FEI Tecnai F20 200kV FEG TEM fitted with a Gatan Orius SC600 CCD camera and an Oxford Instruments 80mm² SDD EDX detector running Aztec software. Magnification of 5k is used for general

viewing of the sample and micrographs of sites of interest are collected under increased magnification of $\approx 10k$. EDX data are collected at a magnification of 22k with a spot size of 5 or 6 and an acquisition time of 20 s. SAED patterns are collected prior to EDX analysis to confirm that the site of interest is free from any spots and indicates a pure amorphous phase. The synthetic C-S-H samples are examined using a FEI Titan Themis 300 microscope operating at 300 kV with microstructural analysis by EDX spectroscopy on a Super-X EDX system with a windowless 4-detector design. The images are taken at magnification of $\approx 20k$, spot size 3 and a live time of 10 s. While collecting EDX data, thin areas rather than thick areas are chosen as the x-rays emitted from the material can be absorbed if the area is thick and this could result in modified values [102]. Damage to the sample can be avoided by minimising exposure to the electron beam by working under lower magnifications for viewing and higher magnifications only when necessary [102][111][128]. The disadvantage of TEM analysis is the difficulty in preparing electron transparent samples. Also, extensive care and attention must be taken during the examination of samples to reduce the potential damage of the samples due to beam exposure. A synthetic wollastonite sample is used as a reference for all the EDX measurements.

Chapter 4 Experimental Methods

4.1 NRVB sample description

Four NRVB samples are provided by RWM for analysis and characterization of the microstructure.

The current formulation of the NRVB is shown in Table 4:1. Originally, a w/s of 0.56 is used but since 2014 a higher w/s of 0.61 has been preferred to improve fluidity of the mix. Four samples of NRVB are compared in this study, as listed in Table 4:2.

Component	Ratio by wt.
CEM I	2.65
Limestone flour	2.9
Hydrated lime	1
Water	4; w/s = 0.61

Table 4:1 Current NRVB formulation.

NRVB used for laboratory testing has been made in 10-50 L batches. The mixes are cast into 100 mm diameter, 200 mm tall cylindrical moulds. Once set, the cylinders are demoulded, wrapped in polythene and then cured at ambient temperature and 90% relative humidity until required.

The NRVB used for ageing experiments is made by Taywood Engineering. This block was stored under calcium hydroxide solution for 6 years prior to leaching and hydrothermal ageing experiments. The leaching experiment for sample S3 consisted of placing discs of ~7 g of the 6-year-old NRVB in a polypropylene pot

with 500 ml of deionised water. After 82 days, the volume of water is increased to 1000 ml to increase the rate of leaching.

Sample	Description
S1	Made in 2014, cured for 28 days and subsequently stored for 1 year.
S2	Made in 1998 and stored for 16 years.
S3*	Made in 1992 and stored under a solution of CH for 6 years, then extensively leached in demineralised water over 541 days and then allowed to age under water for 6 years.
S4*	Made in 1992; stored under CH solution for 6 years, then extensively leached (536 days), followed by hydrothermal treatment at 80°C for ~1183 days; subsequently stored in leachate for 12 years.

* Samples S3 and S4 are from the same NRVB batch.

Table 4:2 Description of the NRVB samples analysed.

To increase the leaching rate further, after 4 months fresh water at a temperature of 40 °C is added, and the sample is allowed to cool naturally. The water is removed and replaced with fresh deionised water 24 times in total, with the period ranging between 1 day and 174 days. The process is stopped after 541 days,

and the samples are sealed and stored in a polypropylene pot under water for 6 years (S3). The leaching experiment for sample S4 consisted of placing about 100 g of crushed 6-year-old NRVB in a polypropylene pot to which 1000 ml of deionised water is added. To increase the leaching rate further, after 4 months fresh water at a temperature of 40 °C is added, and the sample is allowed to cool naturally. After 536 days of leaching, the solid material is placed in Parr acid digestion vessel with 40 ml of final leachate solution and then the digestion vessel is placed in an oven at 80 °C for 1183 days after which the vessel is cooled and left sealed for 12 years (S4). For the analysis of the samples, the solid and liquid are separated by filtration process and the solid is dried inside a glove box at room temperature.

4.2 Synthesis of high Ca/Si ratio C-S-H phases by hydrothermal method

4.2.1 Introduction

It is difficult to synthesize C-S-H phases with $\text{Ca/Si} > 1.5$ unless anhydrous C_3S or C_2S is used as a starting material and precipitation of CH is prevented by using high water/solid ratios, periodical replacement of solution by water or addition of reactive silica. Tajuelo-Rodriguez [63] and Nonat and Lecoq [61] synthesized C-S-H phases with Ca/Si ratio > 1.5 using C_3S (for details refer literature review). Although many researchers have reported the synthesis of high Ca/Si ratio C-S-H phases using methods like double decomposition or silica lime reactions (refer literature review), detailed study showed that these phases are a mixture of C-S-H phases with Ca/Si ratio 1.3 - 1.4 and CH phase. Richardson discussed the

experimental data from many studies in his articles [45] [129]. Renaudin et al. [52] studied C-S-H synthesis using Rietveld refinements of X-ray powder patterns and reported structural continuity from C-S-H (I) type with Ca/Si = 0.8 to C-S-H (II) type with Ca/Si = 1.7. However, detailed inspection of compositions of the synthesized phases showed that the maximum experimental Ca/Si ratio calculated is only 1.36. Ishida et al. [6] [8] successfully synthesized high Ca/Si ratio C-S-H phases using β -C₂S (refer Literature Review for details).

Highly reactive β -C₂S having a specific surface area of 7 m²/g which is stable at room temperature without stabilizers can be synthesised through thermal decomposition of C-S-H phases that are obtained by hydrothermal synthesis [7]. Although there exists three forms (hillebrandite, α – dicalcium silicate hydrate and dellaite) of C-S-H phases having Ca/Si ratio of 2, hillebrandite can be easily synthesized by hydrothermal process [130][131][132]. Torpov et al. [133] also reported that hillebrandite is directly decomposed to β -C₂S on heating.

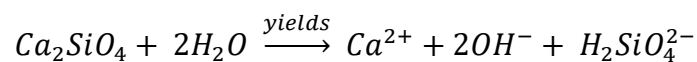
β -C₂S is one of the important constituents of Portland cement. Although, β -C₂S liberates less heat to hydrate than C₃S, the disadvantage is a hydration rate which is much lower than C₃S. Several researchers investigated the synthetic methods to produce β -C₂S and most of the methods constitute the use of a stabilizing agent at room temperature to prevent transformation to the γ -C₂S which is stable at room temperature. It is found that the hydration behaviour varies significantly depending on the type of ions added and on the reaction temperature [5][134][135][136][137][138].

The hydration process of β -C₂S is similar to that of C₃S and the similar process of heat evolution occurs in both cases.

Reaction stage	Chemical processes
Initial stage	Surface hydrolysis and release of ions into solution.
First deceleration	Formation of hydrate coating on C ₃ S surface, retarding dissolution.
Induction period	Retarded nucleation of final hydrates; slow consumption of retarders.
Acceleration period	Accelerating growth of principal hydration products.
Second deceleration	Continued growth of hydration products into large empty spaces.
Final slow reaction	Gradual densification of microstructure around residual unhydrated C ₃ S; CH re-crystallization.

Table 4:3 Typical sequence of hydration of C₃S [102].

When C₂S reacts with water, calcium oxide and silicate ions dissolve resulting in the formation of ionic species.



In the initial stage the rate of heat evolution is reported to be the same as C₃S where surface hydrolysis takes place releasing the ions into the solution [139]. However, the high reactivity of C₃S is related to the presence of O²⁻ ions in its structure which are hydrolysed easily. Barret and Bertrandite [140] showed the rapid release of calcium and silicate ions in both C₂S and C₃S but [Ca²⁺] is lower in C₂S and increases more slowly than in the case of C₃S. The first stage termed

as deceleration period is shown to witness the formation of a C-S-H layer and this precipitation of C-S-H occurs as early as 15 seconds, but the subsequent growth is relatively slower than in the case of C_3S . The NMR characterization done on these early stage products reveal the appearance of hydrated monomeric silica thus confirming that the nature of this layer formed is similar to that formed in C_3S [59][141]. In the hydration process of C_3S it is observed that in the induction period the growth of CH is responsible for the heat evolution and CH nucleation correlates with the rate of hydration. However, there is no large degree of supersaturation with respect to CH seen in the case of C_2S hydration thus being one of the main reasons for the relatively low reactivity of C_2S [142]. Also, the next stages of the hydration process showed some differences in the morphology of C-S-H formed as a result of C_2S hydration and C_3S hydration [143].

The reaction of calcium oxide (CaO) and silicic acid (H_4SiO_4) with water results in the formation of hillebrandite [$Ca_6Si_3O_9(OH)_6$] [7].

On heating hillebrandite at high temperatures, it decomposes to form highly reactive beta dicalcium silicate ($\beta-Ca_2SiO_4$)/($\beta-C_2S$) [7].

4.2.2 Experimental synthesis

The CaO used is made from heating reagent grade $CaCO_3$ at 1000 °C for 3 hours. The silicic acid used is 99.9 % pure, 20 μm from Sigma – Aldrich. The mixture of CaO and H_4SiO_4 taken in 2:1 molar ratio is mixed with Nitrogen sparged – vacuum degassed - deionised water at w/s of 20:1 by weight. The synthesis of C-S-H phases is done inside an acid digestion vessel (Figure 4.1), which can be heated to very high temperatures. The Polytetrafluoroethylene (PTFE) lined acid digestion vessel sourced by Parr Instrument Company (Model – 4748) has a

PTFE cup in a stainless-steel vessel having six cap screws used for sealing (provides inert conditions). It can withstand a temperature of 240 °C and a pressure of 1900 psig. The reactions can be conducted without losing trace elements and without adding contaminants from the outside atmosphere. The reaction mixture is placed in the PTFE cup and the lid of the acid digestion vessel is tightened as much as possible to prevent the entrance of air and hence carbondioxide. Heating the mixture at 200 °C for 7 days inside an oven resulted in the mixture of C-S-H phases (sample A, described in Table 4:4): hillebrandite [$Ca_6Si_3O_9(OH)_6$], scawtite [$Ca_7(Si_3O_9)_2CO_3 \cdot 2H_2O$] and jaffeite [$Ca_6Si_2O_7(OH)_6$].

After the reaction is completed, the oven is allowed to cool down and the PTFE cup is taken out of the acid digestion vessel. The lid of the PTFE cup is opened only in the nitrogen – atmosphere glove box. The product obtained is filtered and washed using 50 % - 50 % (v/v) ethanol and water followed by pure ethanol and then dried inside the glove box.

It has been reported that when silicic acid is used a source of silica, hillebrandite along with jaffeite is formed. This is because of high reaction rate of silicic acid [7]. Also according to Johnson and Roy, at high water pressure, hillebrandite and jaffeite can form together between 175 °C and 235 °C [144]. The formation of scawtite is due to slight contamination from CO₂ [145].

When the solid C-S-H (mixture of hillebrandite, jaffeite and scawtite) synthesised is heated to 600 °C for 1 hour in a muffle furnace, the product obtained (sample B, described in Table 4:4) is a mixture of phases with one being larnite (β -C₂S) and the others being scawtite and hatrurite (Ca₃SiO₅). Scawtite remains in the mixture as the decomposition temperature of scawtite is 750 °C [146].

Sample Name	Reactants	Temperature	w/s	Time
Sample A	CaO, H ₄ SiO ₄	200 °C	20/1	7 days
Sample B	Sample A	600 °C	-	1 hour
Sample C	Sample A	800 °C	-	1 hour

Table 4:4 Reactants and reaction conditions for synthesis of β – C₂S from hillebrandite.



Figure 4.1 Acid digestion vessel used for high temperature and high-pressure reactions.

To remove scawtite from the product, the mixture of solid C-S-H (hillebrandite, jaffeite and scawtite) synthesised is heated at 800 °C for 1 hour in a muffle furnace. The surface area of β -C₂S is only drastically reduced if heated above 800

°C. The product obtained (sample C, described in Table 4:4) is a mixture of phases with one being $\beta\text{-C}_2\text{S}$ and the others being wollastonite (CaSiO_3) and $\gamma\text{-Ca}_2\text{SiO}_4$ in minor quantities.

The $\beta\text{-C}_2\text{S}$ obtained (Sample C, described in Table 4:4) is used as the starting material for static and ball mill hydration experiments [6][8]. The details of the experimental conditions are shown in Table 4:5.

Hydrated samples are prepared by hand mixing the required amount of sample C with Nitrogen sparged – vacuum degassed - deionised water at different w/s ratios for 2 – 3 minutes inside the glove box. For static hydration, different mixtures are made with w/s ratios 0.5 and 1 and hydrated in a water bath at 25 °C for 7 days, 14 days, 28 days and 45 days. The samples are sealed in plastic vials ($V = 5 \text{ ml}$, $H = 30 \text{ mm}$, $\varnothing = 12 \text{ mm}$) and then vacuum sealed in plastic bags. Following the required hydration time, the vacuum sealed plastic bags and plastic vials are carefully opened inside the glove box and the products obtained are filtered and washed with 50 % - 50 % (v/v) ethanol and water followed by pure ethanol. The powders obtained are dried inside the glove box for 24 hours.

The ball mill hydration of sample C synthesised is done at w/s = 10 for different time periods. The products obtained are filtered and washed with 50 % - 50 % (v/v) ethanol and water followed by pure ethanol and then analysed by bulk characterization methods and microscopic techniques. Ball mill hydration is carried out in a Retsch cryomill (without the liquid Nitrogen) having a grinding jar of 25 ml volume with a zirconia ball of about 10 mm diameter. After every 99 minutes of milling (at 20 Hz), the mill is stopped for about 15 minutes to prevent it from overheating.

Sample Name	Reactants	Conditions
SHC - 1	Sample C	w/s = 0.5, 45 days static hydration, 25 °C
SHC - 2	Sample C	w/s = 1, 28 days static hydration, 25 °C
SHC - 3	Sample C	w/s = 0.5, 28 days static hydration, 25 °C
SHC - 4	Sample C	w/s = 1, 14 days static hydration, 25 °C
SHC - 5	Sample C	w/s = 0.5, 14 days static hydration, 25 °C
SHC - 6	Sample C	w/s = 1, 7 days static hydration, 25 °C
BHC - 1	Sample C	w/s = 10, 4 days ball mill hydration
BHC - 2	Sample C	w/s = 10, 8 days ball mill hydration
BHC - 3	Sample C	w/s = 10, 16 days ball mill hydration
BHC - 4	Sample C	w/s = 10, 32 days ball mill hydration

Table 4:5 Reactants and experimental conditions for static and ball mill hydration.

4.3 Synthesis of high Ca/Si ratio C-S-H phases by constant lime concentration method

4.3.1 Introduction

To modernize and modify the work done by Grudemo [9] (described in literature review) a special kind of equipment, Syrris automated laboratory reactor is used.

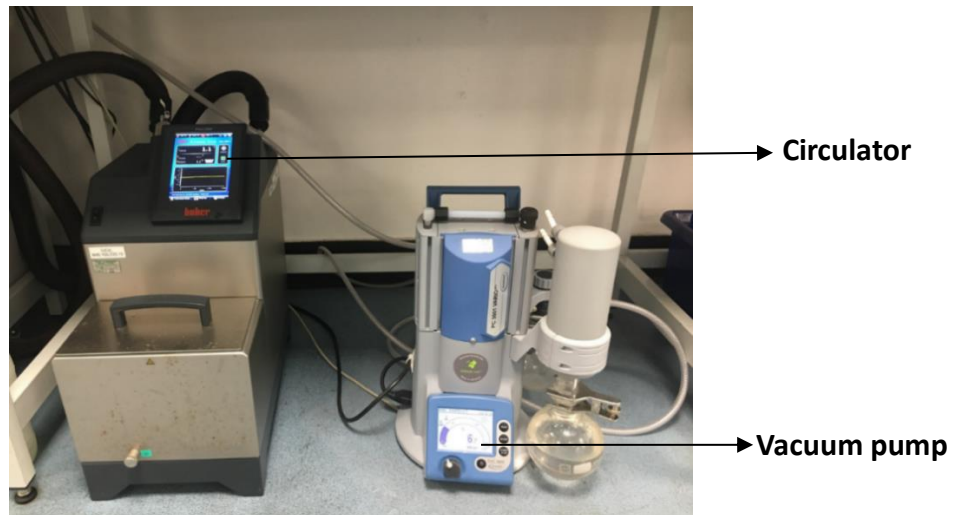
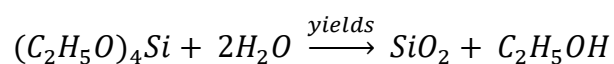


Figure 4.2 Experimental setup showing vacuum pump and circulator.

Figure 4.2 to 4.4 shows the reactor set up. A jacketed vessel (in Figure 4.3) containing a lime solution of known concentration is surrounded by an outer vessel through which thermostat-controlled silicone oil is circulated from the circulator (Figure 4.2) to maintain the desired temperature throughout the reaction. 4% TEOS in ethyl alcohol is added to the solution at a desired rate and silica groups along with ethyl alcohol are formed because of rapid hydrolyzation of TEOS.



C-S-H phases are precipitated by the reaction of silica and lime. This precipitation of C-S-H results in the decrease of Ca^{2+} ion concentration which is compensated by removing water continuously using a vacuum pump (Figure 4.2). The Ca^{2+} ion concentration is continuously monitored by measuring the conductivity of the solution. As it is difficult to measure the concentration continuously during the experiment, conductivity of the experimental solution is measured.

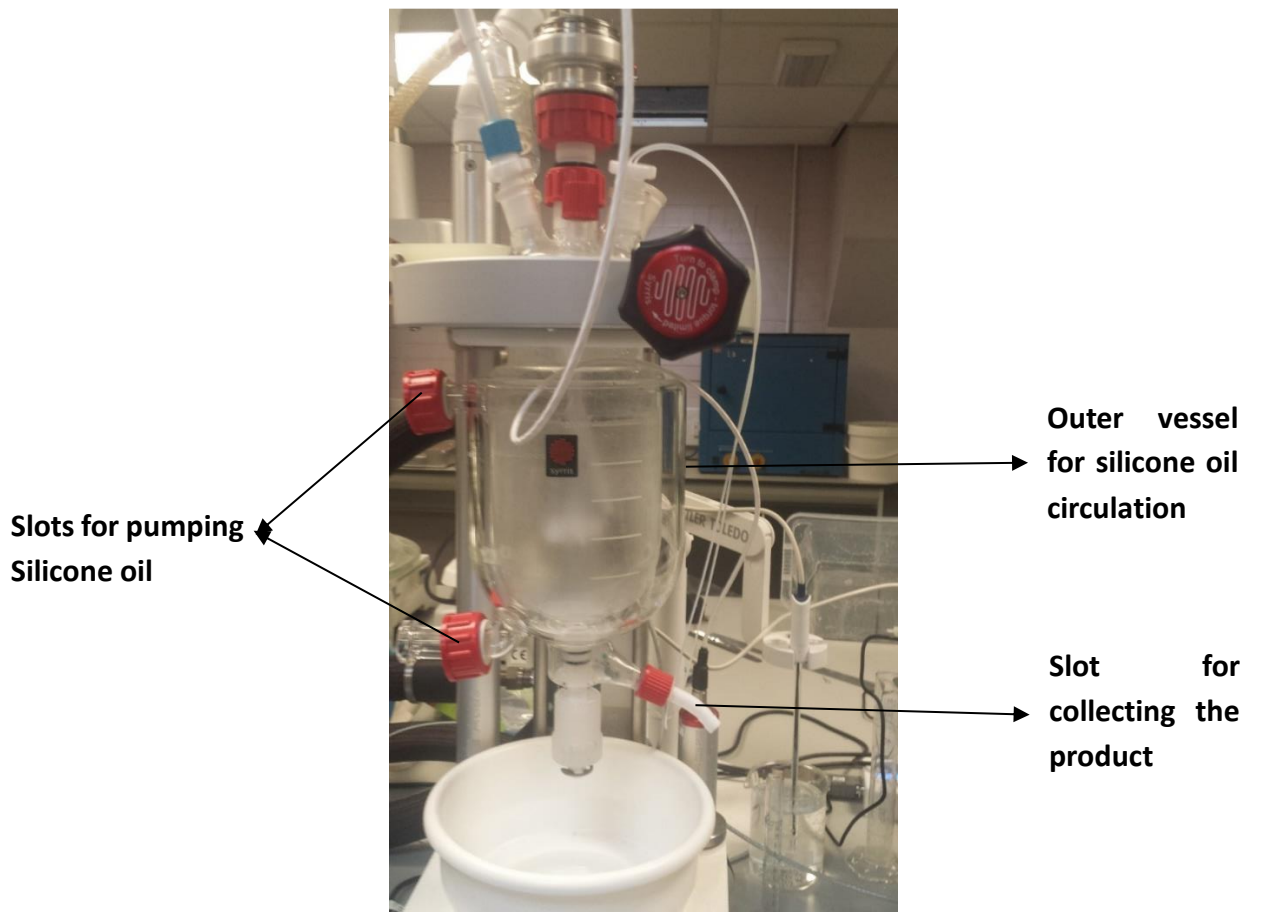


Figure 4.3 Experimental setup showing the reactor.



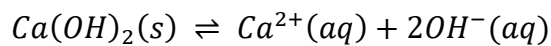
Figure 4.4 Experimental setup showing the lid of the reactor.

At the end of the reaction, the precipitate formed is collected, filtered and washed using 50 % - 50 % (v/v) ethanol and water followed by pure ethanol and then dried inside a glovebox. The precipitate is then analysed to determine the Ca/Si ratio and the filtrate is stored in plastic vials for further analysis.

The main aim of this work is to synthesise C-S-H phases having Ca/Si ratio greater than 1.6, analogous to the C-S-H phases seen in cement pastes.

4.3.2 Experimental Synthesis

Calcium hydroxide (CH) is sparingly soluble in water and an equilibrium is established between the solid and aqueous phases. It is more soluble at lower temperatures than at higher temperatures.



Richardson formulated an equation (shown below) relating to the solubility and temperature based on the data from literature [147]. The data used for the formulation of this equation is taken from Bassett's work [148] where solubilities of CH are measured using large crystals.

The solubility (S) of lime in solution decreases linearly with increasing temperature (T) [147].

$$S = 23.65573 - 0.14507(T) \quad (r^2 = 0.998)$$

Where S is in mmol/L and T is in °C.

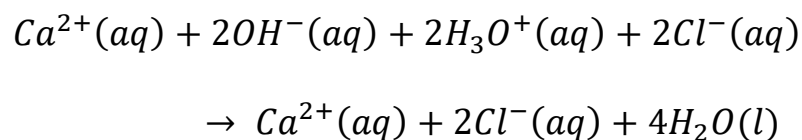
Bassett [148] also reported that higher solubilities can be obtained when very fine crystals are used during the preparation of the stock solution. Solubility up to 25 mmol/L is obtained when fine crystals are used.

$$S = 26.39061 - 0.17164(T)$$

Where S is in mmol/L and T is in °C.

The conductivities and concentrations of CH solutions at seven different temperatures are measured in this work to understand the effect of temperature on the solubility of CH and 98 % extra pure calcium hydroxide from Acros Organics is used for the experiments.

Supersaturated lime solutions are made by stirring an excess amount of CH in Nitrogen sparged - vacuum degassed - deionised water overnight (to remove the potential interference of dissolved CO₂) in an ice bath. Supersaturation is a state of a solution in which more material can be dissolved than could be dissolved under normal circumstances. The stirring is done inside a Nitrogen glovebox in an ice bath to prevent carbonation and increase the solubility of CH in water. The supersaturated lime solutions are filtered using a 13 µm filter paper inside glovebox and clear solutions are obtained. These clear solutions are heated to seven different temperatures: 1 °C, 5 °C, 10 °C, 15 °C, 20 °C, 25 °C and 30 °C inside the glove box. This heating might lead to some precipitation of CH, although it is not visible to the naked eye and the solutions remain clear. The heated solutions are filtered again using a 13 µm filter paper after which conductivities and concentrations are immediately measured. Supersaturated lime solutions are also made directly at seven different temperatures: 1 °C, 5 °C, 10 °C, 15 °C, 20 °C, 25 °C and 30 °C inside the glove box. The solutions are filtered using a 13 µm filter paper after which concentrations are immediately measured. The concentration of lime solutions at different temperatures are measured by acid - base titration using bromothymol blue as an indicator and 0.1 M hydrochloric acid. The concentration of CH is determined from the calculated [OH]⁻.



The conductivities and the corresponding concentration values of lime solution at different temperatures are tabulated in Table 4:6.

The solubility of CH made in an ice bath and then heated to various temperatures is higher compared to the solubility of CH directly made at specific temperatures.

The relation between temperature and solubility is formulated based on the data from this work, tabulated in Table 4:6 (column 2 and 3).

$$S = 26.14463 - 0.19540(T) \quad (r^2 = 0.995)$$

Where S is in mmol/L and T is in °C.

Eight different experiments are conducted using the lime solution prepared in an ice bath and then heated to six different temperatures. Filtration is done inside a glove box. The reaction conditions for all the experiments are described in Table 4:8. Figure 4.5 shows the schematic representation of the experimental set up and the experimental sequence is illustrated in the Figure 4.6.

When CH is added to water, the first step is the dissolution of CH which resulted in an aqueous solution. Thermostat silicone oil from the circulator is circulated through the outer vessel of the jacketed vessel to maintain the desired temperature of the reaction. The solution in the jacketed vessel is continuously stirred at 650 rpm.

A rubber bung with two taps (shown in Figure 4.5) is fitted to the conical flask containing the filtered solution. The jacketed vessel is flushed with N₂ gas for

about 10 minutes before loading the filtrate. Both tap A and tap B are opened where one acts as an inlet for the N₂ gas and the other as an outlet.

Temperature (°C)	Conductivity (mS/cm) (made in an ice bath)	Concentration (mmol/L) (made in an ice bath)	Concentration (mmol/L) (made directly)
30	8.80	20.4	19.5
25	8.88	21.2	20.2
20	9.05	22.2	21.0
15	9.18	23.1	22.1
10	9.31	24.3	23.3
5	9.57	25.0	24.1
1	9.65	26.1	24.9

Table 4:6 Temperatures and the corresponding conductivity and concentration values measured for initial calibrations.

Once the jacketed vessel is flushed with N₂, both taps A and B are closed and then filtrate from the conical flask is loaded into the vessel. Loading is done by connecting the tube with tap A to tap D and tube with tap B to tap E. All the four taps are opened, and the conical flask is lifted and held in a reverse position till all the filtrate is filled in the jacketed vessel. Once the vessel is filled with the filtrate, tap A and tap B are immediately closed and the stirring and circulator are switched on.

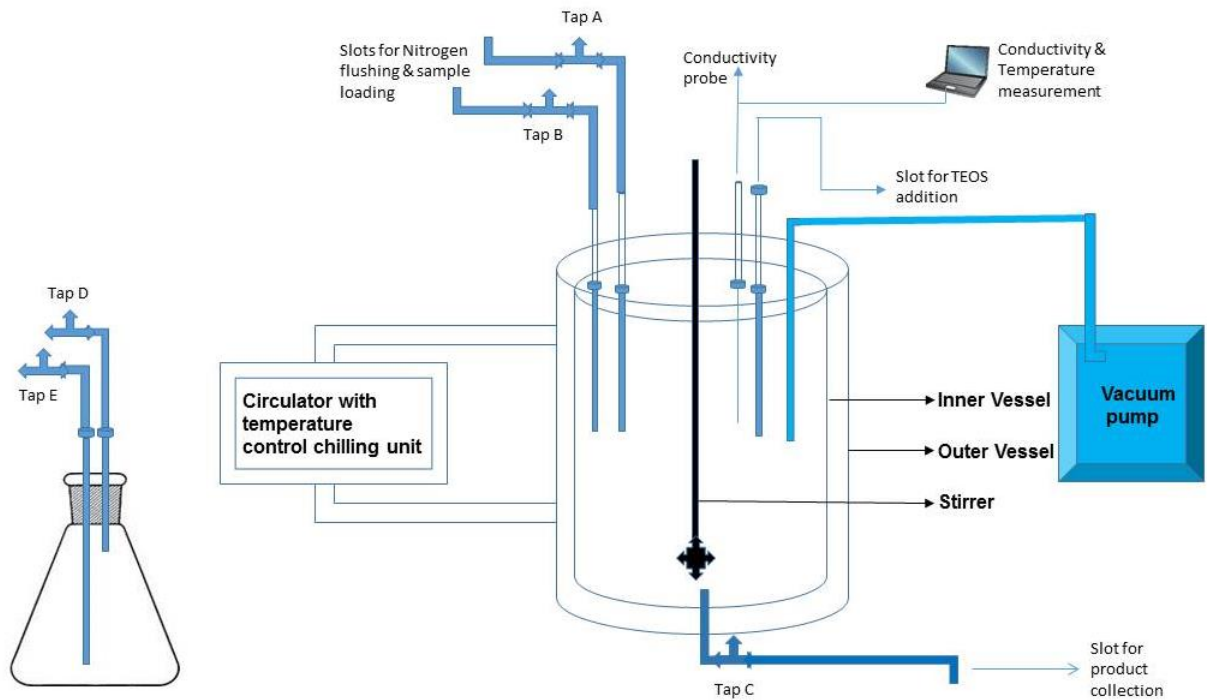


Figure 4.5 Schematic representation of the reaction vessel.

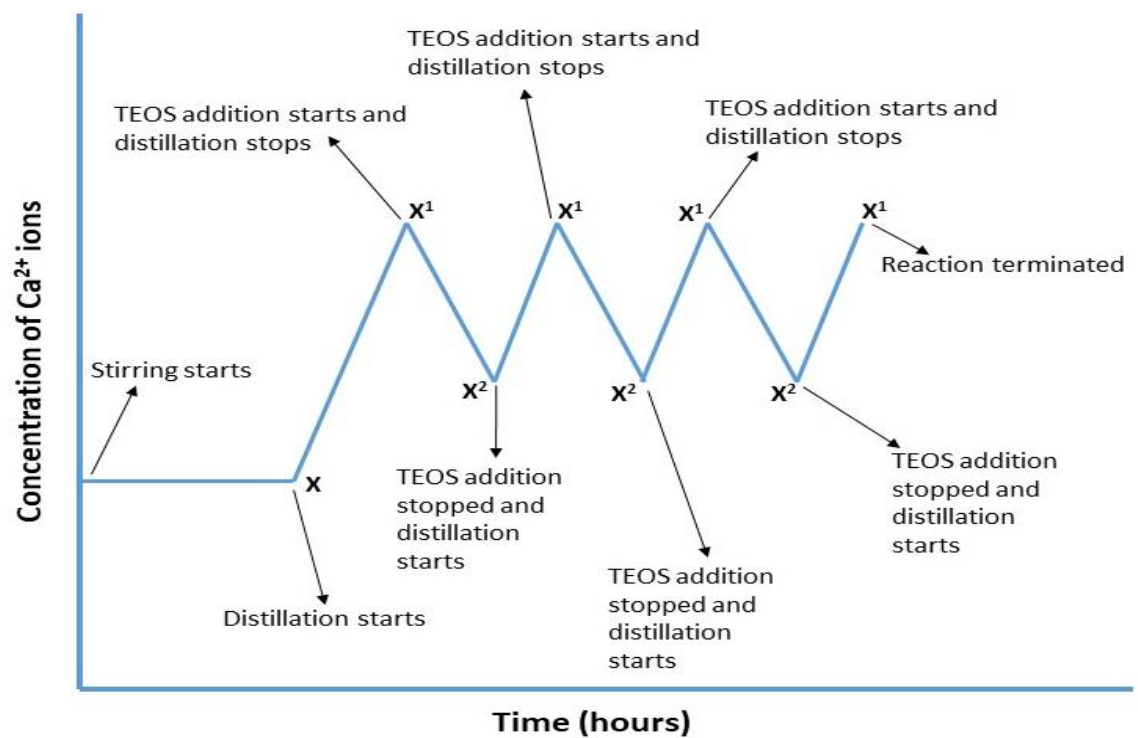


Figure 4.6 Schematic representation of the experiment.

Reaction Temperature (°C)	Initial Conductivity (mS/cm)	Initial Concentration (mmol/L)	Final Conductivity (mS/cm)	Final Concentration (mmol/L)
25	8.90	21.2	9.16	22.0
20	9.01	22.3	9.30	23.1
15	9.18	23.2	9.48	24.1
10	9.36	24.2	9.69	25.2
5	9.54	25.1	9.88	26.1
1	9.68	26.0	9.97	27.0

Table 4:7 Showing the reaction temperatures and the corresponding conductivities and lime concentrations measured.

When the conductivity is constant (X) (Figure 4.6), the process of distillation starts. As the water is continuously removed by the process of distillation by a vacuum pump, the Ca^{2+} ion concentration is increased producing a supersaturated solution, and this is monitored by an increase in the conductivity. Once the conductivity value reaches X^1 , 4 % TEOS in ethanol is added at a desired rate (rate of addition shown in Table 4:8) to the vessel with continuous stirring. Nitrogen gas is continuously flushed through the solution as TEOS is being added to avoid any exposure to air. When silica is added, precipitation of C-S-H starts to happen resulting in the decrease of Ca^{2+} ion concentration. Precipitation relieves supersaturation which is then achieved by vacuum distillation. Table 4:7 shows the initial and final concentrations and conductivities of the lime solution at different temperatures for all the samples synthesized.

Sample Name	Reaction conditions
AR - 1	25 °C, TEOS addition @ 1 ml/min
AR - 2	20 °C, TEOS addition @ 1 ml/min
AR - 3	15 °C, TEOS addition @ 1 ml/min
AR - 4	10 °C, TEOS addition @ 1 ml/min
AR - 5	5 °C, TEOS addition @ 1 ml/min
AR - 6	1 °C, TEOS addition @ 1 ml/min
AR - 7	1 °C, TEOS addition @ 0.5 ml/min
AR - 8	1 °C, TEOS addition @ 0.1 ml/min

Table 4:8 Experimental details and reaction conditions of the C-S-H phases synthesized.

Once the conductivity value reaches X^2 , the TEOS addition is stopped and the vacuum distillation is started. The drop in Ca^{2+} ion concentration is compensated by the removal of water and the supersaturation state is achieved again. This distillation – addition cycle is repeated, and the reaction is terminated when the conductivity probe is no longer submerged in the solution and the liquid level is dropped because of the removal of water. The product is carefully collected in a conical flask with Nitrogen gas being continuously flushed and is filtered and washed inside the glovebox.

C-S-H phases with high Ca/Si ratio are formed as the calcium concentration throughout the synthesis is maintained high and the solution is supersaturated. This results in the precipitation of Ca rich C-S-H phases.

4.4 Leaching and Hydrothermal ageing of synthetic C-S-H gels

Static leaching is done on C-S-H samples synthesized by hydrothermal method (refer section 4.2) and dynamic leaching is done on C-S-H samples synthesized by constant lime concentration method (refer section 4.3). Due to time constraints and the inadequate amount of synthetic C-S-H samples, both the leaching protocols could not be applied on all the C-S-H samples synthesized. Table 4:9 shows the experimental and the sample details of static and dynamic leaching experiments. Nitrogen sparged – vacuum degassed - deionised water is used for both static and dynamic leaching experiments. The target solid/liquid ratio is 1:150. This solid/liquid ratio and equilibration times were chosen in particular to compare the results from this work with that of Harris et al [82]. For static leaching experiments, 0.1 gm of solid is mixed with 15 ml of liquid in plastic tubes inside the glove box and left at about 25 °C for 90 days. The leaching ratio (ratio of volume of leachant to amount of solid taken) is 0.15 m³/kg. After 90 days, the leachates are collected and acidified with ultra-pure nitric acid after which they are stored inside the glove box for further analysis. The nitric acid used is 67-69%, Optima™, for Ultra Trace Elemental Analysis purchased from Fisher. The leached C-S-H samples are collected and dried in the Nitrogen glove box for further characterization.

Sample Name	Reactants (described in Table 4:5 and Table 4:8)	Leaching conditions
SL - 1	SHC - 1	Static leaching – w/s = 150/1
SL - 2	SHC - 2	Static leaching – w/s = 150/1
SL - 3	SHC - 3	Static leaching – w/s = 150/1
SL - 4	SHC - 4	Static leaching – w/s = 150/1
SL - 5	SHC - 5	Static leaching – w/s = 150/1
SL - 6	SHC - 6	Static leaching – w/s = 150/1
SL - 7	BHC - 1	Static leaching – w/s = 150/1
SL - 8	BHC - 2	Static leaching – w/s = 150/1
SL - 9	BHC - 3	Static leaching – w/s = 150/1
DL - 1	AR - 1	Dynamic leaching – w/s = 150/1
DL - 2	AR - 2	Dynamic leaching – w/s = 150/1
DL - 3	AR - 3	Dynamic leaching – w/s = 150/1
DL - 4	AR - 4	Dynamic leaching – w/s = 150/1
DL - 5	AR - 5	Dynamic leaching – w/s = 150/1
DL - 6	AR - 6	Dynamic leaching – w/s = 150/1
DL - 7	AR - 7	Dynamic leaching – w/s = 150/1
DL - 8	AR - 8	Dynamic leaching – w/s = 150/1

Table 4:9 showing the experimental and sample details of static and dynamic leaching experiments.

For dynamic leaching experiments, 0.1 gm of solid is mixed with 15 ml of liquid in plastic tubes inside the glove box and left at about 25 °C. The leaching ratio is 0.15 m³/kg. After 30 days, 12.5 ml of supernatant leachate is decanted, and the container is replaced with an equal volume of Nitrogen sparged – vacuum degassed – deionised water. The leachates collected are acidified using ultra-pure nitric acid after which they are stored in the Nitrogen glove box for further analysis. Two replacements with Nitrogen – sparged – vacuum degassed – deionised water is done and at the end the leached C-S-H samples are collected and dried in the glove box for further characterization. The total volume of the decanted leachate is 40 ml and the cumulative degree of leaching (ratio of total volume of leachate to amount of solid taken) is 0.40 m³/kg.

Hydrothermal ageing is done on C-S-H sample: SHC – 2 (described in Table 4:5). The solid/liquid is 1:50 and the ageing is performed at 80 °C for 6 months in an acid digestion vessel (described in section 4.2) inside an oven. 1 gm of solid is mixed with 50 ml of Nitrogen sparged – vacuum degassed – deionised water in the PTFE cup inside the glove box. The acid digestion vessel is screwed tightly and then placed in an oven. The product collected at the end is filtered and dried inside the glove box.

Chapter 5 Results and discussion of NRVB samples (described in Table 4:2, Experimental Methods)

5.1 TEM - EDX

The TEM micrographs of all the samples are shown in Figures 5.1 – 5.4. The most striking difference between the untreated and aged samples is the morphology. The C-A-S-H phase in S1 and S2 shown in Figure 5.1 and Figure 5.2 has a fine fibrillar morphology whereas the C-A-S-H phase in S3 and S4 shown in Figure 5.3 and Figure 5.4 has a crumpled foil-like morphology. These morphologies are consistent with the Ca/Si ratios measured by EDX analysis tabulated in Table 5:1.

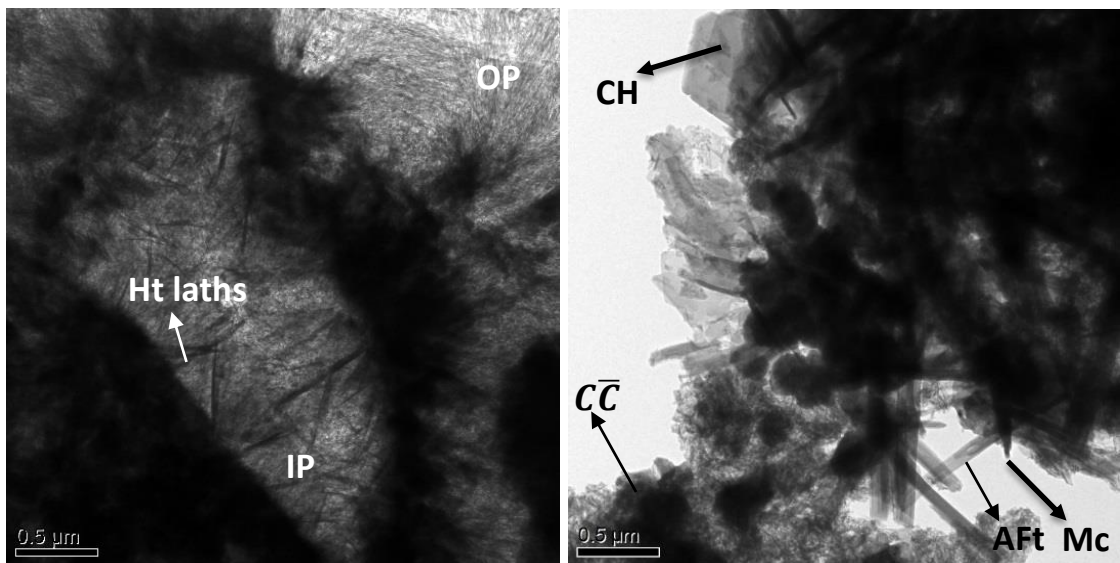


Figure 5.1 TEM micrographs showing different phases present in S1.

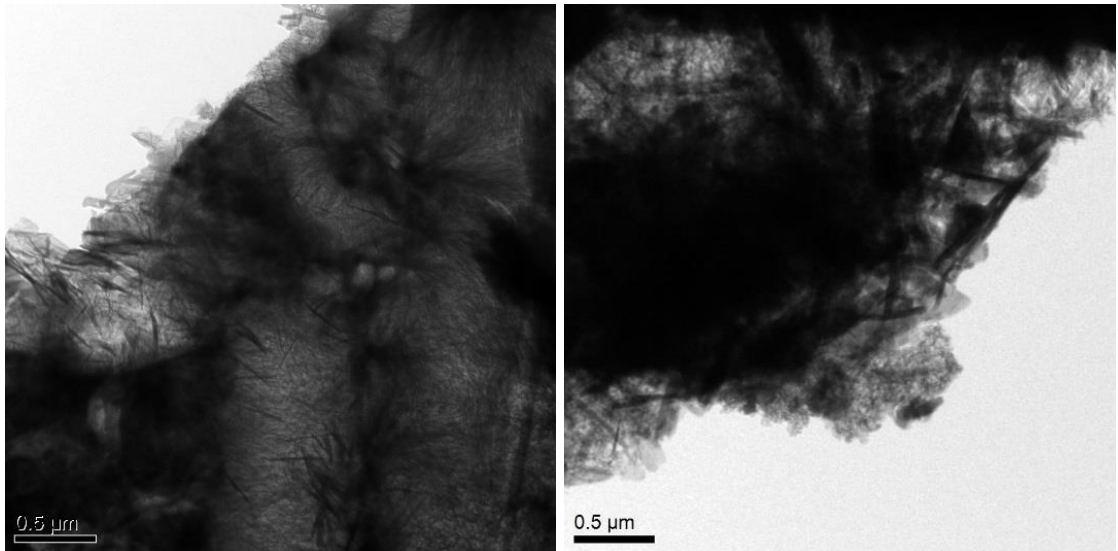


Figure 5.2 TEM micrographs showing different phases present in S2.

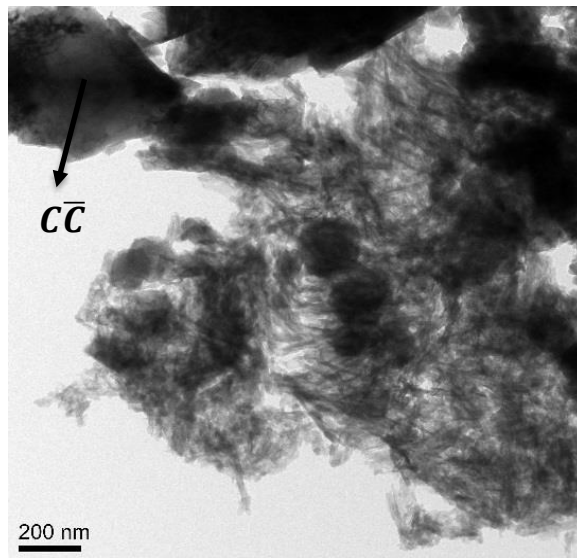


Figure 5.3 TEM micrographs showing different phases present in S3.

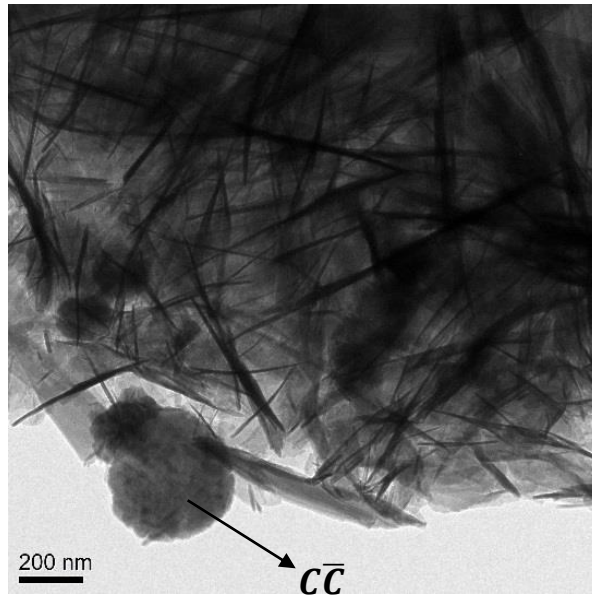


Figure 5.4 TEM micrographs showing different phases present in S4.

All four samples show the presence of microcrystalline CC intermixed with C-A-S-H phase. The untreated samples S1 and S2 also show the presence of CH, Mc, AFt and Ht laths intermixed with C-A-S-H. The source of Mg and Al (presence of Mg and Al was confirmed from EDX data) for formation of Ht could possibly be the clinker material. However, these phases are absent in the aged samples S3 and S4 indicating that these phases have been removed by the process of leaching and hydrothermal ageing. In Figure 5.1, the TEM micrograph clearly shows two phases: Op C-A-S-H and Ip C-A-S-H. The inner product C-A-S-H is intermixed with Ht laths and shows regions with homogeneous fine scale morphology while the outer product shows both coarse and fine fibrillar C-A-S-H [17]. These observations agree with the XRD data and STA traces discussed later.

The mean Ca/Si ratios and Al/Si ratios obtained by TEM – EDX are plotted as atomic ratio plots and these results are compared in Table 5:1. It is made sure that C-A-S-H regions for EDX analysis are free from intermixing with other

crystalline phases by selected area diffraction (SAED). The mean Ca/Si ratio of C-A-S-H phase in S1 and S2 samples is high, 1.92 and 1.88 respectively. These high Ca/Si ratios are consistent with the fibrillar morphology seen in the untreated samples. The Ca/Si ratio of C-A-S-H phase in S3 and S4 samples is much lower, 1.08 and 1.11 respectively. These comparatively lower Ca/Si ratios are consistent with the crumpled foil-like morphology seen in the aged samples.

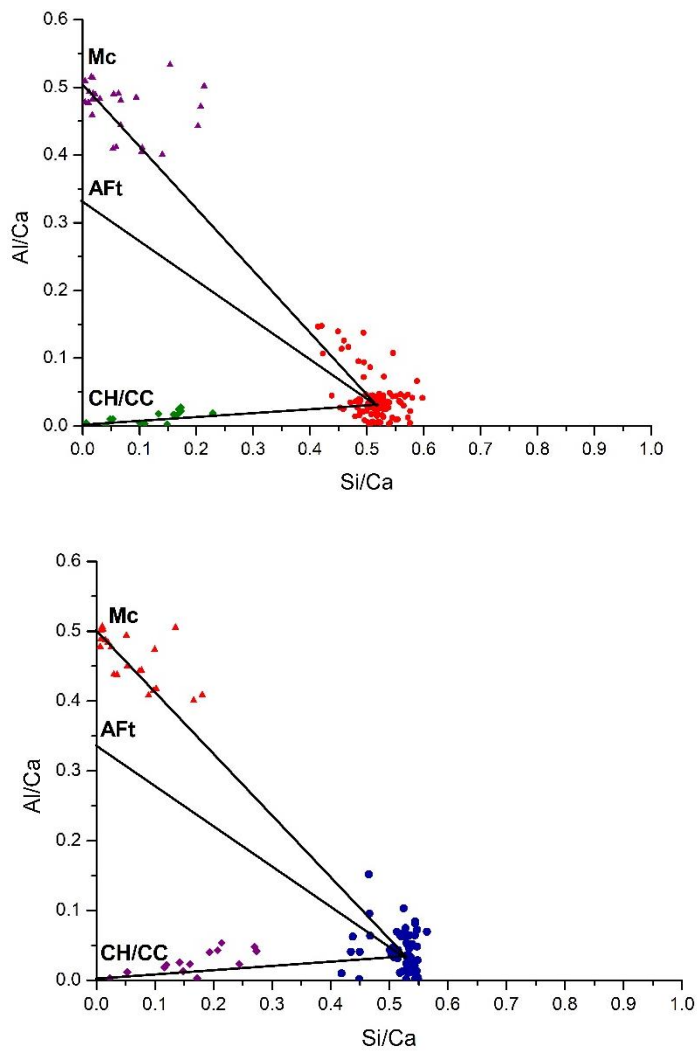


Figure 5.5 Atomic ratio plots for S1 (top) and S2 (bottom).

Lower Ca/Si ratios in both S3 and S4 (Figure 5.6) confirmed the decalcification of the C-A-S-H phase by the process of leaching. Few areas in S3 and S4 with very low Ca/Si ratios are excluded in calculating the mean ratios for the C-A-S-H

phase as they are considered to correspond to the low Ca aluminosilicate gel detected by NMR (discussed in the next section).

The Al/Si ratios (measured from EDX) are 0.05, 0.07, 0.09 and 0.13 respectively for S1, S2, S3 and S4 and these ratios are similar to those obtained from deconvolution of NMR spectra discussed later. There is not much variation in Al/Si ratios between the untreated and aged samples.

The EDX analysis and the atomic ratio plots for the untreated samples S1 and S2 are shown in Figure 5.5. A clear trend line is seen corresponding to CH and $C\bar{C}$ confirming the presence of both the phases intermixed with Op and Ip C-A-S-H. A trend line towards Mc is also seen. However, there are no data points corresponding to the trend lines for AFt. This is because AFt being highly beam sensitive, readily decomposes under the electron beam making it difficult to work under high magnification and collect EDX data [149].

The EDX analysis and the atomic ratio plots for the aged samples S3 and S4 are shown in Figure 5.6. Although the atomic ratio plots show the presence of other phases, these points were excluded while measuring the Ca/Si ratios. A clear trend line is seen corresponding to $C\bar{C}$ confirming the presence of microcrystalline $C\bar{C}$ intermixed with Op and Ip C-A-S-H.

A trend line towards Mc cannot be seen as it is removed by the process of leaching. Although there is AFt present, there are no data points corresponding to the trend lines for AFt. This analysis confirmed the presence of Mc phase and intermixing of pure calcium phases, $C\bar{C}$ and CH in S1 and S2 and $C\bar{C}$ in S3 and S4.

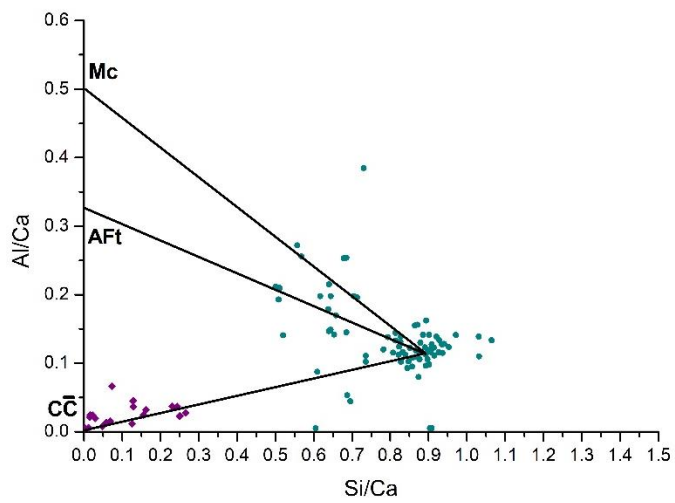
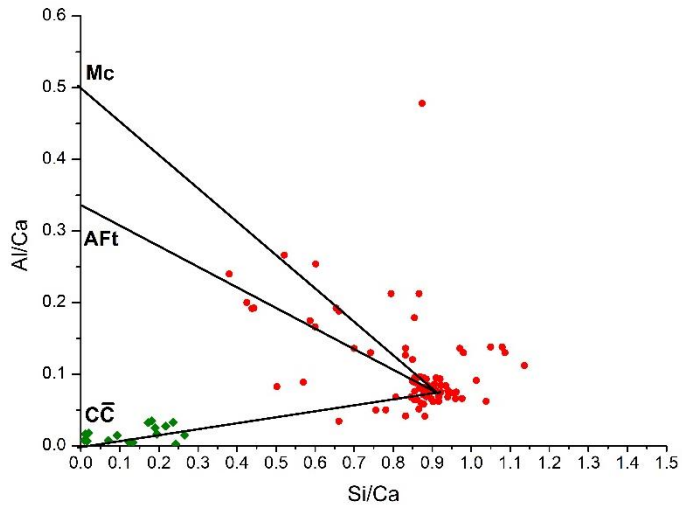


Figure 5.6 Atomic ratio plots for S3 (top) and S4 (bottom).

Sample	N*	Ca/Si	S.D.	Al/Si	S.D.
S1	81	1.92	0.09	0.05	0.03
S2	76	1.88	0.05	0.07	0.04
S3	75	1.08	0.16	0.09	0.04
S4	73	1.11	0.12	0.13	0.03

N* denotes number of analyses.

Table 5:1 Ca/Si ratios of C-A-S-H phase obtained by TEM – EDX.

5.2 ^{29}Si NMR

The deconvoluted ^{29}Si NMR spectra for all the NRVB samples are shown in Figures 5.7 – 5.10 and information regarding the structure of C-A-S-H phase is obtained. The peaks corresponding to the fraction of silicon sites present in various tetrahedral environments are fitted to produce a simulated spectrum. The experimental spectra, the individual frequencies and the simulated spectra, are all shown in the Figures below. While Q^0 (- 71 ppm) corresponds to the isolated tetrahedra present in alite and belite, Q^1 (- 79 ppm), Q^2 (- 85 ppm) and $\text{Q}^{21}(\text{Al})$ (- 82 ppm) correspond to end chain groups, middle chain groups and middle chain groups with one adjacent tetrahedra occupied by aluminium respectively [40][110][115][129]. Broad resonances like Q^3 (- 97 ppm), $\text{Q}^{31}(\text{Al})$ (- 92 ppm) and Q^4 (- 105 ppm) correspond to chain branching sites and three-dimensional network. The fraction of silicon sites present is shown in Table 5:2. Mean aluminosilicate chain length and Al/Si ratios are determined by the equations described in section 3.3 (Characterization Techniques) [124]. While the incorporation of aluminium remained almost constant, the mean chain length increased with the process of ageing. This increase in MCL with age is in agreement with the other studies [108][150].

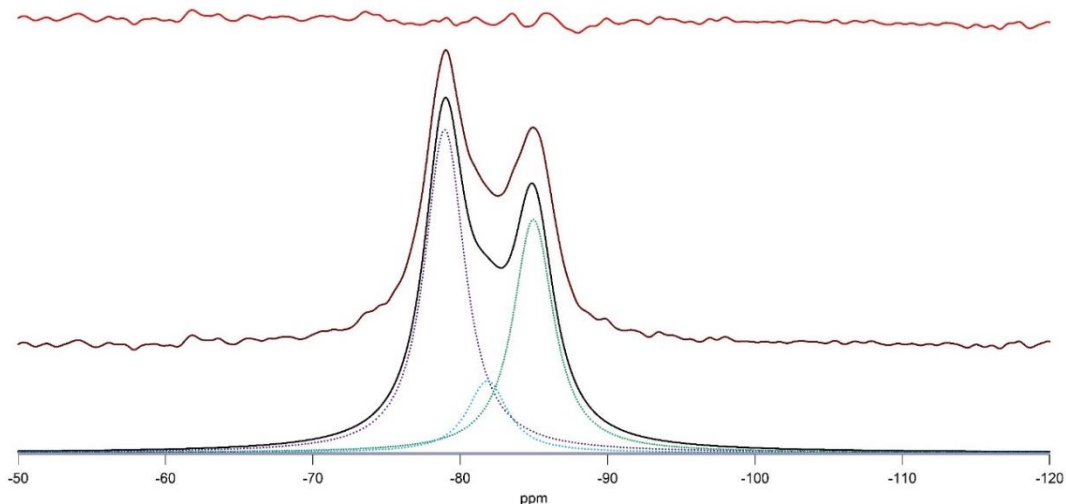


Figure 5.7 ^{29}Si NMR spectra of S1 including experimental spectrum (middle, brown), residual (top, red x1) and the individual frequencies.

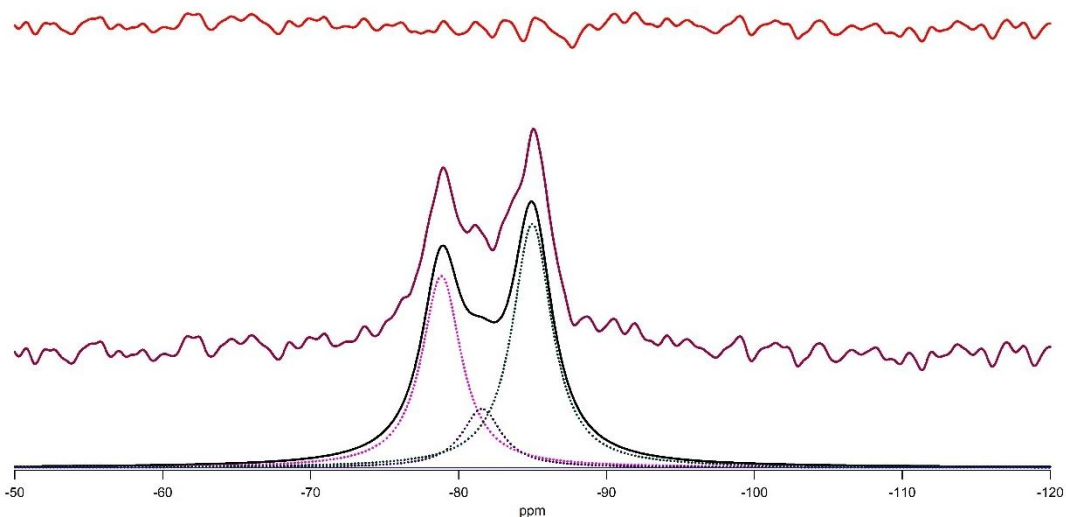


Figure 5.8 ^{29}Si NMR spectra of S2 including experimental spectrum (middle, brown), residual (top, red x1) and the individual frequencies.

Both the spectra in Figures 5.7 and 5.8 show peaks at $\delta = -79$ ppm and $\delta = -85$ ppm corresponding to Q^1 and Q^2 groups. In addition, there is a peak at $\delta = -82$ ppm due to $Q^2(1Al)$ indicating the incorporation of Al in the C-A-S-H phase. Slight increase in the intensity of Q^2 peak is observed in the S2 sample. This

transformation of Q¹ silicate species to Q² sites in S2 indicates the increased level of polymerisation of the silicate chains with time.

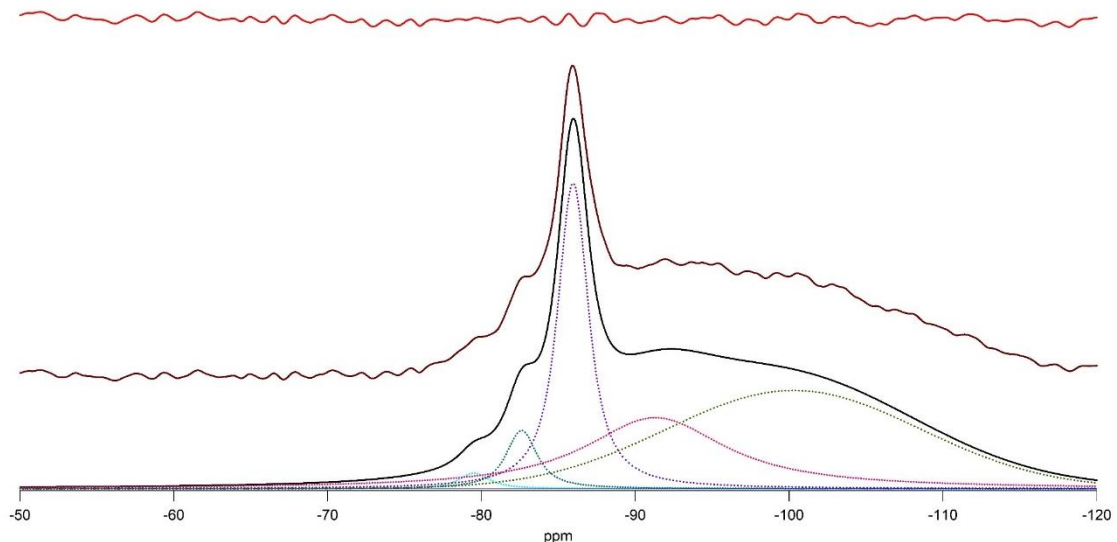


Figure 5.9 ²⁹Si NMR spectra of S3 including experimental spectrum (middle, brown), residual (top, red x1) and the individual frequencies.

The ²⁹Si NMR spectrum for the S3 sample is shown in the Figure 5.9. Besides Q¹, Q² and Q²(1Al) silicate sites the spectrum also shows two other peaks at $\delta = -97$ ppm and $\delta = -105$ ppm corresponding to Q³ and Q⁴ sites respectively. Removal of Ca from the main layers by the process of leaching resulted in the partial destruction of C-A-S-H phase and formation of a low Ca aluminosilicate gel (containing low amounts of Ca) denoted by the presence of Q³ silicate tetrahedra indicating that crosslinking has occurred across the interlayers. The formation of Q⁴ silicate tetrahedra is an indication of a fully decalcified C-A-S-H phase which transforms to an amorphous hydrated silica phase. As Q³ species decompose further, they condense to form Q⁴ species. The presence of Q¹ to Q⁴ in S3 after leaching suggests that the sample is not homogeneous. This possibly could be due to the implementation of leaching protocol on the NRVB blocks.

When the blocks are placed in water, the surface layer degrades more than the core but when sampling is done for the bulk analysis like NMR, both surface and core layers can be present resulting in a spectrum with different silicate species.

The ^{29}Si NMR spectrum for the S4 sample is shown in the Figure 5.10. There is a peak at $\delta = -92$ ppm apart from Q^1 , Q^2 , $\text{Q}^2(1\text{Al})$ and Q^4 corresponding to the presence of $\text{Q}^3(1\text{Al})$ indicating that at least some of the aluminosilicate chains are cross linked. This spectrum is a typical of a tobermorite like C-A-S-H (I) phase.

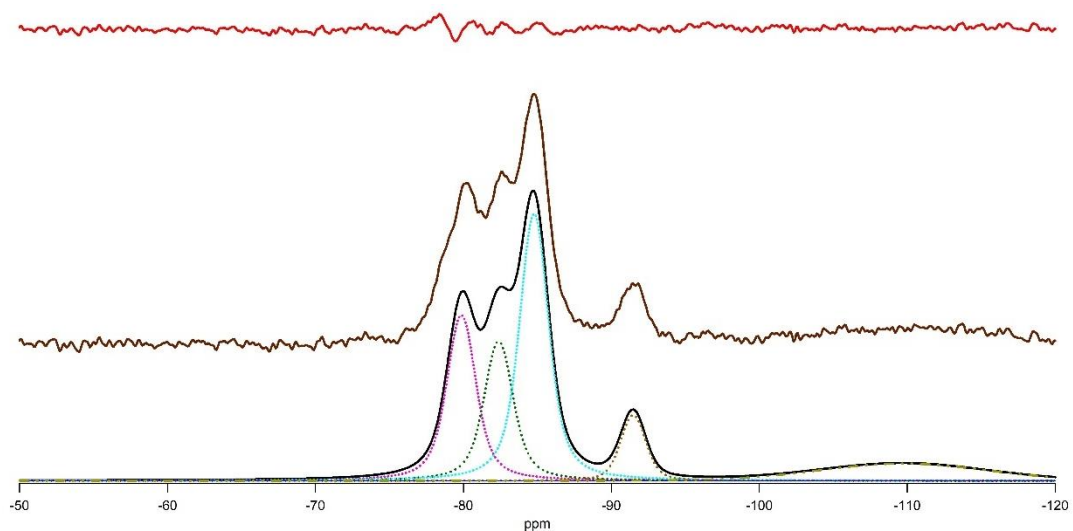


Figure 5.10 ^{29}Si NMR spectra of S4 including experimental spectrum (middle, brown), residual (top, red x1) and the individual frequencies.

It shows that the low Ca aluminosilicate gel that is formed upon leaching of C-A-S-H phase is partly consumed upon subsequent hydrothermal treatment and results in the formation of semi-crystalline C-A-S-H (I) phase [151].

5.3 ^{27}Al NMR

Incorporation of Al in C-A-S-H phase is confirmed from ^{27}Al NMR. Figures 5.11 and 5.12 shows the ^{27}Al spectra of all the NRVB samples. All the four spectra

show a peak between $\delta = 70$ ppm and $\delta = 50$ ppm which corresponds to aluminium in tetrahedra coordination, Al^{IV}.

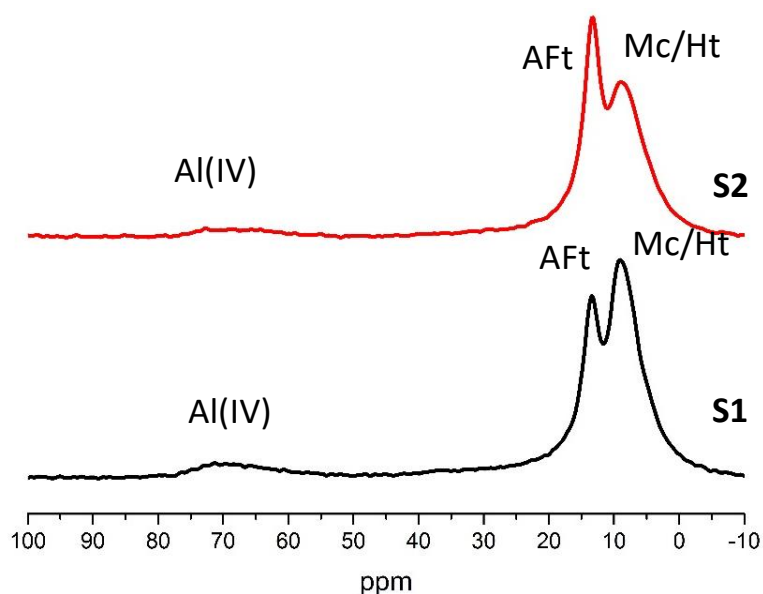


Figure 5.11 ²⁷Al NMR spectra of S1 and S2.

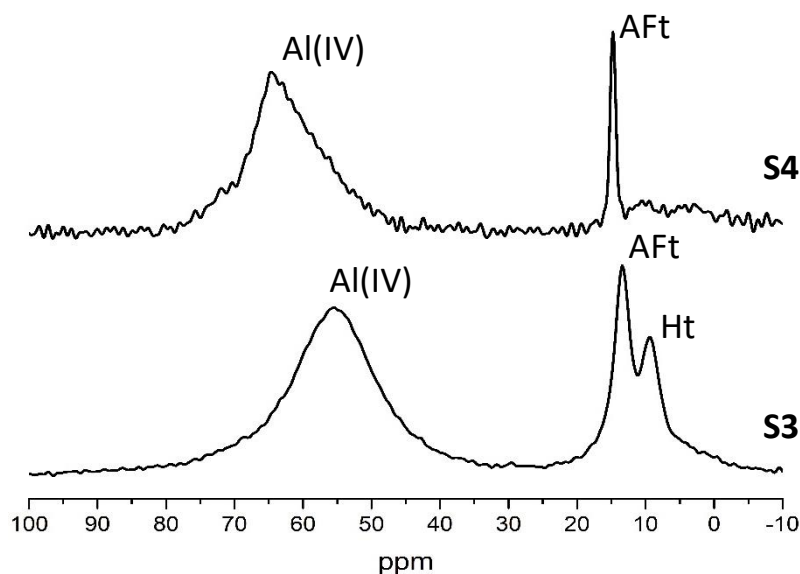


Figure 5.12 ²⁷Al NMR spectra of S3 and S4.

The drift in chemical shift of Al(IV) possibly could be due to the implementation of leaching protocol on the NRVB blocks. When the blocks are placed in water, the surface layer leaches more than the core and when sampling is done for the bulk

analysis like NMR, both surface and core layers can be present resulting in a spectrum with varied chemical shifts. The peaks at $\delta = 13$ ppm and $\delta = 9$ ppm correspond to AFt and Ht/Mc [120]. The broad peak at $\delta = 9$ ppm in Figure 5.12 corresponds to Ht in S3 as Mc phase is removed by the process of leaching and in S4 there is no peak at $\delta = 9$ ppm as the Ht phase is removed by the process of hydrothermal ageing. These results are consistent with the XRD results discussed later. The Al/Si ratios obtained from the deconvolution of the spectra are 0.06, 0.06, 0.08 and 0.12 respectively for S1, S2, S3 and S4.

Sample	Q ¹	Q ²	Q ² (1Al)	Q ^{3*}	Q ⁴	MCL [#]
S1	51.4	37.1	11.4	-	-	4.1
S2	38.8	49.3	11.9	-	-	5.5
S3	1.2	23.8	4.5	25.9	44.6	52.9
S4	23.5	37.9	19.8	7.5	11.3	8.4

* Q³(1Al) for S4

excluding Q³ and Q⁴ for S3 and S4

Table 5:2 Results of deconvolution of ²⁹Si NMR showing % silicate species and MCL.

5.4 STA

The STA data for all the samples shown in Figures 5.13 – 5.16 shows mass loss at 110 °C and 800 °C due to the decomposition of AFt and \overline{CC} respectively. The decomposition of C-A-S-H phase is indicated by the broad peak at 110 °C. In the untreated samples; S1 and S2 there is an additional shoulder for the broad peak at 170 °C attributed to the decomposition of carbonate - containing AFm,

monocarboaluminate (Mc) [152]. The additional mass loss at 450 °C corresponds to the dehydration of CH. A small peak on the trace of leached NRVB (S3) at about 400 °C is attributed to HG.

The peaks for the decomposition of CH and Mc are not present in S3 and S4, indicating that these phases are removed by the process of leaching.

The presence of Mc phase in S1 and S2 is obvious because it is known to be relatively stable and it exists in the presence of $C\bar{C}$ [153][154][155][156]. According to Damidot et al. the availability of carbonate phase initially results in the formation of hemicarboaluminate (Hc) and then Mc [155]. However Hc phase is not identified and these results are in agreement with the findings of Matschei et al. which state that AFt, Mc, $C\bar{C}$ and CH are the important stable phases in limestone blended cements [156].

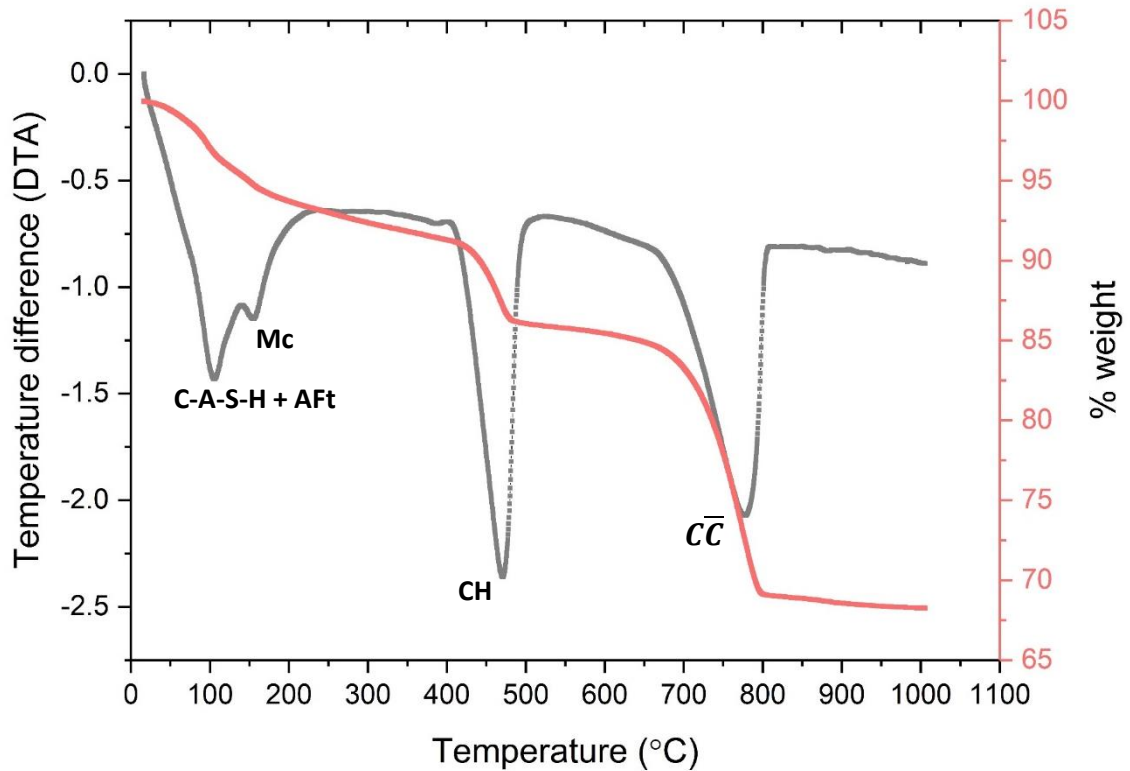


Figure 5.13 STA trace of S1 showing DTA in grey and % TG in red.

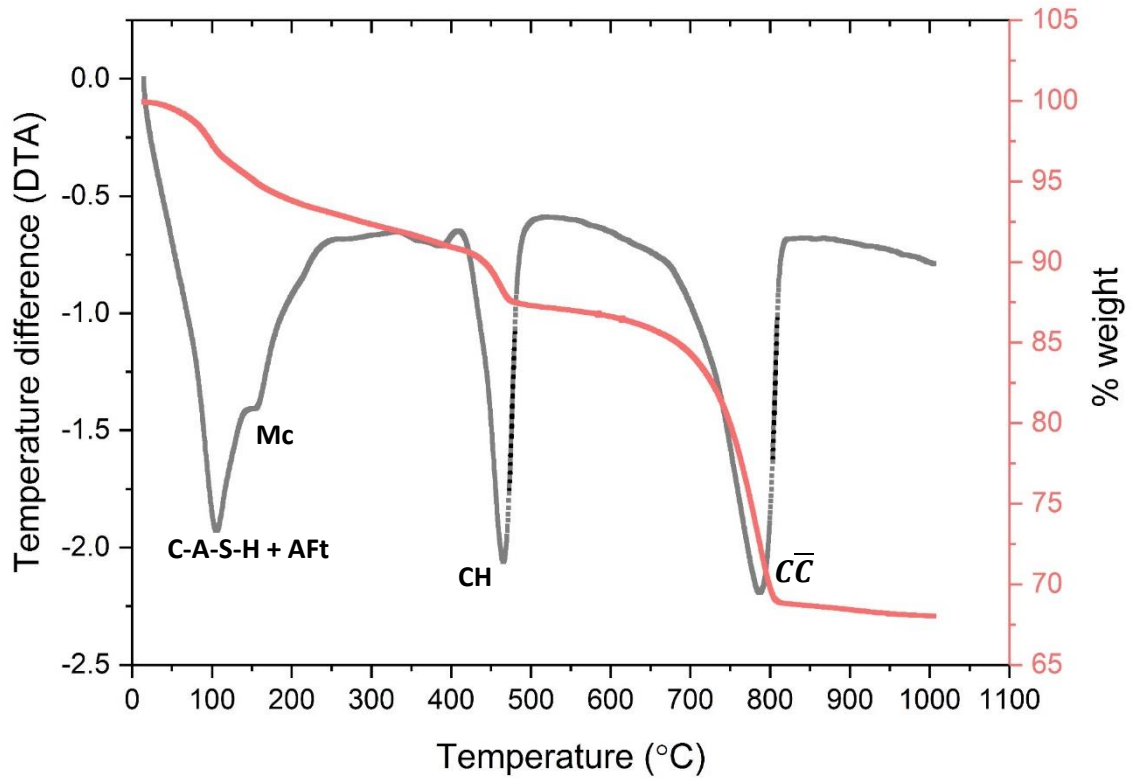


Figure 5.14 STA trace of S2 showing DTA in grey and % TG in red.

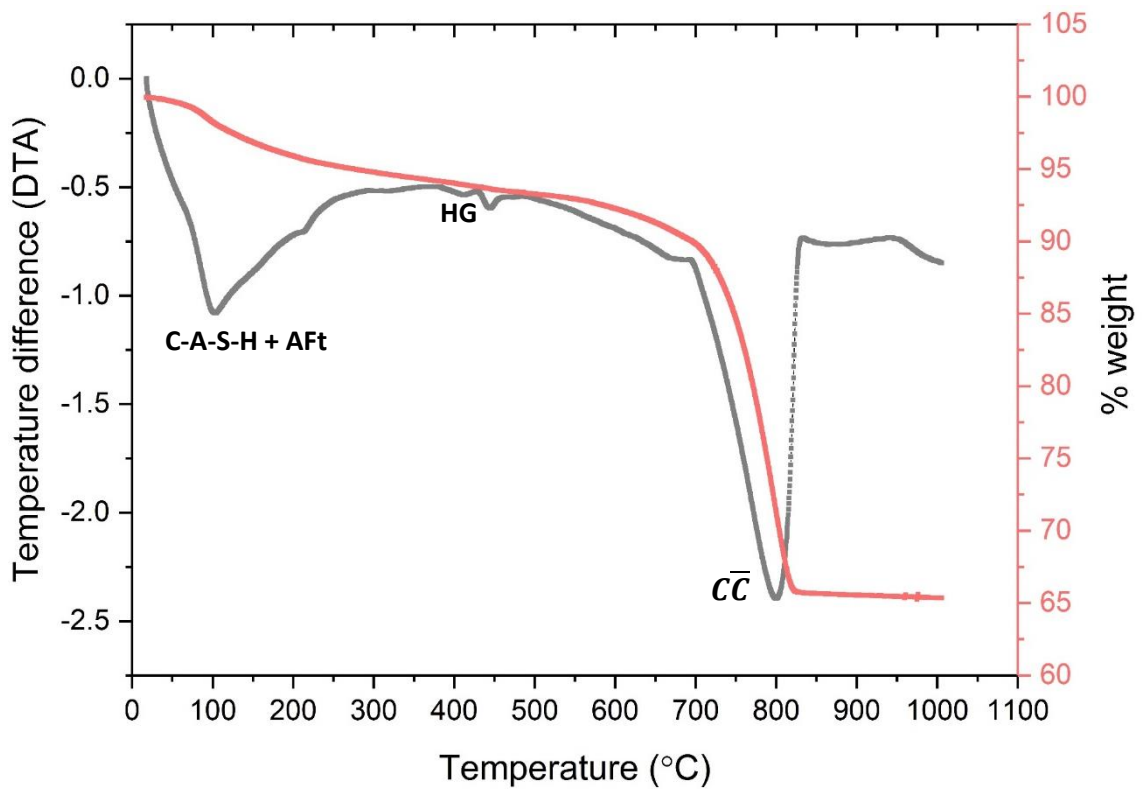


Figure 5.15 STA trace of S3 showing DTA in grey and % TG in red.

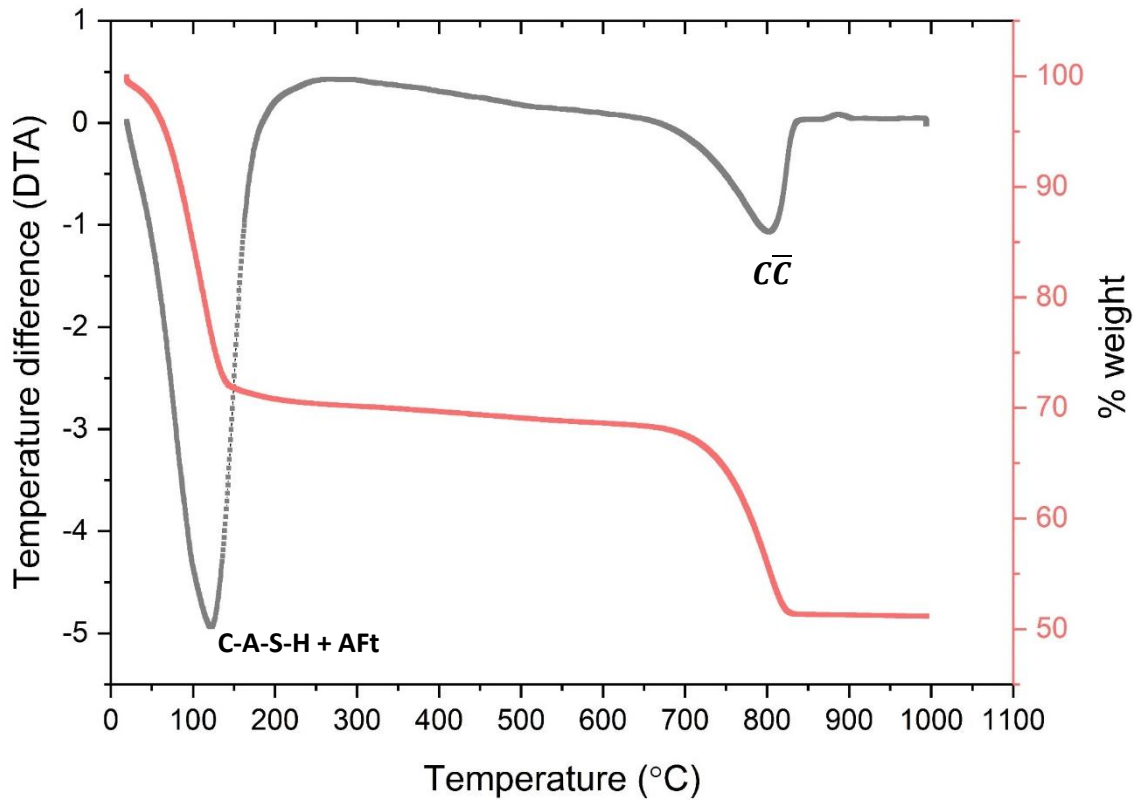


Figure 5.16 STA trace of S4 showing DTA in grey and % TG in red.

Sample	%CH _{res}	% $\overline{C\bar{C}}$ _{res}
S1	24.17	26.67
S2	11.91	29.64
S3	-	59.89
S4	-	75.53

Table 5:3 % CH and % $\overline{C\bar{C}}$ in the NRVB samples.

The calculated amounts of CH and $\overline{C\bar{C}}$ in all the NRVB samples using tangent method are shown in Table 5:3. The calculated $\overline{C\bar{C}}$ amounts in all the NRVB samples increased from an original composition of 27% wt limestone flour. The

amount of $\overline{C\overline{C}}$ in the aged samples S3 and S4 greatly increased when compared to the untreated samples S1 and S2.

5.5 XRD

The XRD patterns for all the NRVB samples are shown in Figures 5.17 and 5.18. These results agree with the STA traces discussed before. The patterns for the untreated samples; S1 and S2 show $\overline{C\overline{C}}$ to be the dominant phase along with a small amount of CH. Minor quantities of AFt, Mc and Ht phases are also evident. The patterns for S3 and S4 samples are also dominated by $\overline{C\overline{C}}$ with a minor quantity of AFt present. The pattern for S3 also includes small amounts of Ht but CH and Mc are removed by the process of leaching. The pattern for S4 shows a basal peak at about 12 Å which indicates the presence of C-A-S-H (I) phase. However, Ht phase is removed by the process of leaching followed by hydrothermal ageing. The peak at $2\theta = 9.1^\circ$ corresponding to AFt explains that the stability of Mc indirectly stabilises AFt in the presence of limestone and hence carbonate form is stable than the sulfate form [152]. The major difference between S3 and S4 is the absence of Ht phase in S4. The relatively low solubility of Ht at neutral pH values is the reason for precipitation of Ht phase and hence it is not removed by the process of leaching but is removed by hydrothermal ageing. The presence of basal peak seen in the XRD trace of S4 is at 2θ equals to 7° . According to the Bragg's law (described in literature review):

$$n\lambda = 2d\sin\theta$$

Where, $n = 1$; $\lambda = 1.5418 \text{ \AA}$; $\theta = 3.5^\circ$

The value of d is calculated to be 12.62 Å. This interlayer distance of about 12 Å is consistent which indicates the presence of a double chain structure.

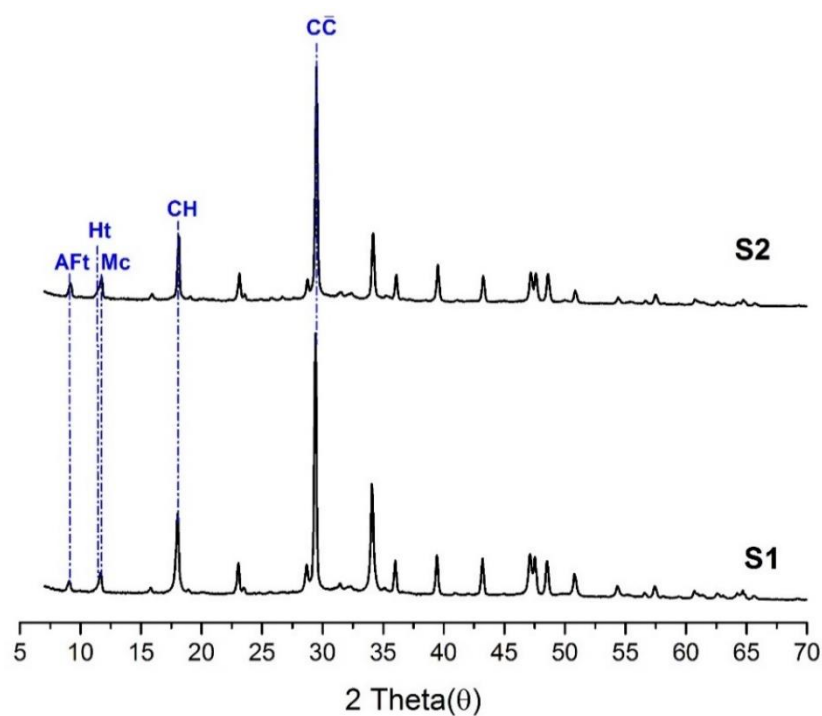


Figure 5.17 XRD traces for S1 and S2.

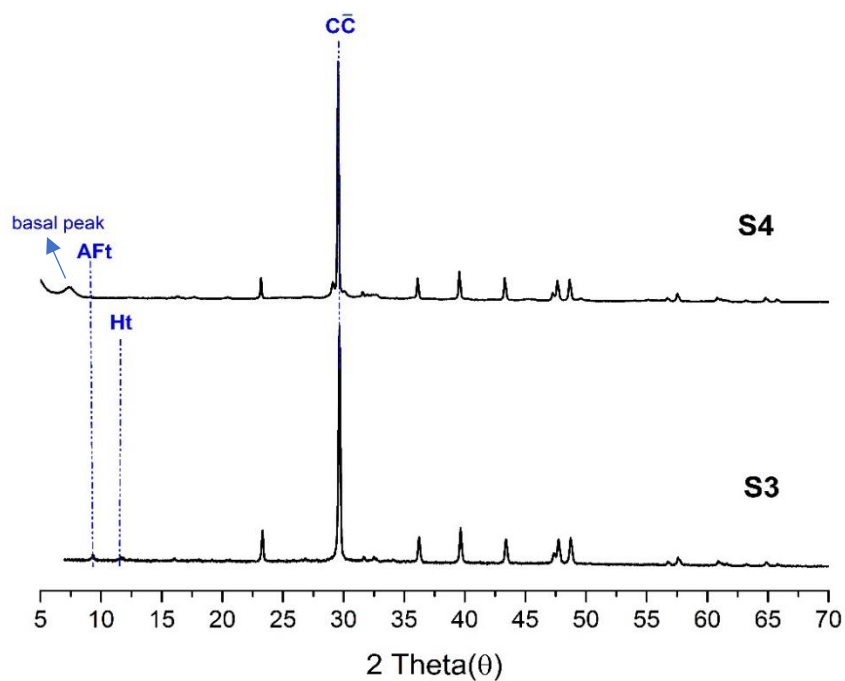
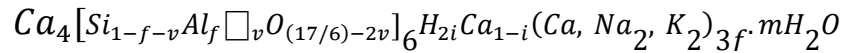


Figure 5.18 XRD traces for S3 and S4.

5.6 Structural chemical formula for C-A-S-H(I) in S4

A structural-chemical formula for the C-A-S-H(I) present in hydrothermally aged NRVB sample is calculated.

The formula for the double chain tobermorite or cross linked C-A-S-H phases is given below [45].



The aluminosilicate part of the structure is contained within the square brackets and the round brackets contain additional interlayer ions needed to charge balance the Al^{3+} substitution for Si^{4+} . The square symbol represents the vacant tetrahedral sites and f and v respectively represent fraction of tetrahedral sites occupied by Al and fraction of tetrahedral sites that are vacant. There are 4 main layer Ca atoms for every 6 tetrahedral sites and i represents the extent of net charge balance by protons or Ca^{2+} ions. There are no silanol groups and no alkali ions are necessary to charge balance the substitution of Al^{3+} and Si^{4+} .

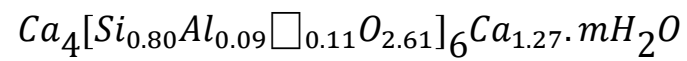
$$V = \frac{1/2Q^1}{3/2Q^1 + Q^2 + 3/2Q^2(1Al) + Q^3 + Q^3(1Al)}$$

$$f = \frac{1/2Q^2(1Al)}{3/2Q^1 + Q^2 + 3/2Q^2(1Al) + Q^3 + Q^3(1Al)}$$

$$Al/Si = \frac{f}{1-f-v}$$

$$MCL = \frac{1-v}{v}$$

The values of the above-mentioned variables are calculated using the data obtained from NMR experiment.



The structural-chemical formula for the C-A-S-H(I) has a Ca/Si of 1.10, Al/Si is 0.11 and the MCL is 8.1, which are close to the values determined by NMR and TEM – EDX experiments.

Chapter 6 Results and discussion of static and ball mill

hydration of β -C₂S

6.1 Characterization results of sample A and sample C (described in Table 4:4, Experimental Methods)

6.1.1 TEM – EDX

The TEM micrographs of Sample A are shown in Figure 6.1. The top left micrograph shows non transparent chunky rod shaped particles corresponding to the presence of scawtite phase and these resemble the microstructures from literature [157]. The middle left micrograph shows lath-like crystals with spreading ends and this corresponds to hillebrandite. These are in agreement with the reported micrographs of hillebrandite in literature [7]. The bottom left micrograph shows crystals with foil-like projections corresponding to the presence of jaffeite. The right images show the corresponding SAED patterns with spots/dots confirming the presence of crystalline phases.

Phase	Ca/Si	S.D	N*
Scawtite	1.13	0.04	25
Hillebrandite	1.97	0.05	35
Jaffeite	2.98	0.04	24

N* is the number of analyses

Table 6:1 TEM - EDX results showing mean Ca/Si ratios for different phases present in sample A.

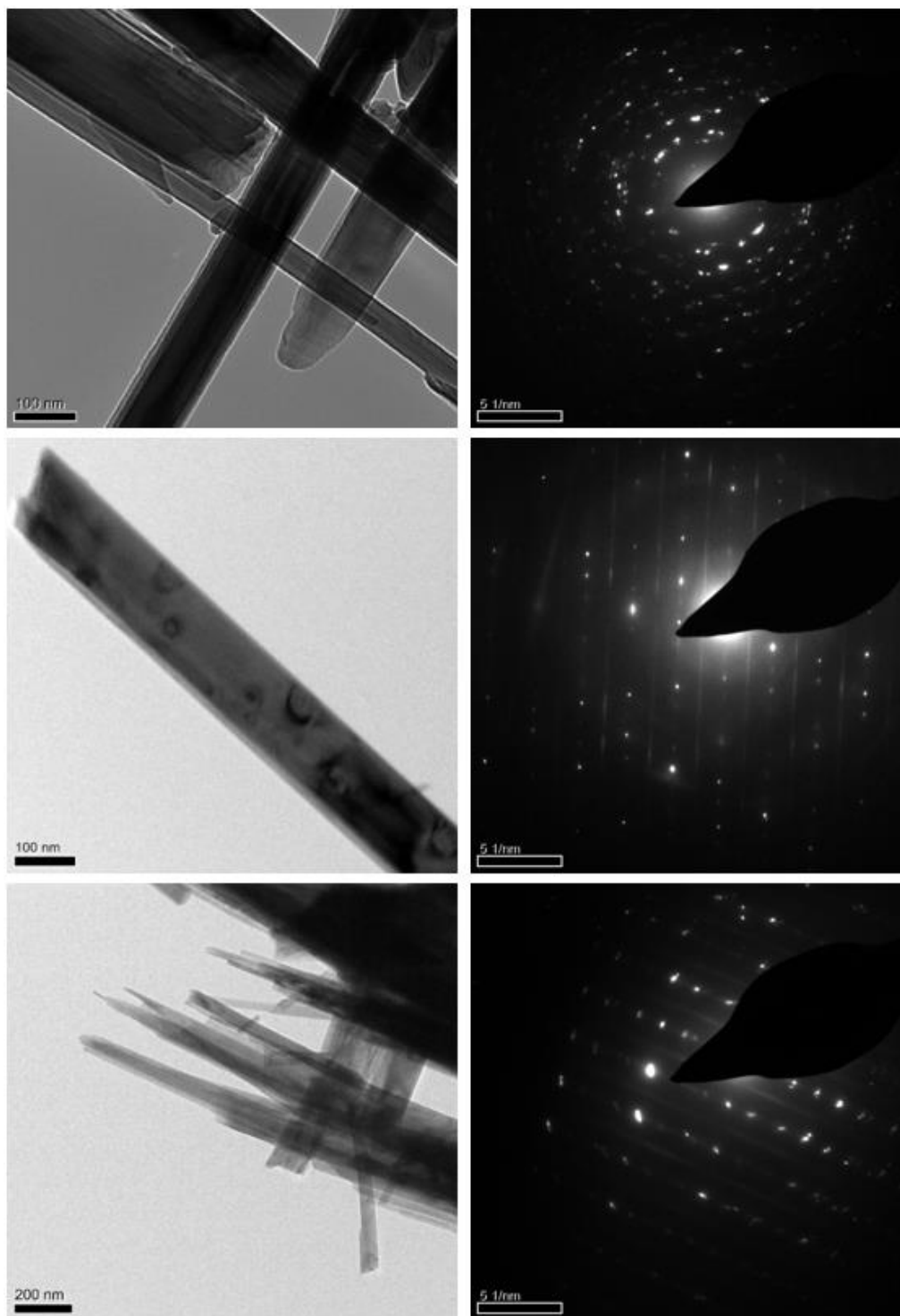


Figure 6.1 TEM images of sample A showing scawtite on top, hillebrandite in middle and jaffeite on bottom.

The mean Ca/Si ratios of different phases measured from EDX analysis are shown in the Table 6:1. Figure 6.2 shows the histograms of the Ca/Si ratios obtained from EDX analysis for all the phases present in the sample.

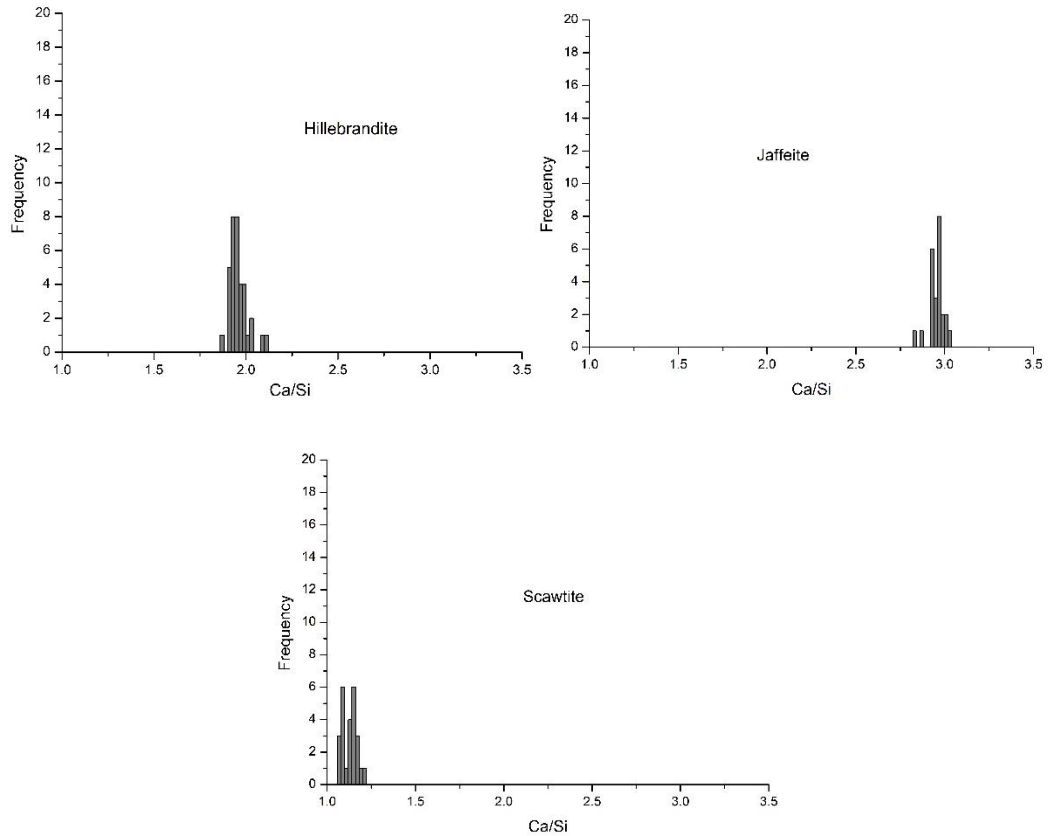


Figure 6.2 Histograms of Ca/Si ratios measured by TEM – EDX for all the phases in sample A.

The TEM micrograph of sample C synthesized is shown in Figure 6.3 along with the corresponding SAED pattern, confirming the presence of a crystalline phase corresponding to β -C₂S phase. The micrograph shows a lath-like crystal. Ishida et al. [7] reported that the crystals begin to bend at the ends when heated above 600 °C and become rounded when heated to 1000 °C. This deformation in the crystals is caused by sintering resulting in the reduction of specific surface area

and reactivity. However, the crystals (Figure 6.3) in this work doesn't show any bending when heated to 800 °C.

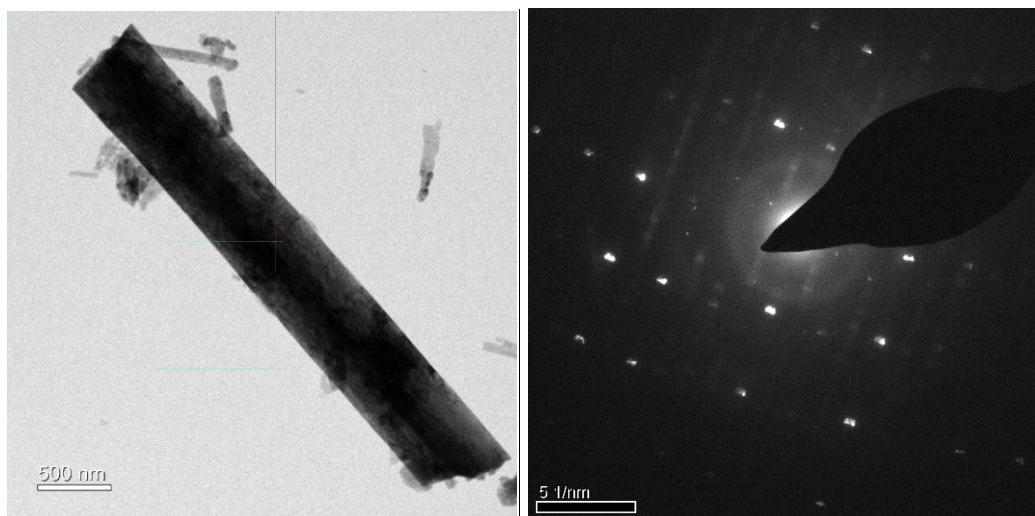


Figure 6.3 TEM micrograph of β -C₂S phase and the corresponding SAED pattern in sample C.

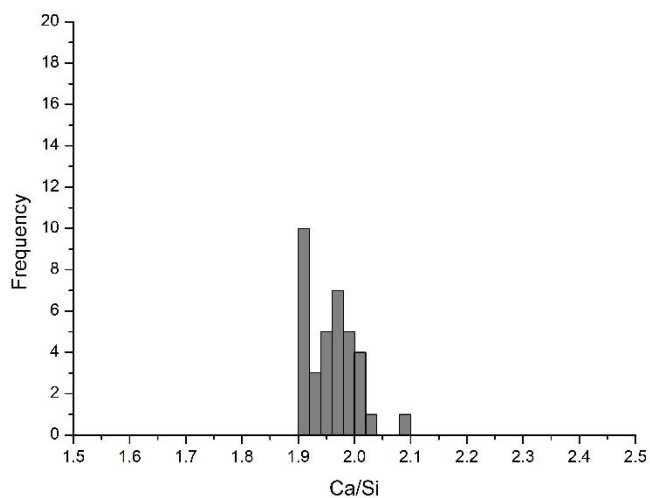


Figure 6.4 Histogram of Ca/Si ratios measured by TEM – EDX for β -C₂S phase in sample C.

Figure 6.4 shows the histogram of the Ca/Si ratios obtained from EDX analysis for the β -C₂S present in the sample. The mean Ca/Si ratio measured from EDX analysis is 1.98 ± 0.04 (N = 36).

6.1.2 ^{29}Si NMR

Figure 6.5 illustrates the deconvolution of ^{29}Si NMR spectrum of sample A. The simulated spectrum is displayed as a sum of the individual frequencies below the experimental spectrum. The residual is shown in red at the top. The individual frequencies are shown for Q¹ and Q² groups.

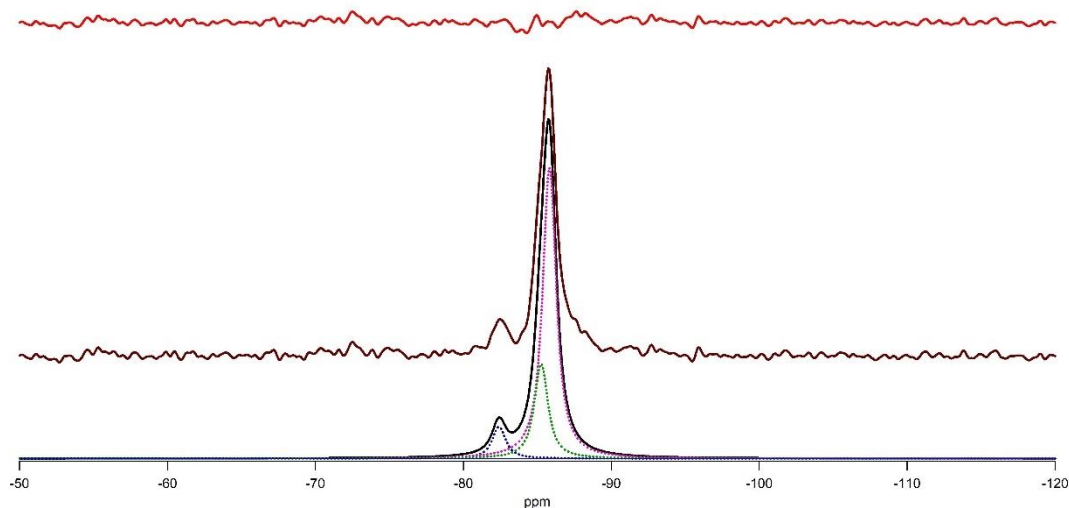


Figure 6.5 ^{29}Si NMR simulated spectrum for sample A including experimental spectrum (middle, brown), residual (top, red x1) and the individual frequencies.

The peak at $\delta = -82.5$ ppm corresponds to Q¹ groups confirming the presence of jaffeite [109]. The peak at $\delta = -85.8$ ppm corresponds to Q² groups confirming the presence of hillebrandite [7]. Scawtite shows two Q² peaks at $\delta = -84$ ppm and $\delta = -85.8$ ppm for Si (1) and Si (2) sites [158]. The peak at $\delta = -85.8$ ppm corresponds to both hillebrandite and scawtite.

Figure 6.6 illustrates the deconvolution of ^{29}Si NMR spectrum of sample C. The simulated spectrum is displayed as a sum of the individual frequencies below the experimental spectrum. The residual is shown in red at the top. The individual

frequencies are shown for Q¹ and Q² groups. The peak at $\delta = -70.9$ ppm corresponds to Q⁰ groups confirming the presence of β -C₂S [8]. The peak at $\delta = -73.2$ ppm corresponds to Q⁰ groups confirming the presence of γ -C₂S [159]. Wollastonite shows three Q² peaks between $\delta = -87$ ppm and $\delta = -89$ ppm. These values are in agreement with the reported data in the literature [158].

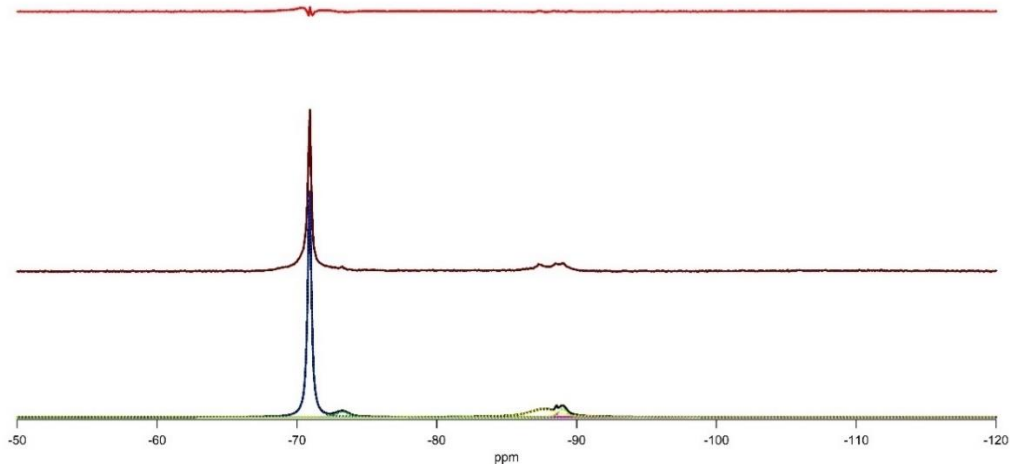


Figure 6.6 ²⁹Si NMR spectrum for sample C including experimental spectrum (middle, brown), residual (top, red x1) and the individual frequencies.

6.1.3 STA and XRD

Figure 6.7 shows an STA curve for sample A and Figure 6.8 an STA curve for sample C. The results show that there are three phases in sample A. The weight loss at about 700 °C corresponds to the decomposition of scawtite. The weight loss at 540 °C corresponds to the decomposition of jaffeite and the weight loss at 570 °C corresponds to the decomposition of hillebrandite. The weight losses before 500 °C might be due to loss of molecular water from the main phase.

Many authors have reported that scawtite forms as a carbonation product of calcium silicate hydrates [157] and the decomposition of scawtite occurs between

700 °C – 740 °C [146]. Ishida et al. [7] reported that hillebrandite decomposes to β -C₂S of low crystallinity in the range of 490 °C – 665 °C. Martin et al. reported that jaffeite decomposes in the range of 500 °C – 550 °C [160].

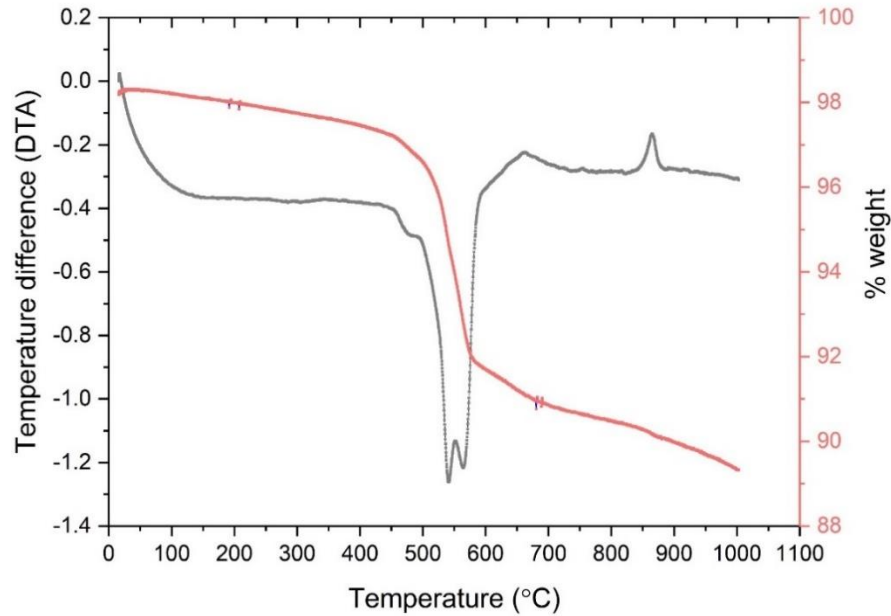


Figure 6.7 STA pattern of C-S-H – sample A, grey curve represents the DTA plot and the red curve represents the % weight loss.

When hillebrandite decomposes to β -C₂S, there is still some significant amount of residual hydroxyl groups retained in the structure. This hydroxylated larnite present starts to dehydroxylate and transforms to α'_L -C₂S in the range of 800 °C – 900 °C [161]. There are also few studies which suggest the transition of protonated larnite to α'_L -C₂S occurs over a range of 670 °C – 840 °C [7]. The exothermic peak seen in the STA traces around 900 °C represents the transformation from β phase to α'_L phase.

The amount of solid residue in sample A and sample C at the end is 89.82 % and 97.25 % respectively.

The XRD pattern of sample A along with reference patterns is shown in Figure 6.9. The experimental XRD pattern matches with three phases: jaffeite with Ca/Si ratio of 3, hillebrandite with Ca/Si ratio of 2 and scawtite with Ca/Si ratio of 1.16. The XRD pattern of sample C along with reference patterns is shown in Figure 6.10. The experimental XRD pattern matches with three phases: larnite, wollastonite and Y-C₂S.

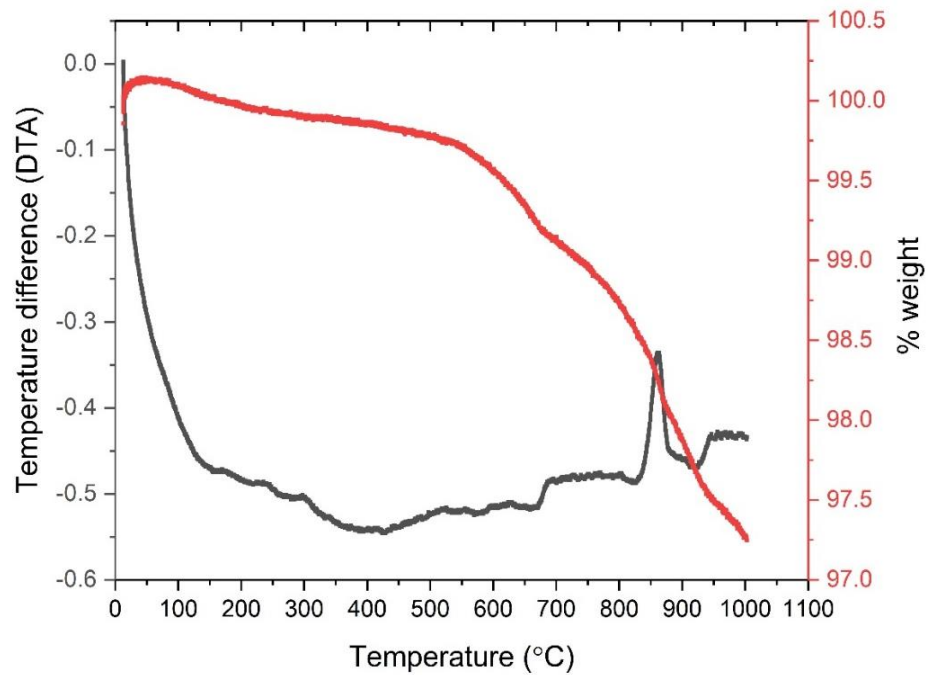


Figure 6.8 STA pattern of C-S-H – sample C, grey curve represents the DTA plot and the red curve represents the % weight loss.

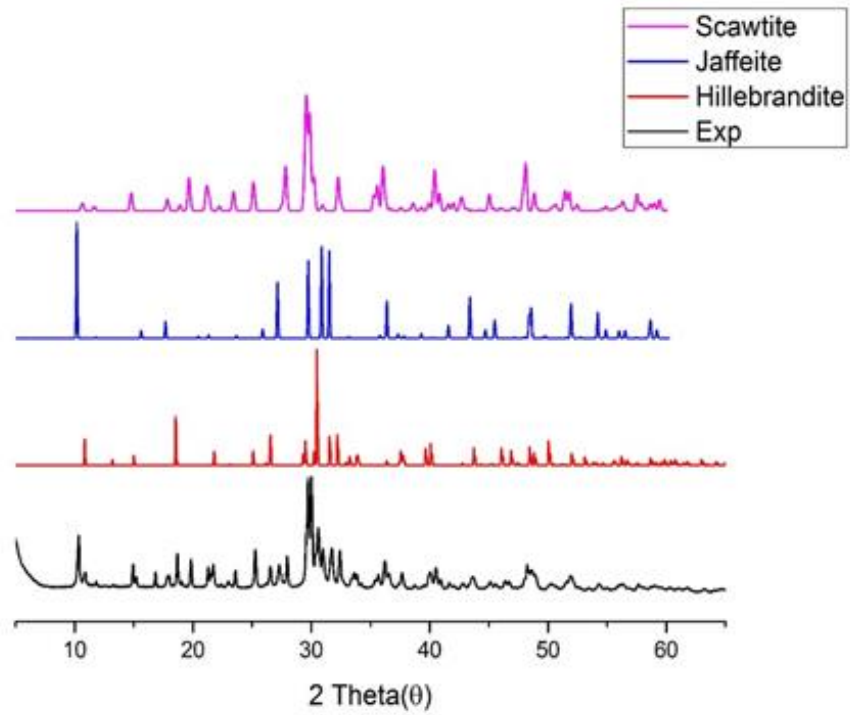


Figure 6.9 XRD pattern of sample A along with the reference patterns.

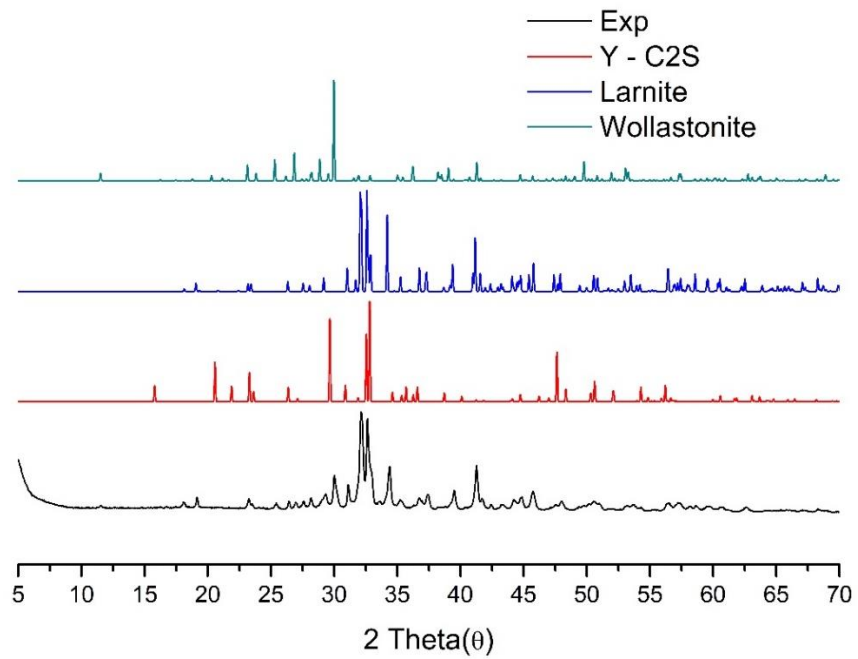


Figure 6.10 XRD pattern of sample C along with the reference patterns.

6.2 Characterization results of static hydrated samples (SHC) (described in Table 4:5, Experimental Methods)

6.2.1 TEM – EDX

The micrographs of samples SHC – 1 and SHC – 2 are shown in Figures 6.11 and 6.12. The micrographs show the presence of C-S-H phase having fibrous morphology in both the samples and the corresponding SAED patterns confirm the presence of an amorphous phase. However, there is also presence of CH (although not identified in TEM) which is discussed later in STA and XRD analyses. The fibrillar morphology seen resembles the morphology of C-S-H phases present in hydrated CEM I [17]. The mean Ca/Si ratios obtained from EDX analysis are shown in Table 6:2. The histograms for the Ca/Si obtained by TEM-EDX are shown in Figure 6.13.

The mean Ca/Si ratio of SHC – 1 (w/s = 0.5) after 45 days of hydration is 1.82 with CH present and the mean Ca/Si ratio of SHC – 2 (w/s = 1.0) after 28 days of hydration is 1.79 with CH present.

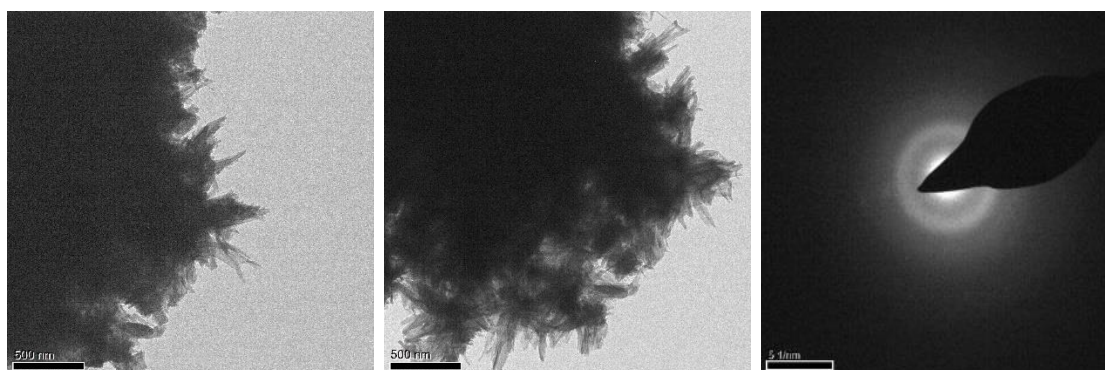


Figure 6.11 TEM micrographs of SHC – 1 along with the SAED pattern.

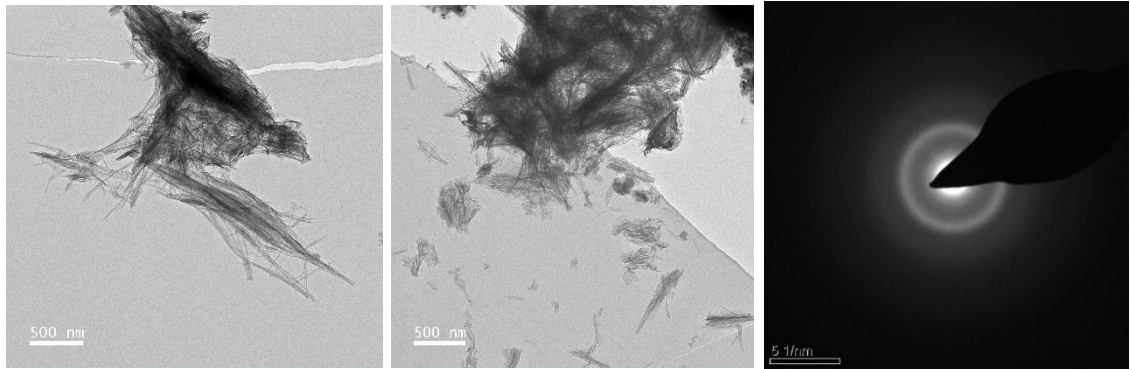


Figure 6.12 TEM micrographs of SHC – 2 along with the SAED pattern.

Sample Name	Ca/Si	N*	S.D
SHC - 1	1.82	45	0.05
SHC - 2	1.79	43	0.04

N* is the number analyses

Table 6:2 Ca/Si ratios of C-S-H phases obtained from TEM – EDX analysis for samples SHC – 1 and SHC – 2.

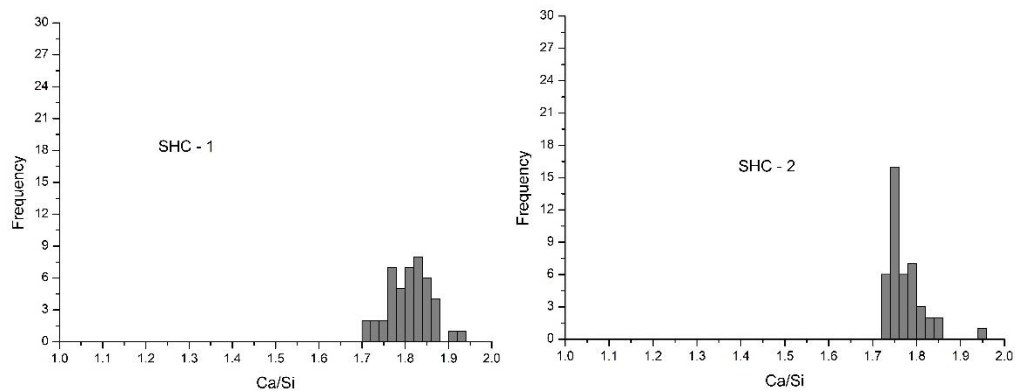


Figure 6.13 Histograms of Ca/Si ratios measured from TEM – EDX for samples SHC – 1 and SHC – 2.

6.2.2 ^{29}Si NMR

The ^{29}Si NMR results of all the static hydrated samples are shown in Figures 6.14 – 6.19. The results are deconvoluted to estimate the percentage of silicate groups and the mean chain length. The experimental spectra, the individual frequencies and the simulated spectra, are all shown in the Figures below. The peaks in the range $\delta = -77$ ppm to -80 ppm correspond to the presence of Q^1 groups while the peaks in the range $\delta = -82$ ppm to -84 ppm correspond to the presence of Q^2 groups representing the process of hydration. The spectra for SHC – 1 and SHC – 2 clearly show more intensity originating from Q^1 groups than Q^2 groups. The presence of these groups indicate that the hydrate possesses dimers or end chain groups and middle chain groups. The MCL calculated is shown in Table 6:3 along with the percentage of silicate species in C-S-H phases obtained from deconvolution of the spectra.

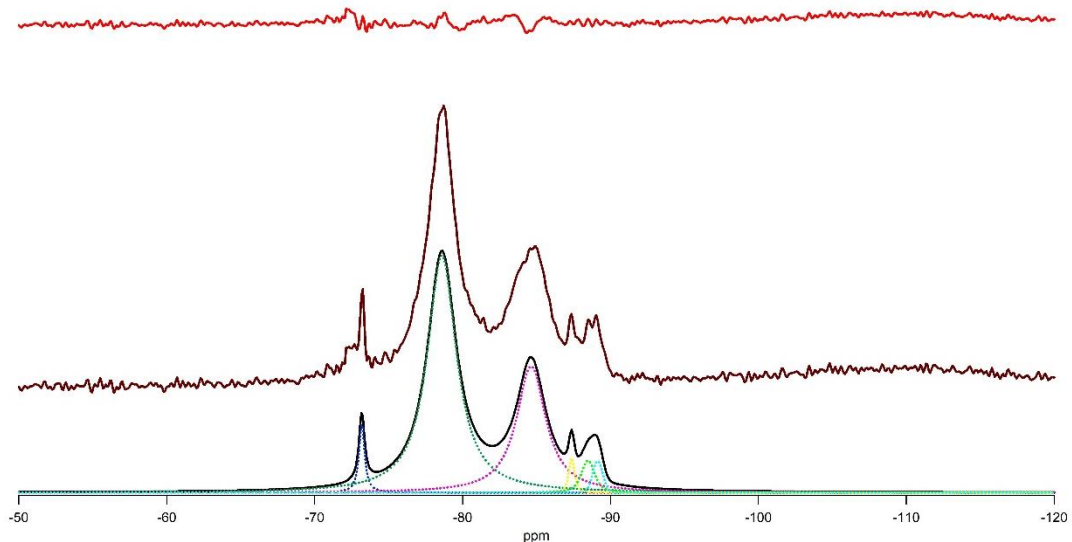


Figure 6.14 ^{29}Si NMR spectra of SHC -1 including experimental spectrum (middle, brown), residual (top, red x1) and the individual frequencies.

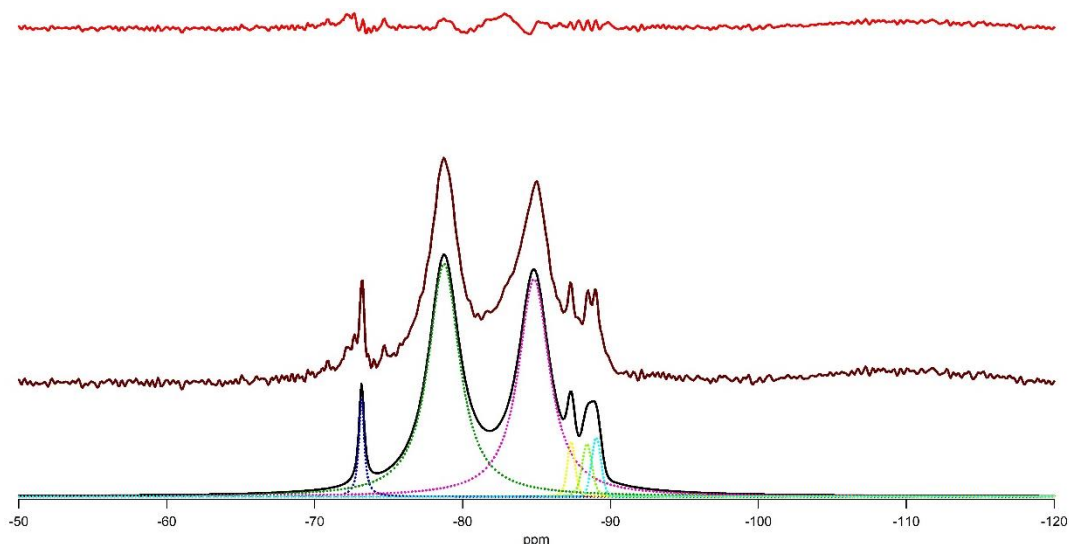


Figure 6.15 ^{29}Si NMR spectra of SHC - 2 including experimental spectrum (middle, brown), residual (top, red x1) and the individual frequencies.

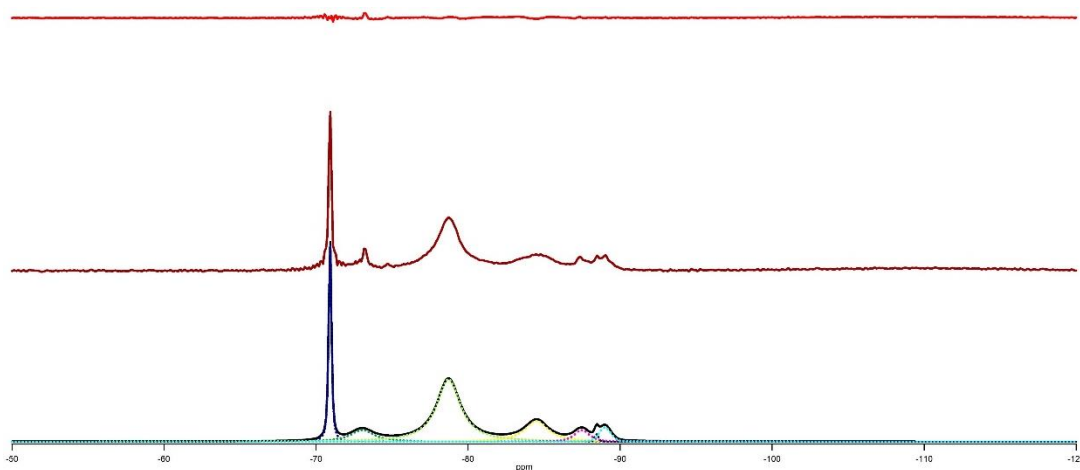


Figure 6.16 ^{29}Si NMR spectra of SHC - 3 including experimental spectrum (middle, brown), residual (top, red x1) and the individual frequencies.

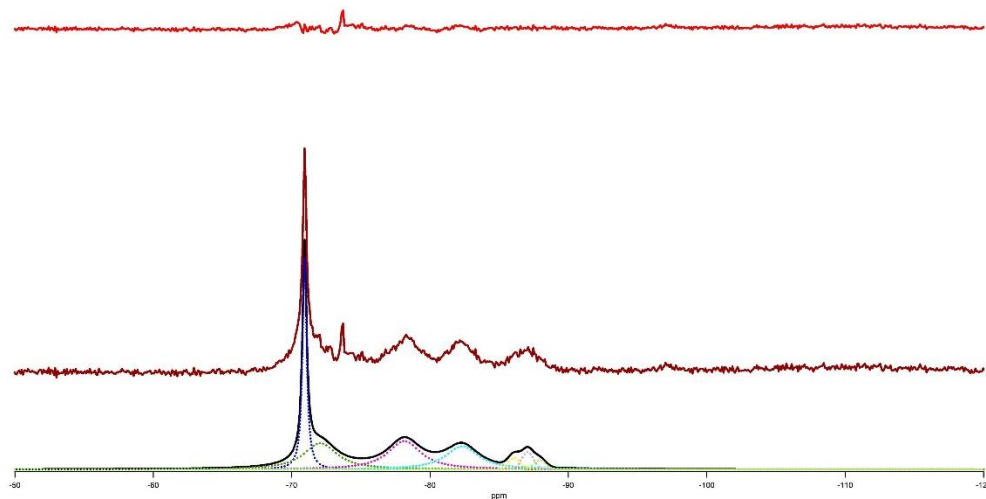


Figure 6.17 ^{29}Si NMR spectra of SHC - 4 including experimental spectrum (middle, brown), residual (top, red x1) and the individual frequencies.

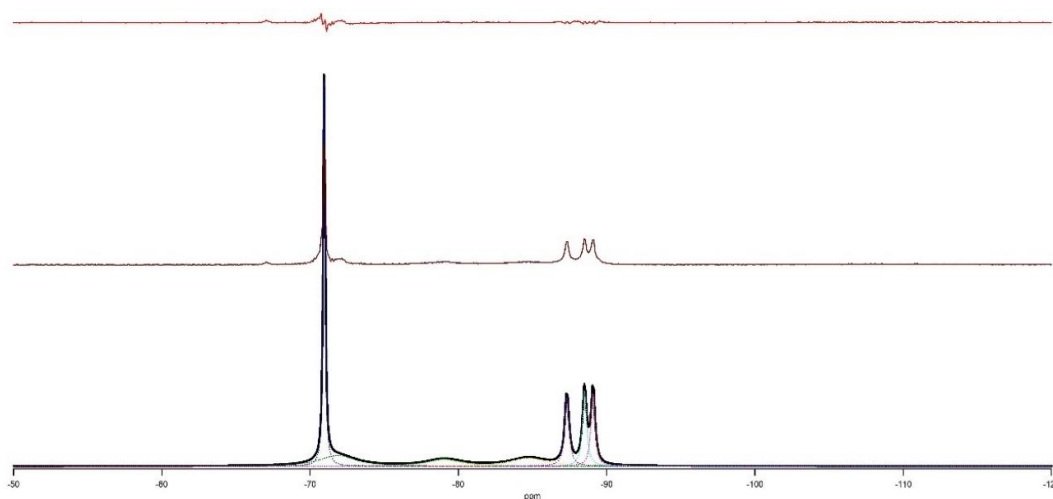


Figure 6.18 ^{29}Si NMR spectra of SHC - 5 including experimental spectrum (middle, brown), residual (top, red x1) and the individual frequencies.

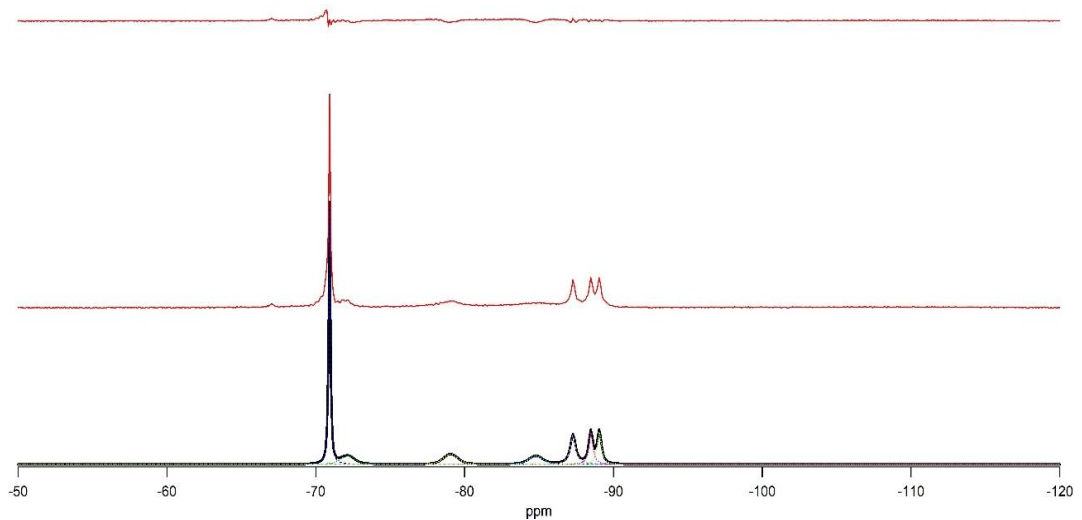


Figure 6.19 ^{29}Si NMR spectra of SHC - 6 including experimental spectrum (middle, brown), residual (top, red x1) and the individual frequencies.

In both the spectra (SHC – 1 and SHC – 2) there is no peak around $\delta = -71$ ppm indicating that the hydration of $\beta\text{-C}_2\text{S}$ is completed. However, there is a peak present around $\delta = -73$ ppm indicating the presence of $\gamma\text{-C}_2\text{S}$ [159]. The existence of $\gamma\text{-C}_2\text{S}$ in the sample even after 45 days of hydration indicates that its reactivity is very low. The three peaks around $\delta = -87$ ppm, $\delta = -88$ ppm and $\delta = -89$ ppm correspond to the presence of wollastonite [158].

The spectra for SHC – 3, SHC – 4, SHC – 5 and SHC – 6 clearly shows the presence of a peak at $\delta = -71$ ppm indicating the existence of $\beta\text{-C}_2\text{S}$. There are also peaks corresponding to Q^1 and Q^2 groups, intensities of which are quite low. This indicates that the hydration of $\beta\text{-C}_2\text{S}$ has started but the process is not completed. The three peaks corresponding to wollastonite are present in all the samples. In all the spectra, Q^1 and Q^2 intensities increase as Q^0 intensity decreases and the amount of Q^1 species formed is greater than Q^2 species.

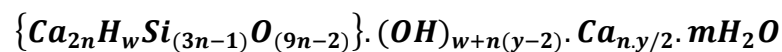
Ishida et al. [6] reported that the static hydration of highly reactive β -C₂S with a specific surface area of 7 m²/g is completed in 28 days and 14 days for w/s ratios 0.5 and 1 respectively, resulting in the formation of C-S-H phase with Ca/Si ratios between 1.77 – 1.82 along with CH phase. However, in the current work, hydration of β -C₂S at w/s 0.5 and 1 is only completed after 45 days and 28 days respectively. Although measurements of particle size and surface area would have given a clear picture on the reactivity, it could be speculated that the slow reactivity is possibly caused by the reduction in specific surface area of β -C₂S during heating of hillebrandite to 800 °C, instead of 600 °C to eliminate scawtite. Ishida et al. [7] reported that heating hillebrandite above 700 °C to obtain β -C₂S resulted in a decrease of specific surface area thus, reducing its reactivity. There are several studies that report the effect of specific surface area on the hydration of β -C₂S. Shibata et al. [162] reported that hydration of β -C₂S with a specific surface area of 1.59 m²/g – 2.10 m²/g at w/s = 0.5 is completed after 168 days.

Sample	Q ¹ (%)	Q ² (%)	MCL	Ca/Si _{TEM-EDX}
SHC - 1	58.1	31.1	3.07	1.82
SHC - 2	46.4	43.3	3.86	1.79
SHC - 3	48.8	16.1	2.65	-
SHC - 4	25.0	20.4	3.63	-
SHC - 5	10.2	8.1	3.58	-
SHC - 6	9.3	11.0	4.36	-

Table 6:3 Results of deconvolution of the ²⁹Si NMR spectra: % silicate species and MCL.

Richardson and Groves' model (described in literature review) [39] is used for the formulation of the C-S-H phases synthesized. Figure 6.20 shows the Ca/Si ratios plotted against the reciprocal mean chain length. The figure also shows the trends for tobermorite and jennite units with various degrees of protonation ($w = 0, 1, 2$). The mean values of Ca/Si ratios represented by filled circles fall between jennite like and tobermorite like regions on the plot, thus confirming the presence of Ca-OH groups in the structure coming either from jennite like structures or solid solution CH. In T/J viewpoint, the Ca-OH groups form a part of the main layer and in T/CH viewpoint, the Ca-OH groups are present in the interlayers. The SAED patterns does not show the presence of any crystalline CH phase and T/J viewpoint seems to be more suitable but the presence of CH cannot be completely excluded. Both the viewpoints have been used to derive the structural chemical formula. However, the removal of Ca by the process of leaching (discussed in the chapter 8) helps to identify the most suitable viewpoint. Since leaching resulted in the alteration of both Ca/Si ratio and silicate structure, it is indicative that the C-S-H phases are a combination of tobermorite and jennite units and follow T/J view point. The alteration of both Ca/Si ratio and silicate structure after leaching suggests that the Ca is removed from the main layers rather than the interlayers.

The general formula for T/J viewpoint:



Where, $n = (MCL+1)/3$ and $y = [(Ca/Si)(6n-2)-4n]/n$

w depends on the value of y

if, $0 \leq y \leq 2$ then $n(2-y) \leq w \leq 2n$

if, $2 \leq y \leq 4$ then $0 \leq w \leq 2n$

if, $4 \leq y \leq 6$ then $0 \leq w \leq n(6-y)$

The values calculated for n , y , w_{\min} (minimum no. of silanol groups) and w_{\max} (maximum number of silanol groups) are tabulated in Table 6:4.

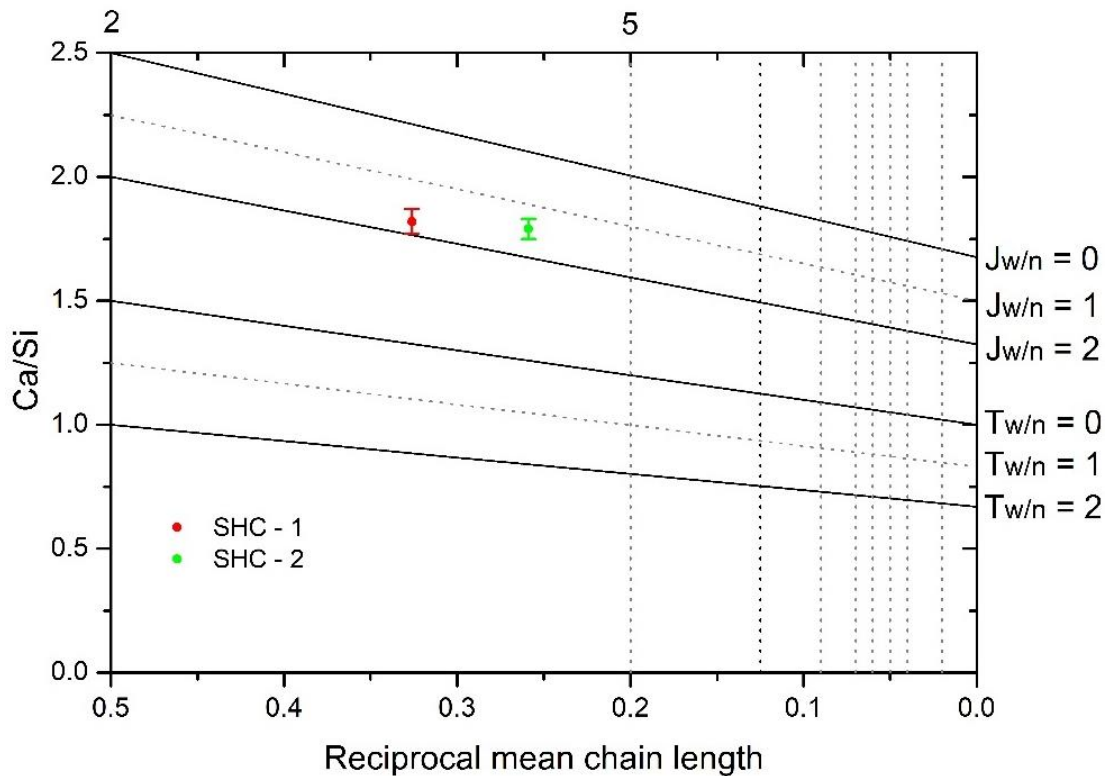
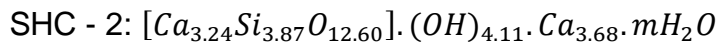
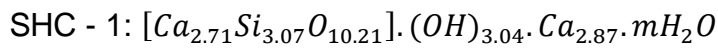


Figure 6.20 Ca/Si obtained by TEM-EDX analysis versus reciprocal mean chain length obtained by NMR analysis. The structural units for tobermorite and jennite with minimum ($w=0$), intermediate ($w=1$) and maximum ($w=2$) degree of protonation are plotted along with data points from current work. The vertical dashed lines represent the $(3n - 1)$ structural units: dimer (2), pentamer (5) etc.

Sample	n	y	W _{min}	W _{max}
SHC - 1	1.36	4.24	0	2.39
SHC - 2	1.62	4.53	0	2.38

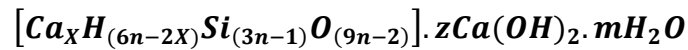
Table 6:4 Calculated values required for the formulation using T/J viewpoint.

The structural chemical formulae for the C-S-H phases synthesized are shown below:



The C-S-H phases synthesized are a combination of T2, T5, J2 and J5 structural units.

The general formula for T/CH viewpoint:



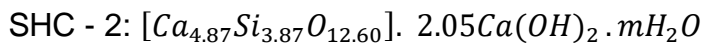
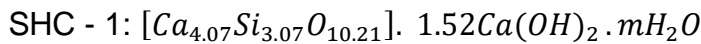
Where, $X = (6n-w)/2$ and $z = (w+n(y-2))/2$

The values calculated for X and z are tabulated in Table 6:5. X and z are calculated using the values of n, y and w_{min} from Table 6:4.

Sample	X	z
SHC - 1	4.07	1.52
SHC - 2	4.87	2.05

Table 6:5 Calculated values required for the formulation using T/CH viewpoint.

The structural chemical formulae for the C-S-H phases synthesized are shown below:

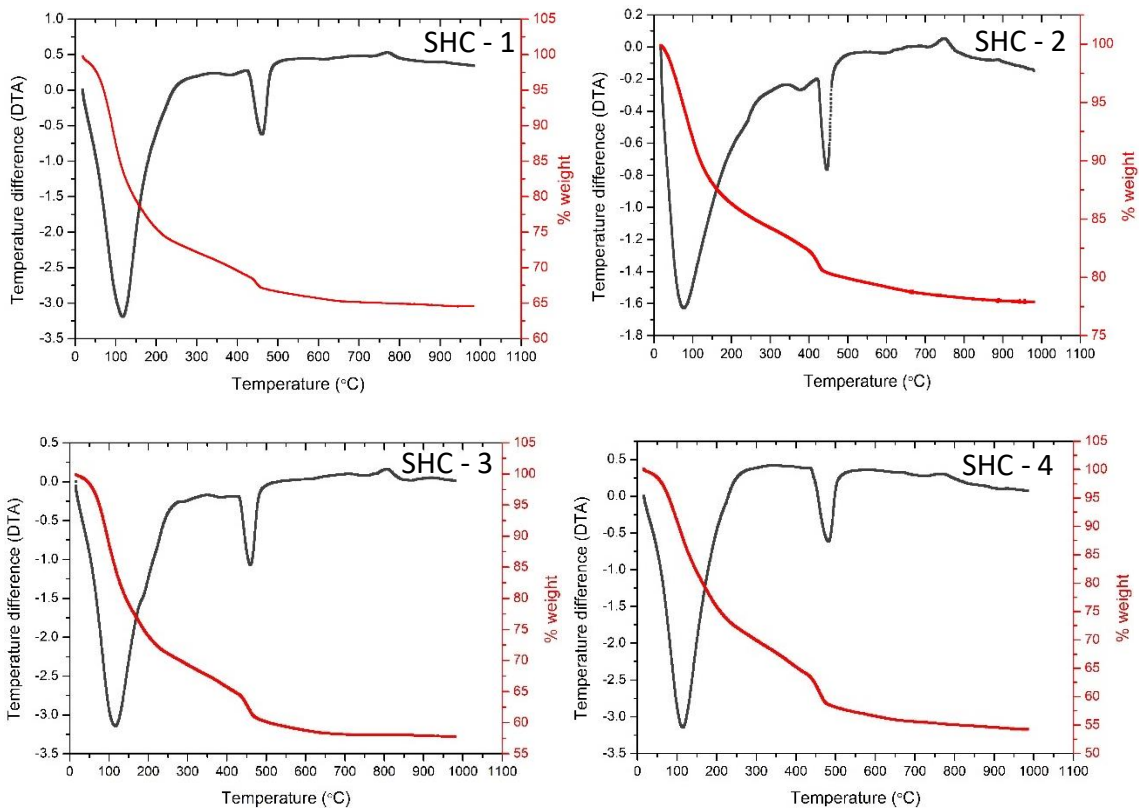


6.2.3 STA and XRD

The STA traces of all the SHC samples are shown in Figure 6.21. The results for all the samples show that the weight loss until 200 °C corresponds to the dehydration of C-S-H phase. The weight loss at 450 °C in all the samples corresponds to the dehydration of CH phase. The presence of CH phase in the samples is in agreement with the results obtained by Ishida et al. [6]. Although Ishida et al. [6] used similar w/s ratios, the β -C₂S they used is potentially more reactive than the β -C₂S phase used in this work (the lower reactivity of β -C₂S discussed in the previous section leads to the slow hydration). Thus, reactivity of β -C₂S is an important factor to be considered which affects its rate of hydration. The DTA curves show an exothermal peak at about 800 °C corresponding to the formation of C₂S. The results for the SHC samples show that longer hydration time results in reduction of CH content. The % CH in all the samples calculated using tangent method are shown in Table 6:6.

Sample	% CH _{res}
SHC - 1	7.9
SHC - 2	10.6
SHC - 3	20.9
SHC - 4	21.1
SHC - 5	27.4
SHC - 6	30.7

Table 6:6 % CH_{res} in all the SHC samples calculated using tangent method.



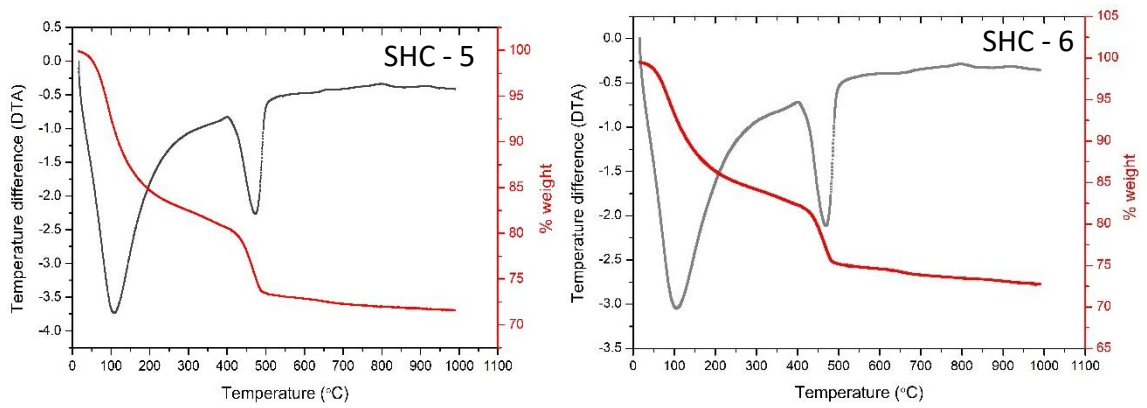


Figure 6.21 STA patterns of SHC samples showing DTA in grey and % TG in red.

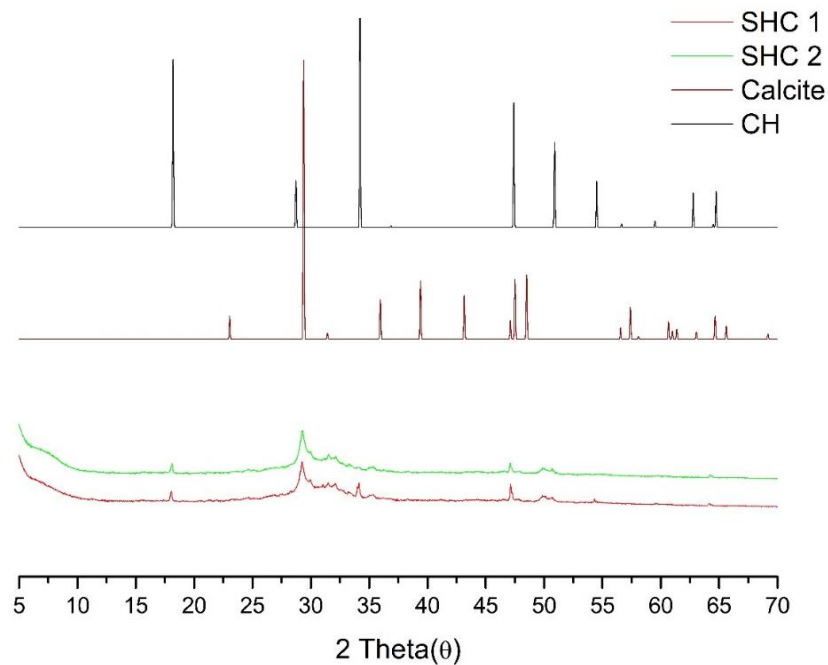


Figure 6.22 XRD patterns of SHC samples along with the reference patterns.

The XRD patterns of SHC – 1 and SHC - 2 along with reference patterns are shown in Figure 6.22. The patterns clearly show the presence of CH phase ($2\theta \sim 18^\circ$) in both the samples.

6.3 Characterization results of ball mill hydrated samples (BHC) (described in Table 4:5, Experimental Methods)

6.3.1 TEM - EDX

The TEM micrographs of the ball mill hydrated samples: BHC – 1, BHC – 2, BHC – 3 and BHC – 4 hydrated for 4, 8, 16 and 32 days respectively are shown in Figures 6.23 – 6.26. In all the samples, C-S-H exhibits dense fibrillar morphology and the diffraction patterns suggest that the C-S-H formed is amorphous in nature. It is clearly seen that the morphology of all the samples is fibrillar regardless the Ca/Si ratio and the hydration time. The mean Ca/Si ratios obtained by EDX are shown in Table 6:7. The Ca/Si ratio after 4 days of hydration is 1.78 with CH phase still present. However, Ishida et. al found that CH is no longer present beyond a 4 day period and the Ca/Si ratio increases to 1.98 – 2.0 [8]. In this work, the samples hydrated show the presence of CH phase (discussed in STA and XRD results later) beyond 16 days and this is because the β -C₂S used for hydration is synthesised by heating hillebrandite at 800 °C thus reducing the surface area and reactivity to an extent.

The histograms for the Ca/Si obtained by TEM-EDX are shown in Figure 6.27.

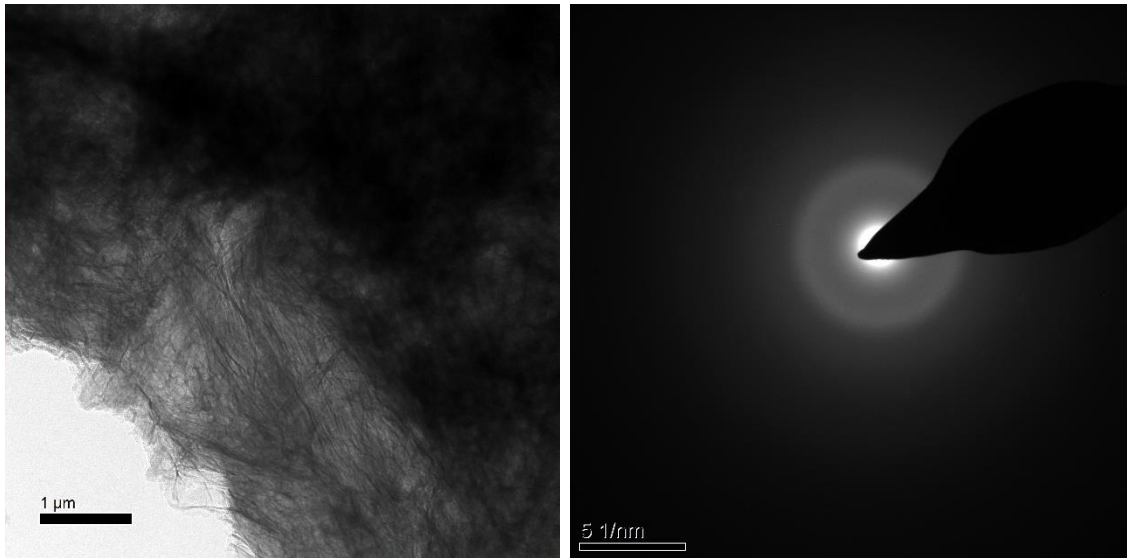


Figure 6.23 TEM micrograph of sample BHC – 1 along with the SAED pattern.

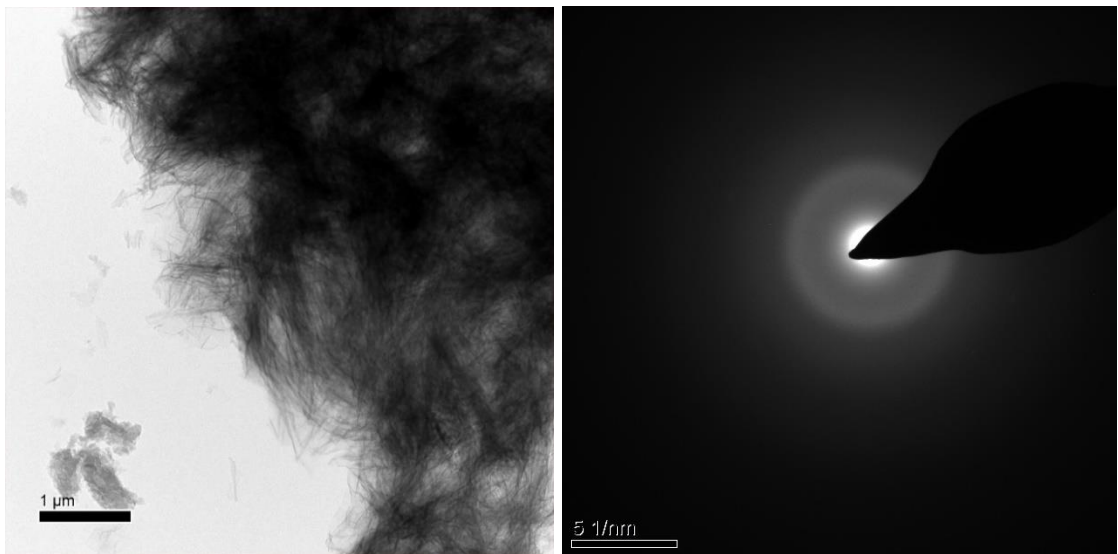


Figure 6.24 TEM micrograph of sample BHC – 2 along with the SAED pattern.

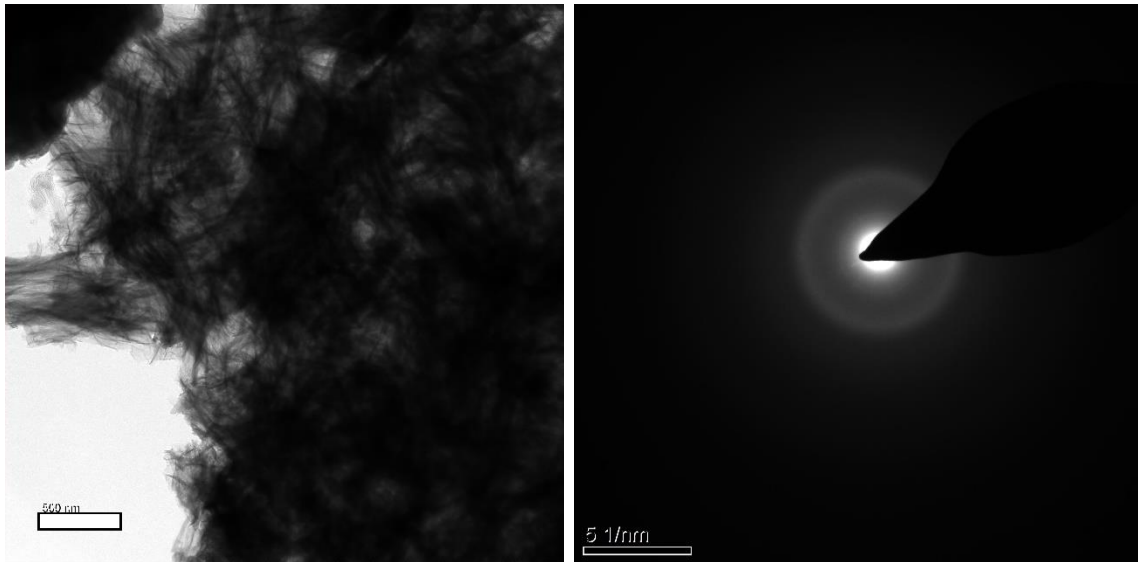


Figure 6.25 TEM micrograph of sample BHC – 3 along with the SAED pattern.

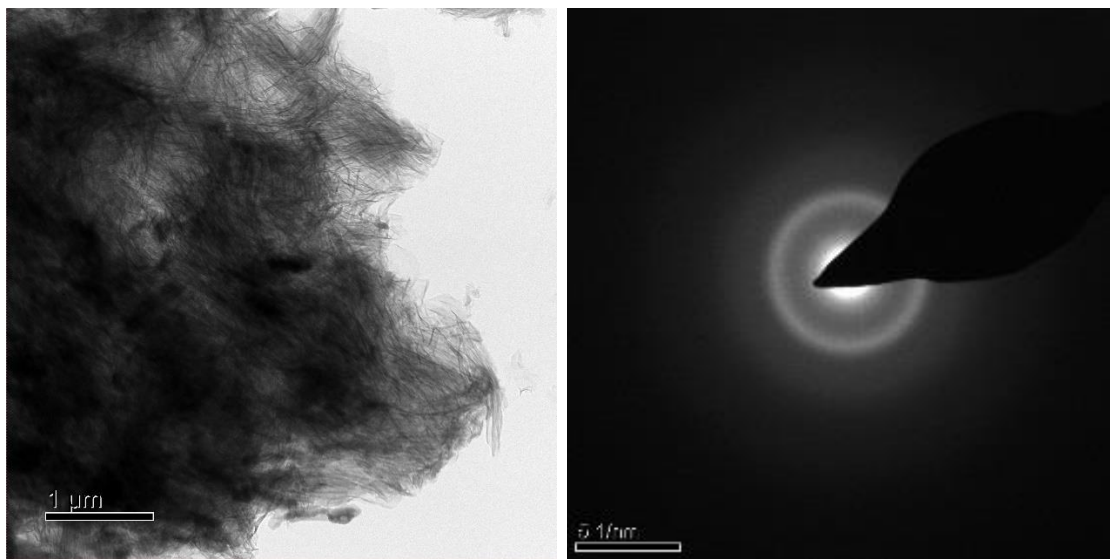


Figure 6.26 TEM micrograph of sample BHC – 4 along with the SAED pattern.

Sample	Ca/Si	N*	S.D
BHC - 1	1.78	44	0.04
BHC - 2	1.83	41	0.03
BHC - 3	1.89	49	0.03
BHC - 4	1.92	50	0.05

N* is the number of analyses

Table 6:7 Ca/Si ratios of C-S-H phases obtained by TEM – EDX for ball mill hydrated samples.

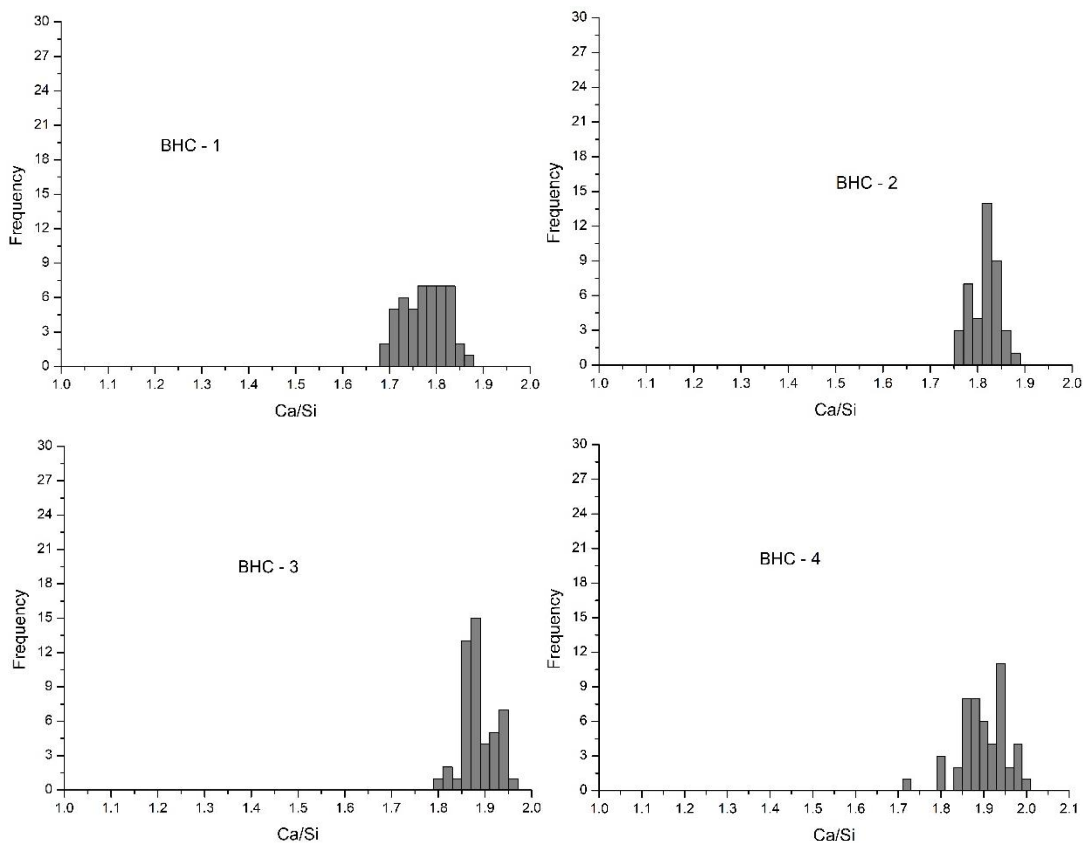


Figure 6.27 Histograms of Ca/Si ratios measured from TEM – EDX for samples BHC – 1, BHC – 2, BHC – 3, BHC – 4.

6.3.2 ²⁹Si NMR

The ²⁹Si NMR spectra of the ball mill hydrated samples, BHC - 1, BHC - 2, BHC - 3 and BHC - 4 are shown in Figures 6.28 – 6.31. The results are deconvoluted to estimate the percentage of silicate groups and the mean chain length. The experimental spectra, the individual frequencies and the simulated spectra all are shown in the Figures below. The peaks in the range $\delta = -77$ ppm to -80 ppm corresponds to the presence of Q¹ groups while the peaks in the range $\delta = -82$ ppm to -84 ppm correspond to the presence of Q² groups. The presence of these groups indicate that the hydrate possesses dimers and middle chain groups. However, in all the spectra Q¹ groups dominate the structure of C-S-H formed. Two frequencies each are used to deconvolute Q¹ and Q² contributions to improve the fitting of the asymmetric peaks and adjust the simulated spectra and the experimental spectra. Although these frequencies are used for deconvolutions, they do not directly represent the species present as the line widths and shapes of the frequencies vary between the samples. The relaxation of these parameters during the fitting process resulted in these variations. The deconvolution of the spectra is used to estimate the % of the silicate species present and to calculate the MCL. The results are shown in Table 6:8.

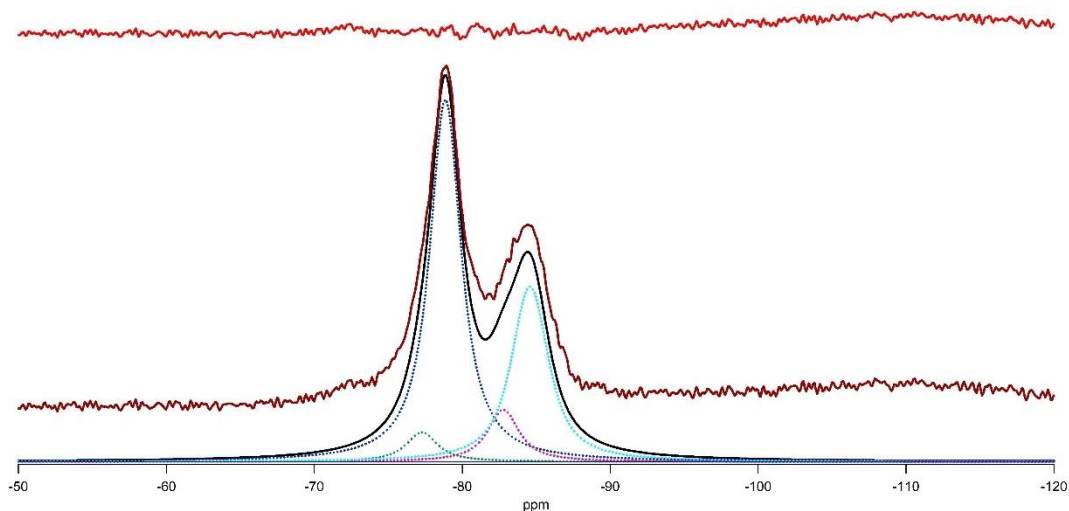


Figure 6.28 ^{29}Si NMR spectra for BHC - 1 showing the experimental spectrum (middle, brown), residual (top, red x1) and the individual frequencies.

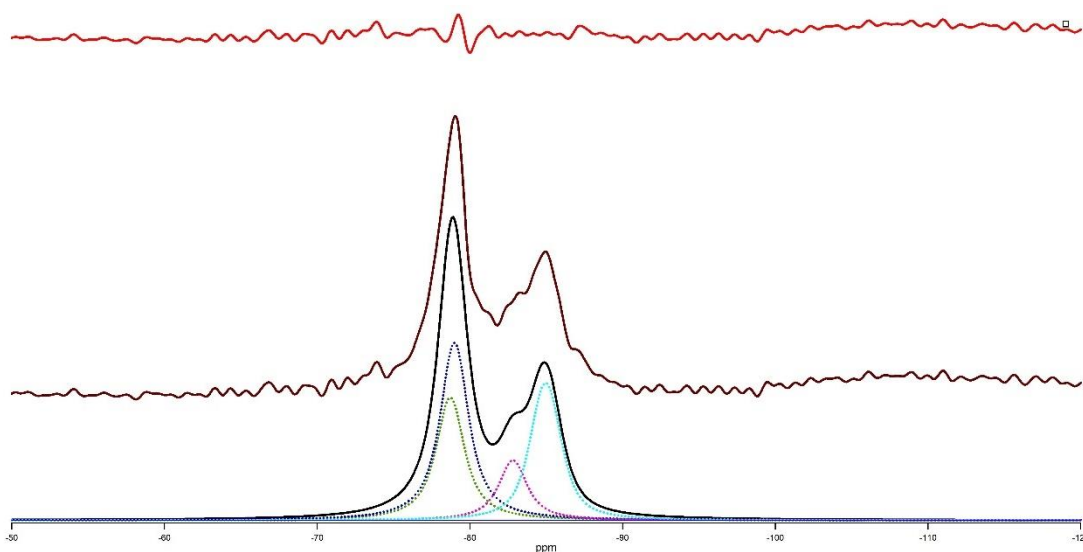


Figure 6.29 ^{29}Si NMR spectra for BHC - 2 showing the experimental spectrum (middle, brown), residual (top, red x1) and the individual frequencies.

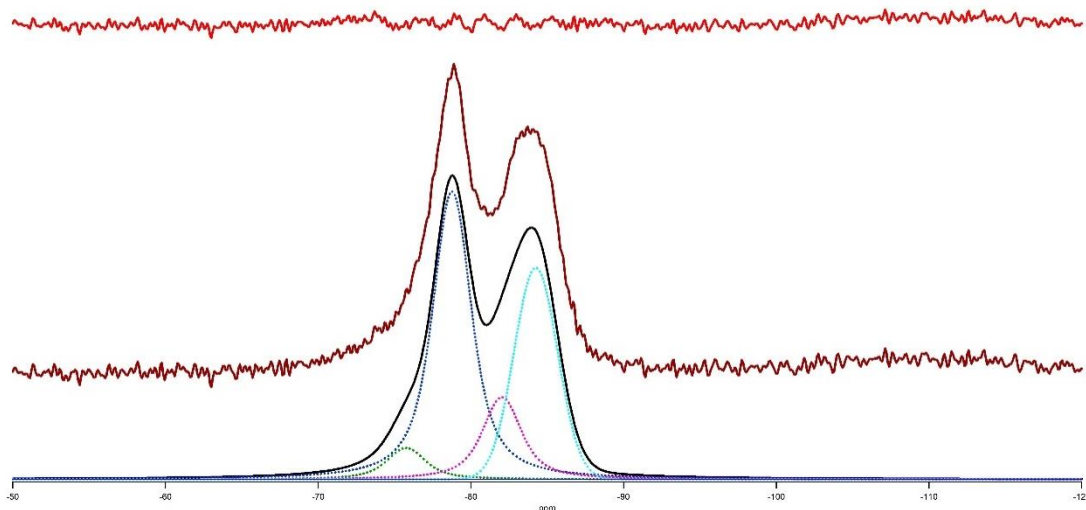


Figure 6.30 ^{29}Si NMR spectra for BHC - 3 showing the including experimental spectrum (middle, brown), residual (top, red x1) and the individual frequencies.

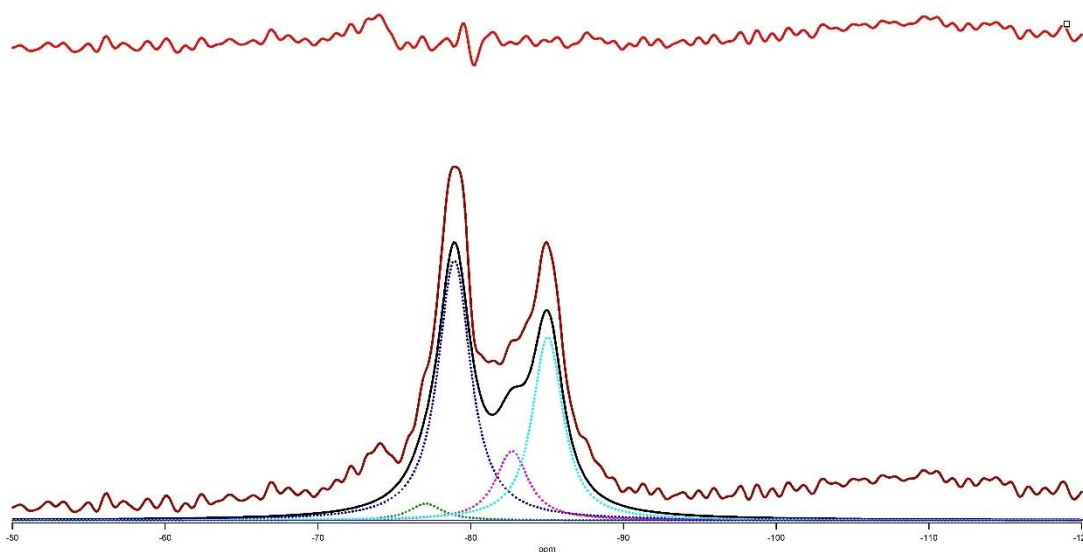


Figure 6.31 ^{29}Si NMR spectra for BHC - 4 showing the experimental spectrum (middle, brown), residual (top, red x1) and the individual frequencies.

Sample	Q ¹ (%)	Q ² (%)	MCL	Ca/Si _{TEM-EDX}
BHC - 1	61.2	38.8	3.27	1.78
BHC - 2	60.7	39.3	3.29	1.83
BHC - 3	54.8	45.2	3.65	1.89
BHC - 4	53.8	46.2	3.72	1.92

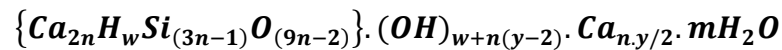
Table 6:8 Results of deconvolution of the ²⁹Si NMR spectra showing % of silicate species and MCL. Ca/Si ratios measured by TEM – EDX are also included.

The comparison of results of static and ball mill hydration clearly shows that ball mill hydration is a faster process than static hydration. This is because of the influence of curing temperature which increases in the case of ball mill hydration due to continuous rotation and a significant amount of mechanical energy is being applied to the system which helps to break up the particles to maximise reactive surface area and thus the reactivity. In this work, there is no presence of any peaks corresponding to the presence of Q⁰ silicate species indicating that the β-C₂S is completely transformed to C-S-H and CH.

Richardson and Groves' model (described in literature review) is used for the formulation of the C-S-H phases synthesized. Figure 6.32 shows the Ca/Si ratios plotted against the reciprocal mean chain length. The figure also shows the trends for tobermorite and jennite units with various degrees of protonation (w = 0, 1, 2). The mean values of Ca/Si ratios are represented by filled circles in the Figure below. The mean values of Ca/Si ratios fall in between tobermorite-like and jennite-like regions on the plot, thus confirming the presence of Ca-OH groups in

the structure coming either from jennite like structures or solid solution CH. In T/J viewpoint, the Ca-OH groups form a part of the main layer and in T/CH viewpoint, the Ca-OH groups are present in the interlayers. The SAED patterns does not show the presence of any crystalline CH phase and T/J viewpoint seems to be more suitable but the presence of CH cannot be completely excluded. Both the viewpoints have been used to derive the structural chemical formula. However, the removal of Ca by the process of leaching (discussed in the chapter 8) helps to identify the most suitable viewpoint. Since leaching resulted in the alteration of both Ca/Si ratio and silicate structure, it is indicative that the C-S-H phases are a combination of tobermorite and jennite units and follow T/J view point. The alteration of both Ca/Si ratio and silicate structure after leaching suggests that the Ca is removed from the main layers rather than the interlayers.

The general formula for T/J viewpoint:



Where, $n = (MCL+1)/3$ and $y = [(Ca/Si)(6n-2)-4n]/n$

w depends on the value of y

if, $0 \leq y \leq 2$ then $n(2-y) \leq w \leq 2n$

if, $2 \leq y \leq 4$ then $0 \leq w \leq 2n$

if, $4 \leq y \leq 6$ then $0 \leq w \leq n(6-y)$

The values calculated for n, y, w_{min} (minimum no. of silanol groups) and w_{max} (maximum number of silanol groups) are tabulated in Table 6:8.

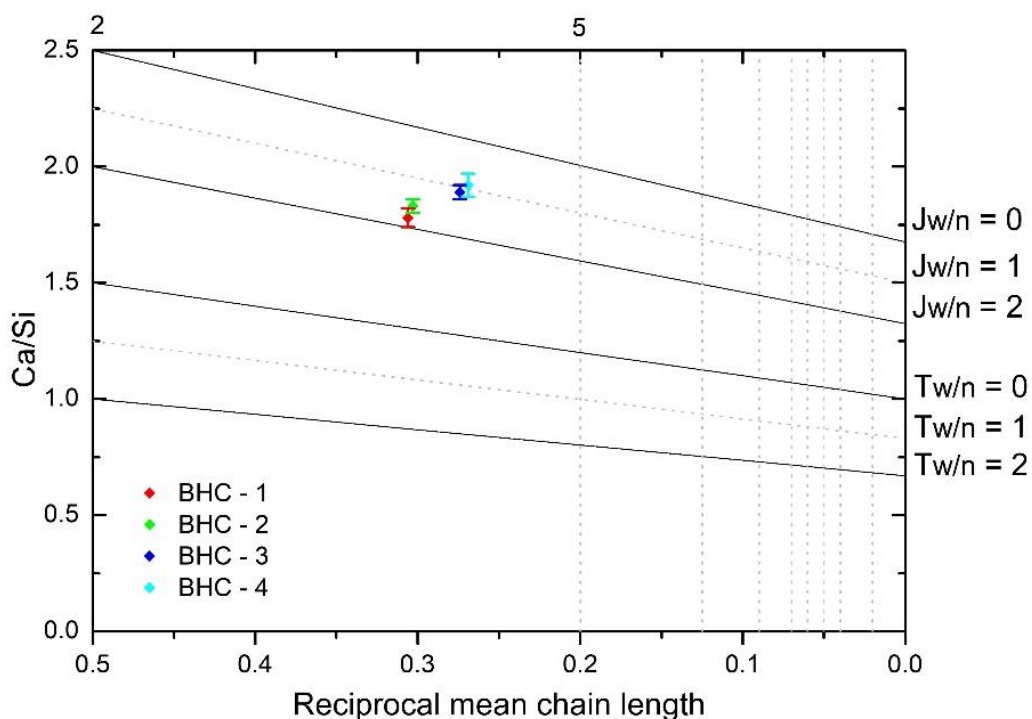
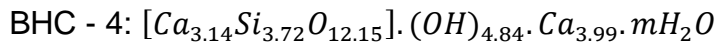
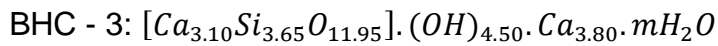
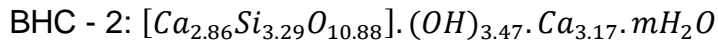
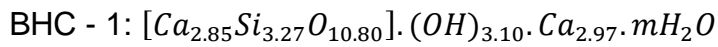


Figure 6.32 Ca/Si obtained by TEM-EDX analysis versus reciprocal mean chain length obtained by NMR analysis. The structural units for tobermorite and jennite with minimum ($w=0$), intermediate ($w=1$) and maximum ($w=2$) degree of protonation are plotted along with data points from current work. The vertical dotted lines represent the $(3n - 1)$ structural units: dimer (2), pentamer (5) etc.

Sample	n	y	W_{\min}	W_{\max}
BHC - 1	1.42	4.18	0	2.59
BHC - 2	1.43	4.42	0	2.26
BHC - 3	1.55	4.90	0	1.70
BHC - 4	1.57	5.08	0	1.45

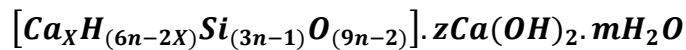
Table 6:9 Calculated values required for the formulation using T/J viewpoint.

The structural chemical formulae for all the C-S-H phases synthesized are shown below:



The C-S-H phases synthesized are a combination of T2, T5, J2 and J5 structural units.

The general formula for T/CH viewpoint:



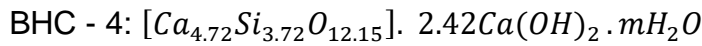
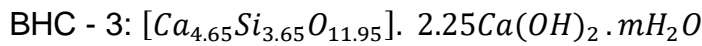
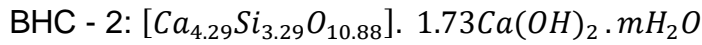
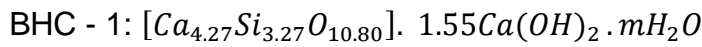
Where, $X = (6n-w)/2$ and $z = (w+n(y-2))/2$

The values calculated for X and z are tabulated in Table 6:10. X and z are calculated using the values of n, y and w_{\min} from Table 6:9.

Sample	X	z
BHC - 1	4.27	1.55
BHC - 2	4.29	1.73
BHC - 3	4.65	2.25
BHC - 4	4.72	2.42

Table 6:10 Calculated values required for the formulation using T/CH viewpoint.

The structural chemical formulae for all the C-S-H phases synthesized are shown below:



6.3.3 STA and XRD

The STA traces of all the BHC samples are shown in Figure 6.33. The results for all the samples show a weight loss until 200 °C corresponding to dehydration of the C-S-H phase. The weight loss at 450 °C in samples BHC – 1, BHC – 2 and BHC – 3 corresponds to the dehydration of CH phase. In sample BHC – 4, there is a weight loss at 650 °C corresponding to the decomposition of $C\bar{C}$ phase. The presence of CH phase in the samples BHC - 1, BHC - 2, BHC - 3 suggests that milling time is not enough for the hydration to be completed. Although Ishida et al. [8] used similar milling times, the β -C₂S they used is potentially more reactive than the β -C₂S used in this work (the lower reactivity of β -C₂S discussed in the previous section leads to the slow hydration). The presence of $C\bar{C}$ in the sample BHC - 4 is due to the exposure of the samples to CO₂ during ball milling or during drying. The DTA curves show an exothermal peak at about 900 °C corresponding to the formation of C₂S. The results of the samples clearly show that longer milling time results in reduction of CH content. The % CH and % $C\bar{C}$ in all the samples calculated using the tangent method are shown in Table 6:11.

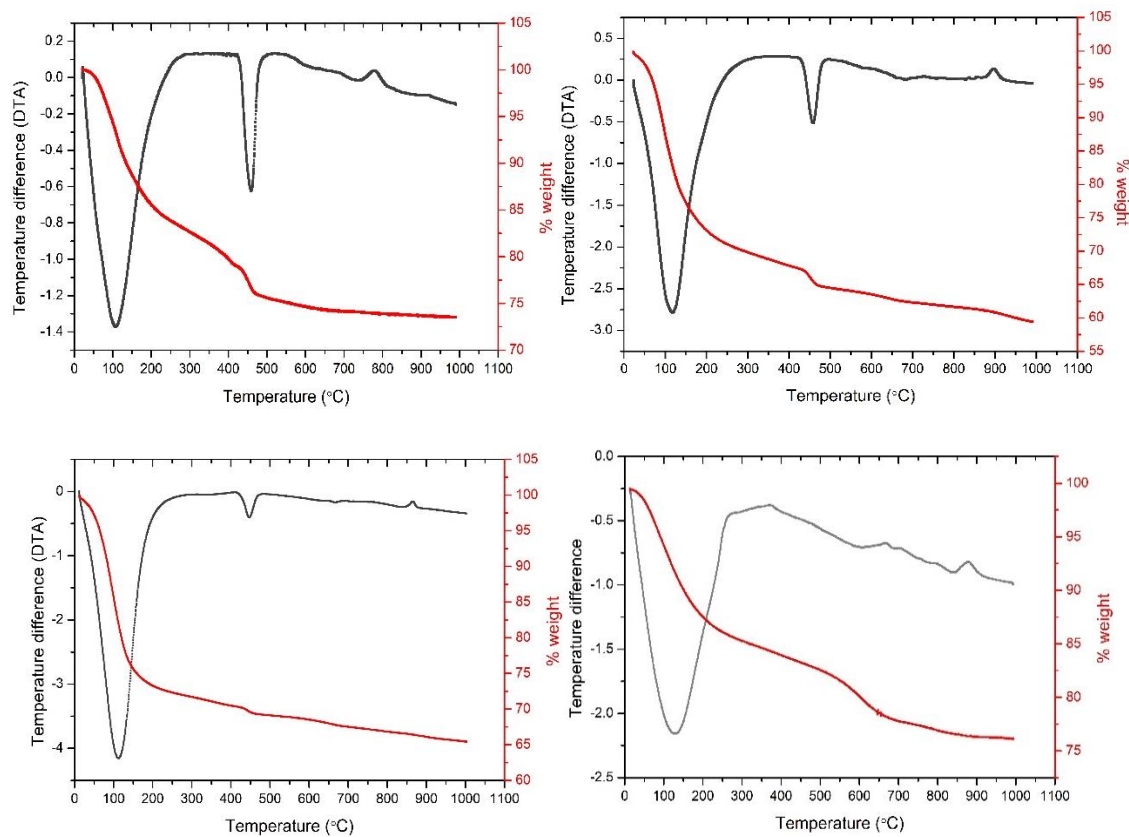


Figure 6.33 STA traces of BHC samples (top left: BHC – 1, top right: BHC – 2, bottom left: BHC – 3, bottom right: BHC – 4) showing DTA in grey and % TG in red.

Sample Name	% CH _{res}	% C \bar{C} _{res}
BHC – 1	7.25	-
BHC – 2	5.57	-
BHC – 3	3.48	-
BHC – 4	-	5.85

Table 6:11 % CH_{res} and % C \bar{C} _{res} in all the BHC samples calculated using tangent method.

The CH phase shows a decreasing trend as the reaction proceeds and the composition of C-S-H becomes stable with Ca/Si ratio increasing to 1.89 and 1.92 in 16 - day and 32 - day hydrated samples respectively. This increase in the Ca/Si ratio with the hydration time indicates that the CH phase re dissolves and reacts with the low Ca/Si ratio C-S-H phase to form C-S-H phase with a higher Ca/Si ratio.

The C-S-H samples when heated to 1000 °C, decomposed to form C₂S and this is evident from the ²⁹Si NMR analysis (Figure 6.34) on the sample heated to 1000 °C. The changes in the silicate anion structure explains the formation of C₂S. Both Q¹ and Q² species present in C-S-H transforms to Q⁰ species indicating the formation of C₂S. The spectrum clearly shows no presence of wollastonite.

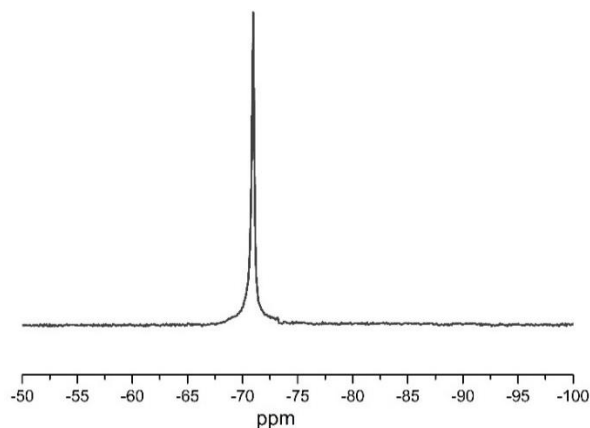


Figure 6.34 ²⁹Si NMR of C-S-H sample heated to 1000 °C.

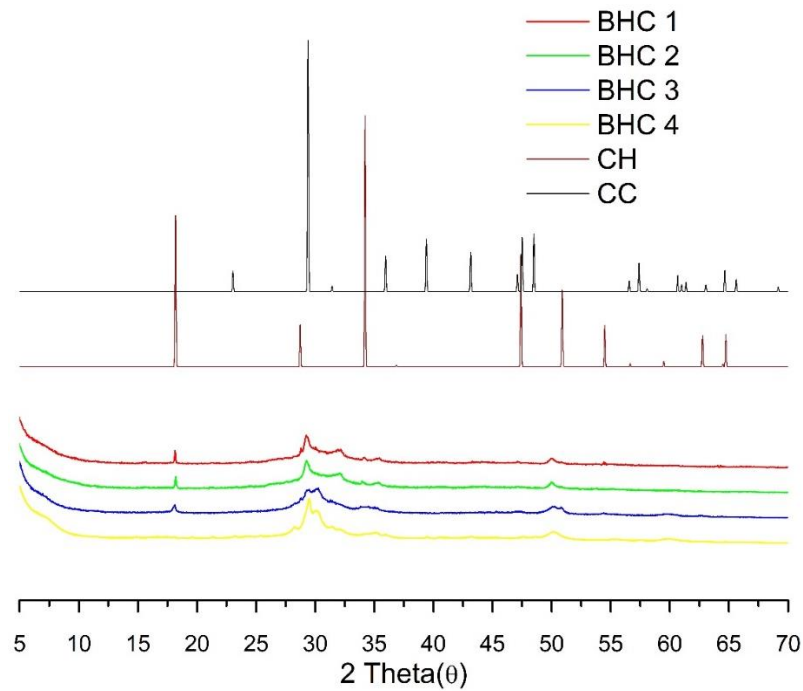


Figure 6.35 XRD patterns of BHC samples along with the reference patterns.

The XRD patterns of all the ball mill hydrated samples are shown in Figure 6.35. The hydration of β -C₂S is completed after 4 days and the resulting product consists of C-S-H and CH. After 16 days, the presence of CH is not observed indicating the presence of C-S-H monophase. However, there is presence $\bar{C}\bar{C}$ which could be from exposure to CO₂ either during the process of ball milling or during drying. The patterns clearly show the presence of CH phase ($2\theta \sim 18^\circ$) in BHC – 1, BHC – 2 and BHC – 3 and presence of $\bar{C}\bar{C}$ in BHC – 4. The CH phase dissolves and reacts with C-S-H as the hydration progresses. There is an indication of variation in basal reflections as Ca/Si ratio increases (BHC – 3 to BHC – 4), although this is not clearly resolved in the patterns.

6.4 Comparison of MCL variation with Ca/Si ratios for static and ball mill hydrated C-S-H phases with reported data from literature

The experimental MCL values (calculated from NMR analysis) of all the C-S-H samples discussed previously are plotted against the mean Ca/Si ratio values (obtained from TEM – EDX) in Figure 6.36. Reported data from literature is also plotted. The dotted lines represent the tobermorite lines with various degrees of protonation: minimum (right), intermediate (middle) and maximum (left) from Richardson and Groves' model. Maximum degree of protonation indicates that the negative charge is entirely balanced by protons in Si-OH groups. Intermediate degree of protonation indicates that the negative charge is balanced equally by proton in Si-OH and Ca. Minimum degree of protonation indicates that the negative charge is balanced entirely by Ca. The experimental data points from this work are comparable to the reported data from literature and all the data fall to the right of the right dotted line indicating the need of presence of Ca-OH groups in the structure. The reported data from literature suggests that there is a drastic decrease in MCL up to Ca/Si ≈ 1 , followed by a slight decrease up to Ca/Si ≈ 1.3 , after which MCL almost remains constant (≈ 3) with increase in Ca/Si ratios. This indicated the formation of dimeric silicate structure and change in MCL is very less after this. The variations in the silicate structure noticed as Ca/Si ratio increases are due to the removal of bridging tetrahedra and incorporation of additional Ca²⁺ ions.

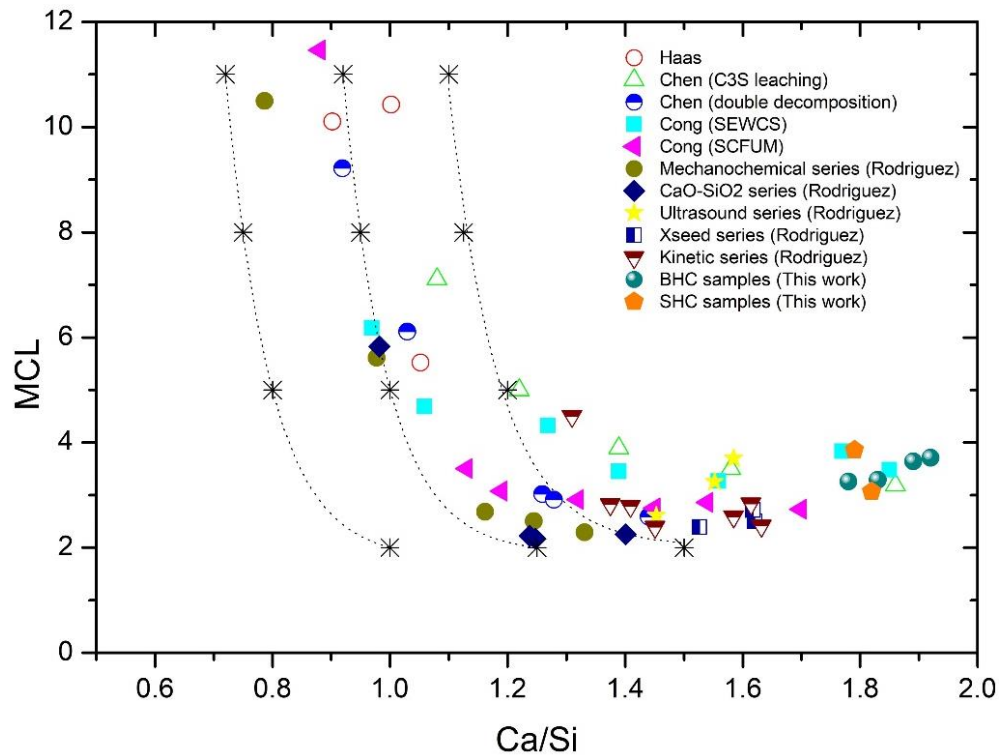


Figure 6.36 Variation of MCL with mean Ca/Si ratios for all the C-S-H samples synthesized. Reported data from literature is also plotted along with various degrees of protonation from Richardson and Groves' model [31][40][41][45][63][163].

The variations in % of silicate species with hydration time for all static and ball mill hydrated samples is illustrated in Figure 6.37. In case of static hydrated samples both Q^1 and Q^2 increase as Q^0 decreases and the amount of Q^1 formed is greater than Q^2 . The Ca^{2+} ion concentration from dissolution of $\beta-C_2S$ decreases with the formation of C-S-H and % Q^1 species increases. In case of ball mill hydrated samples, once all the $\beta-C_2S$ is transformed to C-S-H and CH, intensity of Q^1 species decreases and Q^2 species increases. Once C-S-H becomes a monophase, both Q^1 and Q^2 remains almost constant. However, further data points are required to study this trend.

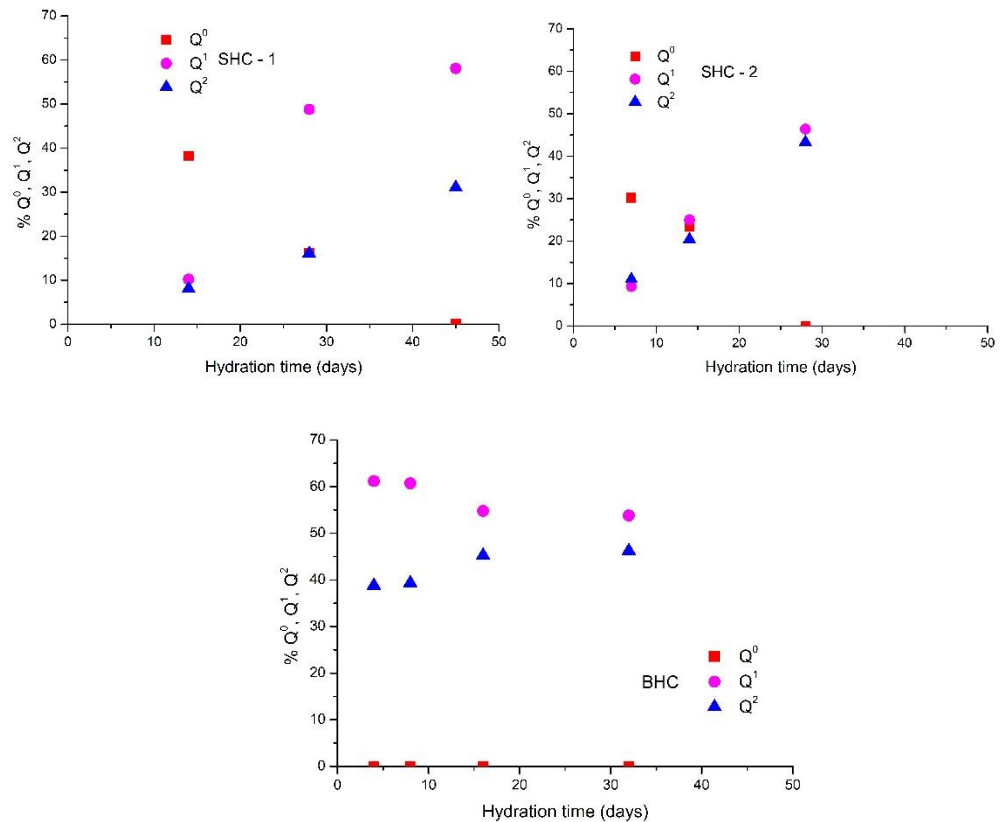


Figure 6.37 Variations of % Q^0 , Q^1 and Q^2 for all the samples plotted against hydration times (top left: SHC samples hydrated at w/s = 0.5, top right: SHC samples hydrated at w/s = 1.0, bottom: BHC samples hydrated at w/s = 10).

The variation in MCL with hydration time of all the samples is shown in Figure 6.38. The MCL in static hydrated samples decreases with the hydration time until all the β - C_2S is transformed to C-S-H and CH. Once all the β - C_2S is transformed to C-S-H and CH, the MCL in ball mill hydrated samples increases with the hydration time and once C-S-H becomes a monophase the MCL approaches an almost constant value. However, further data points are required to study this trend. In ball mill hydration dimer formed is continuously removed by the process of milling and after hydration, polymerization of dimeric species results in high MCL. The rate of hydration of β - C_2S is faster in ball mill hydration process than

in static hydration process. In both ball mill and static hydration methods the C-S-H formed consists of Q¹ and Q² silicate tetrahedra indicating that it is a mixture of dimers and middle chain groups.

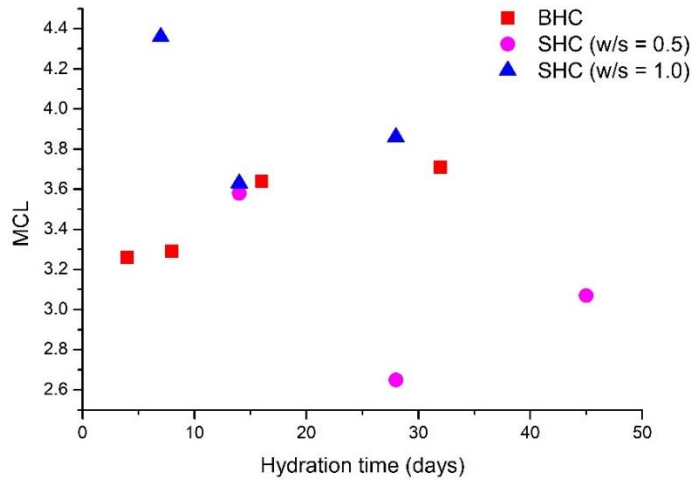


Figure 6.38 Variation of MCL plotted against hydration time for static and ball mill hydrated samples.

Chapter 7 Results and discussion of C-S-H phases synthesised by constant lime concentration method

7.1 Characterization Results of C-S-H phases (described in Table 4.8, Experimental Methods)

7.1.1 TEM - EDX

The TEM micrographs of all the samples are shown in Figures 7.1 – 7.8. The morphology of C-S-H changes from foils to fibrillar as the transition happens from low to high Ca/Si ratio. The TEM micrographs of the C-S-H phases formed at higher temperatures 25 °C and 20 °C and lower lime concentrations (Figure 7.1 and Figure 7.2) show crumpled foil-like morphology that resembles the morphology found in blends of Portland cement and GGBS or neat slag pastes [31] while the TEM micrographs of the C-S-H formed at intermediate temperatures, 15 °C and 10 °C, and therefore increased lime concentrations (Figure 7.3 and Figure 7.4) show C-S-H morphology to be a mixture of foils and fibres. The morphology of the C-S-H phases showed a transformation to dense fibrous morphology at temperatures 5 °C and 1 °C and higher lime concentrations (Figure 7.5 and Figure 7.6). These morphologies resemble the morphologies found in CEM I system, where C-S-H has a Ca/Si ratio of 1.75 and a fibrillar morphology [17]. The morphology is seen to change from foils to fibres with increasing Ca/Si ratio or decreasing content of slag in water activated OPC – slag mixtures [3][124]. However, in alkali activated systems, the morphology remains foil-like despite an increase in Ca/Si ratios [31]. Several researchers observed the transition from foils to fibres with increase in Ca/Si ratio. Grudemo [9] reported the change in morphology from foils to fibres as the Ca/Si ratio increases from

low to high. Kalousek and Prebus [47] also observed a similar change in morphologies from foils to fibres. C-S-H phases with Ca/Si ratios in the range 0.8 – 1.33 showed foil-like morphology while C-S-H phases with Ca/Si ratios in the range 1.5 – 2.0 showed agglomerates and fibrillar morphology. However, few of their samples synthesized are not homogeneous and are possibly a mixture of low Ca/Si C-S-H phase and fibrous lime – rich phase. Rodriguez [164][63] reported the change and transition in morphologies of C-S-H phases synthesized via C_3S hydration under controlled lime concentrations as Ca/Si ratios increases from foils to fibres (see literature review for further details). The morphology of C-S-H phases in AR- 7 and AR – 8 (Figure 7.7 and Figure 7.8) shows the presence of some spiky fibres. The micrographs clearly show that the reaction temperature affects the morphology of C-S-H formed. Higher lime concentrations are achieved at lower temperatures and hence this suggests that the morphology of C-S-H phases formed is determined by the lime concentration. In samples AR – 6, AR – 7, and AR – 8 the reaction temperature remained constant but the rate of addition of TEOS differed. This change noticed in the morphology with respect to lime concentrations explains the transition from fibres to foils in hydration of OPC – slag systems. C-S-H having foil-like morphology is seen to grow from fully reacted PFA particles which have high content of SiO_2 and low content of CaO, while fibrillar morphology is seen in regions of OPC – PFA systems which are exposed to Ca^{2+} rich chemical environments [165]. The EDX points are carefully chosen in areas where the diffraction patterns are free from spots suggesting that the area chosen is amorphous and free from any crystalline phases. The morphology seen in AR – 6, AR – 7 and AR – 8 synthesised at 1 °C and a lime concentration of 26 mmol/L resemble the morphology observed by Rodriguez

[164] at a lime concentration of 27 mmol/L for C-S-H phase synthesised by hydration of C_3S keeping the lime concentration constant.

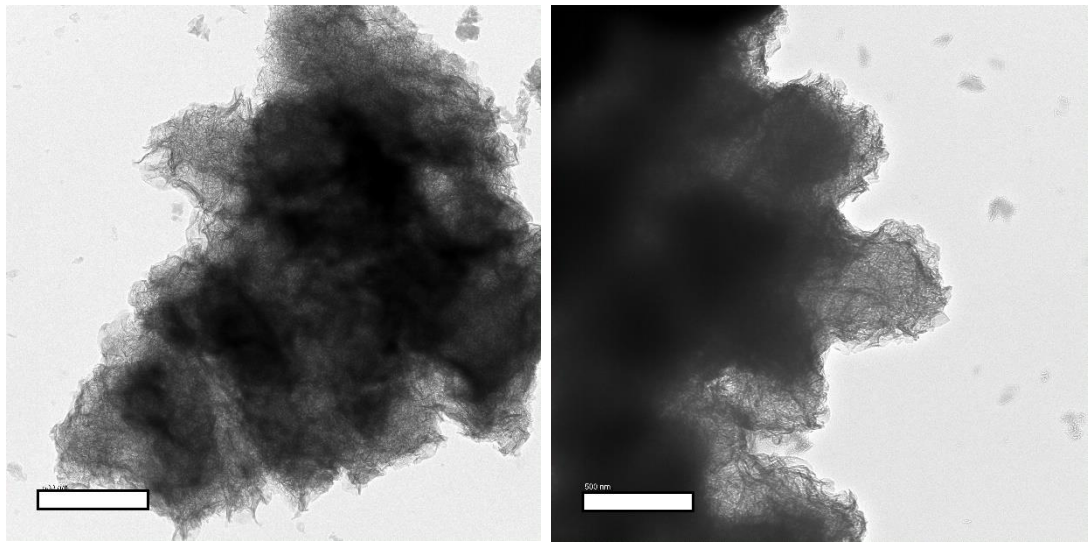


Figure 7.1 TEM micrographs of AR – 1 (synthesized at 25 °C) showing foil-like C-S-H with Ca/Si = 1.51.

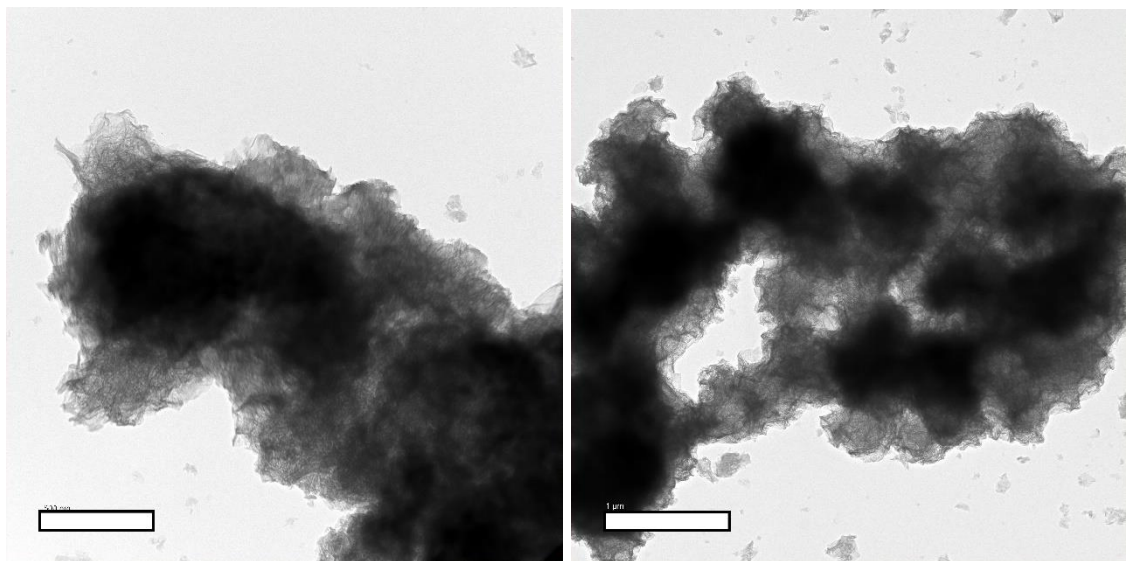


Figure 7.2 TEM micrographs of AR – 2 (synthesized at 20 °C) showing foil-like C-S-H with Ca/Si = 1.56.

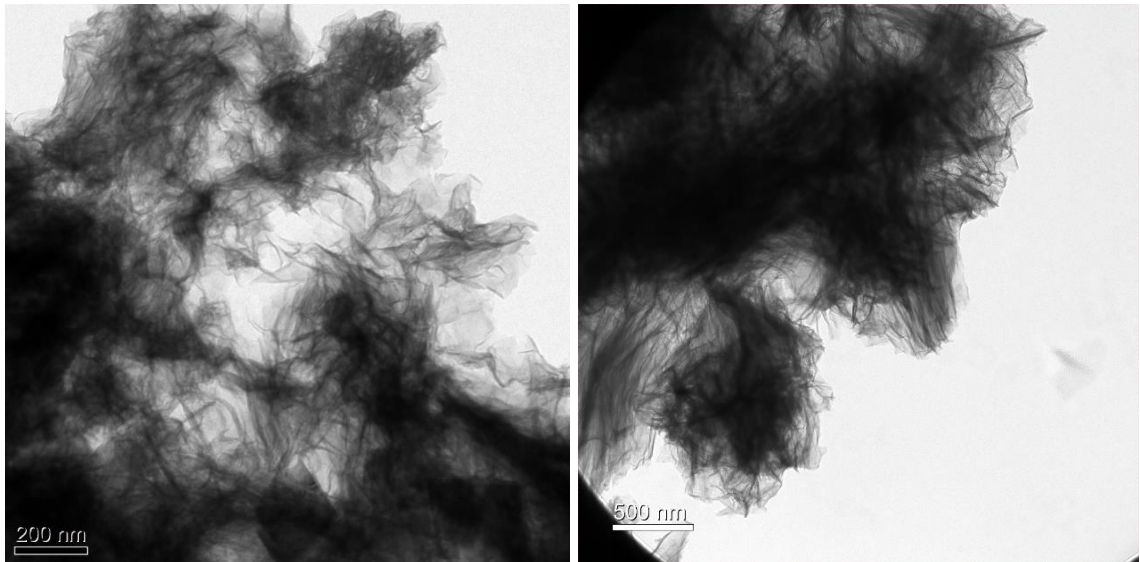


Figure 7.3 TEM micrographs of AR – 3 (synthesized at 15 °C) showing mixture of foils and fibres with Ca/Si = 1.61.

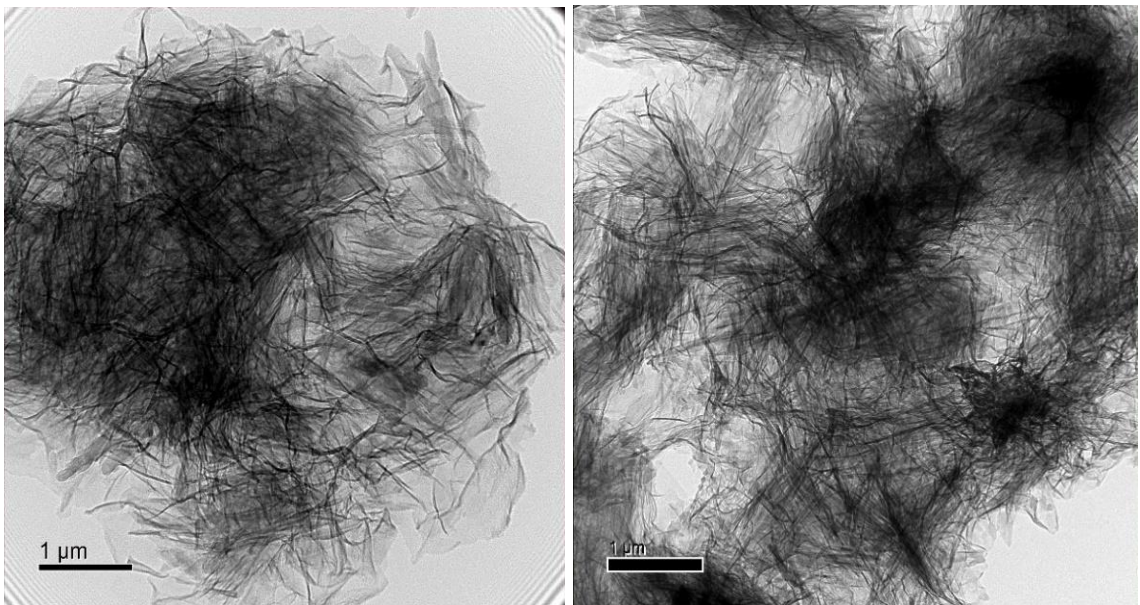


Figure 7.4 TEM micrographs of AR – 4 (synthesized at 10 °C) showing mixture of foils and fibres with Ca/Si = 1.64.

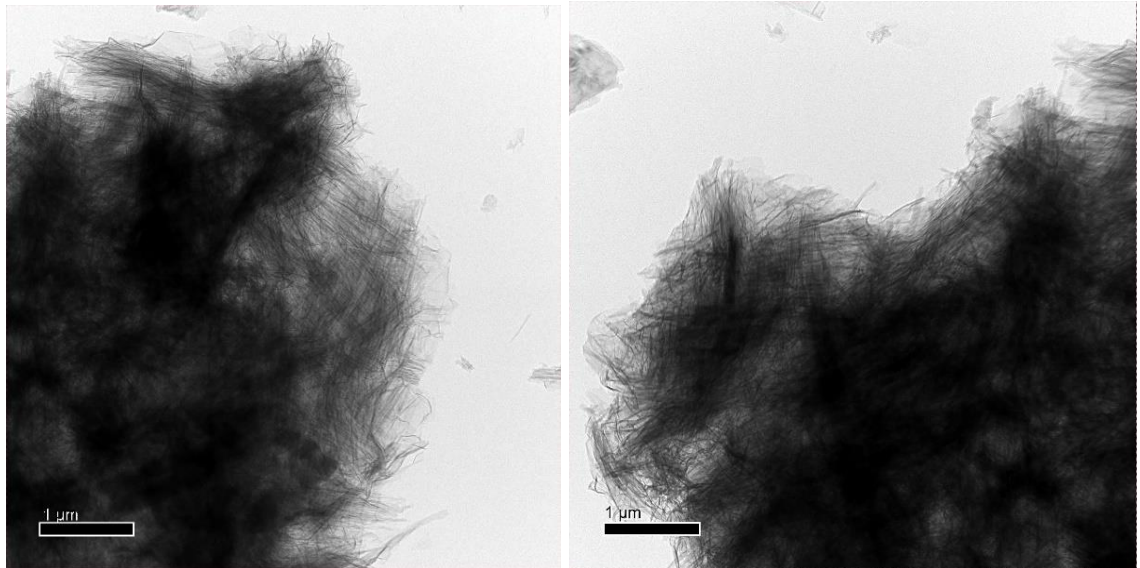


Figure 7.5 TEM micrographs of AR – 5 (synthesized at 5 °C) showing fibrillar C-S-H with Ca/Si = 1.69.

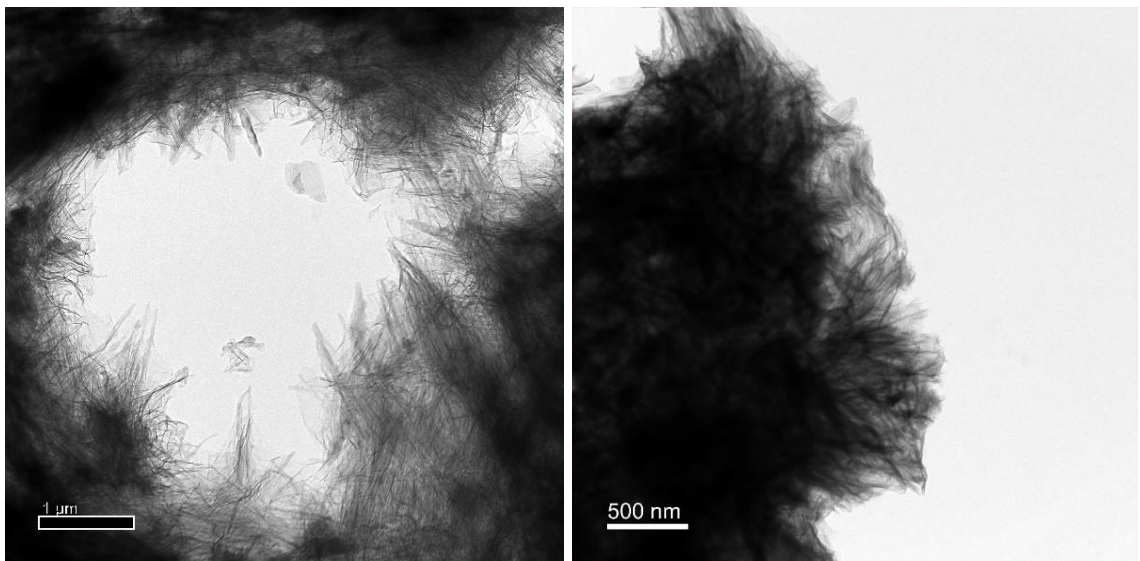


Figure 7.6 TEM micrographs of AR – 6 (synthesized at 1 °C) showing fibrillar C-S-H with Ca/Si = 1.74.

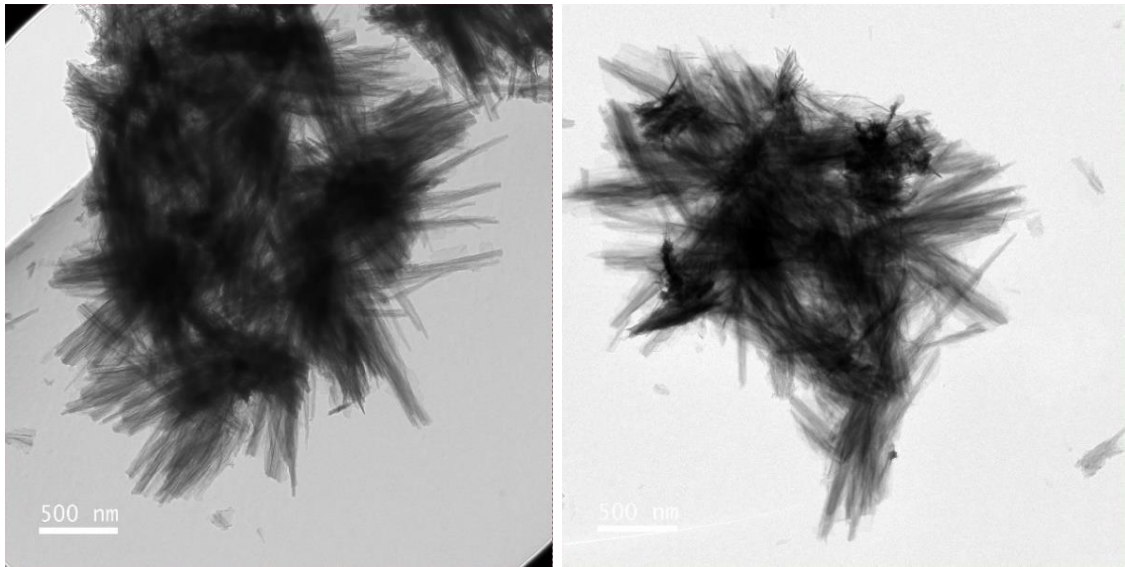


Figure 7.7 TEM micrographs of AR – 7 (synthesized at 1 °C) showing spiky fibres with Ca/Si = 1.79.

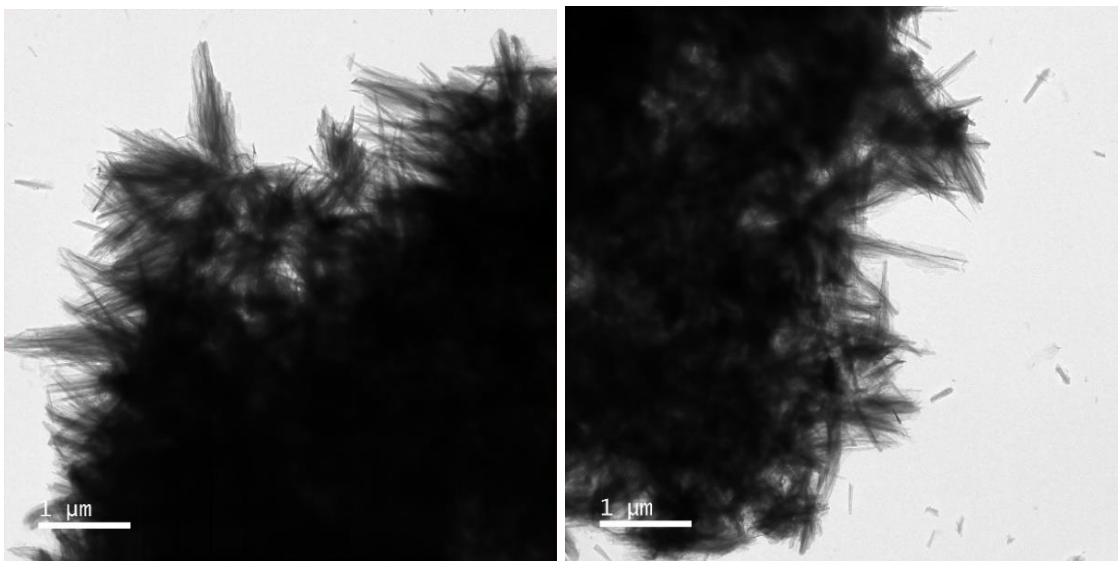


Figure 7.8 TEM micrographs of AR – 8 (synthesized at 1 °C) showing spiky fibres with Ca/Si = 1.81.

Sample Name	Ca/Si	N*	S.D
AR - 1	1.51	32	0.03
AR - 2	1.56	37	0.03
AR - 3	1.61	35	0.02
AR - 4	1.64	39	0.02
AR - 5	1.69	47	0.03
AR - 6	1.74	57	0.03
AR - 7	1.79	61	0.02
AR - 8	1.81	60	0.04

N*: number of analyses

Table 7:1 Atomic ratios of C-S-H phases obtained by TEM – EDX.

The Ca/Si ratios of all the samples are obtained by TEM – EDX analysis. The results are summarised in Table 7:1. Figure 7.9 shows the histograms of the Ca/Si ratios obtained from TEM -EDX analysis.

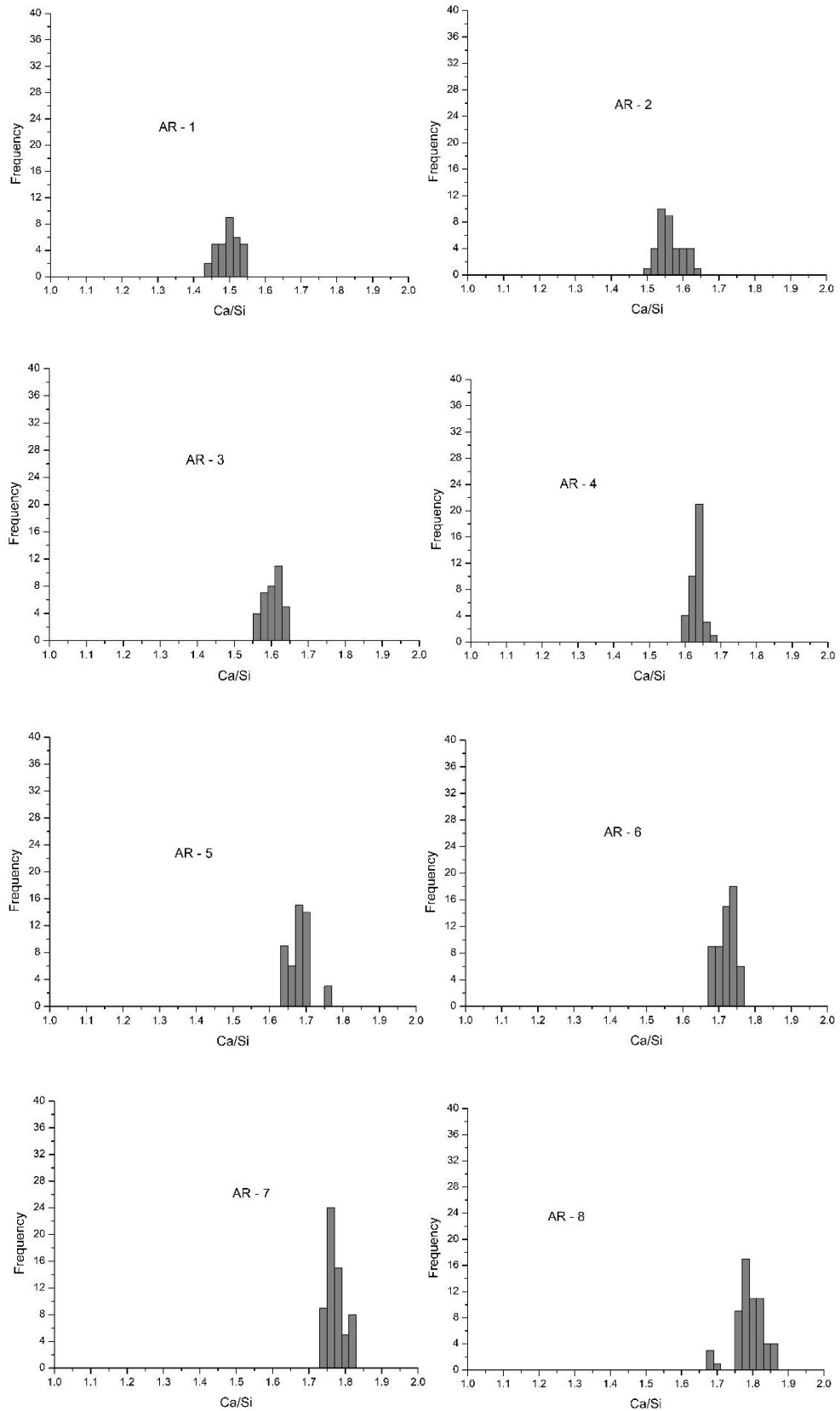


Figure 7.9 Histograms of Ca/Si ratios measured using TEM – EDX.

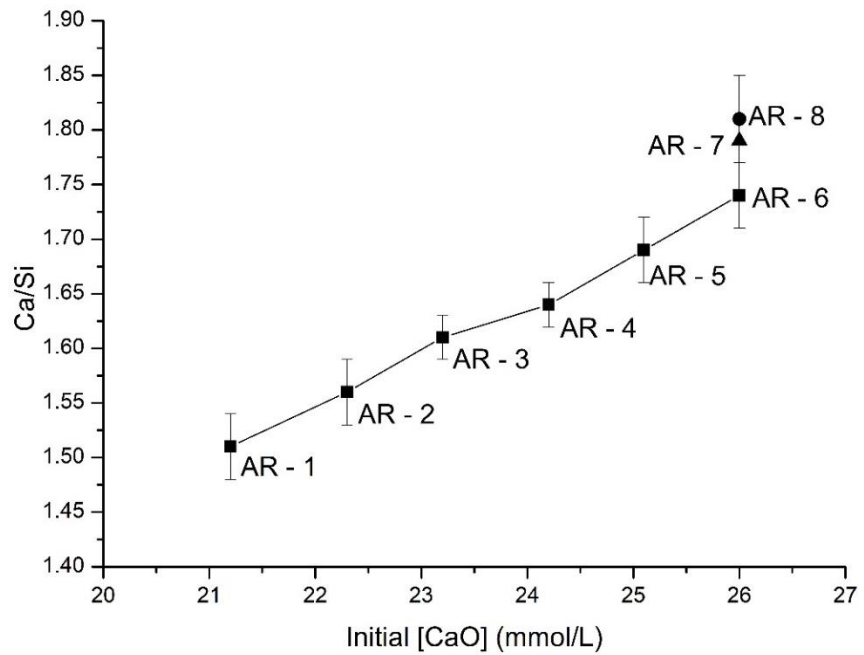
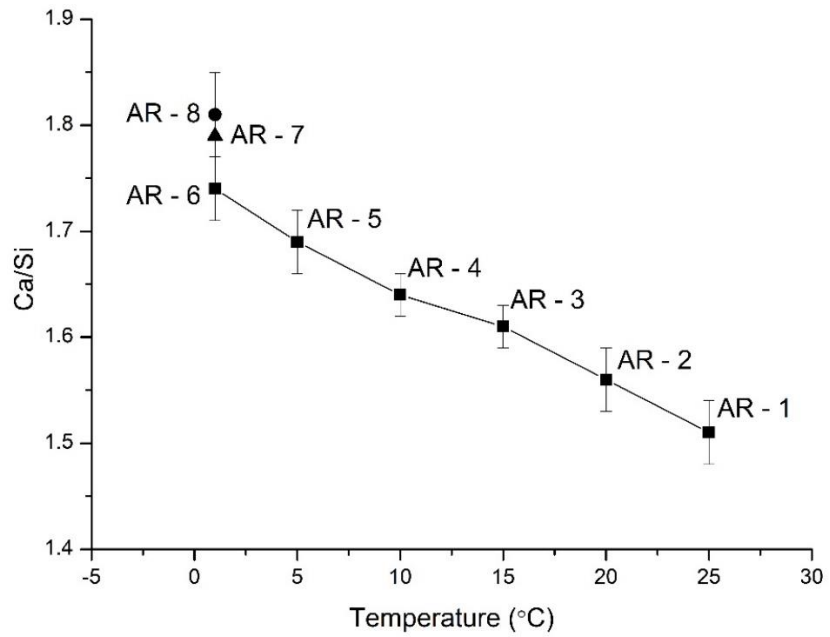


Figure 7.10 Ca/Si ratios obtained from TEM – EDX plotted against reaction temperature (top) and initial lime concentration (bottom). The length of the vertical bars represents the minimum and maximum Ca/Si values and the dark circles represent the mean values.

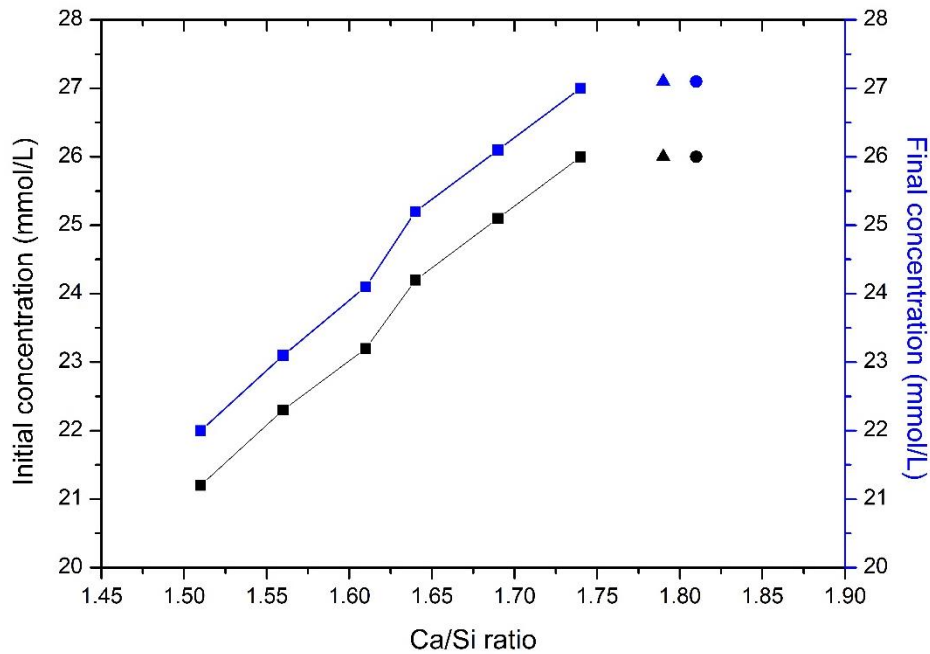


Figure 7.11 Mean Ca/Si ratios of the samples with the corresponding initial and final lime concentrations measured.

The solubility of lime increases with a decrease in temperature (see Experimental Methods) and the Ca/Si ratio increases with the decrease in temperature and increase in lime concentration in solution (as shown in Figures 7.10 and 7.11). This happens as there is more Ca^{2+} available to react when lime concentration increases, and the solution is supersaturated with respect to CH.

Taylor [4] synthesized C-S-H phases via various methods having Ca/Si ratios between 0.68 and 1.5 (see Literature Review). Grudemo [9] synthesized C-S-H phases via constant lime concentration method having Ca/Si ratios between 0.678 and 1.558 (see Literature Review). Figure 7.12 shows the plot of Ca/Si ratio in solid vs [CaO] concentration in solution after the synthesis from the current work along with the data reported in literature. Figure 7.13 shows the points depicting data from Taylor's and Grudemo's work along with the data points from the current work. The C-S-H formed at higher temperatures are lower in lime

content and as the temperature decreases, the lime concentration increases. The data points from this work form an extension to the trend line marked by the experimental points reported by Grudemo [9]. The two data points depicting the experiments conducted at 1 °C and 26 mmol/L with different rate of addition of TEOS shows a slight increase in the Ca/Si ratios measured. This shows that another factor affecting the formation of C-S-H phases apart from the lime concentration is the rate of addition of TEOS. However, further experimental data points are required to confirm this. As the rate of addition of TEOS differed, a nanostructurally different C-S-H phase is formed due to slower formation of C-S-H, and this is evident from the spiky fibres seen in TEM micrographs for AR – 7 and AR – 8.

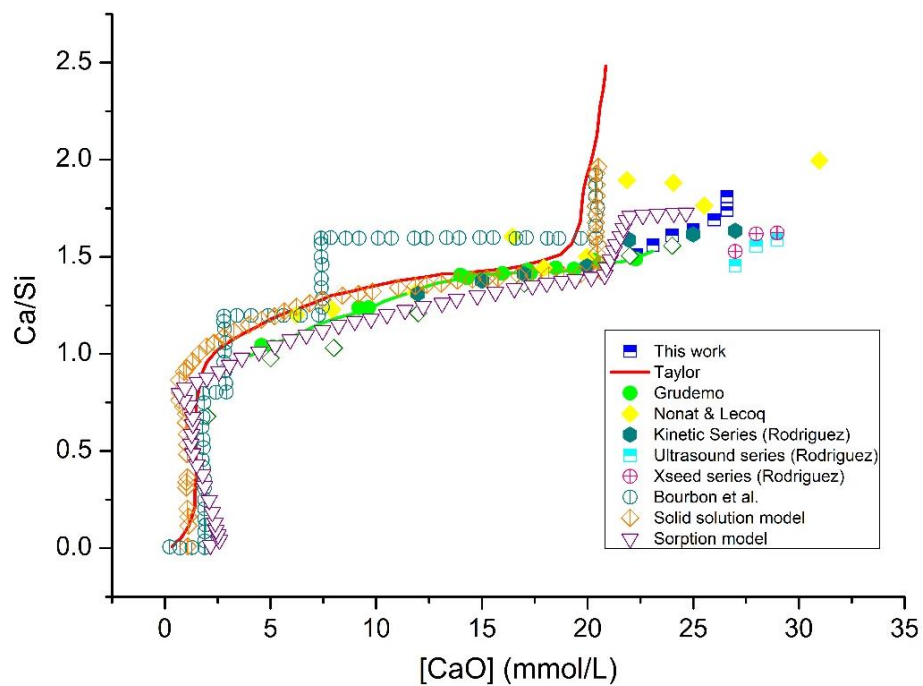


Figure 7.12 Ca/Si ratio vs [CaO] in solution for the present work. Other data reported by Taylor [4], Grudemo [9], Nonat and Lecoq [61], Rodriguez [63], Bourbon et al. [166], Kulik [167] and Haas and Nonat [163] are also plotted.

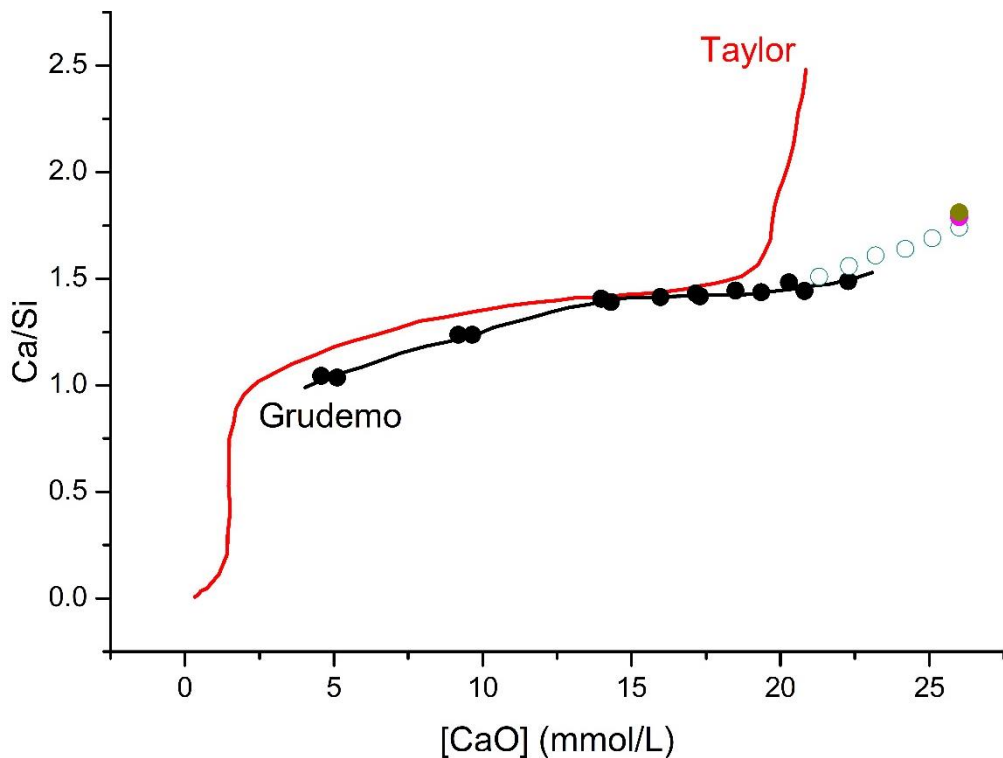


Figure 7.13 Ca/Si ratios vs [CaO] in solution depicting data from Taylor's [4], Grudemo's [9] and current work (blue). The plot on the right side is the enlarged version of the data points from current work.

7.1.2 ²⁹Si NMR

The ²⁹Si NMR spectra for the C-S-H phases synthesised by constant lime concentration method are shown in Figures 7.14 - 7.21. The results are deconvoluted to estimate the percentage of silicate groups and the mean chain length. The deconvoluted spectra, the individual frequencies and the simulated spectra, are all shown in the Figures below. The peaks in the range $\delta = -76$ ppm to $\delta = -80$ ppm corresponds to the presence of Q¹ groups while the peaks in the range $\delta = -82$ ppm to $\delta = -85$ ppm correspond to the presence of Q² groups.

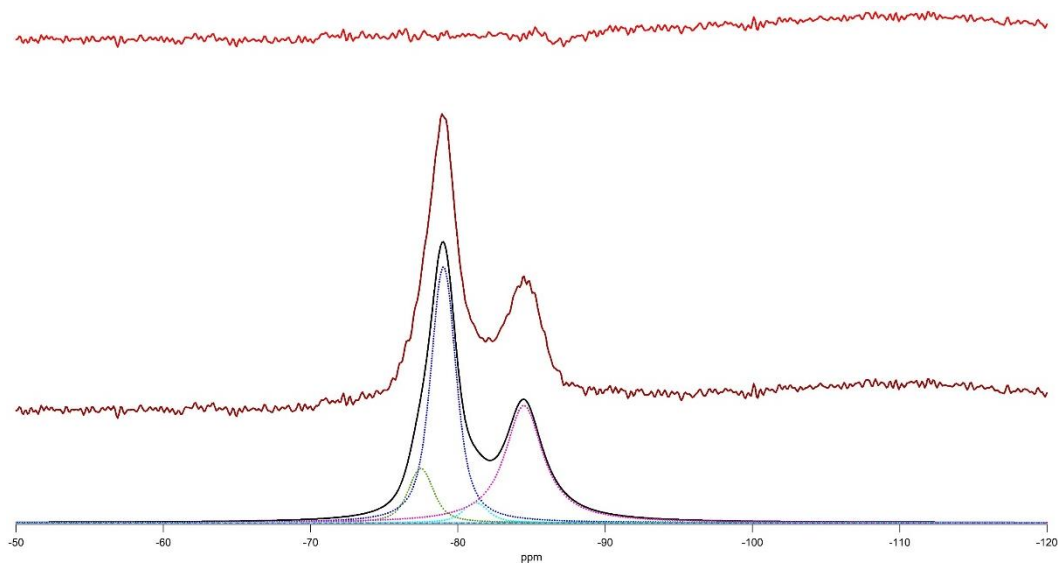


Figure 7.14 ^{29}Si NMR spectra for AR – 1 including experimental spectrum (middle, brown), residual (top, red x1) and the individual frequencies.

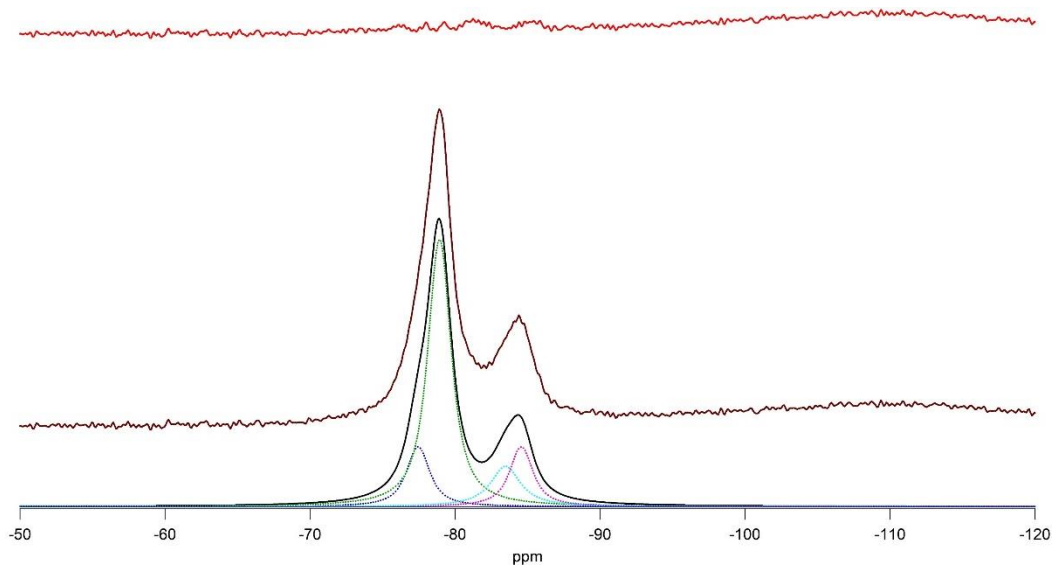


Figure 7.15 ^{29}Si NMR spectra for AR – 2 including experimental spectrum (middle, brown), residual (top, red x1) and the individual frequencies.

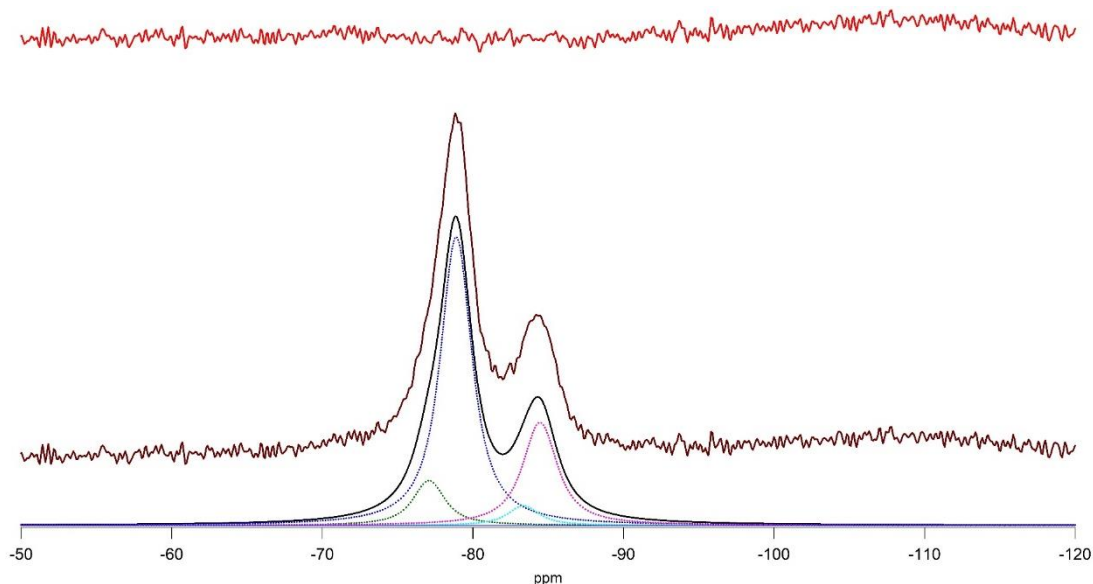


Figure 7.16 ^{29}Si NMR spectra for AR – 3 including experimental spectrum (middle, brown), residual (top, red x1) and the individual frequencies.

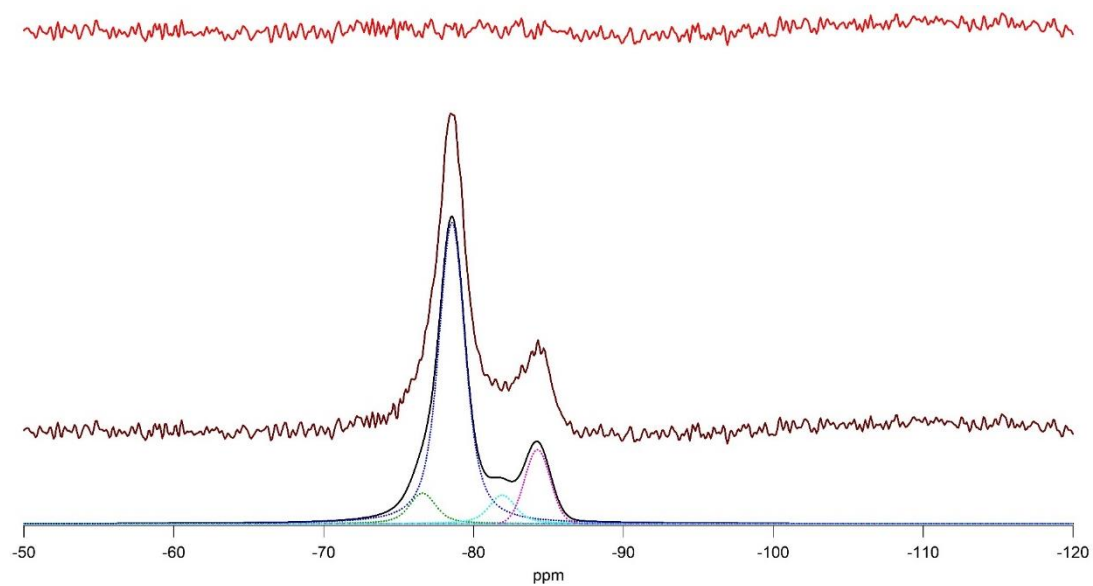


Figure 7.17 ^{29}Si NMR spectra for AR – 4 including experimental spectrum (middle, brown), residual (top, red x1) and the individual frequencies.

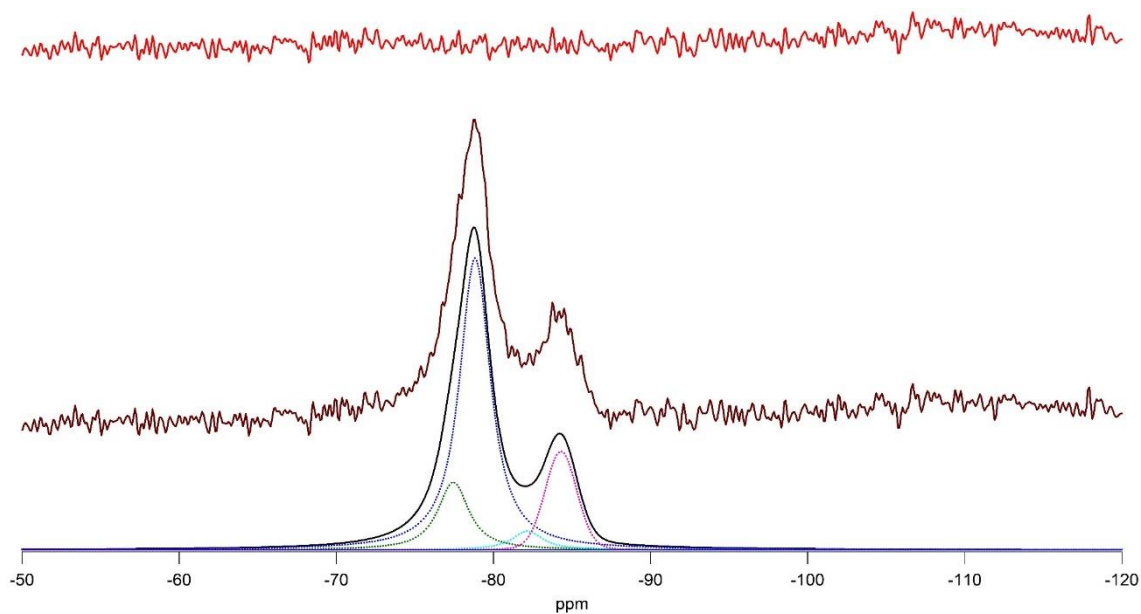


Figure 7.18 ^{29}Si NMR spectra for AR – 5 including experimental spectrum (middle, brown), residual (top, red x1) and the individual frequencies.

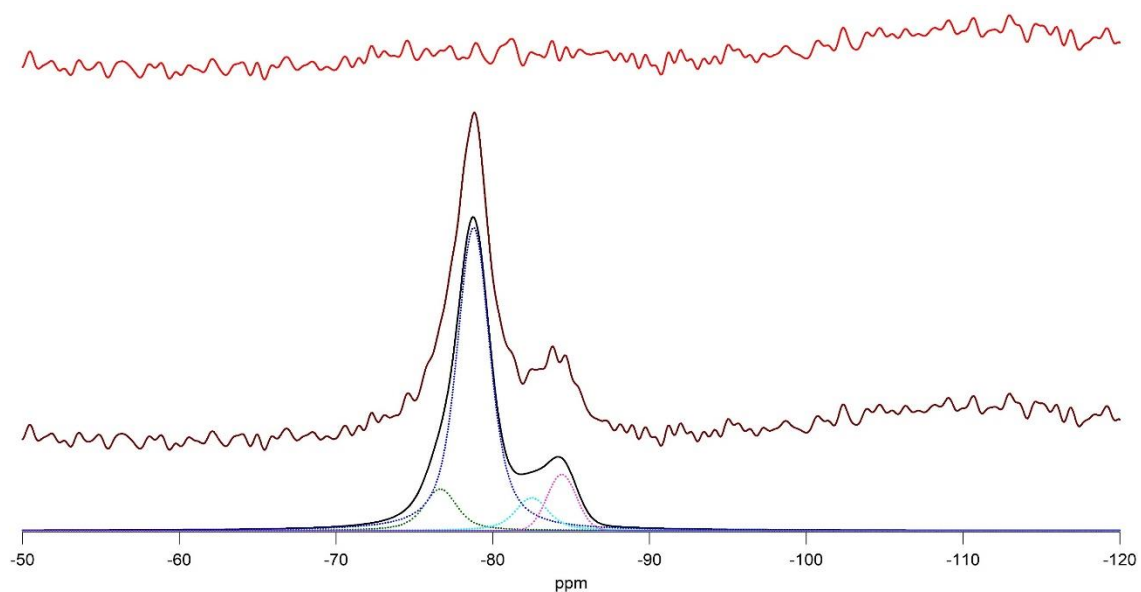


Figure 7.19 ^{29}Si NMR spectra for AR – 6 including experimental spectrum (middle, brown), residual (top, red x1) and the individual frequencies.

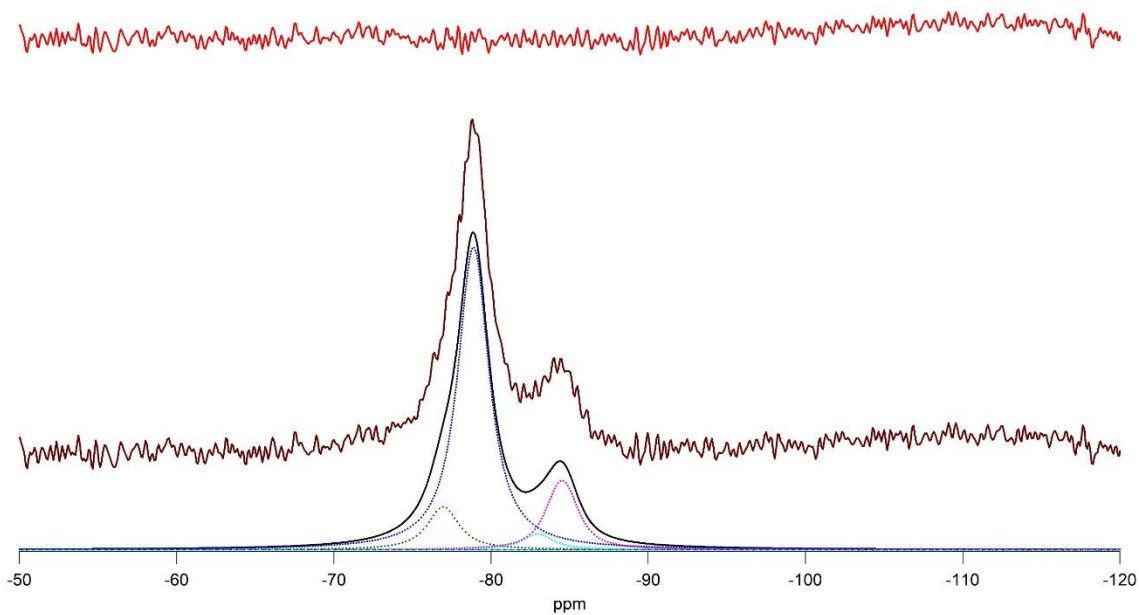


Figure 7.20 ^{29}Si NMR spectra for AR – 7 including experimental spectrum (middle, brown), residual (top, red x1) and the individual frequencies.

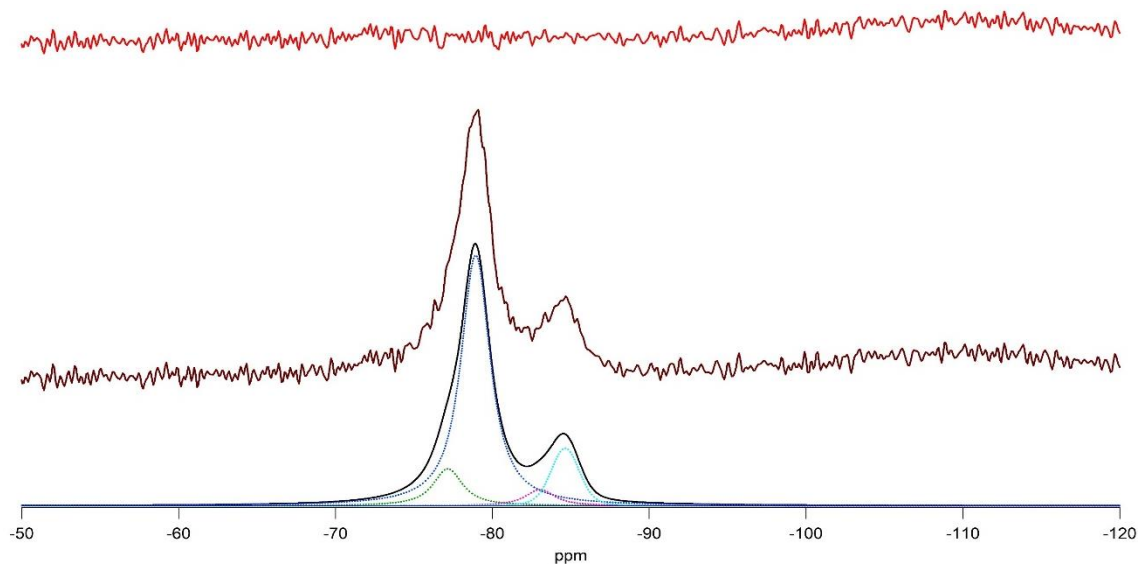


Figure 7.21 ^{29}Si NMR spectra for AR – 8 including experimental spectrum (middle, brown), residual (top, red x1) and the individual frequencies.

Sample	Q ¹ (ppm)		Q ² (ppm)	
AR - 1	-77.48	-79.02	-81.20	-84.48
AR - 2	-77.45	-78.93	-83.48	-84.57
AR - 3	-77.08	-78.89	-83.36	-84.46
AR - 4	-76.60	-78.56	-81.91	-84.26
AR - 5	-77.44	-78.82	-82.16	-84.29
AR - 6	-76.65	-78.77	-82.49	-84.40
AR - 7	-77.95	-78.88	-82.98	-84.51
AR - 8	-77.16	-78.93	-83.04	-84.64

Table 7:2 Chemical shifts of Q¹ and Q² peaks used for deconvolutions of the spectra.

The absence of Q³ groups at $\delta = -94$ ppm indicates that only single dreierketten are present. The spectra show more intensity originating from Q¹ groups than Q² groups. The presence of these groups indicate that the hydrate possesses dimers or end chain groups and middle chain groups. The intensity of Q¹ groups become stronger as the reaction temperature decreases. An increased amount of end chain groups can be seen in the spectra for the C-S-H phases synthesised at 1 °C. Two frequencies each are used to deconvolute Q¹ and Q² contributions to improve the fitting of the asymmetric peaks and adjust the simulated spectra and the experimental spectra. Although these frequencies are used for deconvolutions, they do not directly represent the species present as the line widths and shapes of the frequencies vary between the samples. The relaxation

of these parameters during the fitting process resulted in these variations. Table 7:2 shows the variations in the chemical shifts in all spectra.

Sample	Q ¹ (%)	Q ² (%)	MCL	Ca/Si _{TEM-EDX}	Reaction temperature (°C)
AR - 1	57.7	42.2	3.46	1.51	25
AR - 2	74.0	26.0	2.70	1.56	20
AR - 3	71.6	28.4	2.79	1.61	15
AR - 4	79.5	20.5	2.51	1.64	10
AR - 5	79.9	20.1	2.50	1.69	5
AR - 6	82.7	17.3	2.41	1.74	1
AR - 7	81.1	18.8	2.46	1.79	1
AR - 8	83.0	17.1	2.40	1.81	1

Table 7:3 Results of deconvolution of the ²⁹Si NMR spectra: % silicate species and MCL.

Figure 7.22 shows mean silicate chain length (MCL) plotted as a function of Ca/Si ratio and it is clearly seen that as Ca/Si ratio increases, the MCL decreases. The decrease in mean chain length may be due to low Si concentrations and high Ca concentrations in solution and as a result Ca/Si ratio of C-S-H increases. Also, as the lime concentration increases, there is more available Ca and the pH increases thus forming Ca-OH bonds.

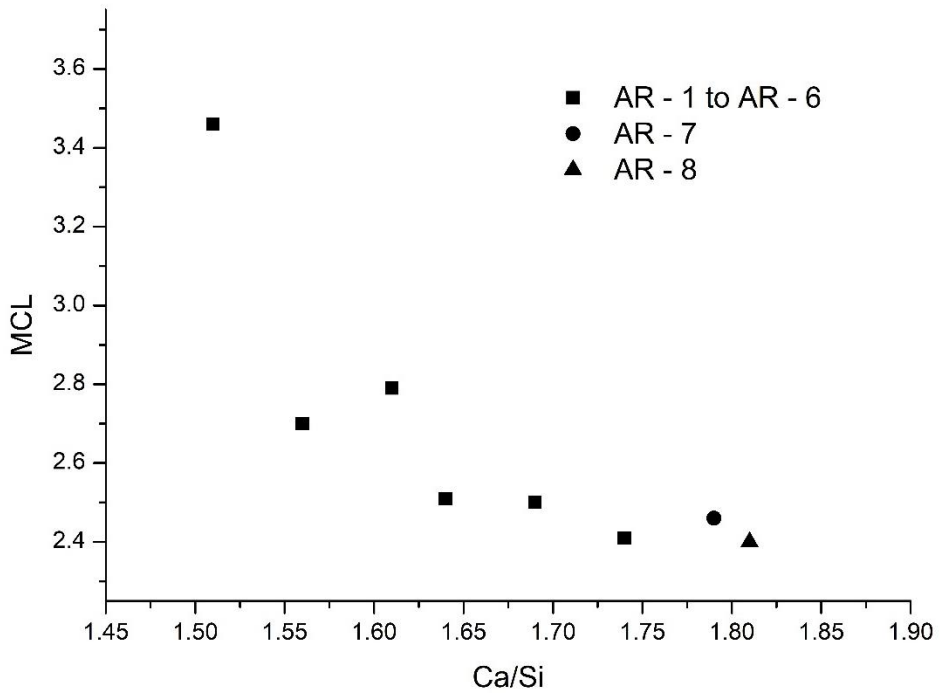


Figure 7.22 Mean silicate chain lengths calculated from ^{29}Si NMR data plotted against mean Ca/Si ratios calculated from TEM - EDX.

The MCL calculated is shown in Table 7:3 and it follows a decreasing trend as the reaction temperature drops from 25 °C to 1 °C. In the samples AR – 6, AR – 7 and AR – 8 the reaction temperature remained constant but the rate of addition of TEOS differed. As the TEOS addition rate decreases, the percentage of end chain groups increase further and the MCL decreases. The presence of less silica in the samples with high Ca/Si ratio C-S-H phases indicate the formation of dimeric silicate units rather than long silicate chains. This supports the decreasing trend in MCL with increasing Ca/Si ratios.

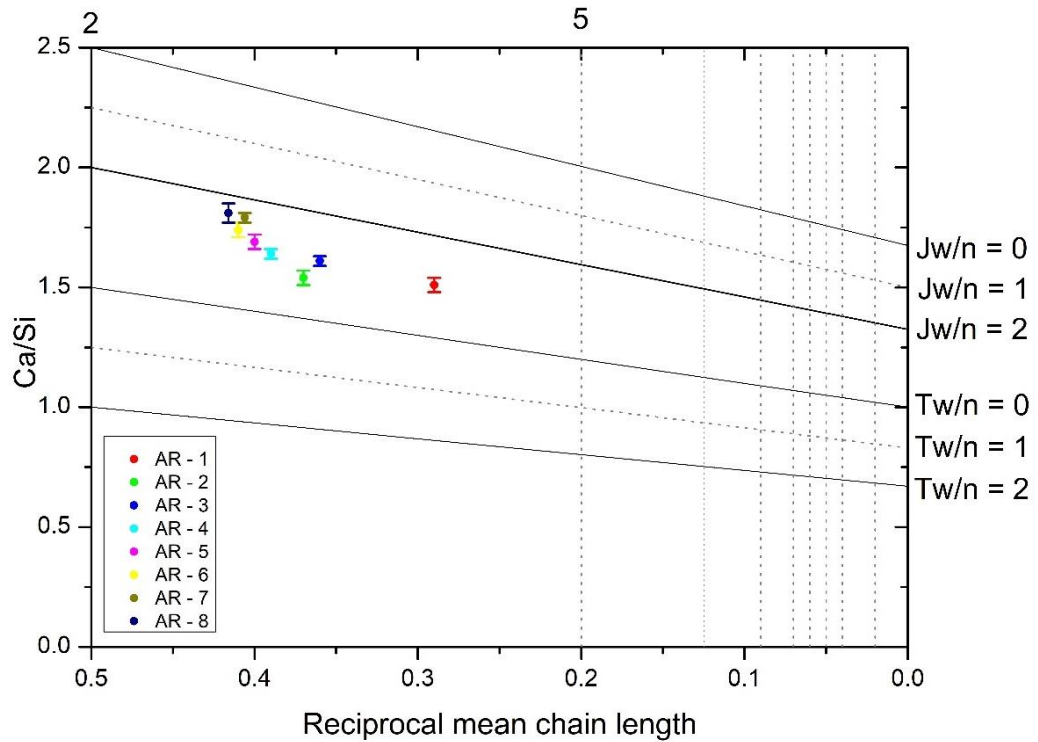


Figure 7.23 Ca/Si obtained by TEM-EDX analysis versus reciprocal mean chain length obtained by NMR analysis. The structural units for tobermorite and jennite with minimum ($w=0$), intermediate ($w=1$) and maximum ($w=2$) degree of protonation are plotted along with data points from current work. The vertical dashed lines represent the $(3n - 1)$ structural units: dimer (2), pentamer (5) etc.

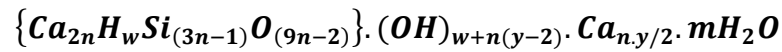
Richardson and Groves' model (described in Literature Review) is used for the formulation of the C-S-H phases synthesized. Figure 7.23 shows the Ca/Si ratios plotted against the reciprocal MCL. The Figure also shows the trends for tobermorite and jennite units with various degrees of protonation ($w = 0, 1, 2$). The mean values of Ca/Si ratios represented by filled circles in the Figure above fall between the tobermorite and jennite like regions on the plot, thus confirming the presence of Ca-OH groups in the structure coming either from jennite like structures or solid solution CH. In T/J viewpoint, the Ca-OH groups form a part of

the main layer and in T/CH viewpoint, the Ca-OH groups are present in the interlayers. The SAED patterns does not show the presence of any crystalline CH phase and T/J viewpoint seems to be more suitable but the presence of CH cannot be completely excluded. Both the viewpoints have been used to derive the structural chemical formula. However, the removal of Ca by the process of leaching (discussed in the chapter 8) helps to identify the most suitable viewpoint. Since leaching resulted in the alteration of both Ca/Si ratio and silicate structure, it is indicative that the C-S-H phases are a combination of tobermorite and jennite units and follow T/J view point. The alteration of both Ca/Si ratio and silicate structure after leaching suggests that the Ca is removed from the main layers rather than the interlayers.

Sample	n	y	W _{min}	W _{max}
AR - 1	1.49	3.03	0	2.98
AR - 2	1.23	2.83	0	2.47
AR - 3	1.26	3.11	0	2.53
AR - 4	1.17	3.04	0	2.34
AR - 5	1.17	3.25	0	2.34
AR - 6	1.14	3.39	0	2.28
AR - 7	1.15	3.64	0	2.31
AR - 8	1.14	3.68	0	2.27

Table 7:4 Calculated values required for the formulation using T/J viewpoint.

The general formula for T/J viewpoint:



Where, $n = (MCL+1)/3$ and $y = [(Ca/Si)(6n-2)-4n]/n$

w depends on the value of y

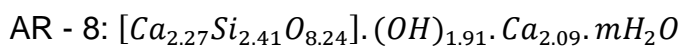
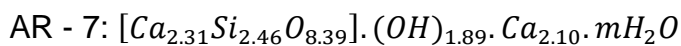
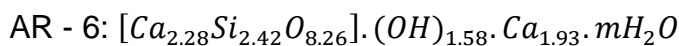
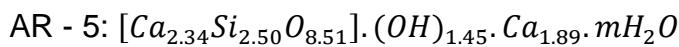
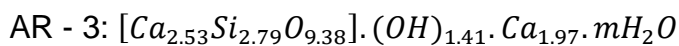
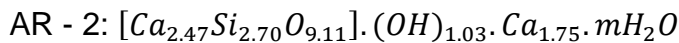
if, $0 \leq y \leq 2$ then $n(2-y) \leq w \leq 2n$

if, $2 \leq y \leq 4$ then $0 \leq w \leq 2n$

if, $4 \leq y \leq 6$ then $0 \leq w \leq n(6-y)$

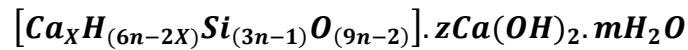
The values calculated for n, y, w_{min} (minimum no. of silanol groups) and w_{max} (maximum number of silanol groups) are tabulated in Table 7:4.

The structural chemical formulae for all the C-S-H phases synthesized are shown below:



The C-S-H phases synthesized are a combination of T2, T5, J2 and J5 structural units.

The general formula for T/CH viewpoint:



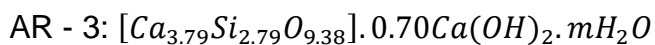
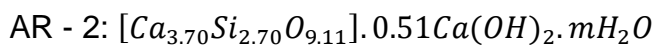
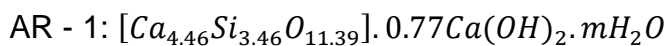
Where, $X = (6n-w)/2$ and $z = (w+n(y-2))/2$

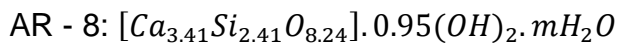
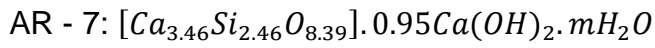
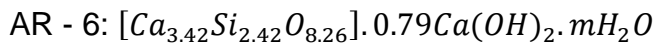
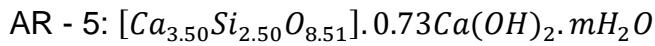
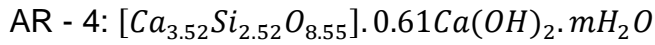
The values calculated for X and z are tabulated in Table 7:5. X and z are calculated using the values of n, y and w_{min} from Table 7:4.

Sample	X	z
AR - 1	4.46	0.77
AR - 2	3.70	0.51
AR - 3	3.79	0.70
AR - 4	3.52	0.61
AR - 5	3.50	0.73
AR - 6	3.42	0.79
AR - 7	3.46	0.95
AR - 8	3.41	0.95

Table 7:5 Calculated values required for the formulation using T/CH viewpoint.

The structural chemical formulae for all the C-S-H phases synthesized are shown below:





The experimental MCL (calculated from NMR analysis) values of all the C-S-H samples synthesized are plotted against the mean Ca/Si ratio values (obtained from TEM – EDX) in Figure 7.24. Reported data from literature is also plotted.

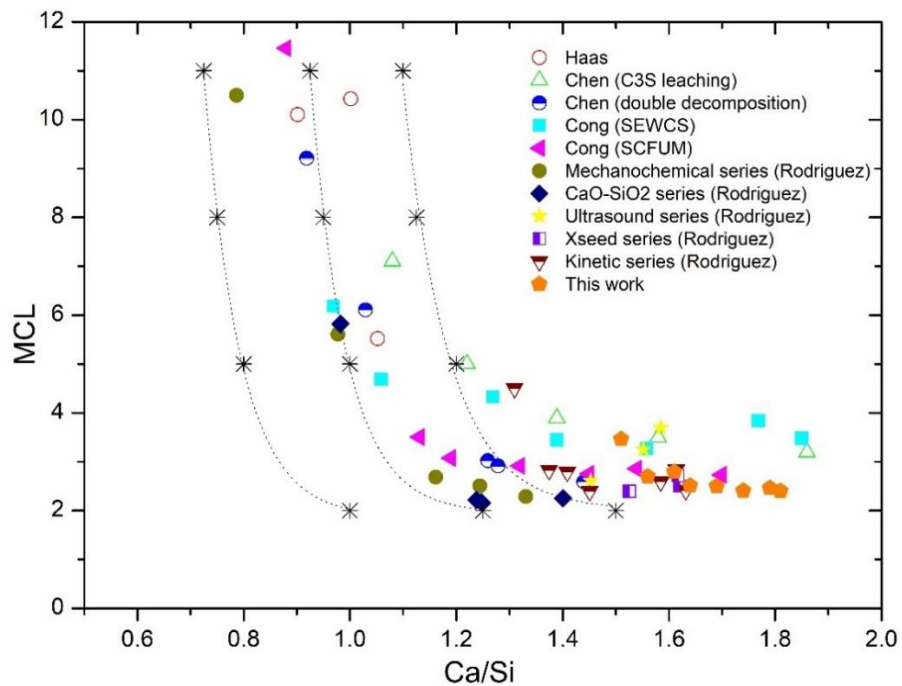


Figure 7.24 MCL versus Ca/Si ratios for all the C-S-H samples synthesized. Reported data from literature is also plotted along with various degrees of protonation from Richardson and Grove’s model [31][41][45][63][163] .

The dotted lines represent the tobermorite lines with various degrees of protonation: minimum (right), intermediate (middle) and maximum (left) from

Richardson and Groves' model. Maximum degree of protonation indicates that the negative charge is entirely balanced by protons in Si-OH groups. Intermediate degree of protonation indicates that the negative charge is balanced equally by proton in Si-OH and Ca. Minimum degree of protonation indicates that the negative charge is balanced entirely by Ca. All the data points from this work fall to the right of the right dotted line indicating the need of presence of Ca-OH groups in the structure. The reported data from literature suggests that there is a drastic decrease in MCL up to Ca/Si \approx 1, followed by a slight decrease up to Ca/Si \approx 1.3, after which MCL almost remains constant (\approx 3) with increase in Ca/Si ratios. This indicates the formation of dimeric silicate chains and change in MCL is much less after this. The variations in the silicate structure noticed as Ca/Si ratio increases are due to the removal of bridging tetrahedra and incorporation of additional Ca²⁺ ions.

7.1.3 STA and XRD

The STA traces for the samples are shown in Figure 7.25. In all the traces there is a mass loss below 200 °C due to the dehydration of C-S-H phase. Also, can be seen a weight loss at 450 °C and 700 °C in all the samples which corresponds to the decomposition of CH and $C\bar{C}$ respectively. The DTA curves show an exothermal peak at about 900 °C corresponding to the formation of C₂S. The C-S-H samples when heated to 1000 °C, decomposed to form C₂S and this is evident from the ²⁹Si MAS NMR analysis (Figure 7.27) on the sample heated to 1000 °C. Both Q¹ and Q² species present in C-S-H transforms to Q⁰ species indicating the formation of C₂S. ²⁹Si NMR spectrum clearly shows no presence of wollastonite. Figure 7.26 shows the DSC trace of C-S-H sample synthesized at 5 °C. This sample is synthesized separately and is different from AR – 5. The CO₂

trace (Figure 7.26) shows a peak corresponding to the release of CO₂ at about 900 °C indicating the liberation of CO₃ groups possibly trapped on the surface and the release of CO₂ at about 700 °C corresponds to the decomposition of crystalline C \bar{C} . The H₂O trace (Figure 7.26) shows a peak corresponding to the release of H₂O at about 450 °C indicating the decomposition of CH phase and maximum release of water is seen upto about 200 °C.

The (w/w) percentage of CH and C \bar{C} in all the samples is calculated using tangent method and the values obtained are shown in Table 7:6. The % CH_{res} is the weight fraction of initial reactant that is left unreacted and %C \bar{C} _{res} is the weight fraction of calcite at the end, formed due to undesired carbonation. However, there is no specific trend seen in these values with respect to the reaction temperature or lime concentration. This can be concluded as the result of errors while conducting the experiments.

Sample	%CH _{res}	%C \bar{C} _{res}
AR – 1	1.24	1.45
AR – 2	0.04	-
AR – 3	0.26	2.98
AR – 4	0.28	3.21
AR – 5	0.16	0.71
AR – 6	1.03	1.74
AR – 7	1.58	3.03
AR – 8	0.27	0.64

Table 7:6 The residual % CH and % C \bar{C} of the C-S-H phases calculated from STA data.

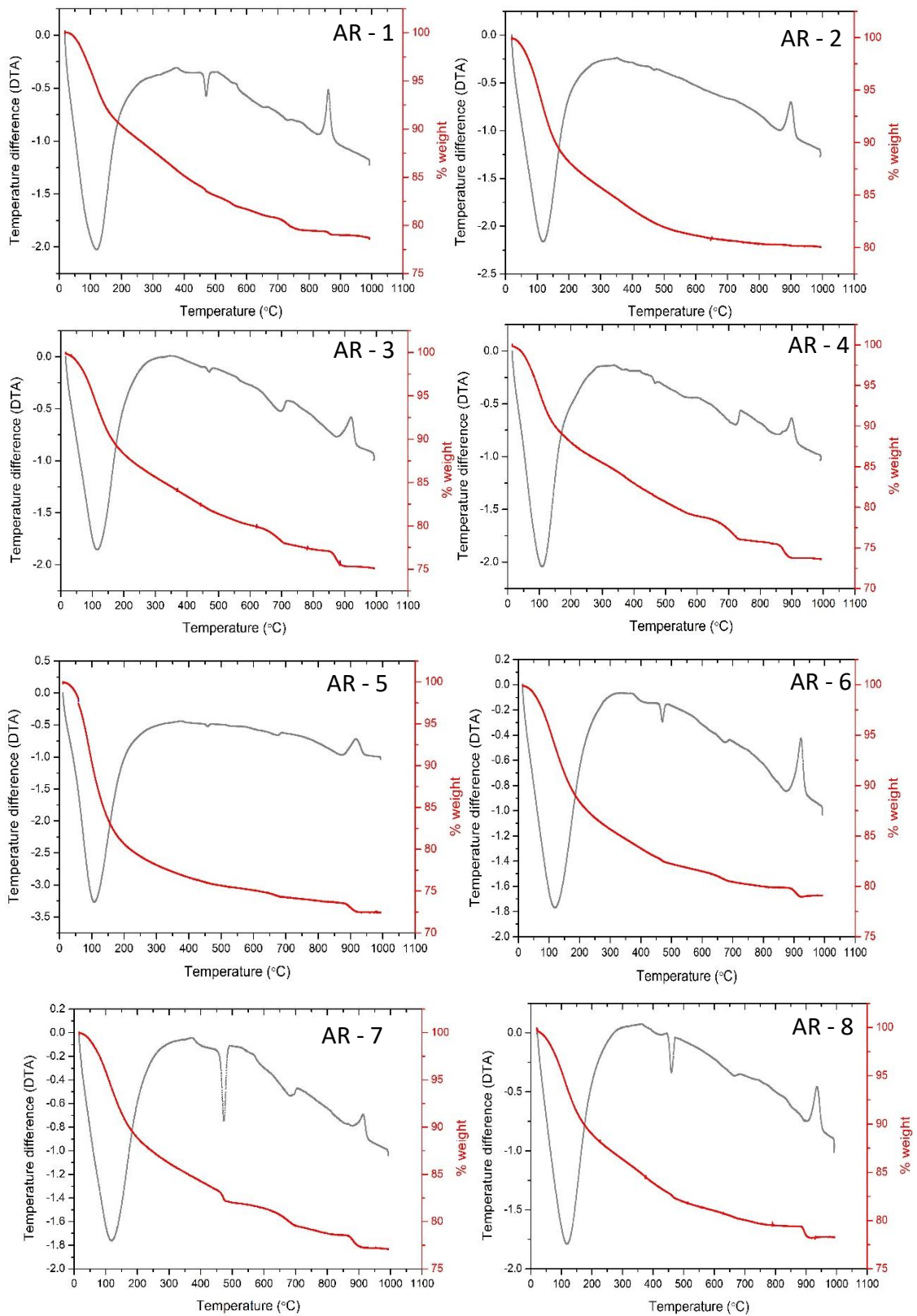


Figure 7.25 STA traces of all C-S-H samples synthesized showing DTA in grey and % TG in red.

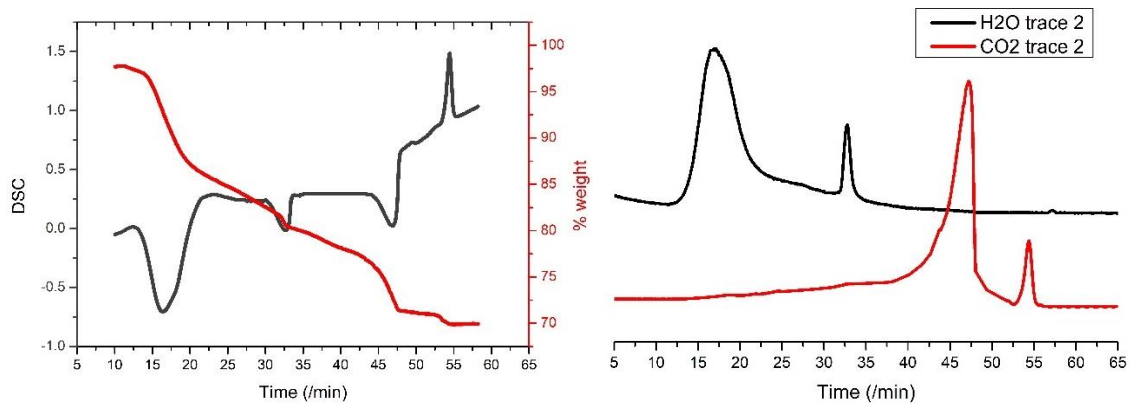


Figure 7.26 DSC (grey) and % TG (red) curves along with water and CO₂ traces of the C-S-H phase synthesized at 5 °C.

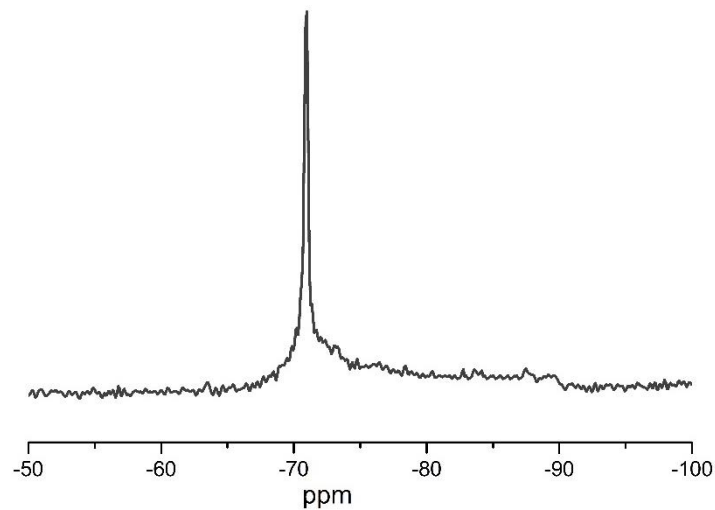


Figure 7.27 ²⁹Si MAS NMR spectra of C-S-H phase (synthesized at 5 °C) heated to 1000 °C.

The XRD patterns of all the samples synthesized are shown in Figure 7.28 together with reference patterns for CH and $C\bar{C}$. The presence of C-S-H is seen as a hump at $29^\circ < 2\theta < 31^\circ$. The presence of CH and $C\bar{C}$ does not depict any specific trend, these can be considered as experimental errors.

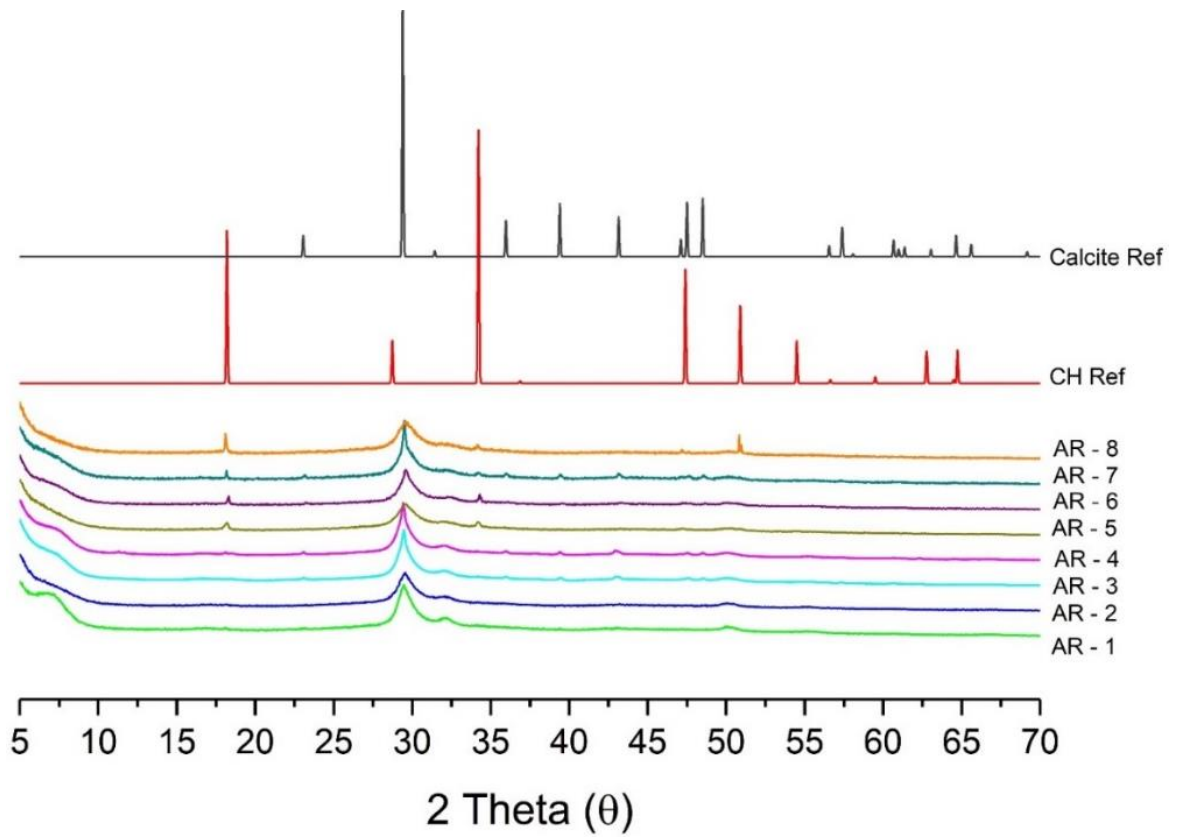


Figure 7.28 XRD patterns of the C-S-H samples with the reference patterns for CH and $\bar{C}\bar{C}$.

Chapter 8 Results and discussion of artificial ageing on synthetic C-S-H samples

8.1 Characterization results of C-S-H samples (described in Table 4:9, Experimental Methods)

8.1.1 TEM – EDX of static leached C-S-H samples

The TEM micrographs of static leached samples (SL) are shown in Figure 8.1. The micrographs show the presence of an amorphous C-S-H phase in all the samples having foil like morphology. There is also presence of CC which is discussed later in STA analysis.

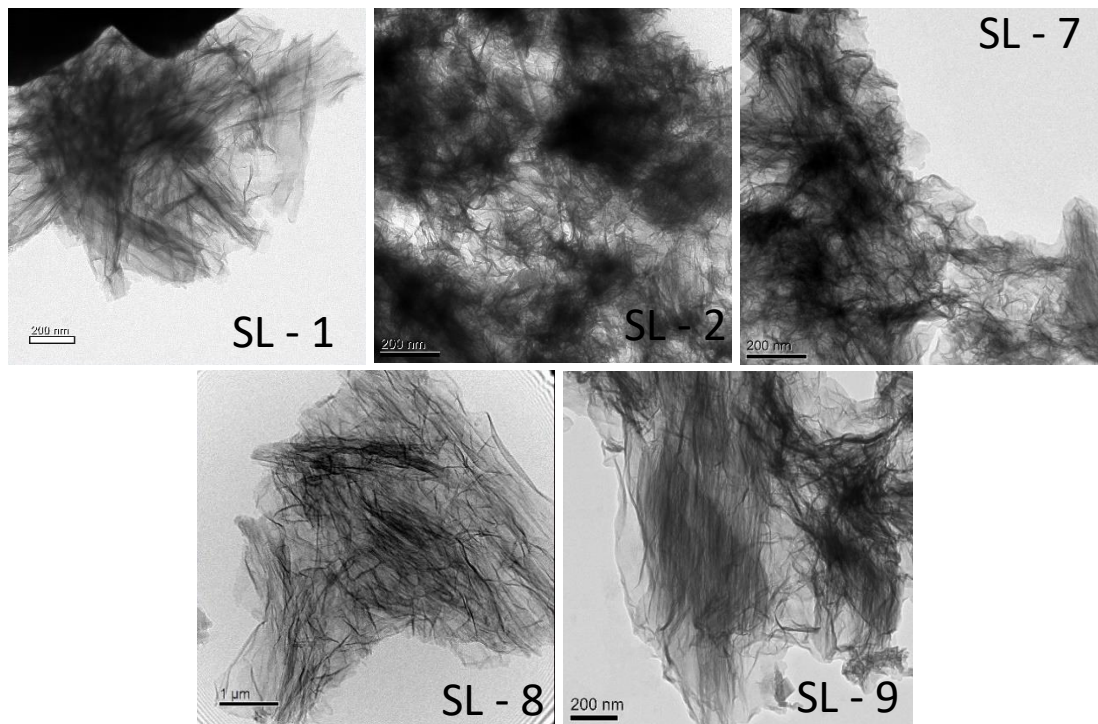


Figure 8.1 TEM micrographs of static leached samples (top left: SL – 1, top right: SL – 2, middle left: SL – 7, middle right: SL – 8, bottom: SL – 9) showing foil-like morphology.

The foil-like morphology seen resembles the morphology of C-S-H phases present in aged cements [168]. The mean Ca/Si ratios obtained from EDX analysis are shown in Table 8.1. The histograms for the Ca/Si ratios obtained by TEM-EDX are shown in Figure 8.2. The Ca/Si ratios obtained show low standard deviation indicating that the samples are all homogeneous in composition. The transformation from fibrillar morphology before leaching to foil-like morphology after leaching can be explained by the loss of Ca^{2+} ions accompanied by the lengthening of silicate chains (discussed in the next section). This kind of change in morphology from fibres to foils is also seen in cement pastes blended with increased slag content [3][123]. The mean Ca/Si ratios plotted against degree of leaching for all the static leached samples is shown in Figure 8.3. The use of straight lines in Figure 8.3 is only to depict the data points clearly before and after leaching. They do not describe the linear behaviour.

Sample	Ca/Si	N*	S.D
SL - 1	1.40	36	0.02
SL - 2	1.37	30	0.02
SL - 7	1.43	35	0.02
SL - 8	1.46	33	0.01
SL - 9	1.49	31	0.01

Table 8:1 Mean Ca/Si ratios of C-S-H phases obtained by TEM – EDX.

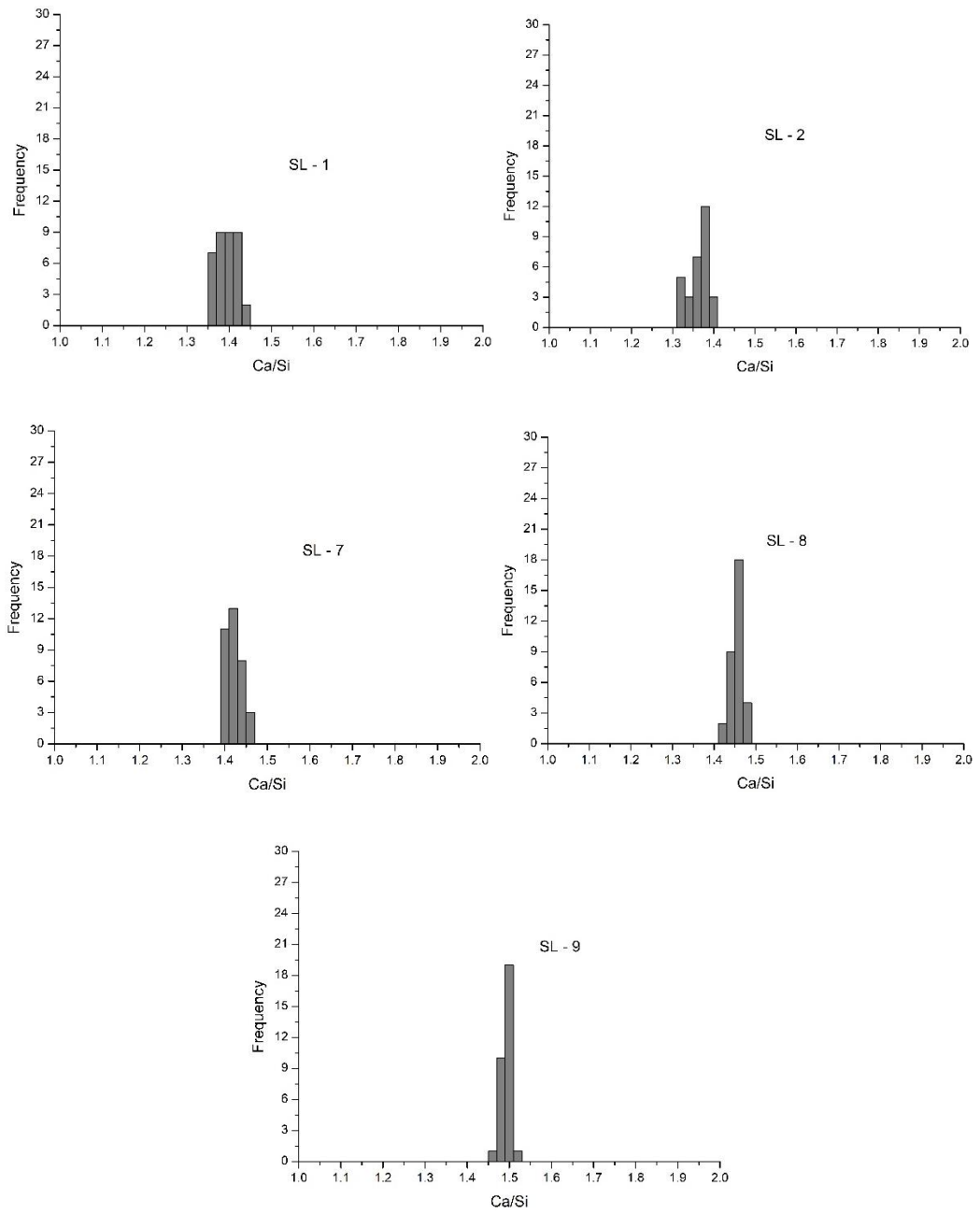


Figure 8.2 Histograms of Ca/Si ratios measured using TEM – EDX.

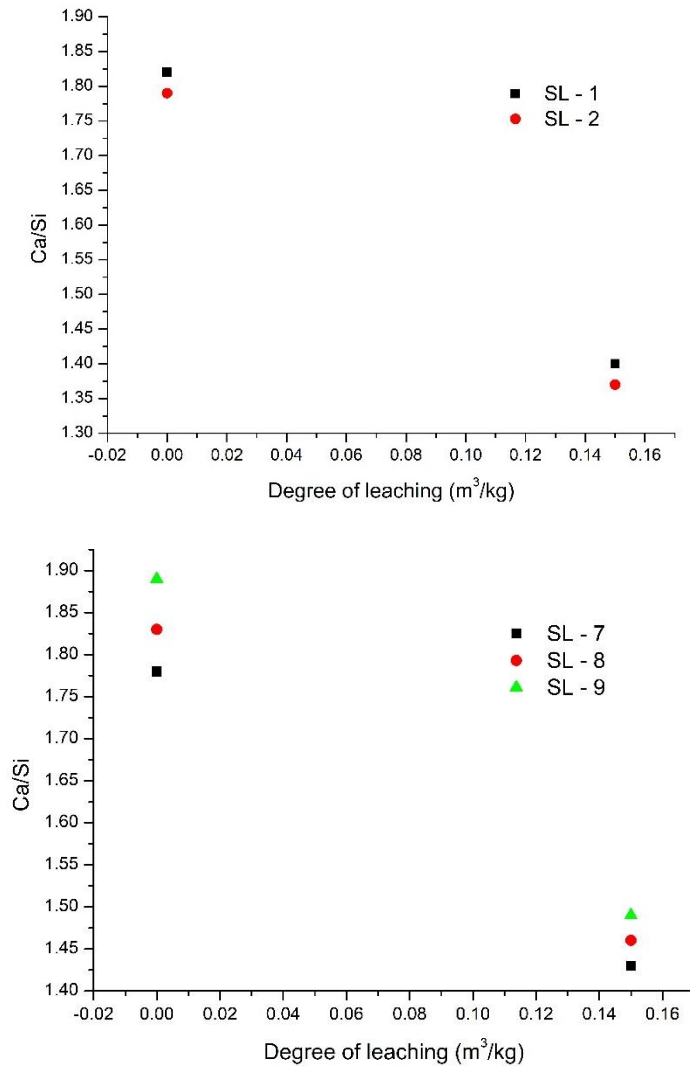
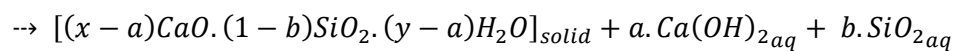
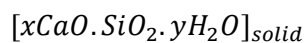


Figure 8.3 Mean Ca/Si ratios plotted against degree of leaching for all the static leached samples.

Harris et al. [169] observed that dissolution of C-S-H gels is incongruent initially with preferential dissolution of calcium from C-S-H gels with a higher Ca/Si ratio and this incongruent dissolution behaviour is followed by congruent dissolution.

Incongruent dissolution [82][85] of C-S-H gel can be described as:



Incongruent dissolution denotes that the ratio a/b initially is not equal to x . As the value of x decreases by the process of leaching, the ratio a/b decreases and as congruent dissolution is achieved, it becomes equal to x . Berner reported the static dissolution data indicating the congruently dissolving composition is at a Ca/Si ratio of 0.8 [85] after which Ca/Si ratio in solid becomes equal to Ca/Si ratio in solution. Atkinson et al. [170] suggested a value of 0.8-0.9. This behaviour of congruent dissolution is not seen in these samples and this could be because of the termination of the leaching process before the congruency is reached.

8.1.2 ^{29}Si NMR of static leached C-S-H samples

The ^{29}Si NMR spectra for all the static leached samples are shown in Figures 8.4 – 8.8. The results are deconvoluted to estimate the percentage of silicate groups and the mean chain length. The deconvoluted spectra, the individual frequencies and the simulated spectra, are all shown in the Figures below. The peaks in the range $\delta = -78$ ppm to -80 ppm correspond to the presence of Q^1 groups while the peaks in the range $\delta = -82$ ppm to -85 ppm correspond to the presence of Q^2 groups. The presence of these groups indicate that the hydrate possesses dimers and middle chain groups. The MCL calculated is shown in Table 8:2 along with the percentage of silicate species in C-S-H phases obtained from deconvolution of the spectra. The silicate structure of all the samples is dominated by Q^2 species. The spectra show that leaching results in an increase in Q^2 silicate species and the silicate structure is modified by decalcification. The removal of Ca by leaching from the C-S-H phases is evident by a decrease in Ca/Si ratios and an increase in MCL. Two frequencies are used to deconvolute Q^2 contribution to improve the fitting of the asymmetric peaks and adjust the simulated spectra and the experimental spectra. Although these frequencies are

used for deconvolutions, they do not directly represent the species present as the line widths and shapes of the frequencies vary between the samples. The relaxation of these parameters during the fitting process resulted in these variations.

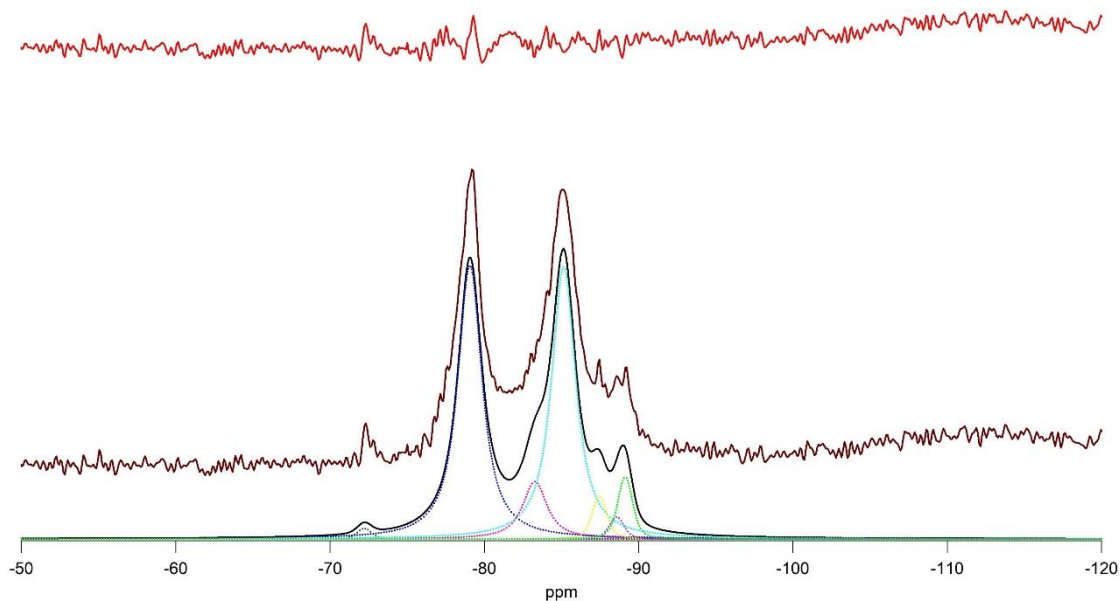


Figure 8.4 ^{29}Si NMR spectra of SL - 1 including experimental spectrum (middle, brown), residual (top, red x1) and the individual frequencies.

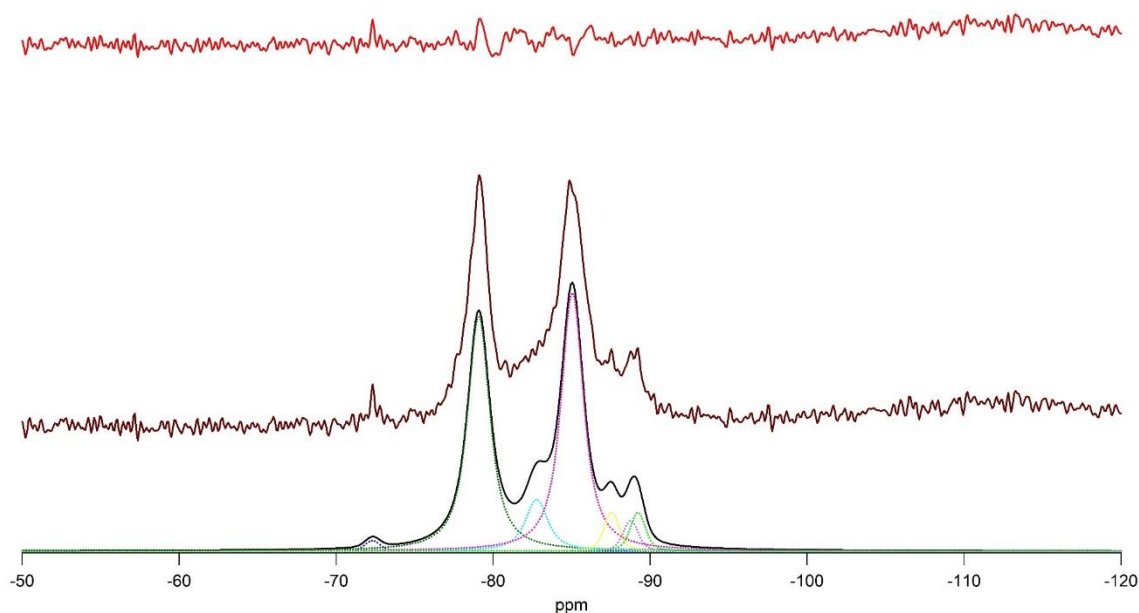


Figure 8.5 ^{29}Si NMR spectra of SL - 2 including experimental spectrum (middle, brown), residual (top, red x1) and the individual frequencies.

In both the spectra (SL - 1 and SL - 2), there is a peak present around $\delta = -73$ ppm indicating the presence of $\text{Y-C}_2\text{S}$ [159]. The existence of $\text{Y-C}_2\text{S}$ in the samples indicate that its reactivity is very low. The three peaks around $\delta = -87$ ppm, $\delta = -88$ ppm and $\delta = -89$ ppm correspond to the presence of wollastonite [158].

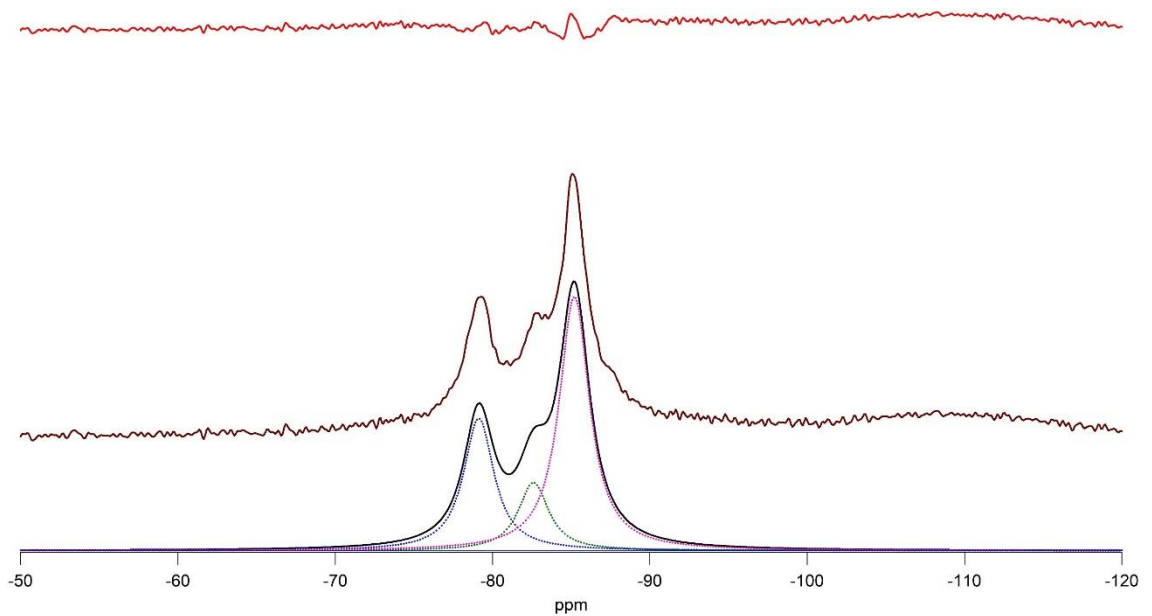


Figure 8.6 ^{29}Si NMR spectra of SL - 7 including experimental spectrum (middle, brown), residual (top, red x1) and the individual frequencies.

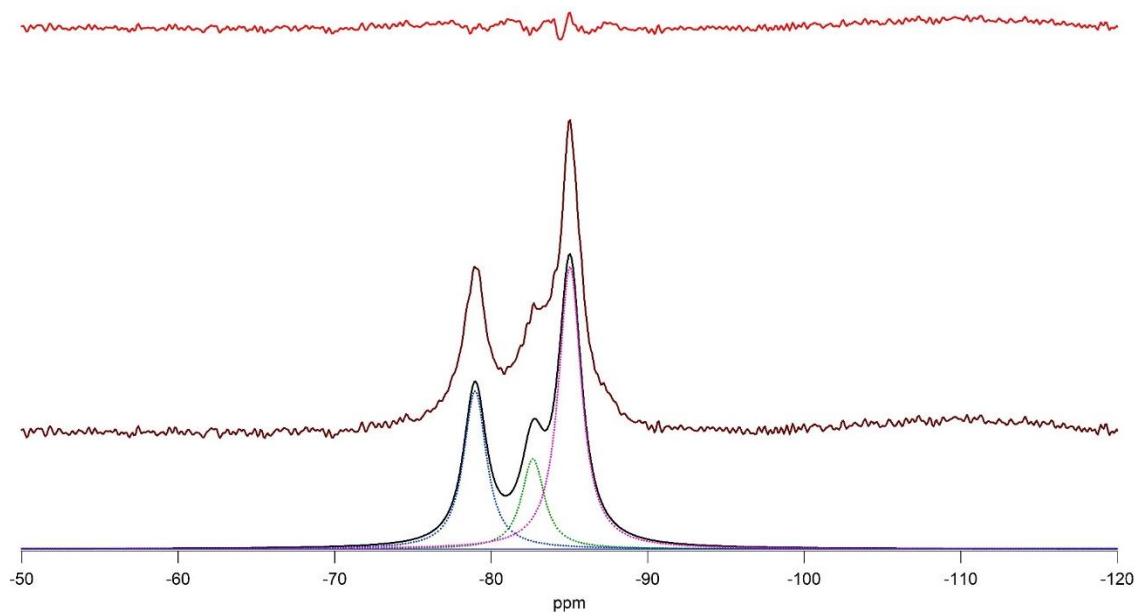


Figure 8.7 ^{29}Si NMR spectra of SL - 8 including experimental spectrum (middle, brown), residual (top, red x1) and the individual frequencies.

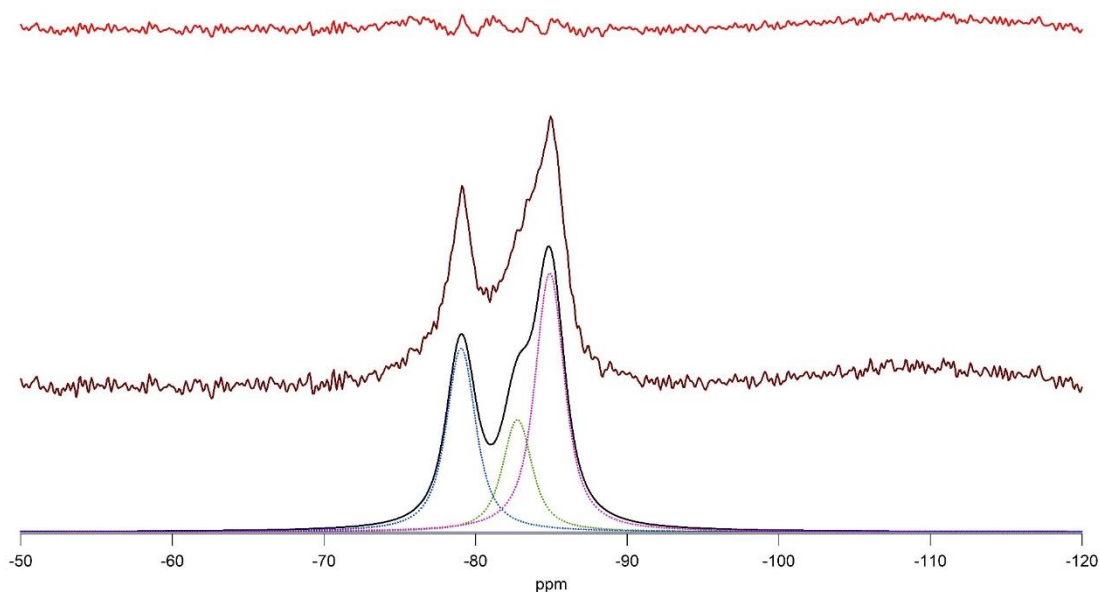


Figure 8.8 ^{29}Si NMR spectra of SL - 9 including experimental spectrum (middle, brown), residual (top, red x1) and the individual frequencies.

Sample	Q ¹ (%)	Q ² (%)	MCL	Ca/Si _{TEM-EDX}
SL - 1	40.7	49.0	4.40	1.40
SL - 2	38.3	50.6	4.64	1.37
SL - 7	29.1	70.9	6.87	1.43
SL - 8	29.8	70.2	6.71	1.46
SL - 9	33.1	66.9	6.04	1.49

Table 8:2 Results of deconvolution of the ²⁹Si NMR spectra: % silicate species and MCL.

The decomposition of C-S-H results in removal of all the Ca²⁺ ions from the interlayer and principal layers resulting in the formation of amorphous silica with Q³ and Q⁴ groups. However, in the samples discussed here there is no presence of Q³ and Q⁴ groups.

Richardson and Groves' model (described in Literature Review) is used for the formulation of the C-S-H phases synthesized. Figure 8.9 shows the Ca/Si ratios plotted against the reciprocal mean chain length. Figure also shows the trends for tobermorite and jennite units with various degrees of protonation ($w = 0, 1, 2$). The mean values of Ca/Si ratios are represented by filled circles in the Figure above. The mean values of Ca/Si ratios fall between the tobermorite and jennite like regions on the plot, thus confirming the presence of Ca-OH groups in the structure coming either from jennite like structures or solid solution CH. In T/J viewpoint, the Ca-OH groups form a part of the main layer and in T/CH viewpoint, the Ca-OH groups are present in the interlayers. Although, the SAED patterns and STA (discussed later) does not show the presence of crystalline/amorphous

CH phase and T/J view point seems to be suitable, the possibility of T/CH cannot be completely excluded. Both the viewpoints have been used to derive the structural chemical formula. However, the C-S-H phases before leaching (discussed in chapter 6) follow T/J view point and hence T/J viewpoint seems more suitable for the phases after leaching.

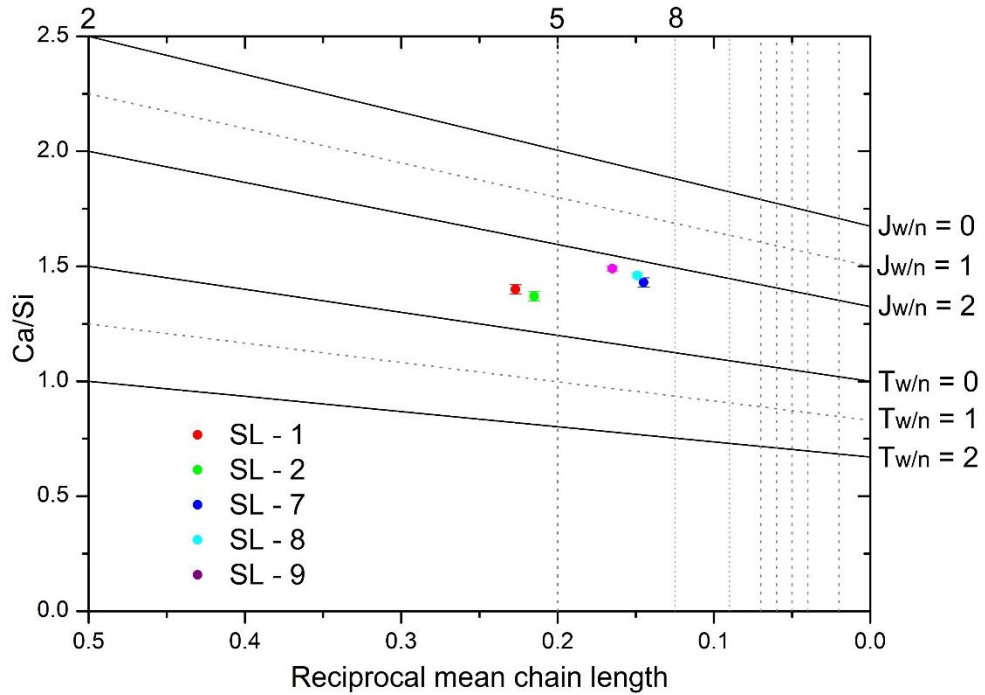
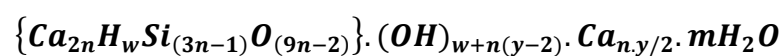


Figure 8.9 Ca/Si obtained by TEM-EDX analysis versus reciprocal mean chain length obtained by NMR analysis. The structural units for tobermorite and jennite with minimum (w=0), intermediate (w=1) and maximum (w=2) degree of protonation are plotted along with data points from current work. The vertical dashed lines represent the (3n - 1) structural units: dimer (2), pentamer (5) etc.

The general formula for T/J viewpoint:



Where, $n = (MCL+1)/3$ and $y = [(Ca/Si)(6n-2)-4n]/n$

w depends on the value of y

if, $0 \leq y \leq 2$ then $n(2-y) \leq w \leq 2n$

if, $2 \leq y \leq 4$ then $0 \leq w \leq 2n$

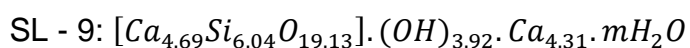
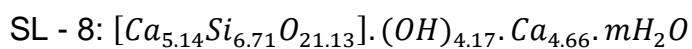
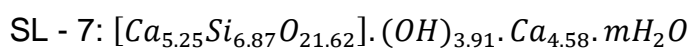
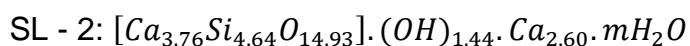
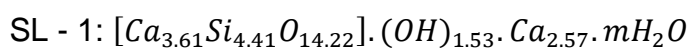
if, $4 \leq y \leq 6$ then $0 \leq w \leq n(6-y)$

The values calculated for n, y, w_{\min} (minimum no. of silanol groups) and w_{\max} (maximum number of silanol groups) are tabulated in Table 8:3.

Sample	n	y	w_{\min}	w_{\max}
SL - 1	1.80	2.85	0	3.60
SL - 2	1.88	2.76	0	3.76
SL - 7	2.62	3.49	0	5.24
SL - 8	2.57	3.62	0	5.14
SL - 9	2.35	3.67	0	4.68

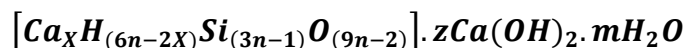
Table 8:3 Calculated values required for the formulation using T/J viewpoint.

The structural chemical formulae for all the C-S-H phases synthesized are shown below:



Samples SL – 1 and SL – 2 are a combination of dimeric and pentameric units, T2, T5, J2, J5. Samples SL – 7, SL – 8 and SL – 9 are a combination of T2, T5, T8, J2, J5, J8 units.

The general formula for T/CH viewpoint:



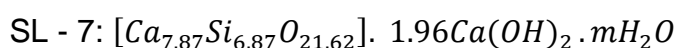
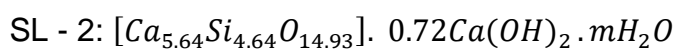
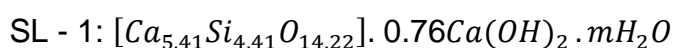
Where, $X = (6n-w)/2$ and $z = (w+n(y-2))/2$

The values calculated for X and z are tabulated in Table 8:4. X and z are calculated using the values of n, y and w_{min} from Table 8:3.

Sample	X	z
SL – 1	5.41	0.76
SL – 2	5.64	0.72
SL – 7	7.87	1.96
SL – 8	7.71	2.09
SL – 9	7.04	1.96

Table 8:4 Calculated values required for the formulation using T/CH viewpoint.

The structural chemical formulae for all the C-S-H phases synthesized are shown below:

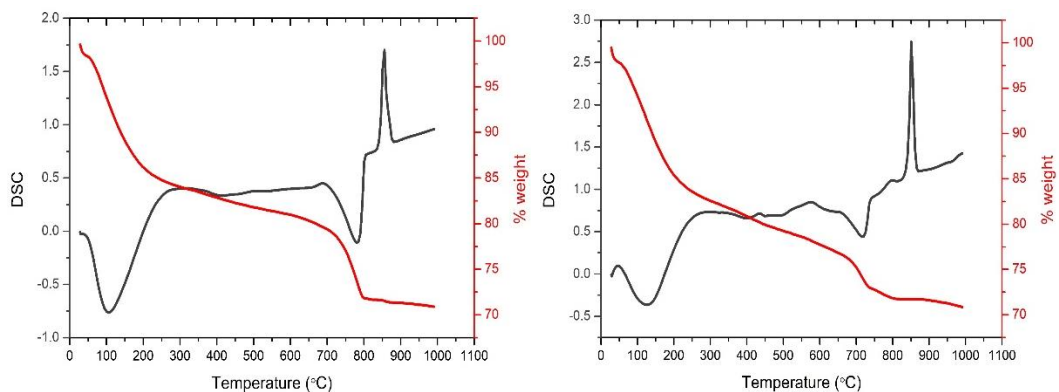


SL - 8: $[Ca_{7.71}Si_{6.71}O_{21.13}] \cdot 2.09Ca(OH)_2 \cdot mH_2O$

SL - 9: $[Ca_{7.04}Si_{6.04}O_{19.13}] \cdot 1.96Ca(OH)_2 \cdot mH_2O$

8.1.3 STA of static leached C-S-H samples

The STA traces of all the static leached samples are shown in Figure 8.10. Along with TG and DSC, gas analysis is also performed to monitor the gases expelled from the samples. All the water and CO₂ traces are shown in Figure 8.11. The results for all the samples show that the weight loss until 200 °C corresponds to the dehydration of C-S-H phase. This matches with the peak corresponding to release of water shown in water trace. The weight loss at about 500 °C in the samples is associated to the decarbonation of amorphous $C\bar{C}$. Thiery et al [99] reported three decomposition modes indicating carbonation: mode I (780 °C – 990 °C), mode II (680 °C – 780 °C) and mode III (550 °C – 680 °C). While mode I and mode II attribute to the decomposition of crystalline phases of CaCO₃ (calcite, aragonite and vaterite), mode III is known to attribute to the presence of amorphous CaCO₃. These poorly crystalline and thermally unstable polymorphs are believed to result from decomposition of C-S-H phases.



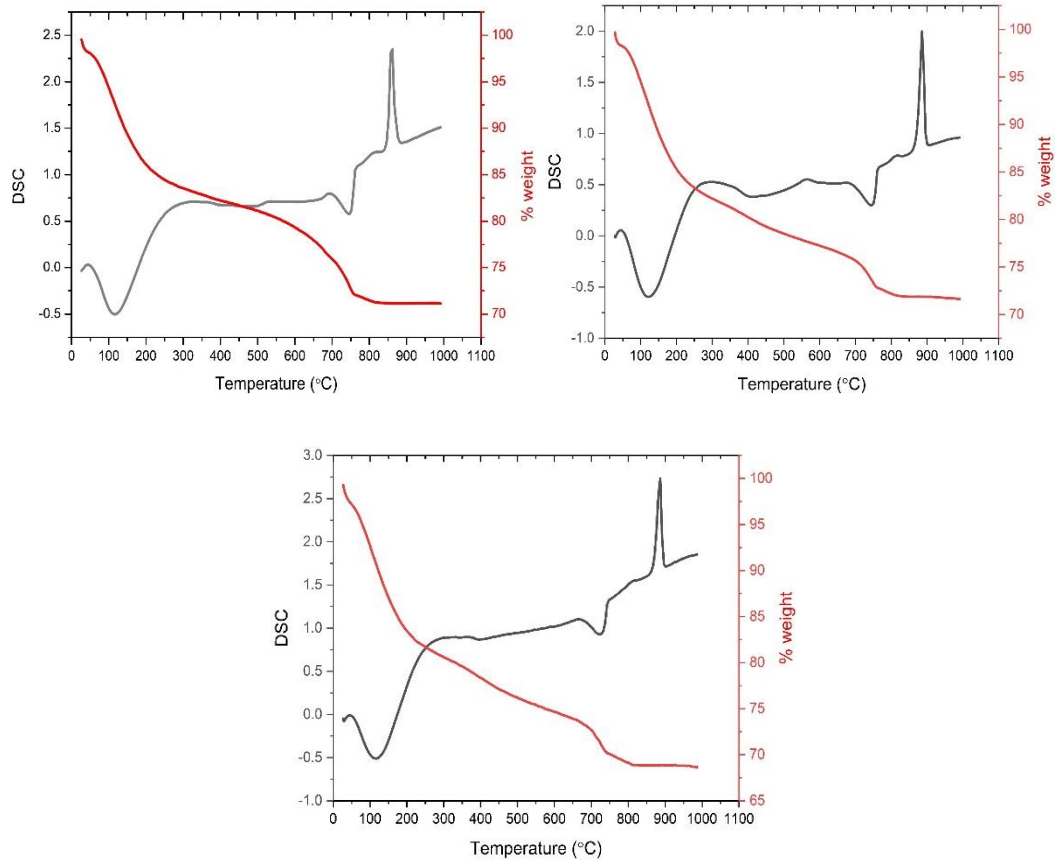


Figure 8.10 STA patterns of SL samples showing DSC in grey and % TG in red (top left: SL – 1, top right: SL – 2, middle left: SL – 7, middle right: SL – 8, bottom: SL – 9).

The presence of a small hump at 450 °C in the H₂O traces indicates the presence of a small amount CH phase in the samples and most of this phase is removed by the process of leaching (Section 6.2.3 shows the STA traces of these phases before leaching). All the samples show carbonation with weight loss between 700 °C – 800 °C corresponding to the decomposition of crystalline $C\bar{C}$. The DSC curves show an exothermal peak at about 850 °C corresponding to the formation of β -wollastonite [171]. It is also observed that the formation of β -wollastonite occurs at higher temperatures as the Ca/Si ratio increases. Figure 8.12 and Table 8:5 shows the transformation temperature of C-S-H samples to β -wollastonite.

This increasing trend in the transformation temperature with Ca/Si ratio is reported by Rodriguez [63][172].

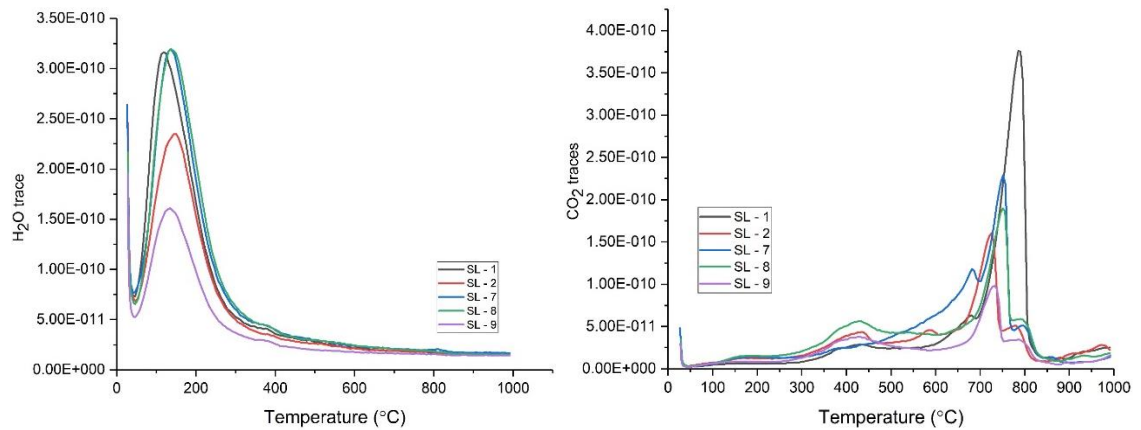


Figure 8.11 Water and CO₂ traces of all the static leached samples.

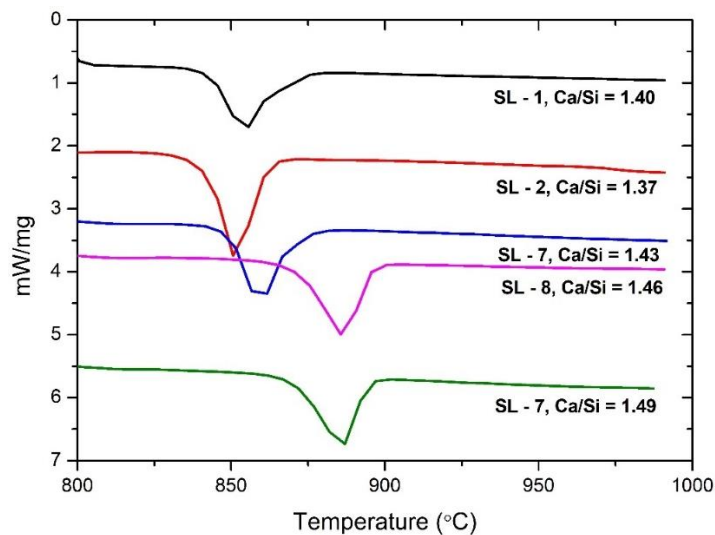


Figure 8.12 DSC curves showing the transformation temperature of C-S-H to β -wollastonite in all the static leached samples.

Leaching results in the removal of most of the CH phase and formation of $\bar{C}\bar{C}$ if C-S-H gels are exposed to CO₂. The formation of $\bar{C}\bar{C}$ is a result of the reaction of CO₃²⁻ ions from CO₂ with Ca²⁺. The Ca²⁺ ions required are obtained by the

dissolution of CH and C-S-H, thus increasing the polymerisation of the C-S-H structure.

Sample	Ca/Si _{TEM - EDX}	Temperature of transformation (°C)
SL – 1	1.40	855.635
SL – 2	1.37	850.637
SL – 7	1.43	861.665
SL – 8	1.46	885.646
SL – 9	1.49	887.044

Table 8:5 Variation in transformation temperature of C-S-H to β -wollastonite with mean Ca/Si ratios.

8.1.4 TEM - EDX of dynamic leached samples

The microstructures of extensively leached C-S-H gels in demineralised water are discussed. The TEM micrographs of all dynamic leached samples are shown in Figures 8.13 – 8.20. The foil-like morphology seen resembles the morphology of C-S-H phases present in aged cements [168]. The mean Ca/Si ratios obtained from EDX analysis are shown in Table 8.6. The histograms for the Ca/Si ratios obtained by TEM-EDX are shown in Figure 8.21. The transformation from fibrillar morphology before leaching to foil-like morphology after leaching can be explained by the loss of Ca²⁺ ions accompanied by the lengthening of silicate chains. This kind of change in morphology from fibres to foils is also seen in cement pastes blended with increased slag content [3][123]. Figure 8.22 shows the mean Ca/Si ratios of all the samples plotted against degree of leaching.

The Ca/Si ratios measured indicate that the leaching resulted in the formation of C-S-H gels with almost similar solid composition. This suggests that the dissolutions approach congruency. Harris et al. [169] observed that dissolution of C-S-H gels is incongruent initially with preferential dissolution of calcium from C-S-H gels with a higher Ca/Si ratio and this incongruent dissolution behaviour is followed by congruent dissolution. The results obtained are in agreement with that of Harris et al. [82] where leaching of various gels ultimately resulted in phases with similar constant compositions. Berner reported the static dissolution data indicating that the congruently dissolving composition is at a Ca/Si ratio of 0.8 [85] after which Ca/Si ratio in solid becomes equal to Ca/Si ratio in solution. Atkinson et al. [170] suggested a value of 0.8-0.9. However, the value for congruency as suggested by various researchers is not obtained in these experiments as the process of leaching is terminated before the congruency is reached.

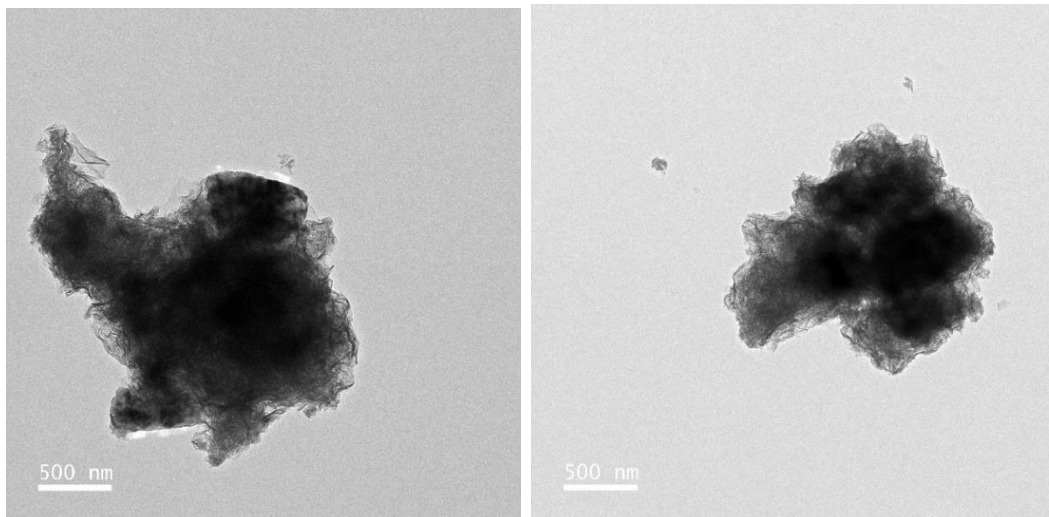


Figure 8.13 TEM micrographs of DL - 1 showing foil-like morphology.

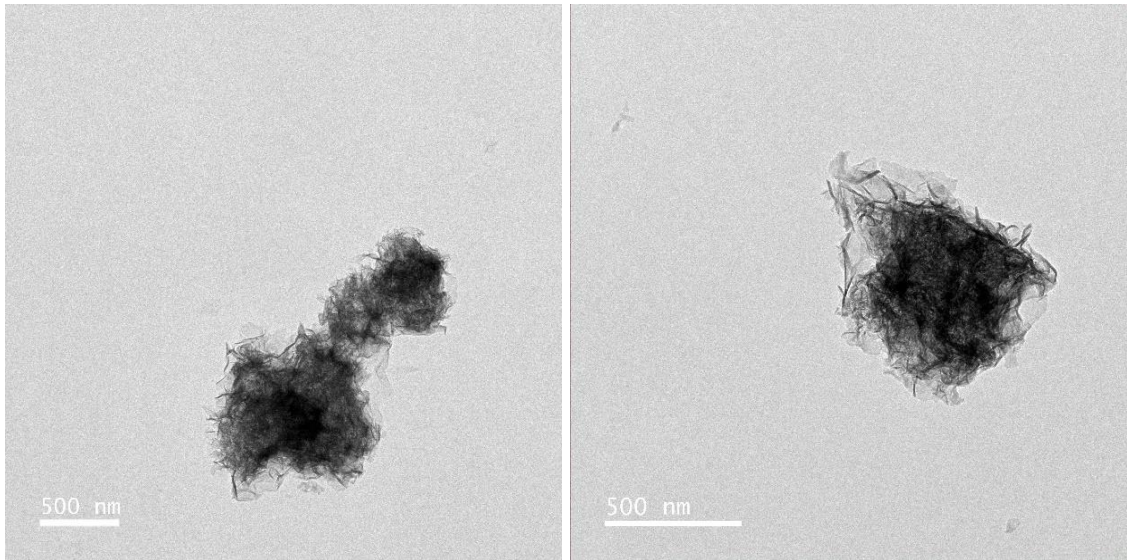


Figure 8.14 TEM micrographs of DL - 2 showing foil-like morphology.

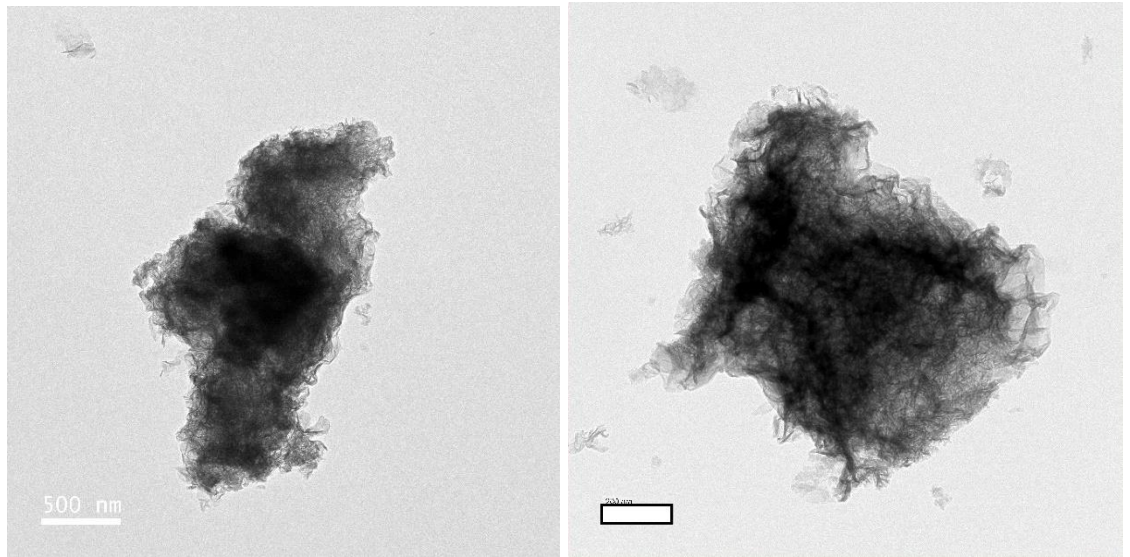


Figure 8.15 TEM micrographs of DL - 3 showing foil-like morphology.

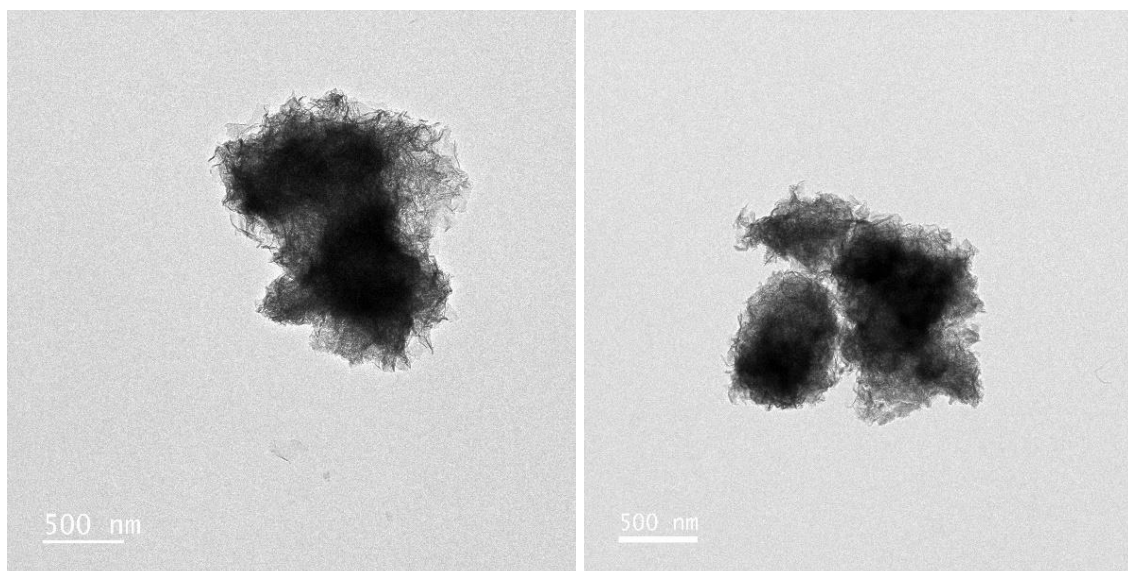


Figure 8.16 TEM micrographs of DL - 4 showing foil-like morphology.

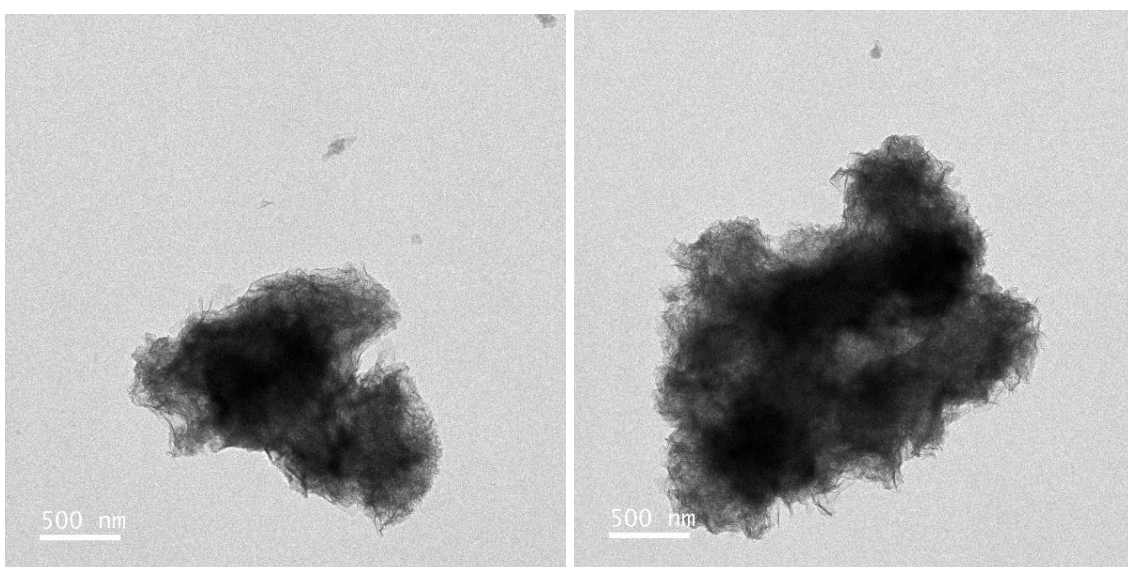


Figure 8.17 TEM micrographs of DL - 5 showing foil-like morphology.

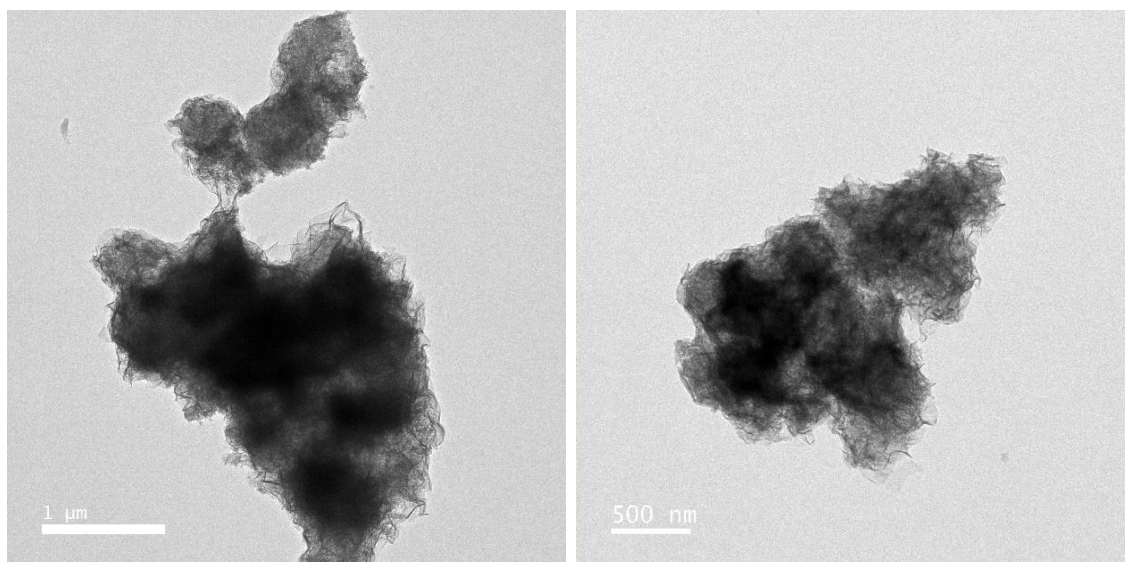


Figure 8.18 TEM micrographs of DL - 6 showing foil-like morphology.

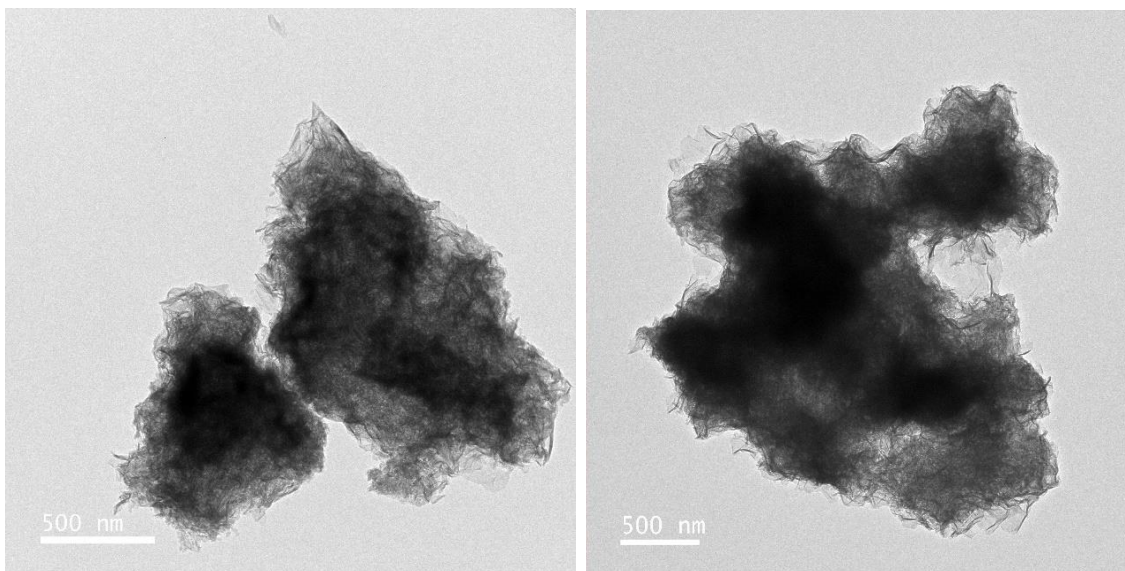


Figure 8.19 TEM micrographs of DL - 7 showing foil-like morphology.

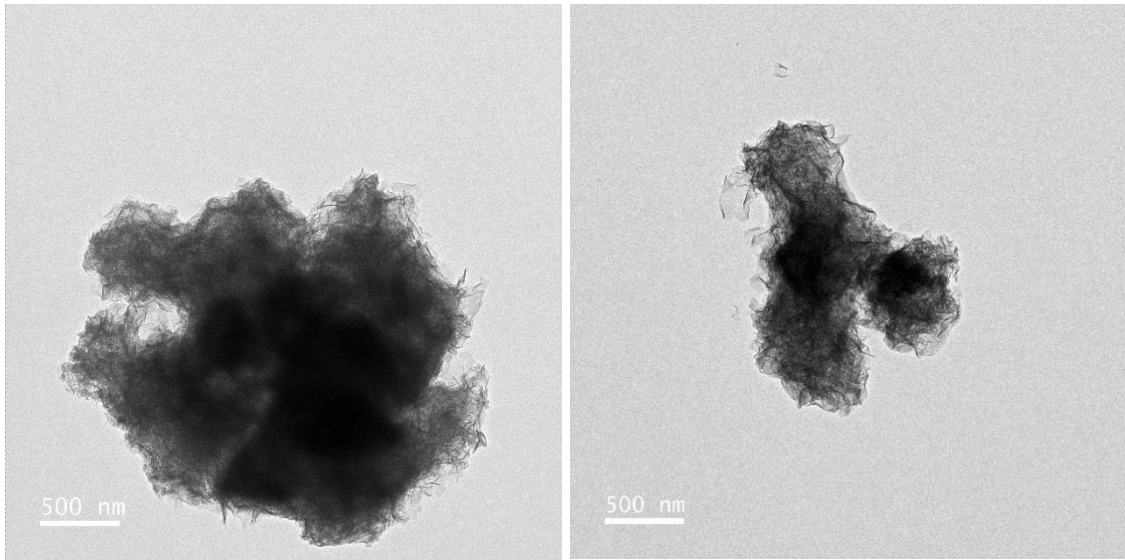
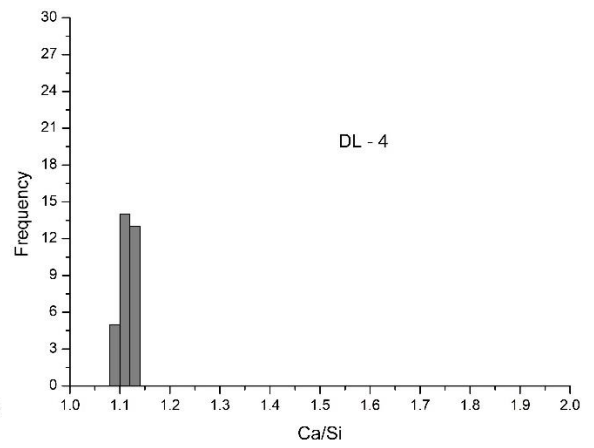
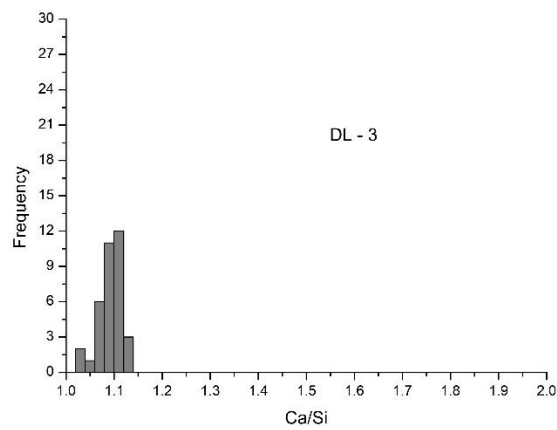
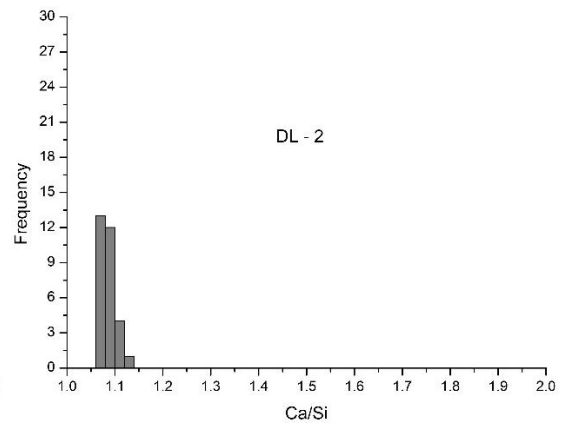
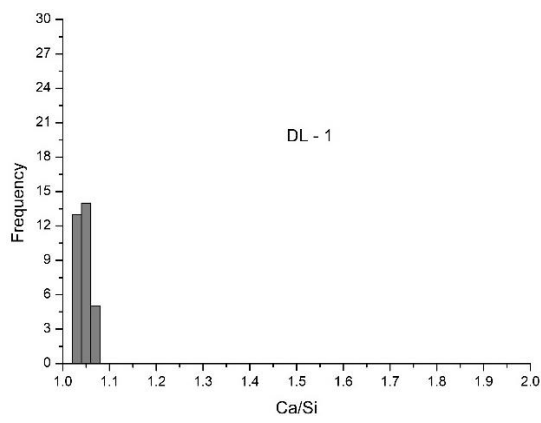


Figure 8.20 TEM micrographs of DL - 8 showing foil-like morphology.



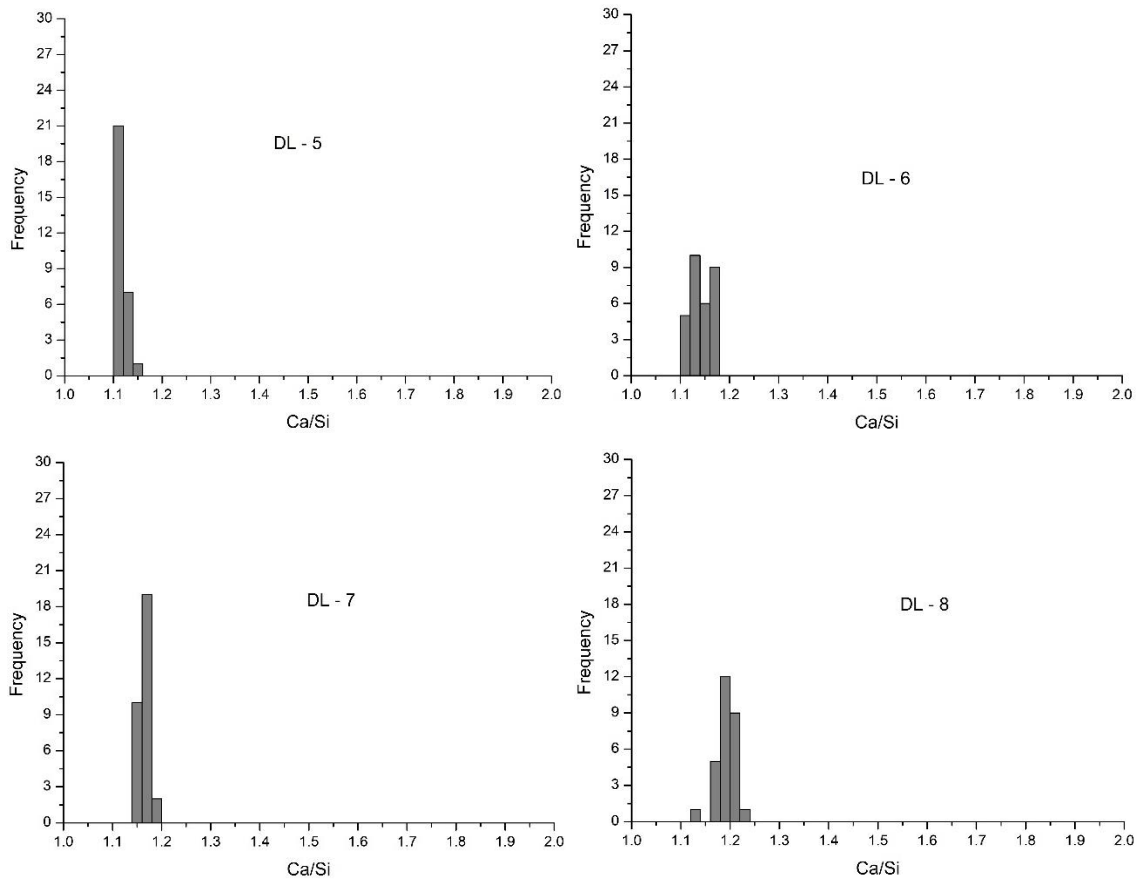


Figure 8.21 Histograms of Ca/Si ratios measured using TEM – EDX.

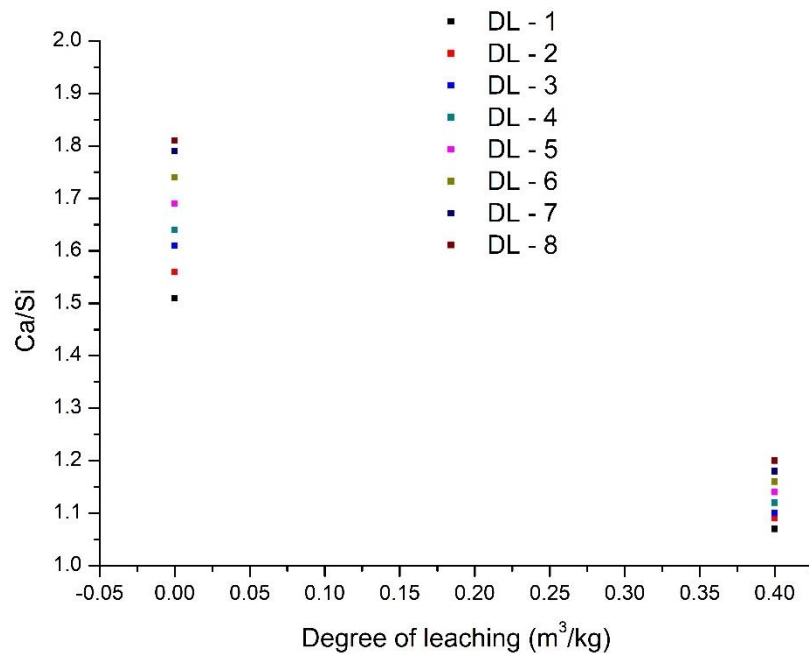


Figure 8.22 Mean Ca/Si ratios versus degree of leaching plotted for all the dynamic leached samples.

Sample	Ca/Si	S.D	N*
DL – 1	1.06	0.01	32
DL – 2	1.09	0.01	30
DL – 3	1.10	0.02	35
DL – 4	1.12	0.02	32
DL – 5	1.14	0.01	29
DL – 6	1.16	0.02	30
DL – 7	1.18	0.01	31
DL – 8	1.20	0.02	28

Table 8:6 Mean Ca/Si ratios of C-S-H phases obtained from TEM – EDX analysis for all the dynamic leached samples.

8.1.5 ²⁹Si NMR of dynamic leached C-S-H samples

The ²⁹Si NMR spectra of all the dynamic leached samples, are shown in Figures 8.23 – 8.28. The simulated spectrum is displayed as a sum of the individual frequencies and the experimental spectrum. The residual is shown in red at the top. The individual frequencies are shown for Q¹ and Q² groups. The results are deconvoluted to estimate the percentage of silicate groups and the mean chain length. The peaks in the range $\delta = -77$ ppm to -80 ppm corresponds to the presence of Q¹ groups while the peaks in the range $\delta = -82$ ppm to -84 ppm correspond to the presence of Q² groups respectively. The presence of these groups indicate that the hydrate possesses dimers and middle chain groups.

However, in all the spectra Q^2 groups dominate the structure of C-S-H formed. Two frequencies are used to deconvolute Q^2 contributions to improve the fitting of the asymmetric peaks and adjust the simulated spectra and the experimental spectra. Although these frequencies are used for deconvolutions, they do not directly represent the species present as the line widths and shapes of the frequencies vary between the samples. The relaxation of these parameters during the fitting process resulted in these variations. The deconvolution of the spectra is used to quantify the silicate species present and to calculate the MCL. The results are shown in Table 8:7. The spectra show that leaching results in an increase in Q^2 silicate species and the silicate structure is modified by decalcification. The removal of Ca^{2+} by leaching from the C-S-H phases is evident by a decrease in Ca/Si ratios and an increase in MCL. The decomposition of C-S-H results in the removal of all the Ca ions from the interlayer and principal layers, resulting in the formation of amorphous silica with Q^3 and Q^4 groups. However, in the samples discussed here there is no presence of Q^3 and Q^4 groups.

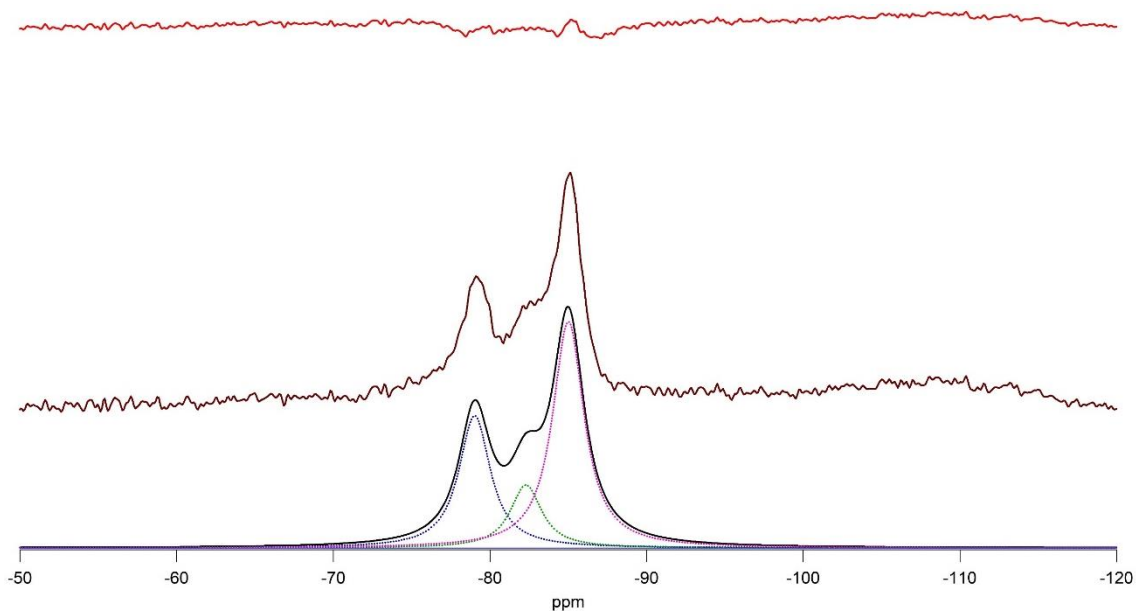


Figure 8.23 ^{29}Si NMR spectra for DL – 3 showing the experimental spectrum (middle, brown), residual (top, red x1) and the individual frequencies.

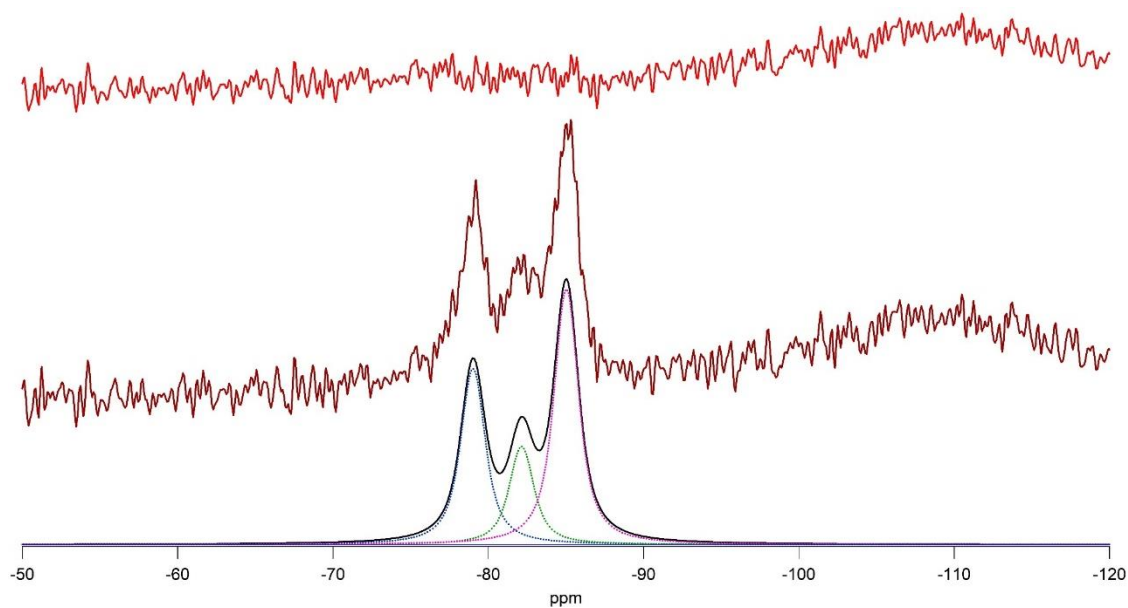


Figure 8.24 ^{29}Si NMR spectra for DL – 4 showing the experimental spectrum (middle, brown), residual (top, red x1) and the individual frequencies.

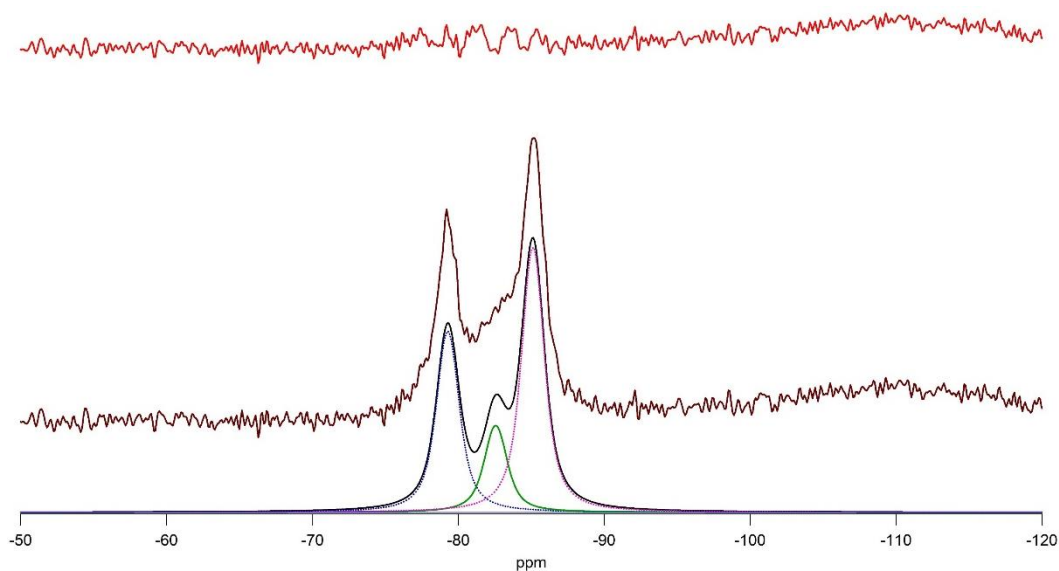


Figure 8.25 ^{29}Si NMR spectra for DL – 5 showing the experimental spectrum (middle, brown), residual (top, red x1) and the individual frequencies.

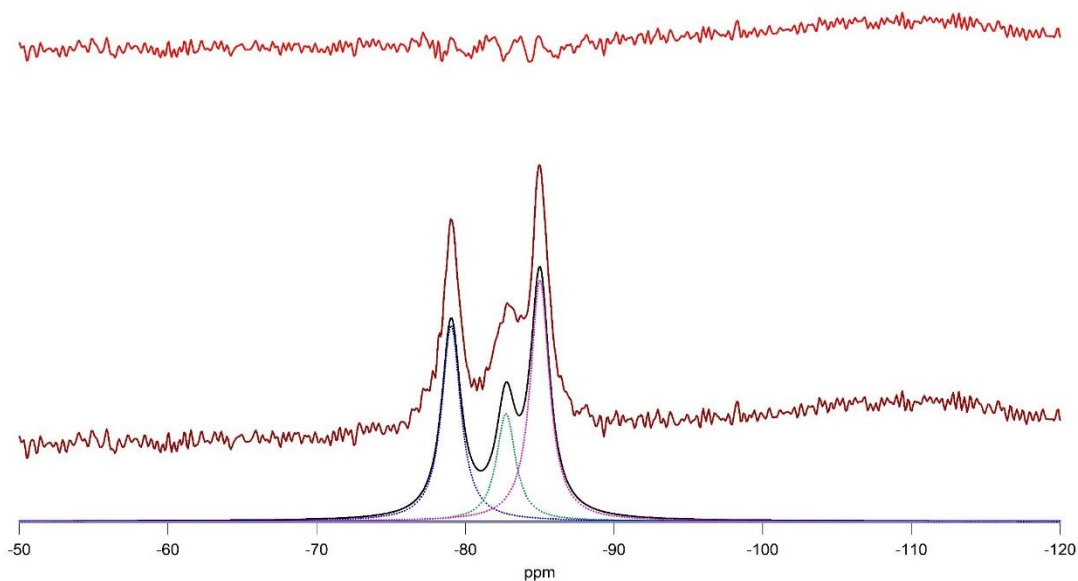


Figure 8.26 ^{29}Si NMR spectra for DL – 6 showing the experimental spectrum (middle, brown), residual (top, red x1) and the individual frequencies.

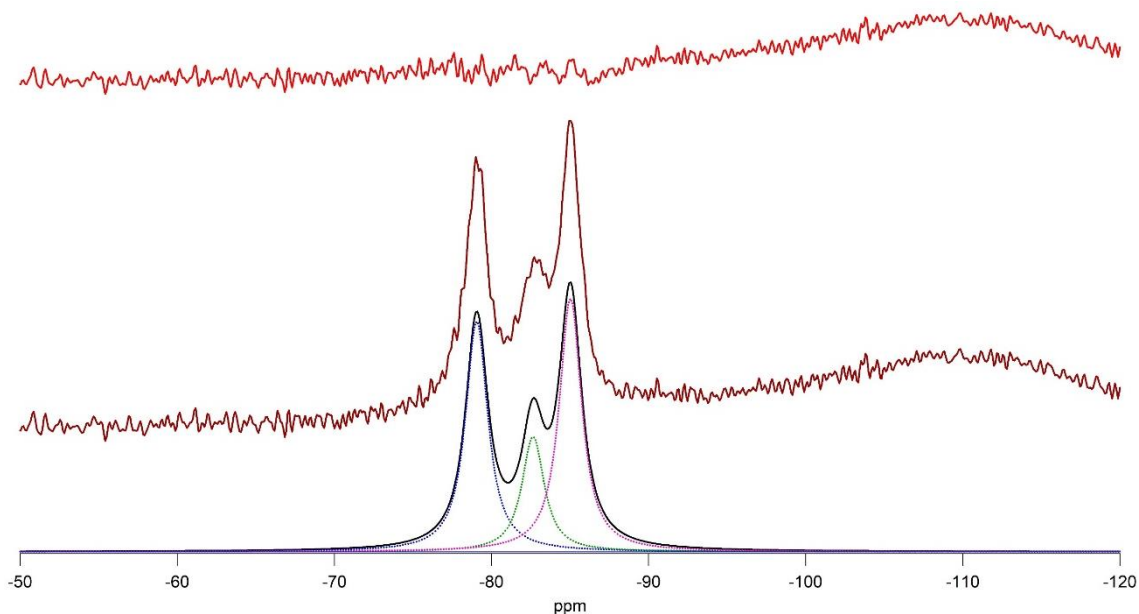


Figure 8.27 ^{29}Si NMR spectra for DL – 7 showing the experimental spectrum (middle, brown), residual (top, red x1) and the individual frequencies.

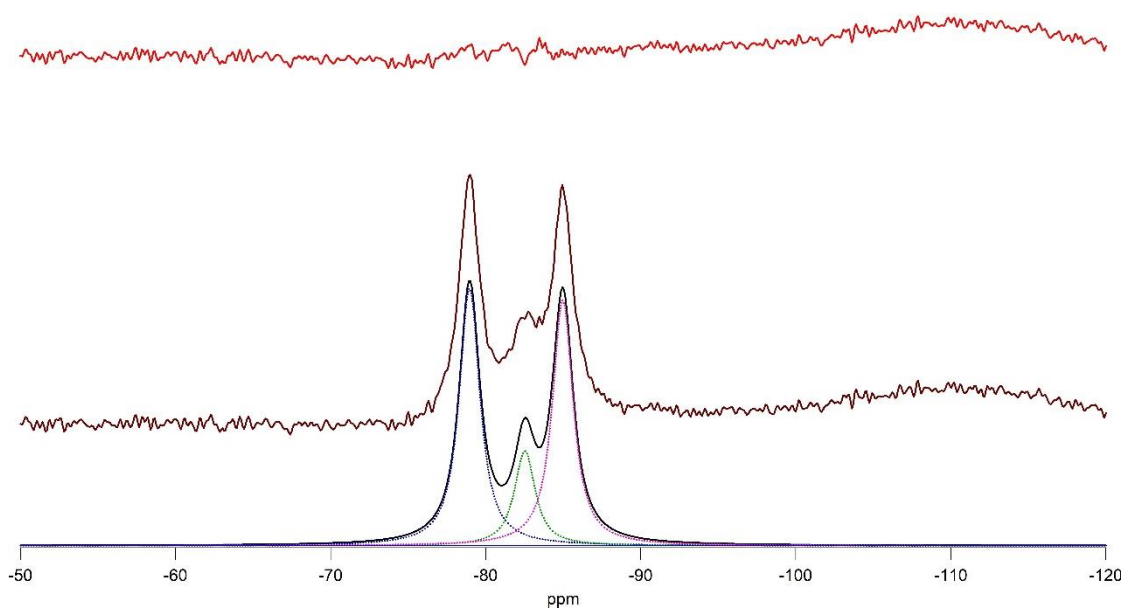


Figure 8.28 ^{29}Si NMR spectra for DL – 8 showing the experimental spectrum (middle, brown), residual (top, red x1) and the individual frequencies.

The absence of Q³ groups at $\delta = -94$ ppm indicates that only single dreierketten are present. Figure 8.29 shows mean silicate chain length (MCL) plotted against mean Ca/Si ratio and it is clearly seen that as Ca/Si ratio increases, the MCL decreases.

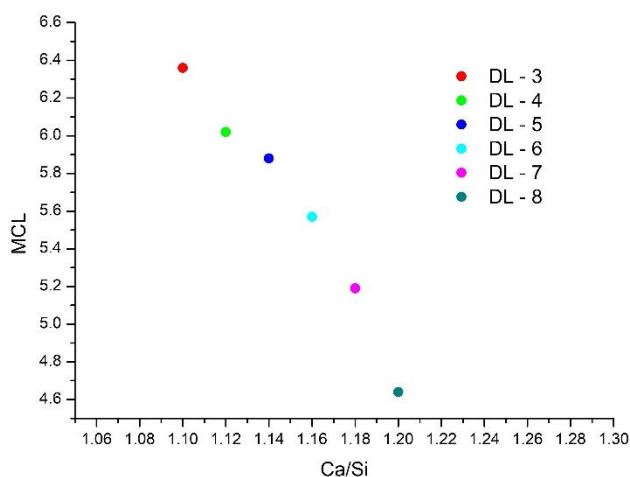


Figure 8.29 Mean silicate chain lengths calculated from ²⁹Si NMR data plotted against Ca/Si ratios measured from TEM - EDX.

Sample	Q ¹ (%)	Q ² (%)	MCL	Ca/Si _{TEM-EDX}
DL – 3	31.4	68.6	6.37	1.10
DL – 4	33.2	66.7	6.02	1.12
DL – 5	34.0	66.0	5.88	1.14
DL – 6	35.9	64.1	5.57	1.16
DL – 7	38.5	61.5	5.19	1.18
DL – 8	43.1	56.9	4.64	1.20

Table 8:7 Results of deconvolution of the ²⁹Si NMR spectra showing % of silicate species and MCL. Mean Ca/Si ratios measured by TEM – EDX are also included.

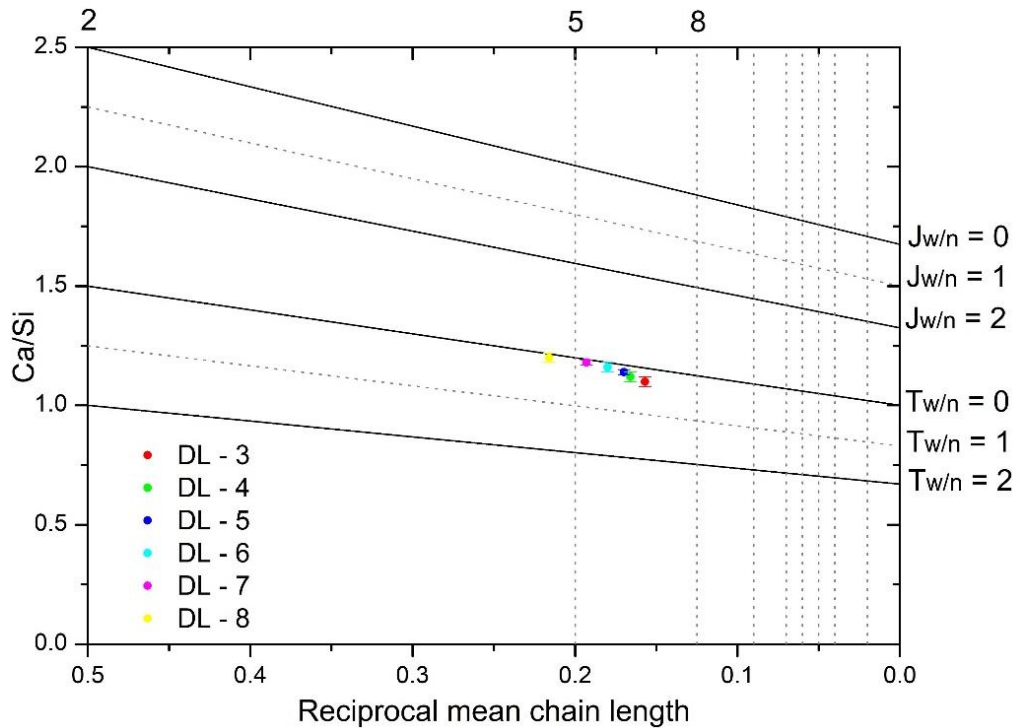
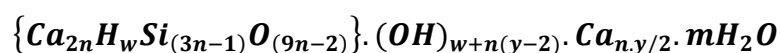


Figure 8.30 Mean Ca/Si obtained by TEM-EDX analysis versus reciprocal mean chain length obtained by NMR analysis. The structural units for tobermorite and jennite with minimum ($w=0$), intermediate ($w=1$) and maximum ($w=2$) degree of protonation are plotted along with data points from current work. The vertical dotted lines represent the $(3n - 1)$ structural units: dimer (2), pentamer (5) etc.

Richardson and Groves' model (described in Literature Review) is used for the formulation of the C-S-H phases synthesized. Figure 8.30 shows the Ca/Si ratios plotted against the reciprocal mean chain length. Figure also shows the trends for tobermorite and jennite units with various degrees of protonation ($w = 0, 1, 2$). The mean values of Ca/Si ratios are represented by filled circles in the Figure above. The mean values of Ca/Si ratios fall in the tobermorite like region on the plot, and no Ca-OH groups are required in the structure coming either from jennite like structures or solid solution CH.

The T/J formulation is chosen with a general formula:



Where, $n = (MCL+1)/3$ and $y = [(Ca/Si)(6n-2)-4n]/n$

w depends on the value of y

if, $0 \leq y \leq 2$ then $n(2-y) \leq w \leq 2n$

if, $2 \leq y \leq 4$ then $0 \leq w \leq 2n$

if, $4 \leq y \leq 6$ then $0 \leq w \leq n(6-y)$

The values calculated for n, y, w_{min} (minimum no. of silanol groups) and w_{max} (maximum number of silanol groups) are tabulated in Table 8:8.

Sample	n	y	w_{min}	w_{max}
DL – 3	2.46	1.70	0.73	4.91
DL – 4	2.34	1.76	0.56	4.68
DL – 5	2.29	1.85	0.35	4.59
DL – 6	2.19	1.90	0.22	4.38
DL – 7	2.06	1.94	0.13	4.13
DL – 8	1.88	1.92	0.14	3.76

Table 8:8 Calculated values required for the formulation using T/J viewpoint.

The minimum degree of protonation is chosen according to the position of mean Ca/Si ratio values with respect to the tobermorite trends. The structural chemical formulae for all the C-S-H phases synthesized are shown below:

DL - 3: $[Ca_{4.91}H_{0.73}Si_{6.37}O_{20.11}] \cdot Ca_{2.09} \cdot mH_2O$

DL - 4: $[Ca_{4.68}H_{0.56}Si_{6.02}O_{19.05}] \cdot Ca_{2.06} \cdot mH_2O$

DL - 5: $[Ca_{4.59}H_{0.35}Si_{5.88}O_{18.65}] \cdot Ca_{2.12} \cdot mH_2O$

DL - 6: $[Ca_{4.38}H_{0.22}Si_{5.57}O_{17.71}] \cdot Ca_{2.08} \cdot mH_2O$

DL - 7: $[Ca_{4.13}H_{0.13}Si_{5.19}O_{16.58}] \cdot Ca_{2.00} \cdot mH_2O$

DL - 8: $[Ca_{3.76}H_{0.14}Si_{4.64}O_{14.92}] \cdot Ca_{1.81} \cdot mH_2O$

All the samples can be explained as a combination of T2, T5, T8 units.

8.1.6 STA of dynamic leached C-S-H samples

The STA traces of all the dynamic leached samples are shown in Figure 8.31. Along with TG and DSC, gas analysis is also performed to monitor the gases expelled from the samples. All the water and CO₂ traces are shown in Figure 8.32. The results for all the samples show that the weight loss until 200 °C corresponds to the dehydration of C-S-H phase. This matches with the peak corresponding to release of water shown in water trace. The weight loss at about 450 °C in the samples is associated to the decarbonation of amorphous C \bar{C} . The absence of CH phase in the samples indicates that this phase is removed by the process of leaching. All the samples show carbonation with weight loss between 700 °C – 800 °C corresponding to the decomposition of crystalline C \bar{C} . The DSC curves show an exothermal peak at about 850 °C corresponding to the formation of β -wollastonite [171]. It is also observed that the formation of β -wollastonite occurs at higher temperatures as the Ca/Si ratio increases. Figure 8.33 shows the transformation temperature of C-S-H samples to β -wollastonite and Table 8:9 shows the values of onset transformation temperature for all the C-S-H samples.

This increasing trend in the transformation temperature with Ca/Si ratio is reported by Rodriguez [63][172].

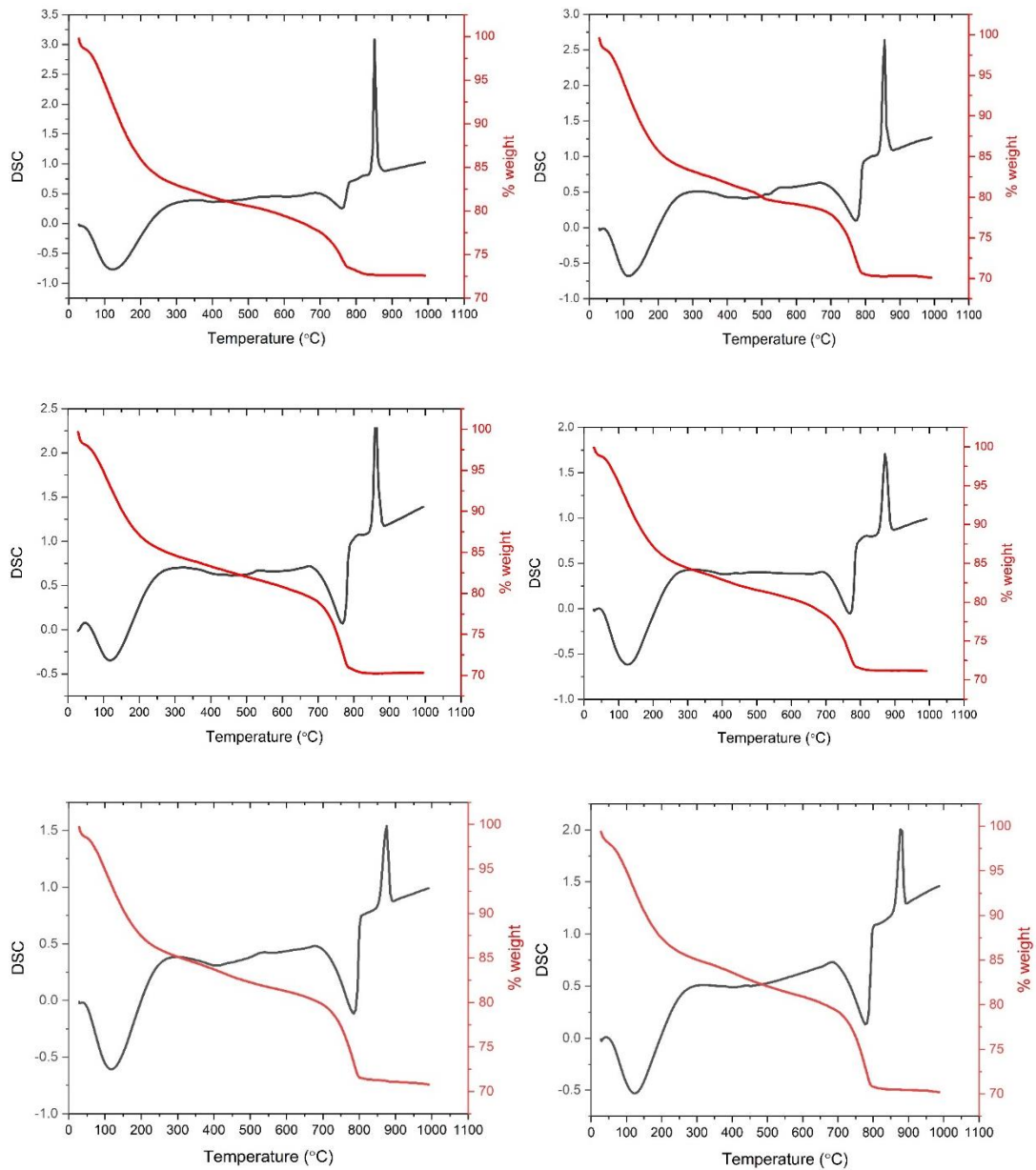


Figure 8.31 STA patterns of DL samples showing DSC in grey and % TG in red (top left: DL – 3, top right: DL – 4, middle left: DL – 5, middle right: DL – 6, bottom left: DL – 7, bottom right: DL – 8).

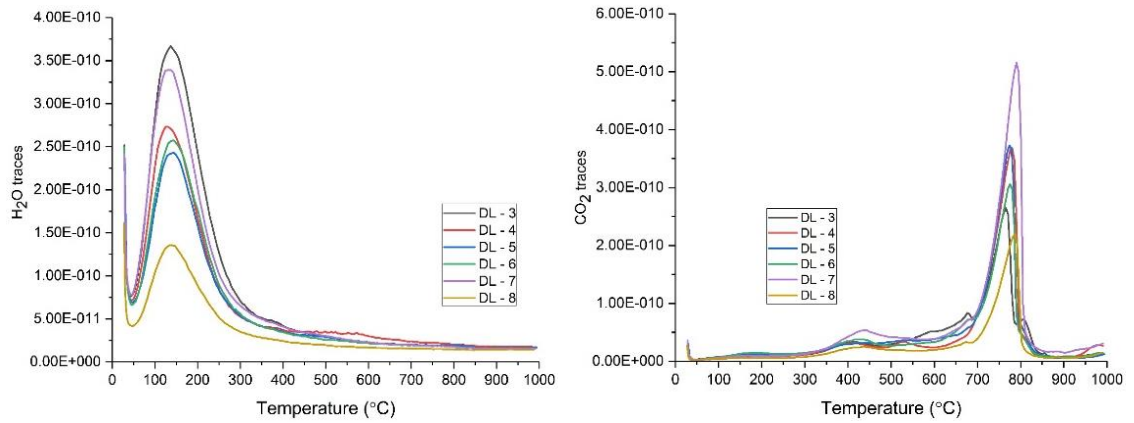


Figure 8.32 Water and CO₂ traces of all the dynamic leached samples.

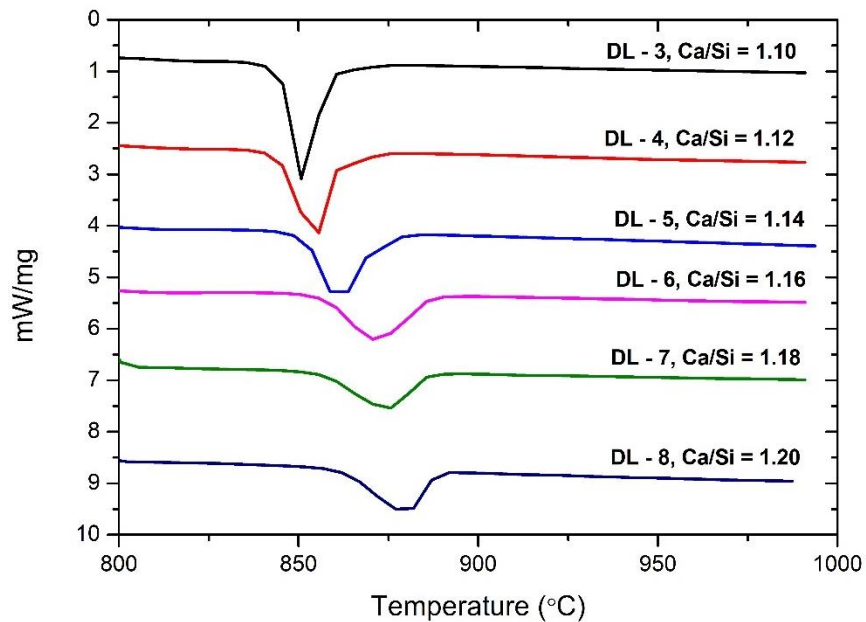


Figure 8.33 DSC curves showing the transformation temperature of C-S-H to β -wollastonite in all the dynamic leached samples.

Leaching results in the removal of CH phase and formation of $C\bar{C}$ if C-S-H gels are exposed to CO₂. The formation of $C\bar{C}$ is a result of the reaction of CO₃²⁻ ions from CO₂ with Ca²⁺. The Ca²⁺ ions required are obtained by the dissolution of CH and C-S-H, thus increasing the polymerisation of the C-S-H structure.

Sample	Ca/Si _{TEM - EDX}	Temperature of transformation (°C)
DL – 3	1.10	850.711
DL – 4	1.12	855.690
DL – 5	1.14	863.758
DL – 6	1.16	870.661
DL – 7	1.18	875.646
DL – 8	1.20	877.036

Table 8:9 Variation in transformation temperature of C-S-H to β -wollastonite with mean Ca/Si ratios.

8.1.7 TEM-EDX of hydrothermally aged C-S-H sample

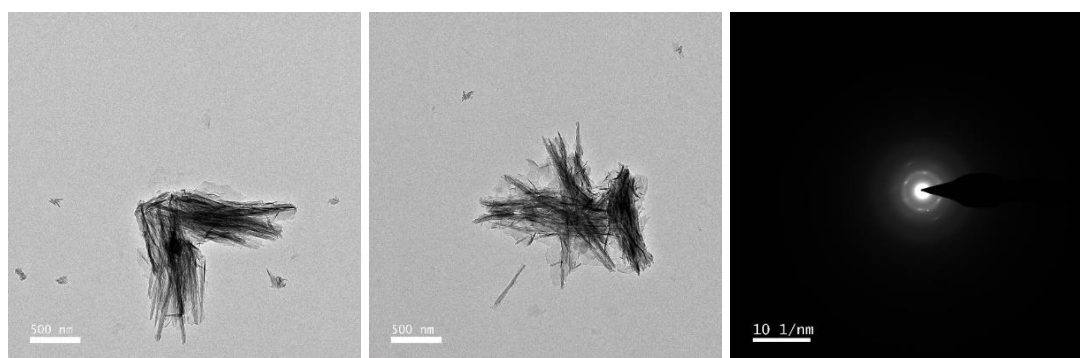


Figure 8.34 TEM micrographs of hydrothermally aged C-S-H sample showing foil-like morphology with Ca/Si = 1.54. The SAED pattern is also shown.

The TEM micrographs along with the SAED pattern of hydrothermally aged C-S-H sample are shown in Figure 8.34. The C-S-H exhibits foil-like morphology consistent with the decrease in Ca/Si ratio obtained from EDX analysis. The mean Ca/Si ratio obtained is 1.54 ± 0.03 (N = 36). The low standard deviation

indicates the presence of pure phase without any intermixture from other phases.

The histogram for the Ca/Si ratios is shown in Figure 8.35.

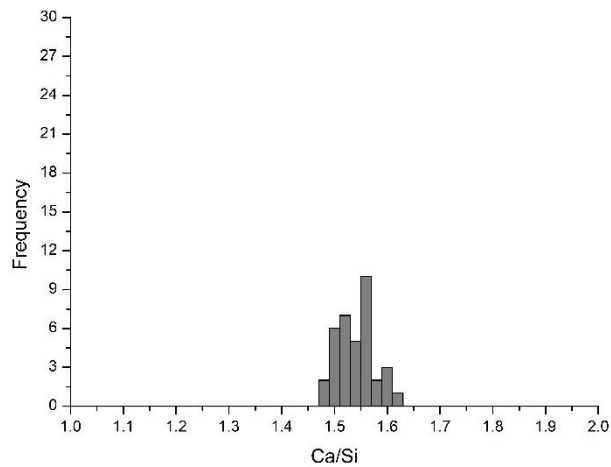


Figure 8.35 Histogram of Ca/Si ratios measured using TEM – EDX.

8.1.8 ²⁹Si NMR of Hydrothermally aged C-S-H sample

The ²⁹Si NMR spectrum for the hydrothermally aged C-S-H sample is shown in Figure 8.36. Deconvolution is done to estimate the percentage of silicate species and the mean chain length. The deconvoluted spectrum, the individual frequencies and the simulated spectrum, are all shown in the Figure below. The peaks at about $\delta = -79$ ppm corresponds to the presence of Q¹ groups and the peak at about $\delta = -84$ ppm corresponds to the presence of Q² species. The presence of these groups indicate that the hydrate possesses dimers and middle chain groups. The MCL calculated is 4.23 and % Q¹ and % Q² species are 45.2 % and 50.5 % respectively. It is clearly seen that the silicate structure is dominated by Q² species. The increased amount of Q² species indicates an increased level of polymerisation which is evident from the lengthening of mean silicate chain length. Two frequencies are used to deconvolute Q¹ contribution to improve the fitting when there are asymmetric peaks and adjust the simulated spectrum and experimental spectrum.

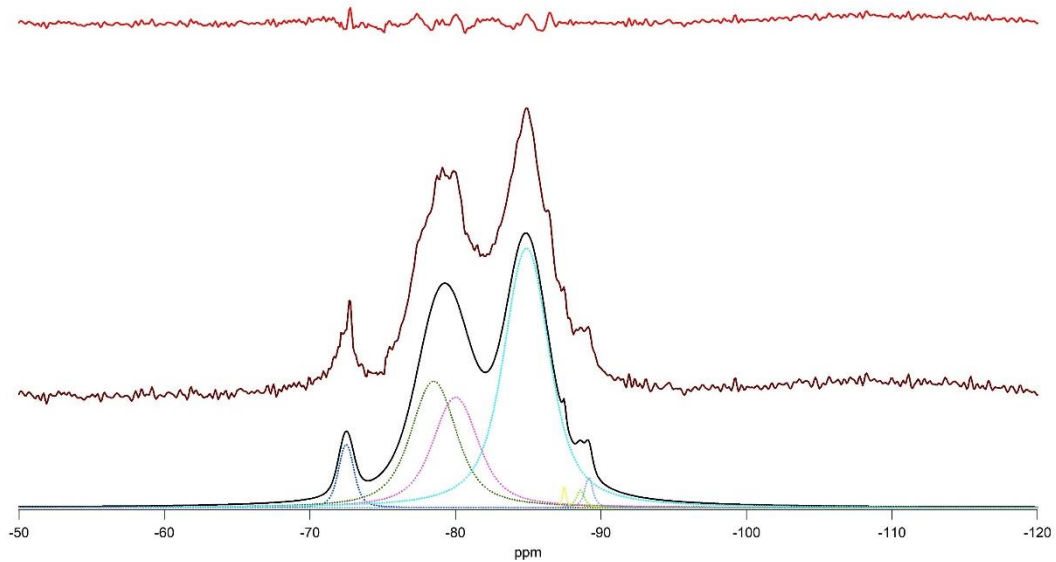


Figure 8.36 ^{29}Si NMR spectra for hydrothermally aged C-S-H sample showing the experimental spectrum (middle, brown), residual (top, red x1) and the individual frequencies.

There is a peak at $\delta = -73$ ppm indicating the presence of Y- C_2S [159] indicating that its reactivity is too low. The three peaks around $\delta = -87$ ppm, $\delta = -88$ ppm and $\delta = -89$ ppm correspond to the presence of wollastonite [158].

Richardson and Groves' model (described in Literature Review) is used for the formulation of the C-S-H phase. Figure 8.37 shows the Ca/Si ratio plotted against the reciprocal mean chain length. Figure also shows the trends for tobermorite and jennite units with various degrees of protonation ($w = 0, 1, 2$). The mean value of Ca/Si ratios is represented by filled circle in the Figure below. The mean value of Ca/Si ratios falls between the tobermorite and jennite like regions on the plot, thus confirming the presence of Ca-OH groups in the structure coming either from jennite like structures or solid solution CH. In T/J viewpoint, the Ca-OH groups form a part of the main layer and in T/CH viewpoint, the Ca-OH groups are present in the interlayers. Since, the STA trace (discussed later) clearly shows the presence of CH in the sample, both T/J and T/CH viewpoints are used

to obtain the structural chemical formula. However, the C-S-H phases before leaching (discussed in chapter 6) follow T/J view point and hence these phases after leaching also follow T/J viewpoint.

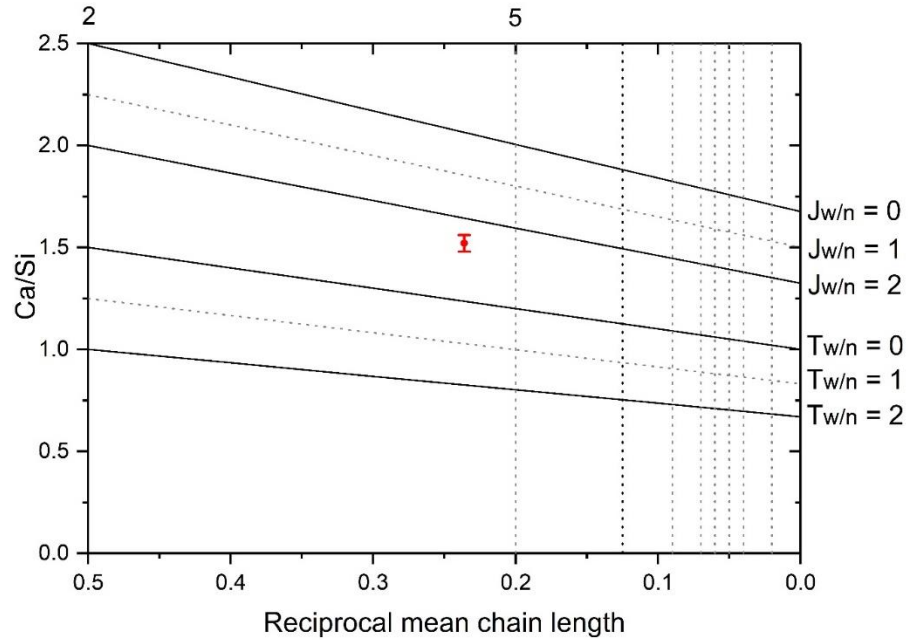
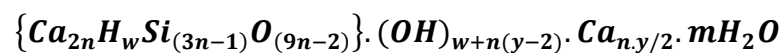


Figure 8.37 Mean Ca/Si obtained by TEM-EDX analysis versus reciprocal mean chain length obtained by NMR analysis. The structural units for tobermorite and jennite with minimum ($w=0$), intermediate ($w=1$) and maximum ($w=2$) degree of protonation are plotted along with data points from current work. The vertical dotted lines represent the $(3n - 1)$ structural units: dimer (2), pentamer (5) etc.

The general formula for T/J viewpoint:



Where, $n = (MCL+1)/3$ and $y = [(Ca/Si)(6n-2)-4n]/n$

w depends on the value of y

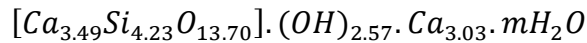
if, $0 \leq y \leq 2$ then $n(2-y) \leq w \leq 2n$

if, $2 \leq y \leq 4$ then $0 \leq w \leq 2n$

if, $4 \leq y \leq 6$ then $0 \leq w \leq n(6-y)$

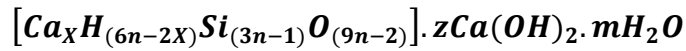
The values calculated for n , y , w_{\min} (minimum no. of silanol groups) and w_{\max} (maximum number of silanol groups) are 1.74, 3.47, 0 and 3.49 respectively.

The structural chemical formula for the hydrothermally aged C-S-H phase synthesized is shown below:



The C-S-H phase is a combination of dimeric and pentameric units, T2, T5, J2, J5.

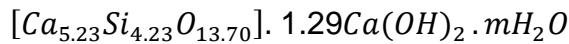
The general formula for T/CH viewpoint:



Where, $X = (6n-w)/2$ and $z = (w+n(y-2))/2$

The values calculated for X and z calculated using the values of n , y and w_{\min} are 5.23, 1.29 respectively.

The structural chemical formulae for the hydrothermally aged C-S-H phase synthesized is shown below:



8.1.9 STA of hydrothermally aged C-S-H sample

The STA traces depicting DSC and TG curves along with gas analysis curves for hydrothermally aged C-S-H sample is shown in Figure 8.38. The weight loss until 200 °C corresponds to the dehydration of C-S-H phase and the weight loss at about 400 °C corresponds to the dehydration of CH phase. These match with the

sharp features that appear in the H₂O trace. The water trace also shows a peak at 500 °C corresponding to the presence of crystalline CH phase. However, the presence of two peaks corresponding to CH in the water trace indicates the possibility of crystal growth and variation in crystal size. The presence of crystalline CH phase indicates its decreased solubility at higher temperatures. The DSC curve shows a larger and more defined peak at about 200 °C than the leached samples (discussed in previous section) indicating a higher degree of crystallisation, thus giving rise to more stable forms. There is also a weight loss at about 800 °C corresponding to the decomposition of crystalline $C\bar{C}$ and this matches with the release of CO₂ in the CO₂ trace. The CO₂ trace also shows a peak at about 500 °C corresponding to the decarbonation of amorphous $C\bar{C}$. The DSC curve also shows an exothermic peak at about 900 °C corresponding to the formation of wollastonite [171].

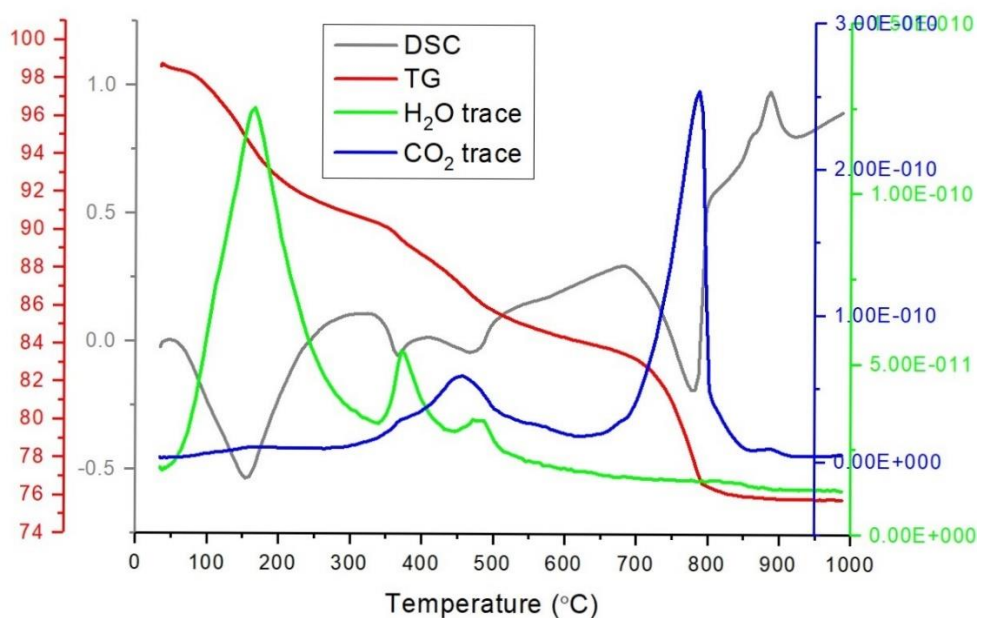


Figure 8.38 STA pattern of hydrothermally aged C-S-H sample showing DSC in grey and % TG in red. Water and CO₂ traces are also shown.

8.1.10 Comparison of MCL variation with Ca/Si ratios for all the artificially aged C-S-H phases

The experimental MCL (calculated from NMR analysis) values of all the aged samples are plotted against the mean Ca/Si ratio values (obtained from TEM – EDX) in Figure 8.39. Reported data from literature is also plotted. The dotted lines represent the tobermorite lines with various degrees of protonation: minimum (right), intermediate (middle) and maximum (left) from Richardson and Groves' model. Maximum degree of protonation indicates that the negative charge is entirely balanced by protons in Si-OH groups. Intermediate degree of protonation indicates that the negative charge is balanced equally by proton in Si-OH and Ca. Minimum degree of protonation indicates that the negative charge is balanced entirely by Ca.

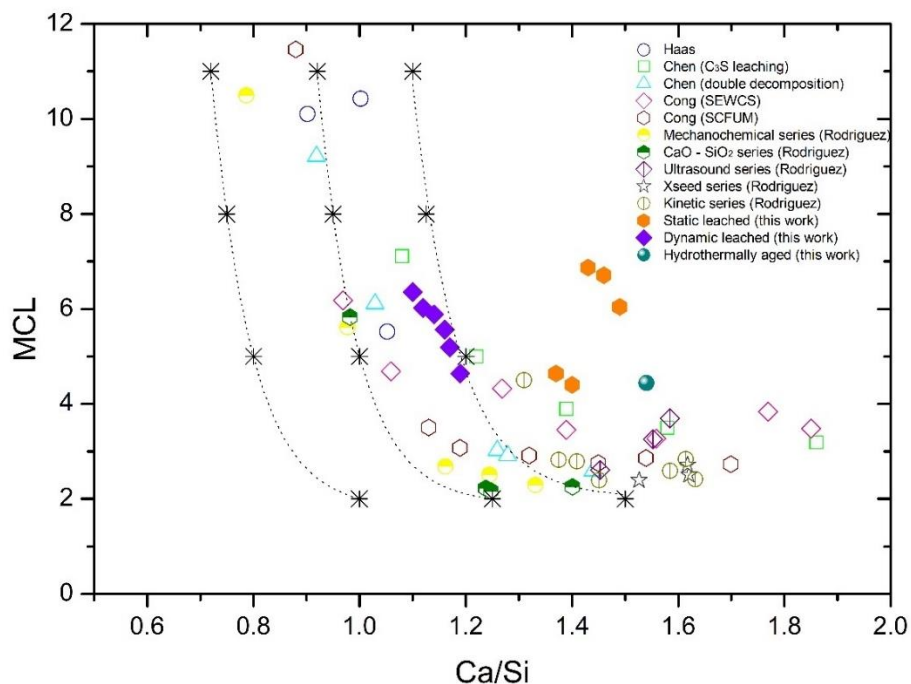


Figure 8.39 MCL versus Ca/Si ratios for all the C-S-H samples synthesized. Reported data from literature is also plotted along with various degrees of protonation from Richardson and Grove's model [31][41][45][63][163].

The tobermorite line with minimum degree of protonation represents the maximum Ca/Si ratio that can be achieved without the Ca-OH groups in the structure. The reported data from literature suggests that there is a drastic decrease in MCL up to Ca/Si \approx 1, followed by a slight decrease up to Ca/Si \approx 1.3, after which MCL almost remains constant (\approx 3) with increase in Ca/Si ratios. This indicates the formation of dimeric silicate chains and change in MCL is very less after this. The variations in the silicate structure noticed as Ca/Si ratio increases are due to the removal of bridging tetrahedra and incorporation of additional Ca²⁺ ions. All the data points from static leaching and hydrothermal ageing fall to the right of the right dotted line indicating the need of presence of Ca-OH groups in the structure. The data points from dynamic leaching fall close to the right dotted line meaning no Ca-OH groups are needed in the structure either from solid solution CH or jennite units.

Chapter 9 Conclusions and further work

The comparative study between synthetic C-S-H phases and cementitious backfills show that the behaviour on ageing is similar, thus providing an evidence that synthetic C-S-H phases are analogous to the C-S-H gels formed on hydration of cements. Single phase synthetic C-S-H phases with Ca/Si ratios in the range 1.5 – 2.0 were successfully synthesized via silica lime reactions and hydration of β -C₂S, without the use of C₃S or alkalis.

The comparative study between the fresh and aged NRVB showed that leaching resulted in removal of CH and Mc phases, reduction in Ca/Si ratio of the C-A-S-H phase accompanied by a change in morphology from fibrillar to foil-like and lengthening of aluminosilicate chains, followed by destruction of C-A-S-H phase and formation of a low-Ca aluminosilicate gel. Leaching followed by hydrothermal treatment resulted in the removal of Ht phase and formation of semi-crystalline C-A-S-H (I) phase.

The C-S-H phases synthesized by static and ball mill hydration via hydrothermal synthesis of β -C₂S showed the formation of C-S-H phases with Ca/Si ratios in the range of 1.79 – 1.82 for static hydrated samples and 1.78 – 1.92 for ball mill hydrated samples. The rate of hydration of β -C₂S is found to be faster in case of ball mill hydration. The morphology in all the samples is seen to be fibrillar, consistent with the high values of Ca/Si ratios obtained. The C-S-H phases synthesised via static hydration showed an increase in the dimeric silicate species as the hydration progressed and the initial formation of C-S-H phases via ball mill hydration showed a high content of dimeric silicate species followed by increased silicate polymerisation and middle chain groups. Ishida et al [8]

suggested that the dimers formed are continuously removed by the process of ball mill hydration. Since dimer is unstable in suspension, rapid polymerisation of dimers yields in an increased MCL. Also, another possibility could be that the rate of polymerisation increases with increase in temperature and time. The temperature in the ball mill hydration process is increased due to milling resulting in long silicate chains. Higher curing temperatures promote the formation of high molecular weight polymers which is slow at 25 °C [112][173][174]. The C-S-H phases synthesised via constant lime concentration method showed the formation of C-S-H phases with Ca/Si ratios in the range of 1.5 – 1.8. The morphology of C-S-H phases seen is found to be dependent on the lime concentration in solution. Samples synthesized at 21 mmol/L and 22 mmol/L (Ca/Si = 1.51 and 1.56) showed foil-like morphology, samples at 23 mmol/L and 24 mmol/L (Ca/Si = 1.61 and 1.64) showed a mixture of foil and fibrillar morphology indicating more directional growth and samples at 25 mmol/L and 26 mmol/L (Ca/Si = 1.69, 1.74, 1.79 and 1.81) showed fibrillar morphology. The decrease in rate of addition of TEOS showed a slight increase in the Ca/Si ratios although the lime concentration in solution remained constant indicating the formation of a nanostructurally different C-S-H phase due to slower formation of C-S-H. However, more data points are required to confirm this. Further work could be done to determine the relation between morphology, composition and rate of TEOS addition. All the samples showed the presence of dimers and middle chain groups with the percentage of dimers increasing with the lime concentration and reduction in mean silicate chain lengths. Pure C-S-H phases with a Ca/Si ratio in the range 1.5 – 1.8 without any intermixture from other Ca rich phases were successfully synthesized and this is evident from the low standard deviation

seen in EDX data points. This indicates that morphology is controlled by the lime concentration in solution.

The process of leaching resulted in alteration of a metastable amorphous C-S-H gel to a more stable phase and the process of hydrothermal ageing resulted in the formation of crystalline solid phases in agreement with the literature [175][176]. Leaching of the C-S-H phases in deionised water was done for both static and dynamic leaching experiments. Samples synthesized via static and ball mill hydration were subjected to undergo static leaching and samples synthesized via constant lime concentration method were dynamically leached. The results of static and dynamic leaching showed the formation of C-S-H phases with Ca/Si ratios in the range of 1.37 – 1.49 (static leaching) and 1.06 – 1.20 (dynamic leaching). The morphology of all the C-S-H phases is seen to be foil-like, consistent with the low Ca/Si ratios. All the samples showed an increased amount of Q² species indicating the removal of Ca from the structure and modification of the silicate structure. The approach towards congruent dissolution is observed in the case of dynamic leaching. In the case of static leaching this behaviour was not observed, possibly because of the termination of the leaching process before the congruency was achieved. The comparison between the leached samples from static leaching and dynamic leaching showed that samples with similar Ca/Si ratio were leached to a higher extent in the case of dynamic leaching. This is because the dynamic leaching process is an extensive leaching process and hence congruency can be reached quickly. The process of hydrothermal ageing resulted in the formation of a crystalline C-S-H phase and the most striking feature is the presence of CH phase indicating its low solubility at higher temperatures. The Ca/Si ratio of the C-S-H sample aged hydrothermally for six

months was 1.54 indicating that greater is the crystallinity, slower is the dissolution kinetics.

The comparison of fresh NRVB sample and synthetic C-S-H phases showed that the C-S-H phases in S1 (chapter 5) are similar to those synthesized by static hydration (SHC) in chapter 6. The morphology of both the phases is fibrillar with high Ca/Si ratio and shorter silicate chains. The sample S2 in chapter 5 can be considered similar to the synthetic C-S-H phases prepared via ball mill hydration (BHC) in chapter 6 where the morphology in both the phases is fibrillar with high Ca/Si ratio and longer silicate chains. The leached sample S3 in chapter 5 can be compared to SL – 7, SL – 8 and SL – 9 in chapter 8 where the morphology is changed to foil-like with a decrease in the Ca/Si ratio and increase in the silicate chain lengths. However, there is no presence of Q³ or Q⁴ phases in any of the artificially aged synthetic C-S-H phases.

The application of Richardson and Groves' model to derive structural chemical formulae and deduce the combination of structural units showed that the C-S-H samples synthesized via static and ball mill hydration by hydrothermal synthesis of β -C₂S and constant lime concentration method require Ca-OH groups regardless the morphology and Ca/Si ratio in the structure. The static leached samples also showed the need for Ca-OH groups in their structures. However, the dynamic leached samples with foil-like morphology could be explained entirely by tobermorite units without the need of Ca-OH groups either from solid solution CH or jennite like units. The hydrothermally aged C-S-H sample also showed the need of Ca-OH groups in its structure. Although both T/J and T/CH viewpoints were equally valid to derive the structural chemical formulae of the phases (chapter 6 & chapter 7) before the process of leaching, the leaching

results (described in chapter 8) showed that all the C-S-H phases synthesized by different methods in this work (described in chapter 6 & chapter 7) follow T/J view point rather than T/CH viewpoint. This is because the Ca is present in the interlayers according to the T/CH viewpoint and removal of this by the process of leaching would only result in a change in Ca/Si ratios but not the silicate structure. But the leaching results clearly showed that both Ca/Si ratio (decreased) and silicate anion structure (more Q² than Q¹) of the C-S-H phases changed indicating that the Ca is removed by the process of leaching from the main layers rather than the interlayers, thus clearly suggesting that C-S-H phases before leaching follow T/J view point. This also indicates that the C-S-H phases after leaching and hydrothermal ageing also follow T/J view point rather than T/CH viewpoint. The morphological and compositional studies on synthetic C-S-H phases discussed in the project provided an understanding of the evolution of the C-S-H phases present in NRVB on leaching and hydrothermal ageing. However, due to time constraints and other limitations, questions do remain that could be addressed in future studies. The study of changes in pH buffering capacity of the C-S-H phases could be investigated in future using the high Ca/Si ratios ratio C-S-H phases synthesized. Quantitative XRD can provide details on the degree of crystallinity of the synthetic C-S-H phases. A comparison of the pH buffering capacity of C-S-H phases with similar Ca/Si ratio but varied degrees of crystallinity can provide an understanding on the affects that crystallinity may have on the pH buffering capacity. The solution analysis of Ca and Si can provide a clear understanding of the kinetics of leaching during the process before congruency is reached. This would then provide a complete understanding on

the effects of ageing and how ageing affects the leaching characteristics of C-S-H.

References

- [1] P. D. Wilson, *The nuclear fuel cycle : from ore to wastes*. Oxford University Press, 1996.
- [2] “Geological Disposal Engineered Barrier System Status Report; DSSC/452/01,” 2016.
- [3] R. Taylor, I. G. Richardson, and R. M. D. Brydson, “Composition and microstructure of 20-year-old ordinary Portland cement-ground granulated blast-furnace slag blends containing 0 to 100% slag,” *Cem. Concr. Res.*, vol. 40, no. 7, pp. 971–983, 2010.
- [4] H. F. W. Taylor, “Hydrated calcium silicates. Part I. Compound formation at ordinary temperatures .,” *J. Chem. Soc.*, pp. 3682–3690, 1950.
- [5] S. Brunauer and S. A. Greenberg, “The hydration of tricalcium silicate and β -dicalcium silicate at room temperature,” in *Chemistry of Cement. Proceedings of the 4th International Symposium, Washington 1960, National Bureau of Standards Monograph, 43, Vol. 1 (US Department of Commerce)*, 1962, pp. 135–165.
- [6] H. Ishida, K. Sasaki, and T. Mitsuda, “Highly reactive β -dicalcium silicate: I, hydration behavior at room temperature,” *J. Am. Ceram. Soc.*, vol. 75, no. 2, pp. 353–358, 1992.
- [7] H. Ishida, K. Mabuchi, and K. Sasaki, “Low-temperature synthesis of β – Ca_2SiO_4 from hillebrandite,” *J. Am. Ceram. Soc.*, vol. 75, no. 9, pp. 2427–2432, 1992.
- [8] H. Ishida, K. Sasaki, A. Mizuno, Y. Okada, and T. Mitsuda, “Highly reactive

- β -dicalcium silicate: IV, ball-milling and static hydration at room temperature,” *J. Am. Ceram. Soc.*, vol. 75, no. 10, pp. 2779–2784, 1992.
- [9] A. Grudemo, “An electronographic study of the morphology and crystallization properties of calcium silicate hydrates.,” *Handl. – Sven. Forskningsinstitutet för Cem. och Betong vid K. Tek. Högskolan i Stock.*, no. 26, pp. 1–103, 1955.
- [10] V. S. Ramachandran and R. F. Feldman, “Concrete Science,” pp. 1–66, 1996.
- [11] J. P. (W. R. G. and C. (US)) Skalny, *Materials science of concrete 1*. United States: Columbus, OH (USA); American Ceramic Society Inc., 1989.
- [12] G. C. Bye, *Portland Cement: Composition, Production and Properties*. Thomas Telford, 1999.
- [13] M. Regourd and A. Guinier, “Cristallochimie des constituants du clinker de ciment Portland,” in *Proc. of the 6th ICCO, Moscow*, 1974, pp. 201–215.
- [14] I. Maki and S. Chromy, “Microscopic study on the Polymorphism of Ca_3SiO_5 ,” *Cem. Concr. Res.*, vol. 8, no. 4, pp. 407–414, 1978.
- [15] G. W. Groves, “Microcrystalline calcium hydroxide in Portland cement pastes of low water/cement ratio,” *Cem. Concr. Res.*, vol. 11, no. 5–6, pp. 713–718, 1981.
- [16] G. W. Groves, P. J. LeSueur, and W. Sinclair, “Transmission electron microscopy and microanalytical studies of ion-beam-thinned sections of tricalcium silicate paste,” *J. Am. Ceram. Soc.*, vol. 69, pp. 353–356, 1986.
- [17] I. G. Richardson and G. W. Groves, “Microstructure and microanalysis of

- hardened ordinary Portland cement pastes," *J. Mater. Sci.*, vol. 28, no. 1, pp. 265–277, 1993.
- [18] H. F. W. Taylor, *Cement Chemistry*. Thomas Telford, 1997.
- [19] J. Bensted, "Y-dicalcium silicate and its hydraulicity," *Cem. Concr. Res.*, vol. 8, no. 1. pp. 73–76, 1978.
- [20] R. Shahsavari, L. Chen, and L. Tao, "Edge dislocations in dicalcium silicates: Experimental observations and atomistic analysis," *Cem. Concr. Res.*, vol. 90, pp. 80–88, 2016.
- [21] R. Taylor, "Characterization of C-S-H in early and late age systems containing admixtures," 2010.
- [22] J. Bensted, "Some applications of conduction calorimetry to cement hydration," *Adv. Cem. Res.*, vol. 1, no. 1, pp. 35–44, 1987.
- [23] K. H. Jost and B. Ziemer, "Relations between the crystal structures of calcium silicates and their reactivity against water," *Cem. Concr. Res.*, vol. 14, no. 2, pp. 177–184, 1984.
- [24] P. Mondal and J. W. Jeffery, "The crystal structure of tricalcium aluminate, $\text{Ca}_3\text{Al}_2\text{O}_6$," *Acta Crystallogr.*, p. 689, 1975.
- [25] Y. Takeuchi, F. Nishi, and I. Maki, "Crystal-chemical characterization of the $3\text{CaOAl}_2\text{O}_3\text{-Na}_2\text{O}$ solid solution series," *Zeitschrift Fur Krist.*, vol. 152, no. 3–4, pp. 259–307, 1980.
- [26] I. Odler and R. Wonnemann, "Effect of alkalis on portland cement hydration. I. Alkali oxides incorporated into the crystalline lattice of clinker minerals," *Cem. Concr. Res.*, vol. 13, no. 4, pp. 477–482, 1983.

- [27] I. Jawed and J. Skalny, "Alkalies in cement: A review I. Forms of alkalies and their effect on clinker formation," *Cem. Concr. Res.*, vol. 7, no. 6, pp. 719–729, 1977.
- [28] R. S. Gollop and H. F. W. Taylor, "Microstructural and microanalytical studies of sulfate attack. II. Sulfate-resisting Portland cement: Ferrite composition and hydration chemistry," *Cem. Concr. Res.*, vol. 24, no. 7, pp. 1347–1358, 1994.
- [29] I. G. Richardson and G. W. Groves, "The incorporation of minor and trace elements into calcium silicate hydrate (CSH) gel in hardened cement pastes," *Cem. Concr. Res.*, vol. 23, no. 1, pp. 131–138, 1993.
- [30] I. Odler, *Hydration, Setting and Hardening of Portland Cement*, Fourth Edi. Elsevier Ltd., 2003.
- [31] I. G. Richardson, "Tobermorite/jennite- and tobermorite/calcium hydroxide-based models for the structure of C-S-H: Applicability to hardened pastes of tricalcium silicate, β -dicalcium silicate, Portland cement, and blends of Portland cement with blast-furnace slag, metakaol," *Cem. Concr. Res.*, vol. 34, no. 9, pp. 1733–1777, 2004.
- [32] E. Bonaccorsi, S. Merlino, and A. R. Kampf, "The crystal structure of tobermorite 14 Å (plombierite), a C-S-H phase," *J. Am. Ceram. Soc.*, vol. 88, no. 3, pp. 505–512, 2005.
- [33] X. Cong and R. J. Kirkpatrick, " ^{29}Si and ^{17}O NMR investigation of the structure of some crystalline calcium silicate hydrates," *Adv. Cem. Based Mater.*, vol. 3, no. 3–4, pp. 133–143, 1996.
- [34] T. C. Powers, "Structure and physical properties of hardened Portland

- cement paste,” *J. Am. Ceram. Soc.*, vol. 41, no. 1, pp. 1–6, 1958.
- [35] R. F. Feldman and P. J. Sereda, “A new model for hydrated Portland cement and its practical implications,” *Eng. J.*, vol. 53, no. 8/9, pp. 53–59, 1970.
- [36] K. Fujii and W. Kondo, “Estimation of thermochemical data for calcium silicate hydrate (C-S-H),” *Commun. Am. Ceram. Soc.*, no. December, pp. C–220, 1983.
- [37] H. F. W. Taylor, “Proposed structure for calcium silicate hydrate gel,” *J. Am. Ceram. Soc.*, vol. 69, no. 6, pp. 464–467, 1986.
- [38] H. F. W. Taylor, “Nanostructure of CSH: Current status,” *Adv. Cem. Based Mater.*, vol. 1, no. 1, pp. 38–46, 1993.
- [39] I. G. Richardson and G. W. Groves, “Models for the composition and structure of calcium silicate hydrate (CSH) gel in hardened tricalcium silicate pastes,” *Cem. Concr. Res.*, vol. 22, no. 6, pp. 1001–1010, 1992.
- [40] X. Cong and R. J. Kirkpatrick, “²⁹Si MAS NMR study of the structure of calcium silicate hydrate,” *Adv. Cem. Based Mater.*, vol. 3, no. 3–4, pp. 144–156, 1996.
- [41] J. J. Chen, J. J. Thomas, H. F. W. Taylor, and H. M. Jennings, “Solubility and structure of calcium silicate hydrate,” *Cem. Concr. Res.*, vol. 34, no. 9, pp. 1499–1519, 2004.
- [42] R. J.-M. Pellenq, A. Kushima, R. Shahsavari, K. J. V. Vliet, M. J. Buehler, S. Yip, F. J. Ulm, “A realistic molecular model of cement hydrates,” *Proc. Natl. Acad. Sci.*, vol. 106, no. 38, pp. 16102–16107, 2009.

- [43] A. J. Allen, J. J. Thomas, and H. M. Jennings, "Composition and density of nanoscale calcium-silicate-hydrate in cement," *Nat. Mater.*, vol. 6, no. 4, pp. 311–316, 2007.
- [44] I. G. Richardson, "The importance of proper crystal-chemical and geometrical reasoning demonstrated using layered single and double hydroxides," *Acta Crystallogr. Sect. B Struct. Sci. Cryst. Eng. Mater.*, vol. 69, no. 2, pp. 150–162, 2013.
- [45] I. G. Richardson, "Model structures for C-(A)-S-H(l)," *Acta Crystallogr. Sect. B Struct. Sci. Cryst. Eng. Mater.*, vol. 70, no. 6, pp. 903–923, 2014.
- [46] J. D. Bernal, J. W. Jeffery, and H. F. W. Taylor, "Crystallographic research on the hydration of Portland cement. A first report on investigations in progress," *Mag. Concr. Res.*, vol. 4, pp. 49–54, 1952.
- [47] G. L. Kalousek and A. F. Prebus, "Crystal chemistry of hydrous calcium silicates: III, Morphology and other properties of tobermorite and related phases," *J. Am. Ceram. Soc.*, vol. 41, pp. 124–132, 1958.
- [48] H. Matsuyama and J. F. Young, "Intercalation of polymers in calcium silicate hydrate: A new synthetic approach to biocomposites," *Chem. Mater.*, vol. 11, no. 1, pp. 16–19, 1999.
- [49] H. Matsuyama and J. F. Young, "Effects of pH on precipitation of quasi-crystalline calcium silicate hydrate in aqueous solution," *Adv. Cem. Res.*, vol. 12, no. 1, pp. 29–33, 2000.
- [50] K. Garbev, G. Beuchle, M. Bornefeld, L. Black, and P. Stemmermann, "Cell dimensions and composition of nanocrystalline calcium silicate hydrate solid solutions. Part 1: synchrotron-based x-ray diffraction," *J. Am. Ceram.*

Soc., vol. 91, no. 9, pp. 3005–3014, 2008.

- [51] L. Black, K. Garbev, and I. Gee, “Surface carbonation of synthetic C-S-H samples: A comparison between fresh and aged C-S-H using X-ray photoelectron spectroscopy,” *Cem. Concr. Res.*, vol. 38, no. 6, pp. 745–750, 2008.
- [52] G. Renaudin, J. Russias, F. Leroux, F. Frizon, and C. Cau-dit-Coumes, “Structural characterization of C-S-H and C-A-S-H samples-Part I: Long-range order investigated by Rietveld analyses,” *J. Solid State Chem.*, vol. 182, no. 12, pp. 3312–3319, 2009.
- [53] H. F. W. Taylor and J. W. Howison, “Relationships between calcium silicates and clay minerals,” *Clay Miner. Bull.*, vol. 3, pp. 98–111, 1956.
- [54] H. F. W. Taylor, “Hydrated calcium silicates. Part V. The water content of calcium silicate hydrate (I),” *J. Chem. Soc.*, no. 1, pp. 163–171, 1952.
- [55] F. B. Kinjiro and W. Kondo, “Heterogeneous equilibrium of calcium silicate hydrate in water at 30°C,” *J. Chem. Soc.*, no. 1081, pp. 645–651, 1981.
- [56] El-Hamaly, K. Mohan and H. F. W. Taylor, “Autoclaved lime - quartz materials II. Thermogravimetry and trimethylsilylation,” *Cem. Concr. Res.*, vol. 8, pp. 671–676, 1978.
- [57] J. A. Gard, J. W. Howison, and H. F. W. Taylor, “Synthetic compounds related to tobermorite: an electron microscope, X ray and dehydration study,” *Magn. Concr. Res.*, no. 11, pp. 151–158, 1959.
- [58] G. Renaudin, J. Russias, F. Leroux, C. Cau-dit-Coumes, and F. Frizon, “Structural characterization of C-S-H and C-A-S-H samples-Part II: Local

- environment investigated by spectroscopic analyses,” *J. Solid State Chem.*, vol. 182, no. 12, pp. 3320–3329, 2009.
- [59] X. Cong and R. James Kirkpatrick, “ ^{17}O and ^{29}Si MAS NMR study of $\beta\text{-C}_2\text{S}$ hydration and the structure of calcium-silicate hydrates,” *Cem. Concr. Res.*, vol. 23, no. 5, pp. 1065–1077, 1993.
- [60] C. Carde, G. Escadeillas, and A. H. François, “Use of ammonium nitrate solution to simulate and accelerate the leaching of cement pastes due to deionized water,” *Mag. Concr. Res.*, vol. 49, no. 181, pp. 295–301, 2009.
- [61] P. Colombet, A. R. Grimmer, H. Zanni, and P. Sozzani, *Nuclear Magnetic Resonance Spectroscopy of Cement-Based Materials*. 1998.
- [62] S. Garrault-Gauffinet, and A. Nonat, “Experimental investigation of calcium silicate hydrate (C-S-H) nucleation,” *J. Cryst. Growth*, vol. 200, no. 3, pp. 565–574, 1999.
- [63] E. Tajuelo Rodriguez, “Relation between composition, structure and morphology in C-S-H,” *Sch. Eng.*, no. February, 2015.
- [64] A. Kumar, B. J. Walder, A. K. Mohamed, A. Hofstetter, B. Srinivasan, A. J. Rossini, K. Scrivener, L. Emsley, and P. Bowen., “The atomic-level structure of cementitious calcium silicate hydrate,” *J. Phys. Chem. C*, vol. 121, no. 32, pp. 17188–17196, 2017.
- [65] A. Kumar, B. J. Walder, A. K. Mohamed, A. Hofstetter, B. Srinivasan, A. J. Rossini, K. Scrivener, L. Emsley, and P. Bowen., “The atomic-level structure of cementitious calcium silicate hydrate – Supporting Information Table of Contents,” *J. Phys. Chem. C*, vol. 121, no. 32, pp. 17188–17196, 2017.

- [66] J. H. Sharp, J. Hill, N. B. Milestone, and E. W. Miller, "Cementitious systems for encapsulation of intermediate level waste," *Proc. ICEM '03 9th Int. Conf. Radioact. Waste Manag. Environ. Remediat.*, pp. 1–10, 2003.
- [67] I. G. Crossland, "Cracking of the Nirex Reference Vault Backfill: A review of its likely occurrence and significance," *Crossl. Consult.*, pp. 1–49, 2007.
- [68] J. C. Kuri, "Leaching of cementitious materials : A Review," *Asian Trans. Eng.*, vol. 05, no. 05, pp. 15–18, 2015.
- [69] A. Haworth, S. Sharland, and C. Tweed, "Modelling of the degradation of cement in a nuclear waste repository," *Mater. Res. Soc. Symp. Proc. Cambridge Univ Press*, pp. 447–454, 1989.
- [70] D. E. Macphee, K. Luke, F. P. Glasser, and E. E. Lachowski, "Solubility and aging of calcium silicate hydrates in alkaline solutions at 25°C," *J. Am. Ceram. Soc.*, vol. 72, no. 4, pp. 646–654, 1989.
- [71] M. L. D. Gougar, B. E. Scheetz, and D. M. Roy, "Ettringite and C-S-H Portland cement phases for waste ion immobilization: A Review," *Waste Manag.*, vol. 16, no. 4, pp. 295–303, 1996.
- [72] W. Lin, A. Cheng, R. Huang, C. Chen, and X. Zhou, "Effect of calcium leaching on the properties of cement-based composites," *J. Wuhan Univ. Technol. Mater. Sci. Ed.*, vol. 26, no. 5, pp. 990–997, 2011.
- [73] U. R. Berner, "Evolution of pore water chemistry during degradation of cement in a radioactive waste repository environment," *Waste Manag.*, vol. 12, no. 2–3, pp. 201–219, 1992.
- [74] P. Faucon, F. Adenot, M. Jorda, and R. Cabrillac, "Behaviour of crystallised

- phases of Portland cement upon water attack," *Mater. Struct.*, vol. 30, no. 8, pp. 480–485, 1997.
- [75] K. Haga, M. Shibata, M. Hironaga, S. Tanaka, and S. Nagasaki, "Silicate anion structural change in calcium silicate hydrate gel on dissolution of hydrated cement," *J. Nucl. Sci. Technol.*, vol. 39, no. 5, pp. 540–547, 2002.
- [76] C. Carde, R. François, and Jean Michel Torrenti, "Leaching of both calcium hydroxide and C-S-H from cement paste: Modelling the mechanical behavior," *Cem. Concr. Res.*, vol. 26, no. 8, pp. 1257–1268, 1996.
- [77] C. Carde and R. François, "Effect of the leaching of calcium hydroxide from cement paste on mechanical and physical properties," *Cem. Concr. Res.*, vol. 27, no. 4, pp. 539–550, 1997.
- [78] F. Adenot and M. Buil, "Modelling of the corrosion of the cement paste by deionised water," *Cem. Concr. Res.*, vol. 22, pp. 489–496, 1992.
- [79] K. Haga, M. Shibata, M. Hironaga, S. Tanaka, and S. Nagasaki, "Change in pore structure and composition of hardened cement paste during the process of dissolution," *Cem. Concr. Res.*, vol. 35, no. 5, pp. 943–950, 2005.
- [80] C. Carde, and R. François, "Modelling the loss of strength and porosity increase due to the leaching of cement pastes," *Cem. Concr. Compos.*, vol. 21, no. 3, pp. 181–188, 1999.
- [81] M. Kersten, "Aqueous solubility diagrams for cementitious waste stabilization systems. 1. The C-S-H solid-solution system," *Environ. Sci. Technol.*, vol. 30, no. 7, pp. 2286–2293, 1996.

- [82] A. W. Harris, P. Biddle, A. Hollinrake, M. C. Manning, W. M. Tearle, and C. J. Tweed, "Testing of models of the dissolution of cements - Leaching of synthetic CSH gels," *AEAT/ERRA-0368*, 2002.
- [83] E. J. Reardon, "Problems and approaches to the prediction of the chemical composition in cement/water systems," *Waste Manag.*, vol. 12, no. 2–3, pp. 221–239, 1992.
- [84] M. M. Rahman, S. Nagasaki, and S. Tanaka, "Model for dissolution of CaO-SiO₂-H₂O gel at Ca/Si>1," *Cem. Concr. Res.*, vol. 29, no. 7, pp. 1091–1097, 1999.
- [85] U. R. Berner, "Modelling the incongruent dissolution of hydrated cement minerals," *Radiochim. Acta*, vol. 44–45, no. 2, pp. 387–394, 1988.
- [86] F. H. Heukamp, F. J. Ulm, and J. T. Germaine, "Mechanical properties of calcium-leached cement pastes: Triaxial stress states and the influence of the pore pressures," *Cem. Concr. Res.*, vol. 31, no. 5, pp. 767–774, 2001.
- [87] K. L. Scrivener and J. F. Young, *Mechanisms of Chemical Degradation of Cement-based Systems*, Taylor and Francis. 1997.
- [88] D. C. Molcuilaire, C. E. A. Saclay, and G. Yvette, "Leaching of cement: Study of the surface layer," *Cem. Concr. Res.*, vol. 26, no. 11, pp. 1707–1715, 1996.
- [89] P. Faucon, F. Adenot, J. . Jacquinot, J. . Petit, R. Cabrillac, and M. Jorda, "Long-term behaviour of cement pastes used for nuclear waste disposal: review of physico-chemical mechanisms of water degradation," *Cem. Concr. Res.*, vol. 28, no. 6, pp. 847–857, 1998.

- [90] J. J. Chen, "The Nanostructure of Calcium Silicate Hydrate," Northwestern University, 2003.
- [91] G. W. Groves, A. Brough, I. G. Richardson, and C. M. Dobsont, "Progressive changes in the structure of hardened C₃S cement pastes due to carbonation," *J. Am. Ceram. Soc.*, vol. 74, no. 11, pp. 2891–2896, 1991.
- [92] G. W. Groves, D. I. Rodway, and I. G. Richardson, "The carbonation of hardened cement pastes," *Adv. Cem. Res.*, vol. 3, no. 11, pp. 117–125, 1990.
- [93] G. M. N. Baston, M. M. Cowper, and T. A. Marshall, "Sorption properties of aged cements," *Mineral. Mag.*, vol. 76, no. 8, pp. 3411–3423, 2012.
- [94] *Geological Disposal: - Geosphere Status Report; DSSC/453/01*, no. December. 2016.
- [95] C. R. Wilding, "The performance of cement based systems.," *Cem. Concr. Res.*, vol. 22, no. 299–310, pp. 457–459, 1992.
- [96] M. Cowper, *Chapter 7, Barrier performance of cements and concretes in nuclear waste repositories, European Commission 4th Framework Program, Contract No. F14W-CT96-0030, Report EUR 19780.* .
- [97] J. L. Mier-Buenhombre, "Thermal analysis of inorganic materials," p. 12.
- [98] V. S. Ramachandran, "Thermal Analysis," pp. 127–173.
- [99] M. Thiery, G. Villain, P. Dangla, and G. Platret, "Investigation of the carbonation front shape on cementitious materials: Effects of the chemical kinetics," *Cem. Concr. Res.*, vol. 37, no. 7, pp. 1047–1058, 2007.
- [100] B. K. Marsh and R. L. Day, "Pozzolanic and cementitious reactions of fly

- ash in blended cement pastes,," *Cem. Concr. Res.*, pp. 301–310, 1988.
- [101] A. K. Chatterji, "X-Ray Diffraction," in *Analytical Techniques in Concrete Science and Technology*, 1958, pp. 275–332.
- [102] P. Bensted, J. Barnes, Ed., *Structure and Performance of Cements*, 2nd ed. Spon Press, Taylor and Francis Group.
- [103] B. D. Cullity, "*Elements of X Ray diffraction*," pp. 531, 1956.
- [104] K. Mackenzie and M. Smith, "Multinuclear Solid-State NMR of Inorganic Materials," in *Multinuclear Solid-State NMR of Inorganic Materials*, vol. 6, Eds. Pergamon, 2002, pp. v–vii.
- [105] W. Reusch, "Nuclear Magnetic Resonance Spectroscopy," *Michigan State Univ. Dep. Chem.*, pp. 1–13, 2013.
- [106] K. Scrivener, R. Snellings, and B. Lothenbach, *A practical guide to microstructural analysis of cementitious materials*. 2016.
- [107] L. Doerrer, "NMR spectroscopy in inorganic chemistry (Iggo, Jonathan A.)," *J. Chem. Educ.*, vol. 78, p. 1469, 2001.
- [108] E. Lippmaa, M. Mägi, M. Tarmak, W. Wieker, and A. R. Grimmer, "A high resolution ^{29}Si NMR study of the hydration of tricalciumsilicate," *Cem. Concr. Res.*, vol. 12, no. 5, pp. 597–602, 1982.
- [109] D. R. Roberts, F. P. Glasser, G. M. M. Bell, M. J. Taylor, E. E. Lachowski, and J. Bensted, "Study of calcium silicate hydrates by solid state high resolution ^{29}Si nuclear magnetic resonance," *Adv. Cem. Res.*, vol. 3, no. 9, pp. 23–27, 1990.
- [110] M. Mägi, E. Lippmaa, A. Samoson, G. Engelhardt, and A. R. Grimmer,

- “Solid-state high-resolution silicon-29 chemical shifts in silicates,” *J. Phys. Chem.*, vol. 88, no. 8, pp. 1518–1522, 1984.
- [111] I. G. Richardson, A. R. Brough, G. W. Groves, and C. M. Dobson, “The characterization of hardened alkali-activated blast-furnace slag pastes and the nature of the calcium silicate hydrate (C-S-H) phase,” *Cem. Concr. Res.*, vol. 24, no. 5, pp. 813–829, 1994.
- [112] J. Hirlljac, Z. Q. Wu, and J. F. Young, “Silicate polymerization during the hydration of alite,” *Cem. Concr. Res.*, vol. 13, no. 6, pp. 877–886, 1983.
- [113] J. Francis, “Investigations of calcium silicate hydrate structure using silicon-29 Nuclear Magnetic Resonance Spectroscopy,” *Comm. Am. Ceram. Soc.*, vol. 120, pp. 118–120, 1988.
- [114] I. G. Richardson and G. W. Groves, “The structure of the calcium silicate hydrate phases present in hardened pastes of white Portland cement/blast-furnace slag blends,” *J. Mater. Sci.*, vol. 32, no. 18, pp. 4793–4802, 1997.
- [115] I. G. Richardson, A. R. Brough, R. Brydson, G. W. Groves, and C. M. Dobson, “Location of aluminium in substituted calcium silicate hydrate (C-S-H) gels as determined by Si-29 and Al-27 NMR and EELS,” *J. Am. Ceram. Soc.*, vol. 76, no. 9, pp. 2285–2288, 1993.
- [116] J. Skibsted, H. J. Jakobsen, and C. Hall, “Direct observation of aluminum guest ions in the silicate phases of cement minerals by ²⁷Al MAS NMR spectroscopy,” *J. Chem. Soc. Trans.*, vol. 90, no. 14, pp. 2095–2098, 1994.
- [117] K. J. D. MacKenzie and M. E. Smith, Eds., “Chapter 10 - NMR of Other Quadrupolar Nuclei,” in *Multinuclear Solid-State NMR of Inorganic Materials*, vol. 6, Pergamon, 2002, pp. 629–683.

- [118] E. Oldfield, R. A. Kinsey, K. A. Smith, J. A. Nichols, and R. J. Kirkpatrick, "High-resolution NMR of inorganic solids. Influence of magnetic centers on magic-angle sample-spinning lineshapes in some natural aluminosilicates," *J. Magn. Reson.*, vol. 51, no. 2, pp. 325–329, 1983.
- [119] J. Skibsted, E. Henderson, and H. J. Jakobsen, "Characterization of calcium aluminate phases in cements by ^{27}Al MAS NMR spectroscopy," *Inorg. Chem.*, vol. 32, no. 6, pp. 1013–1027, 1993.
- [120] T. F. Sevelsted and J. Skibsted, "Carbonation of C-S-H and C-A-S-H samples studied by ^{13}C , ^{27}Al and ^{29}Si MAS NMR spectroscopy," *Cem. Concr. Res.*, vol. 71, pp. 56–65, 2015.
- [121] C. A. Love, "Microstructure And Silicate Anion Structure Of Hardened Blended Cement Pastes," 2002.
- [122] W. Sinclair and G. W. Groves, "Transmission electron microscopy and X-ray diffraction of doped dicalcium silicate," *J. Am. Ceram. Soc.*, vol. 67, no. 5, pp. 325–330, 1984.
- [123] I. G. Richardson, "The nature of the hydration products in hardened cement pastes," *Cem. Concr. Compos.*, vol. 22, no. 2, pp. 97–113, 2000.
- [124] I. G. Richardson and G. W. Groves, "Microstructure and microanalysis of hardened cement pastes involving ground granulated blast-furnace slag," *J. Mater. Sci.*, vol. 27, no. 22, pp. 6204–6212, 1992.
- [125] W. Eitel, O. E. Muller, and O. E. Radczewski, "Examination of clay minerals with the ultramicroscope," *Berichte der Dtsch. Keramischen Gesellschaft*, vol. 20, no. 4, pp. 165–178, 1939.

- [126] A. Grudemo, "The microstructure of cement gel phases," in *Trans. Roy. Inst. Technol., Stockholm, Sweden*, 1965, pp. 1–287.
- [127] A. Grudemo, "The microstructure of hardened cement paste," in *4th ISCC*, 1962, pp. 615–647.
- [128] D. Viehland, J.-F. Li, L.-Y. Yuan, and Z. Xu, "Mesostructure of calcium silicate hydrate (C-S-H) gels in Portland cement paste: short-range ordering, nanocrystallinity, and local compositional order," *J. Am. Ceram. Soc.*, vol. 79, no. 7, pp. 1731–1744, 1996.
- [129] I. G. Richardson, J. Skibsted, L. Black, and R. J. Kirkpatrick, "Characterisation of cement hydrate phases by TEM, NMR and Raman spectroscopy," *Adv. Cem. Res.*, vol. 22, no. 4, pp. 233–248, 2010.
- [130] G. O. Assarsson, "Hydrothermal reactions between calcium hydroxide and amorphous silica; The reactions between 120°C and 160°C," *J. Phys. Chem.*, vol. 62, pp. 223–228, 1958.
- [131] T. Mitsuda and S. Banno, "Hydrothermal formation of pseudowollastonite from lime-quartz mixtures at 165 and 200°C," *Cem. Concr. Compos.*, vol. 7, pp. 457–460, 1977.
- [132] G. Bell, J. Bensted, and F. P. Glasser, "Characterization of hydrothermally-treated calcium silicate and oilwell cement hydration products," *Adv. Cem. Res.*, vol. 2, no. 6, pp. 61–72, 1989.
- [133] N. A. Torpov, K. S. Nikogosyan, and A. I. Boikova, "On the dehydration of the hydrated calcium silicate - hillebrandite," *Zhurnal Neorg. Khimii*, vol. 4, pp. 1159–1164, 1959.

- [134] J. F. Young and H. S. Tong, "Microstructure and strength development of beta-dicalcium silicate pastes with and without admixtures," *Cem. Concr. Res.*, vol. 7, pp. 627–636, 1977.
- [135] I. Jelenić and A. Bezjak, "On the hydration kinetics of α' - and β -modifications of dicalcium silicate," *Cem. Concr. Res.*, vol. 11, no. 3, pp. 467–471, 1981.
- [136] M. Collepardi and L. Massidda, "Hydration of beta dicalcium silicate alone and in the presence of CaCl_2 or $\text{C}_2\text{H}_5\text{OH}$," *J. Am. Ceram. Soc.*, vol. 56, no. 4, pp. 181–183, 1973.
- [137] I. Jelenic, A. Bezjak, and M. Bujan, "Hydration of B_2O_3 -stabilized- α' - and β modifications of dicalcium silicate," *Cem. Concr. Res.*, vol. 8, pp. 173–180, 1978.
- [138] P. Fierens and J. Tirlocq, "Effect of synthesis temperature and cooling conditions of beta dicalcium silicate on its hydration rate," *Cem. Concr. Res.*, vol. 13, pp. 41–48, 1983.
- [139] R. Trettin, G. Oliev, C. Stadelmann, and W. Wieker, "Very early hydration of dicalcium silicate-polymorphs," *Cem. Concr. Res.*, vol. 21, no. 5, pp. 757–764, 1991.
- [140] P. Barret and D. Bertrandie, "Aqueous solubility relationships for 2~types of calcium silicate hydrate - Comment," *J. Am. Ceram. Soc.*, vol. 71, no. 2, pp. C113–C115, 1988.
- [141] Y. Tong, H. Du, and L. Fei, "CP/MAS NMR studies of the initial hydration processes of activated and ordinary beta-dicalcium silicates," *Cem. Concr. Res.*, vol. 20, no. 6, pp. 986–991, 1990.

- [142] H. S. Tong, "Composition of solutions in contact with hydrating beta dicalcium silicate," *Cem. Concr. Res.*, vol. 60, p. 321, 1977.
- [143] J. F. Young and H. S. Tong, "Microstructure and strength development of beta-dicalcium silicate pastes with and without admixtures," *Cem. Concr. Res.*, vol. 7, no. 6, pp. 627–636, 1977.
- [144] H. Sarp and D. R. Peacor, "Jaffeite, a new hydrated calcium silicate from the Kombat mine, Namibia," *Am. Mineral.*, vol. 74, no. 9–10, pp. 1203–1206, 1989.
- [145] B. R. I. Harker, "Scawtite and its synthesis," *Mineral. Mag.*, vol. 34, no. 1935, pp. 232–236, 1965.
- [146] E. R. Cantrill, M. G. Stevens, A. Ray, and L. Aldridge, "The use of DTA to determine the effects of mineralizers on the cement-quartz autoclave reactions. Part 1. Gibbsite addition," *Thermochim. Acta*, vol. 224, no. C, pp. 241–246, 1993.
- [147] I. G. Richardson, A. V. Girão, R. Taylor, and S. Jia, "Hydration of water- and alkali-activated white Portland cement pastes and blends with low-calcium pulverized fuel ash," *Cem. Concr. Res.*, vol. 83, pp. 1–18, 2016.
- [148] H. Bassett, "Notes on the system lime-water, and on the determination of calcium," *J. Chem. Soc.*, pp. 1270–1275, 1934.
- [149] P. Barnes and J. Bensted, *Structure and Performance of Cements, Second Edition*. Taylor & Francis, 2002.
- [150] M. D. Andersen, H. J. Jakobsen, and J. Skibsted, "Characterization of white Portland cement hydration and the C-S-H structure in the presence of

- sodium aluminate by ^{27}Al and ^{29}Si MAS NMR spectroscopy," *Cem. Concr. Res.*, vol. 34, no. 5, pp. 857–868, 2004.
- [151] J. Reinik *et al.*, "Alkaline modified oil shale fly ash: Optimal synthesis conditions and preliminary tests on CO_2 adsorption," *J. Hazard. Mater.*, vol. 196, pp. 180–186, 2011.
- [152] M. Zajac, A. Rossberg, G. Le Saout, and B. Lothenbach, "Influence of limestone and anhydrite on the hydration of Portland cements," *Cem. Concr. Compos.*, vol. 46, pp. 99–108, 2014.
- [153] B. Lothenbach, K. Scrivener, and R. D. Hooton, "Supplementary cementitious materials," *Cem. Concr. Res.*, vol. 41, no. 12, pp. 1244–1256, 2011.
- [154] B. Lothenbach and F. Winnefeld, "Thermodynamic modelling of the hydration of Portland cement," *Cem. Concr. Res.*, vol. 36, no. 2, pp. 209–226, 2006.
- [155] D. Damidot, S. Stronach, A. Kindness, M. Atkins, and F. P. Glasser, "Thermodynamic investigation of the $\text{CaOAl}_2\text{O}_3\text{CaCO}_3\text{H}_2\text{O}$ closed system at 25°C and the influence of Na_2O ," *Cem. Concr. Res.*, vol. 24, no. 3, pp. 563–572, 1994.
- [156] T. Matschei, B. Lothenbach, and F. P. Glasser, "The AFm phase in Portland cement," *Cem. Concr. Res.*, vol. 37, no. 2, pp. 118–130, 2007.
- [157] L. Stevula and J. Petrovic, "Formation of scawtite from mixtures of CaO , magnesite and quartz under hydrothermal conditions," *Cem. Concr. Res.*, vol. 11, pp. 549–557, 1981.

- [158] M. R. Hansen, H. J. Jakobsen, and J. Skibsted, “²⁹Si chemical shift anisotropies in calcium silicates from high-field ²⁹Si MAS NMR spectroscopy,” *Inorg. Chem.*, vol. 42, no. 7, pp. 2368–2377, 2003.
- [159] H. Ishida, S. Yamazaki, K. Sasaki, and Y. Okada, “α - dicalcium silicate hydrate: preparation, decomposed phase, and its hydration,” *J. Am. Ceram. Soc.*, vol. 76, no. 7, pp. 1707–1712, 1993.
- [160] M. Palou, V. Živica, and L. Bágel, “Influence of hydrothermal curing on G-oil well cement properties,” *Build. Res. J.*, vol. 60, no. 3, pp. 223–230, 2012.
- [161] S. Shaw, C. M. B. Henderson, and B. U. Komanschek, “Dehydration/recrystallization mechanisms, energetics, and kinetics of hydrated calcium silicate minerals: An in situ TGA/DSC and synchrotron radiation SAXS/WAXS study,” *Chem. Geol.*, vol. 167, no. 1–2, pp. 141–159, 2000.
- [162] S. Shibata, K. Kishi, K. Asaga, M. Daimon, and P. R. Shrestha, “Preparation and hydration of β-C₂S without stabilizer,” *Cem. Concr. Res.*, vol. 14, no. 3, pp. 323–328, 1984.
- [163] J. Haas and A. Nonat, “From C-S-H to C-A-S-H: Experimental study and thermodynamic modelling,” *Cem. Concr. Res.*, vol. 68, pp. 124–138, 2015.
- [164] E. Tajuelo Rodriguez, I. G. Richardson, L. Black, E. Boehm-Courjault, A. Nonat, and J. Skibsted, “Composition, silicate anion structure and morphology of calcium silicate hydrates (C-S-H) synthesised by silica-lime reaction and by controlled hydration of tricalcium silicate (C₃S),” *Adv. Appl. Ceram.*, vol. 114, no. 7, pp. 362–371, 2015.
- [165] A. V. Girão, I. G. Richardson, R. Taylor, and R. M. D. Brydson, “Cement

and concrete research composition , morphology and nanostructure of C – S – H in 70 % white Portland cement – 30 % fly ash blends hydrated at 55 ° C .,” *Cem. Concr. Res.*, vol. 40, no. 9, pp. 1350–1359, 2010.

- [166] P. Blanc, X. Bourbon, A. Lassin, and E. C. Gaucher, “Chemical model for cement-based materials: Thermodynamic data assessment for phases other than C-S-H,” *Cem. Concr. Res.*, vol. 40, no. 9, pp. 1360–1374, 2010.
- [167] D. A. Kulik, “Improving the structural consistency of C-S-H solid solution thermodynamic models,” *Cem. Concr. Res.*, vol. 41, no. 5, pp. 477–495, 2011.
- [168] S. Jia and I. G. Richardson, “Micro- and nano-structural evolutions in white Portland cement/pulverized fuel ash cement pastes due to deionized-water leaching,” *Cem. Concr. Res.*, vol. 103, 2017, pp. 191–203, 2018.
- [169] A. W. Harris, M. C. Manning, W. M. Tearle, and C. J. Tweed, “Testing of models of the dissolution of cements - Leaching of synthetic CSH gels,” *Cem. Concr. Res.*, vol. 32, no. 5, pp. 731–746, 2002.
- [170] A. Atkinson, J. A. Hearne, and C. F. Knights, “Aqueous chemistry and thermodynamic modelling of CaO-SiO₂-H₂O Gels,” *J. Chem. Soc. Dalton Trans*, pp. 2371–2379, 1989.
- [171] K. Suzuki, T. Nishikawa, H. Ikenaga, and S. Ito, “Effect of NaCl or NaOH on the formation of CSH,” *Cem. Concr. Res.*, vol. 16, no. 3, pp. 333–340, 1986.
- [172] E. Tajuelo Rodriguez, K. Garbev, D. Merz, L. Black, and I. G. Richardson, “Thermal stability of C-S-H phases and applicability of Richardson and Groves’ and Richardson C-(A)-S-H(I) models to synthetic C-S-H,” *Cem.*

Concr. Res., vol. 93, pp. 45–56, 2017.

- [173] J. Francis Young, “Investigations of calcium silicate hydrate structure using silicon-29 nuclear magnetic resonance spectroscopy,” *J. Am. Ceram. Soc.*, vol. 71, no. 3, p. C-118-C-120, 1988.
- [174] Y. Okada, K. Sasaki, B. Zhong, H. Ishida, and T. Mitsuda, “Formation processes of β -C₂S by the decomposition of hydrothermally prepared C-S-H with Ca(OH)₂,” *J. Am. Ceram. Soc.*, vol. 77, no. 5, pp. 1319–1323, 1994.
- [175] A. Atkinson, J. A. Hearne, and C. F. Knights, “Aqueous chemistry and thermodynamic modelling of CaO-SiO₂-H₂O gels at 80°C,” *HMIP-RR-91.045*, 1991.
- [176] M. Atkins, F. P. Glasser, L. P. Moroni, and J. J. Jack, “Thermodynamic modelling of blended cements at elevated temperatures (50-90°C),” *HMIP-RR-94.011*, 1994.